Data-driven and Hybrid Models for the Underwater Radiated Noise of Cavitating Marine Propellers

Miltiadis Kalikatzarakis

A thesis submitted in fulfillment of the requirements

for the degree of Doctor of Philosophy

Department of Naval Architecture, Ocean & Marine Engineering
University of Strathclyde, Glasgow

February 3, 2023

This thesis is the result of the author's original research. It has been composed by the author and has not been previously submitted for examination which has led to the award of a degree.

Signed: Miltiadis Kalikatzarakis

Date: February 3, 2023

Acknowledgements

Entities should not be multiplied beyond necessity.

William of Ockham

First and foremost, I would like to express my sincere gratitude to my supervisors Prof. Andrea Coraddu and Prof. Luca Oneto. Their endless dedication, knowledge, and particularly patience, made this journey possible. Without their continuous support and guidance throughout these years, the results presented in this work would not have been obtained.

I would also like to thank Prof. Stefano Gaggero, Prof. Giorgio Tani, and Prof. Diego Villa who significantly enriched this work by constantly providing invaluable input, comments, and feedback. Finally, a warm thank you to Prof. Mehmet Atlar, who kindly provided the experimental data that made this work possible.

Abstract

The sustainability of anthropogenic activities is a fundamental problem requiring a multidisciplinary approach in order to be properly addressed. Recently, underwater radiated noise has been categorized as a form of pollution, due to the substantial increase of underwater noise levels on oceans worldwide, with severe effects on the marine ecosystem. For propeller-driven vessels, cavitation is the most dominant noise source, producing both structure-borne and radiated noise. As such accurate predictions of the noise signature are fundamental for the design of silent, yet efficient, propellers.

In this respect, this work investigates a novel hybrid (combined physics-based and data-driven) model for the prediction of underwater radiated noise of marine propellers. By relying on both the engineering knowledge (through the physics-based model), and advanced statistical inference procedures (through the data-driven model), the hybrid model will be capable of providing an accurate, yet computationally cheap, assessment of the noise levels emitted by a cavitating marine propeller. The proposed model relies on a novel hybridization strategy that is able to truly blend the knowledge of the underlying physical phenomena with information contained in historical data. This strategy allows the development of that models able to properly, i.e., physically plausibly, extrapolate as physics-based models, while being extremely accurate and computationally inexpensive as data-driven models. In particular, knowledge of the underlying physical phenomena is leveraged during model structure, model building, and in model enrichment: a dedicated feature engineering process is considered to extract meaningful information from available experimental data, as well as the noise estimates of a computationally efficient physics-based model. Everything is empowered by state-of-the-art learning algorithms from the field of Machine Learning that take advantage of

all information sources.

The proposed model is tested on a series of complex extrapolation scenarios, in which the numerical predictions are compared with measurements collected in an extensive experimental campaign conducted at the Emerson Cavitation Tunnel of Newcastle University. The results support the feasibility of the proposed approach in all scenarios considered. The proposed model shows enhanced capabilities in predicting the underwater radiated noise levels: It commits low errors that are certainly acceptable during the early stage design process, and delivers predictions that are in agreement with state-of-the-art engineering knowledge of the underlying physical phenomena.

Contents

List of Figures

List of Tables

Nomenclature

Abbreviations

1D	Mono-Dimensional
2D	Two-Dimensional
3D	Three-Dimensional
ANN	Artificial Neural Network
BAR	Blade Area Ratio
BBO	Black Box Optimisation
BDT	Binary Decision Tree
BEM	Boundary Element Method
BPF	Blade Passing Frequency
BTS	Bootstrap
CFD	Computational Fluid Dynamics
CLT	Contracted and Loaded-Tip propellers
CPP	Controllable Pitch Propeller
DARPA	Defence Advanced Research Projects Agency
DDM	Data-Driven Model
DES	Detached Eddy Simulation
DFT	Discrete Fourier Transformation
DNS	Direct Numerical Simulation
DTMB	David Taylor Model Basin
ECT	Emerson Cavitation Tunnel
EE	Error Estimation
ELM	Extreme Learning Machine
EM	Ensemble Methods
ERM	Empirical Risk Minimisation
ETV	Empirical Tip Vortex Model
EU	European Union
F1A	Farassat formulation 1A of the FWH
FEM	Finite Element Method
FFT	Fast Fourier Transformation
FR	Feature Ranking
FRV	Fisheries Research Vessel
FWH	Ffowcs Williams and Hawkings acoustic analogy
GPR	Gaussian Process Regressor
HM	Hybrid Model
HO	Holdout
HSVA	Hamburg Ship Model Basin
IMO	International Maritime Organisation
INSEAN	Italian National Institute for Naval Architecture Studies and Testing

ITTC International Towing Tank Conference

kCV k-fold Cross Validation

KM Kernel Method

KRLS Kernel Regularised Least Squares

LES Large Eddy Simulation

LOGO Leave One Geometry Out

LOO Leave-One-Out

LORSO Leave One Rotational Speed Out

LOWO Leave One Wakefield Out

LSM Lifting Surface Method

MAE Mean Absolute Error

MAPE Mean Absolute Percentage Error

ML Machine Learning

MLP Moderately Loaded Propeller

MS Model Selection

MSPS Meridian Standard Propeller Series

OF Objective Function

p-FWH Permeable FWH

PDE Partial Differential Equation

PDF Probability Density Function

PDR Pitch-to-Diameter Ratio

PM Physics-based Model

PPMCC Pearson Product-Moment Correlation Coefficient

PPTC Potsdam Propeller Test Case

PSO Particle Swarm Optimisation

RANS Reynolds-Averaged Navier-Stokes

ReLU Rectified Linear Unit

RF Random Forest

RM Resampling Method

ROPAX Roll-on / Roll-off Passenger vessel

SGD Stochastic Gradient Descent

SOLAS International Convention for the Safety of Life at Sea

SPL Sound Pressure Level

SRM Structural Risk Minimisation

SVA Schiffbau-Versuchsanstalt Potsdam

TPK Test against Prior Knowledge

TVC Tip Vortex Cavitation

TVI Tip Vortex Index

URN Underwater Radiated Noise

VLM Vortex Lattice Method

Greek Symbols

α Angle [deg]

$\boldsymbol{\alpha}$ Parameters of the KRLS model

α Confidence level [%]

β Gas - vapour fraction [–]

Γ Circulation [m^2/s]

γ Gaussian kernel hyperparameter [–]

δ Parameter of the Adam algorithm [–]

ϵ Learning rate of the ANN

ζ_i Parameters of the Adam algorithm

η Efficiency

θ Angular position of the key blade [deg]

ι Dimensionality of input space $\mathcal{X}$

κ Probability density function

λ	Hyperparameter regulating the under-fitting over-fitting trade-off
μ	Rule associating $\mathcal{X} \to \mathcal{Y}$
ν	Kinematic viscosity [m2/s]
ρ	Density [kg/m^3]
σ	Cavitation index [-]
$\mathtt{\sigma}$	Standard deviation
τ	Thickness [m]
$\boldsymbol{\phi}$	Feature mapping from $\mathcal{X}$ to $\mathcal{G}$
ϕ	Perturbation potential [–]
φ	Activation function of the ELM
$\boldsymbol{\xi}$	Parameters of the ANN model
$\boldsymbol{\psi}$	Activation function of the ANN
ω	Angular velocity [rad/s]

Roman Symbols

$\mathscr{A}$	Learning algorithm
$\mathtt{A}$	Activation matrix of the ELM
$\mathtt{a}$	Cosine Fourier coefficient
a	Area [m^2]
b	Bias
$\mathbb{B}$	Batch
$\mathcal{B}$	Bubble set
$\mathtt{b}$	Sine Fourier coefficient
$\lfloor bn \rfloor$	Bootstrap samples to construct each BDT
c	Coefficient
$\mathtt{C}$	Complexity measure
$\mathtt{c}$	Propeller section chord [m]
C_p	Pressure coefficient
$\mathtt{CI}$	Confidence Interval
$\boldsymbol{d}$	Distance between two points in computation domain [m]
$\mathtt{d}$	Dimensionality of feature space $\mathcal{G}$ of KMs or ELMs
D	Diameter [m]
$\mathcal{D}_n$	Dataset of n samples
$\boldsymbol{e}$	Unit normal [–]
$\mathcal{F}$	Hypothesis space
$\mathtt{f}_i$	Composition of functions for a multi-layered ANN
f	Frequency [Hz]
g	Acceleration of gravity [m/s^2]
$\mathcal{G}$	Feature space
h	Model
$\mathcal{H}$	Set of hyperparameters
$\mathfrak{H}$	Set of $\mathcal{H}$
$\mathtt{h}_i$	Number of neurons on layer i of the ANN or ELM
$\mathtt{h}$	Propeller reference point immersion.
I	Identity matrix
$\mathtt{I}$	Indicator function
$\boldsymbol{I}$	Feature importance vector
J	Advance ratio [–]
k	Number of folds for kCV
$\boldsymbol{K}$	Kernel matrix
$\mathtt{K}$	Kernel function
K_q	Torque coefficient [–]
K_t	Thrust coefficient [–]
l	Length [m]

ℓ	Loss function
$\hat{\mathtt{L}}$	Empirical error
$\mathcal{L}_{\ell}^{r}$	Learning set r containing ℓ samples of $\mathcal{D}_n$
$\mathtt{L}$	Generalisation error
L	Number of layers composing the ANN
m	Parameter of the β-distribution
$\hat{\mathtt{m}}$	Bias-corrected $\mathtt{m}$
$\mathtt{M}$	Error metric
$\mathtt{m}$	Moving average of the gradients of the ANN's loss function w.r.t. $\boldsymbol{\xi}$
n	Number [–]
$\mathtt{n}$	Rotational speed of the propeller
o	Dimensionality of output space $\mathcal{Y}$
p	Pressure [Pa]
$\mathtt{p}$	Propeller section pitch [m]
Q	Torque [Nm]
r	Radial distance [m]
$\mathcal{R}$	Region of BDT
$\mathtt{r}$	Propeller section rake [m]
s	Wetted surface [m^2]
$\boldsymbol{s}$	Parameter vector
$\mathtt{s}$	Propeller section skew [deg]
$\boldsymbol{S}$	Noise spectrum [dB]
$\mathcal{S}$	Parameter space
T	Thrust [N]
t	Time [sec]
$\mathcal{T}_{t}^{r}$	Test set r containing t samples of $\mathcal{D}_n$
u	Velocity [m/s]
$\hat{\mathtt{u}}$	Bias-corrected $\mathtt{u}$
$\mathcal{U}$	Uniform distribution
$\mathtt{u}$	Moving average of the squared gradients of the ANN's loss function w.r.t. $\boldsymbol{\xi}$
v	Volume [m^3]
$\mathcal{V}_{v}^{r}$	Validation set r containing v samples of $\mathcal{D}_n$
$\boldsymbol{w}$	Weight vector
$\boldsymbol{W}$	Weight matrix
$\mathcal{W}$	Parameter space of the ANN
$\boldsymbol{x}$	Input vector
$\mathcal{X}$	Input space
$\boldsymbol{y}$	Output vector
$\mathcal{Y}$	Output space
$\boldsymbol{z}$	Point in computational domain
$\mathtt{z}$	Propeller section camber [m]
Z	Propeller blades [-]

Superscripts

$*$	Normalised value
$\diamond$	Optimal value
1	1 Hz band
C	Class
ι	Dimensionality of input space $\mathcal{X}$
o	Dimensionality of output space $\mathcal{Y}$
P	Panel
p	parameters
q	Time-steps
r	Resampling index

s	Radial sections
t	Number of samples of test set $\mathcal{T}_t^r$
u	Chord-wise sections

Subscripts

0	Initial condition
∞	Undisturbed quantity in the fluid domain
θ	Tangential component
G	Geometric
ℓ	Number of samples of learning set $\mathcal{L}_\ell^r$
n	Rotational speed of the propeller
r	Resampling index
s	Split
t	Number of samples of test set $\mathcal{T}_t^r$
v	Number of samples of validation set $\mathcal{V}_v^r$
a	Advance
atk	Attack
atm	Atmospheric
B	Blade
b	Bubble
bo	Bubble oscillations
bp	Blade passage
btc	Batch
bw	Bubble wall
c	Cavity
d	Delay
e	particle
eq	Equilibrium
f	Fluid
g	Gas
h	Propeller hub
hi	High
i	Internal
lo	Low
max	Maximum
n	Number of samples of $\mathcal{D}_n$
o	Open water
obj	Objective
P	Proctor vortex
p	Propeller
pi	Polytropic index
pl	Pressure level
ref	Reference value
rel	Relative
rms	Root mean square value
s	Sound
st	Surface tension
sw	Swarm
T	Tait's law of compressibility
te	Trailing Edge
tf	Total field
tip	Propeller tip
ts	Timestep
v	Vapour
vc	Vortex cavity
w	Wakefield
x	Axial component

Other Symbols

$(\cdot \odot \cdot)$	Element-wise (Hadamard) product
$(\cdot \oslash \cdot)$	Element-wise (Hadamard) division
$(\cdot)^{+}$	Moore-Penrose pseudo-inverse matrix
$(\cdot)^{\intercal}$	Matrix or vector transposition
$(\cdot)^{\odot(\cdot)}$	Element-wise raising to power
$\nabla(\cdot)$	Vector differential operator

Chapter 1

Introduction

Abstract

This chapter provides background information and the motivations behind this work. A brief discussion on the problem of noise emissions from shipping is presented, and the contribution of marine propellers is discussed. The need for modeling methodologies that can accurately predict underwater radiated noise from marine propellers is also addressed, along with open problems faced by designers and researchers in the field. In this context, the main aim and objectives of this work are outlined, demonstrating the ambitions and expectations of the research performed.

1.1 Background and Motivation

The sustainability of anthropogenic activities is nowadays a fundamental problem requiring a multidisciplinary approach in order to be properly addressed. In a broad sense, sustainability concerns the control of the adverse effects on the environment caused by human activities[1]. Within the maritime industry, the impact of vessels on the environment was considered just in terms of atmospheric pollutant formation from the prime movers [19], release of toxic compounds from hull coatings [20], or importation of exotic biological species through ballast water [21] and biofouling [22].

Underwater Radiated Noise (URN) was just recently categorized as a form of pollution [23] due to the substantial increase of noise pollution on oceans worldwide [24].

[1] `https://ec.europa.eu/info/strategy/international-strategies/sustainable-development-goals`

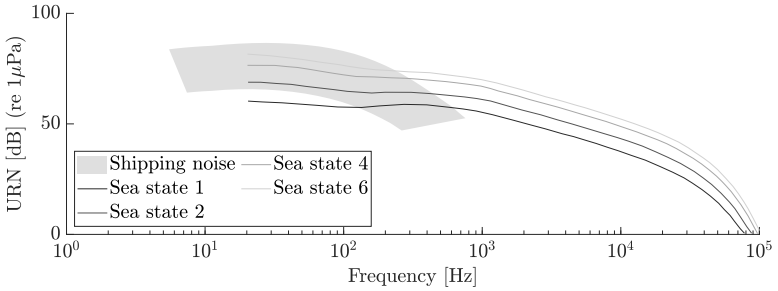

Figure 1.1: Generalised ocean ambient noise spectra levels for a deep-water site with the receiver located at 1000[m] depth (adapted from [1]).

While multiple noise sources exist in the ocean, both natural and anthropogenic, shipping as a whole contributes to a large proportion of the total ambient sound level, particularly in the frequency range between 10 - 1000[Hz]. An impression of the magnitude of shipping noise is presented in Figure 1.1, which quantifies the effect of shipping- and wind-related noise at four different sea-states. It has been recognised that URN has severe effects on the marine ecosystem [25, 26], and also affects the crew and passenger comfort [27]. Several regulatory bodies have urged the industry to address the harmful effects of noise pollution [28, 29] and take precautionary measures [30]. In addition, apart from environmental concerns, URN abatement is compulsory in maritime warfare. Navies are conducting continuous research and development activities in stealth technology optimisation and quiet submarines, with the aim of reducing their noise signature as it determines their detectability, operability, and survivability [31, 32]. From an engineering standpoint, the feasibility of designing vessels with underwater noise requirements depends on the availability of appropriate numerical methods that will allow the designer to assess each design's radiated noise as early as possible in the ship design process, and make informed decisions on how to re-assess and adjust the design as needed.

In general, the noise signature of a seagoing vessel is composed of a variety of sources including rotating machinery, hull-form, and propellers [33]. Among these, the propeller is the most significant noise contributor and the subject of increased interest in academia and the industry [34]. Non-cavitating propellers generate the highest noise levels at frequencies below 200[Hz] while cavitating propellers can emit

noise up to frequencies of 1[MHz] dominating the audible noise spectrum [34, 35]. As a consequence, a considerable amount of effort has been spent in investigating and implementing propeller URN mitigation strategies, primarily through the design of novel propeller geometries [36–41].

Naturally, the feasibility assessment of any potential solution requires the accurate and timely evaluation of generated URN at a variety of operating conditions. Currently, the primary means of assessing URN in the maritime context are model scale tests and numerical models. Model scale tests in cavitation tunnels or de-pressurised towing tanks are considered to be the most reliable method. However, these tests are generally expensive and time-consuming, which renders their use impractical during the early design stages where numerous iterations are required [42].

Numerical methods are available and can be employed for URN prediction, with a large part of ongoing research focusing on Computational Fluid Dynamics (CFD) models [42, 43]. These usually couple high-fidelity CFD methods, such as Large Eddy Simulation (LES) or Detached Eddy Simulation (DES), with the Ffowcs Williams & Hawkings (FWH) acoustic analogy [44, 45]. Although capable of providing accurate predictions, most state-of-the-art methods are still computationally expensive, and their usage remains limited outside academia [42, 46]. Furthermore, conducting trade-off analyses and performing optimisation or sensitivity studies with these models still remains a challenging endeavour [47–49].

1.2 Research aim and objectives

These considerations have guided the focus of this work towards the following research question:

Research Question. *Is it possible to develop a numerical method for the noise prediction of cavitating marine propellers, using strictly information available at the early stage design process, that is at least as accurate as, and computationally cheaper than, current state-of-the-art CFD methods?*

The vision is that, if such a method is indeed possible to develop, it will facili-

tate optimisation and trade-off studies to be performed with reasonable computational effort, which will lead to more silent propeller designs.

To answer this research question, the following objectives have been defined:

1. Review the state-of-the-art numerical models available in the literature for URN prediction of cavitating marine propellers.
2. Explore and identify applicable approaches, and assess their usefulness for the early propeller design stage.
3. Implement the chosen approach.
4. Identify appropriate analyses that can quantify the accuracy, applicability, robustness, and interpretability of the proposed approach.
5. Demonstrate the applicability of the proposed approach through several validation studies reflecting realistic scenarios applicable to academia and the industry.
6. Highlight the limitations and problems of the proposed approach, and suggest improvements and research questions that need to be addressed in the future.

1.3 Dissertation layout

This work is organised in 9 chapters. The current chapter provided a brief introduction to the shipping noise problem and its relevance, a small summary of the current research efforts, and addressed the aim and main objectives of this work.

Following, Chapter 2 discusses more extensively the problem of noise radiation from shipping in general, and from cavitating marine propellers in particular. The impact of shipping noise in the marine environment is discussed, and the contribution of marine propellers and cavitation to this problem is addressed. Furthermore, the underlying physical processes governing sound generation and radiation from seagoing vessels and propellers are presented and discussed in the context of shipping noise.

Chapter 3 provides a comprehensive review of the state-of-the-art approaches related to the prediction of URN from marine propellers in cavitating and non-cavitating conditions. The advantages and disadvantages of the various approaches are presented and open challenges are identified and discussed, justifying the selection of the proposed approach.

Chapter 4 discusses the methodology proposed in this work. Namely, it provides a short summary of the PMs and DDMs that comprise the HM, and discusses in detail the model selection and error estimation process for the HM in its entirety. In addition, it describes the feature engineering process, which aims to provide an information-rich, yet compact representation of all the aspects that govern URN emitted from cavitating marine propellers and the formation of the URN spectra. In addition, it presents a series of case studies conducted with the aim of verifying the various sub-models that comprise it. When possible, the predictions of the various models will be compared directly with experimental data from the pertinent literature. If experimental data is not available, numerical experiments will be conducted with the aim of confirming the findings of past studies regarding the behavior of each sub-model, and verifying the quality of the obtained predictions.

Chapter 5 discusses the set of case studies employed to demonstrate the feasibility of the proposed approach, and to quantify the accuracy of the proposed models. Whereas most studies in the literature conduct comparisons between experimental and numerical data on a limited set of cases, more than 430 experiments from two universities have been made available and are utilised in this work.

Chapter 6 provides a detailed analysis and comparison between the experimental results of the case studies detailed in Chapter 5, and the numerical results of the methodology underlined in Chapter 4.

Finally, Chapter 7 concludes this work by discussing the limitations of the proposed approach, and open questions that need to be addressed in future works.

1.4 Summary

In this chapter, background information and the motivations behind this work have been discussed. Open problems have been briefly addressed, which form the basis behind the aim and main objectives of this work, and the layout of this dissertation has been provided. In the following chapter, a more critical and complete overview of the noise pollution problem is given.

Chapter 2

Marine Propeller Noise

Abstract

This chapter provides a background to the problem of noise radiation from shipping in general, and from cavitating marine propellers in particular. The impact of shipping noise in the marine environment is discussed, and the contribution of marine propellers and cavitation to this problem is addressed. The underlying physical processes governing sound generation and radiation from seagoing vessels and propellers are also presented, and are put into the context of shipping noise.

2.1 Introduction

This chapter provides an overview to the topic of marine propeller noise, discussing its societal importance and historical perspectives, and the underlying physics that govern the relevant phenomena. It serves as a formal introduction to this topic, and allows the reader to fully appreciate its relevance and complexity. Firstly, the fundamental principles of noise generation and radiation of sound are highlighted in Section 2.2. Subsequently, Section 2.3 discusses the impact of shipping noise on the marine environment, covers the relevant regulatory framework, and puts the principles of hydroacoustics into perspective. Section 2.4 focuses on the noise emitted by marine propellers, as one of the most important contributors to shipping noise. Finally, Section 2.5 concludes this chapter.

2.2 Fundamentals of hydroacoustics

Hydroacoustics is one of the fastest-growing fields of research in the science of acoustics. Since the beginning of the 20^{th} Century, partly motivated by two world wars and the Cold War, and strongly supported by the developments in computer technology, a fast increase in experimental and theoretical investigations has taken place in all aspects of hydroacoustics, and even new areas of research, like acoustical oceanography and seismo-acoustics, have been formed [50]. Nevertheless, the now-widespread field of hydroacoustics started nearly $2,300$ years ago with Aristotle (384 - 322 B.C.), who may have been the first to note that, similar to air, sound could be heard underwater.

In essence, sound is a mechanism of energy transfer through a medium via propagating pressure, density, and velocity fluctuations. These fluctuations are of small amplitude compared to the state of the rest of the fluid, and they are governed by the same properties of the medium in which they occur. Their governing equations are the equations of continuum mechanics, equally applicable to gases, liquids, and solids. Namely, the mass, momentum, and energy equations, as well as the relevant thermodynamic principles [51].

The basic equations of acoustics follow from the linearisation of the full equations of mass and momentum conservation, and the equation of state. Assuming a Newtonian fluid, and neglecting all molecular relaxation and diffusion effects, thus allowing the stress on any fluid element to consist simply of a normal pressure, and allowing pressure to be a function of density only, the inhomogeneous wave equation arises [52]

$$\left(\nabla^2 - \frac{1}{u_s^2}\frac{d^2}{dt^2}\right)\rho(\boldsymbol{z},t) = F(\boldsymbol{z},t), \tag{2.1}$$

which describes the propagation of sound due to an arbitrary source $F(\boldsymbol{z},t)$ located in a point $\boldsymbol{z}$ of the fluid domain, and whose contribution tends to zero in the far-field. In Equation (2.1), u_s refers to the local sound velocity, and ρ corresponds to the instantaneous density fluctuation constituting a sound wave [52].

In practice, most acoustic sources present themselves as a superposition of idealised noise sources. These idealised sources include the monopole, dipole, and quadrupole.

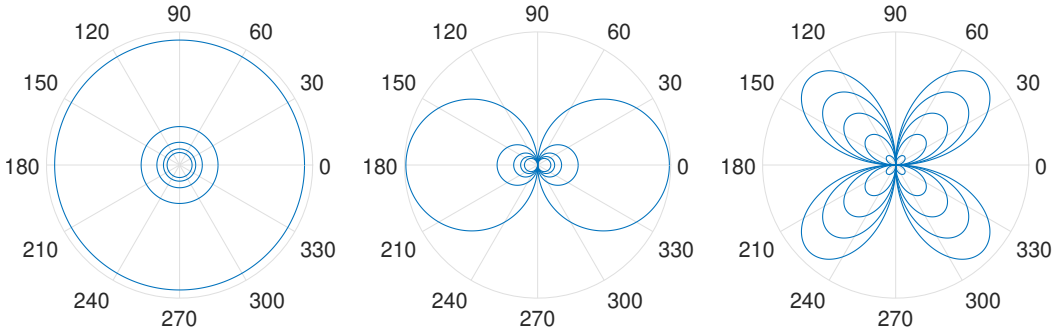

(a) Monopole. (b) Dipole. (c) Quadrupole.

Figure 2.1: Noise directivity patterns of idealised noise sources.

The monopole source can be considered as a pulsating sphere of a certain radius, periodically pushing the fluid away from and attracting it towards to the centre of the sphere, generating pressure waves equally in all directions, according to Figure 2.1(a). A dipole source can be formed by displacing two oppositely signed monopoles (i.e. one is expanding while the other is contracting) located a short distance apart from each other, thus generating pressure waves according to Figure 2.1(b). Finally, a quadrupole source is generated by two oppositely signed dipoles, located a short distance apart from each other. The pressure waves generated by a quadrupole are presented in Figure 2.1(c).

The amount of noise generated by an acoustic source depends on the amplitude of the pressure wave generated, which is proportional to the strength of the source, the distance to the receiver, as well as the acoustic energy absorbed by the medium that the sound wave travels on, which tends to damp the sound waves away from the source [53]. The source strength is primarily dictated by the physical phenomena causing the sound, for instance cavitation or turbulence in the context of this work. Absorption losses are dependent on the fluid's physical properties tied to the dissipation of the particle motions [53]. This is a brief and simplified overview of the basic principles governing the generation and radiation of sound, or noise (unwanted sound), in any medium. In this work, focus is given in the URN of vessels in general, and of cavitating propellers in particular, both of which are discussed in the following sections.

2.3 Shipping noise

The need for silent vessels in underwater warfare and other military applications always had a significant impact on the developments in hydroacoustics. Navies are conducting continuous research and development activities in stealth technology optimisation and quiet submarines, with the aim of reducing their noise signature, which directly affects their detectability, operability, and survivability [32]. This relation has frequently given this field a heavy military element, which oftentimes overshadows the many important civil applications of hydroacoustics.

With over 80% of global trade by volume, or 70% by value, being transported by 94% of the world's fleet [54], the impact of the maritime industry on the environment is increasingly monitored and controlled. Up to now, the impact of vessels on the environment was considered just in terms of atmospheric pollutant formation from the prime movers [19], release of toxic compounds from hull coatings [20], or importation of exotic biological species through ballast water [21] and biofouling [22]. URN was just recently categorized as a form of pollution due to the substantial increase of noise pollution on oceans worldwide [23]. It is known to affect crew and passenger comfort [27], and to have severe effects on the marine ecosystem [25, 26]. It is also known that the noise levels of most sources on-board dominate ambient noise levels in many regions around the world [55], and their frequency overlaps with the acoustic range of most marine mammals [56]. Furthermore, an increasing trend on the overall noise levels has also been observed since 1950, with measurements conducted in the Pacific Ocean showing that these levels have been increasing by about 3[dB] per decade [57], which corresponds to a doubling of the noise intensity every 10 years. Considering that, due to the high sound velocity in water, a single vessel can be heard at a distance of tens of kilometers [55], the magnitude of the consequences from shipping noise is significant.

2.3.1 Regulatory framework

For these reasons, several regulatory bodies have urged the industry to address the harmful effects of noise pollution [28] and take precautionary measures [30]. For in-

stance, the issue of URN and its impact on marine mammals was first raised by the International Maritime Organisation (IMO) in 2004 [58], where it was noted that continuous anthropogenic noise in the ocean was primarily generated by shipping. In 2008 the IMO Marine Environmental Protection Committee (MEPC) agreed to develop *non-mandatory* technical guidelines to minimise the introduction of incidental noise from commercial shipping operations into the marine environment, in an aim to reduce potential adverse impacts on marine life.

Mandatory restrictions by IMO were first imposed in 2012, with the adoption of a regulation [59] during the International Convention for the Safety of Life at Sea (SOLAS) to require new-build vessels to reduce on-board noise and to protect personnel from noise, in accordance with the "Code on noise" levels on-board. This Code sets out mandatory maximum noise level limits for machinery spaces, control rooms, workshops, accommodation, and other spaces on-board vessels. In addition, in 2014 IMO approved guidelines on the reduction of URN from commercial shipping, to address adverse impacts on marine life. However, given the complexities associated with ship design and construction, these guidelines focused mainly on the primarily sources of URN, namely the propellers, hull-form, on-board machinery, and provided various operational and maintenance recommendations [60]. In the latest MEPC 76, held in June 2021, several amendments to mandatory instruments were adopted [61], none related to URN. Nonetheless, the Committee agreed to commence further work on the topic, agreeing to include a new output on review of the guidelines adopted in 2014, and the identification of next steps, with a target completion in 2023.

IMO is not the only regulatory body providing guidelines and imposing restrictions related to URN from the shipping sector. For instance, the European Union (EU) has defined the Marine Strategy Framework Directive [62] which aims to achieve a good environmental status, including URN limits in the European marine waters. Moreover, various monitoring campaigns of URN are currently under development as part of the QuiteMED2[1] and the JOMOPANS[2] projects. Canada, as of 2019, has also adopted measures to reduce URN levels in the British Columbia region [63], with further rec-

[1] `https://www.quietmed2.eu`
[2] `https://www.jonasproject.eu`

ommendations being expected near the end of 2023.

As a consequence, several classification societies have now introduced the "silent" class notation, with the first one being Det Norske Veritas in 2010 [64, 65], followed by Bureau Veritas which issued rule NR614 on URN in 2014 [66], specifying noise limits for "URN-controlled" and "URN-advanced" vessels, Registro Italiano Navale in 2017 with the silent DOLPHIN class [67], American Bureau of Shipping [68] making a distinction on the noise limits between "commercial" and "research" vessels, and China Classification Society that also distinguished vessels in three categories [69] in 2018. Similar distinction criteria were issued by Lloyd's Register in 2018 [70], making a distinction between "transit", "quiet", and "research" vessels.

2.3.2 Noise signatures of seagoing vessels

According to a comprehensive review conducted by the International Towing Tank Conference (ITTC) Specialist Committee on Hydrodynamic Noise [17], the noise signature of a seagoing vessel is composed of a variety of sources related to rotating machinery, hullform, and propeller operation, and covers a wide range of frequencies, as presented in Table 2.1.

Noise levels for large commercial vessels lie within the range of 180 - 195[dB], with maximum levels occurring in frequencies between 10 - 125[Hz], resulting from the vibrations of propulsion-related machinery [28, 71]. These levels are dependent on the vessel type, speed, load, operating mode, and implementation of noise-reduction measures. The differences per vessel type and vessel speed can be observed in Figure 2.2, which provides recorded noise levels for 71 vessels of 9 types at different cruising speeds. These obtained from the Ship Underwater Radiated Noise Database of the University of Southampton developed as part of the EU-funded SONIC project[3]. Examples of typical URN spectra are illustrated in Figure 2.3 on one third-octave band. Figure 2.3(a) corresponds to the 173[m] Overseas Harriette cargo vessel [72], and Figure 2.3(b) to the 44.5[m] Hugh R. Sharp Research vessel [73]. As can be observed from Figure 2.3(a), an increase in vessel speed results in an increase of the noise levels in most frequencies.

[3] `https://web-archive.southampton.ac.uk/vesselnoise.soton.ac.uk/index.html`

Table 2.1: Dominant sources of URN on a modern vessel [17].

Source	Frequency range		Impact	
	Low [Hz]	High [kHz]	Environment	Vessel
Propeller & appendage-related sources				
Non-cavitating tonal components	Blade-passing frequencies		Low / medium	High
Singing	100	2	High	High
Non-cavitating broadband noise	1	20	Low	Low
Cavitating tonal components	Blade-passing frequencies		High	High
Appendage cavitation	100	20	Medium	Medium
Hullform-related sources				
Propeller-hull interaction	Natural frequency		Low	High
Wave breaking	100	10	Low	Low
Slamming	1	0.1	Low	Low
Propulsion and electric power generation				
Sea water cooling systems	100	10	Medium	Medium
Main engines	1	0.5	Medium	High
Transmission systems	10	1	Low	Medium
Auxiliary engines	10	2	Low	Medium
Other critical systems				
Active sonar (military)	100	50	High	Medium
Active sonar (echo-sounder)	10	30	Low	Low
Active sonar (navigation)	10	100	Low	Low
Airguns	1	0.1	High	Low

Below the cavitation inception speed (10[kn]), the highest URN levels occur due to the propulsion-related equipment on-board at the lower end of the frequency spectrum. As speed increases above cavitation inception, the high-frequency noise is dominated by cavitation phenomena, whereas the low-frequency noise occurs due to both machinery equipment and cavitation. At the highest vessel speed (16[kn]) the URN spectrum is dominated in its entirety by cavitation noise. Similar results have been observed for small and medium-size vessels, such as tugboats, supply, fishing, and research vessels, which typically emit noise levels in the range of 165 - 180[dB]. Nevertheless, while broadband noise levels are usually lower for large commercial vessels, small and medium-sized vessels can produce noise of sufficient level to contribute to marine ambient noise under unfavourable conditions [74]. This can be seen in Figure 2.3(b), which demonstrates the increased noise levels occurring at higher vessel speeds, which were attributed to propeller cavitation.

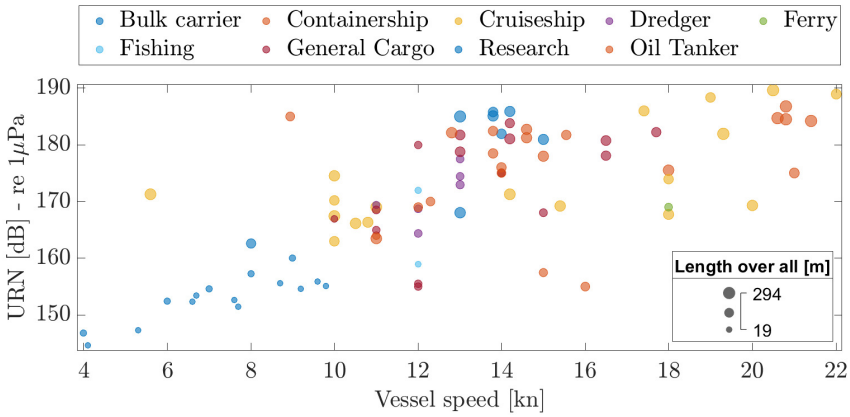

Figure 2.2: Overall broadband noise levels for various vessel types and speeds.

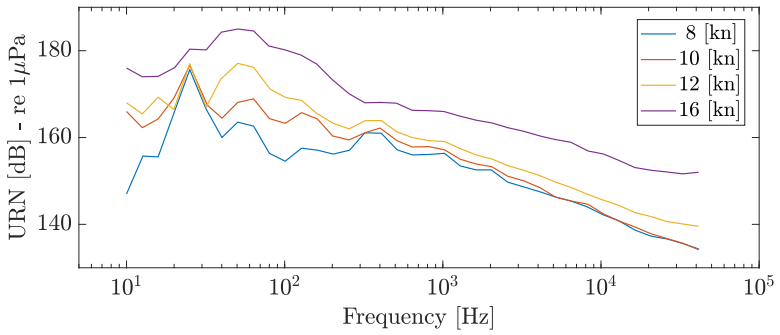

(a) Overseas Harriette cargo vessel.

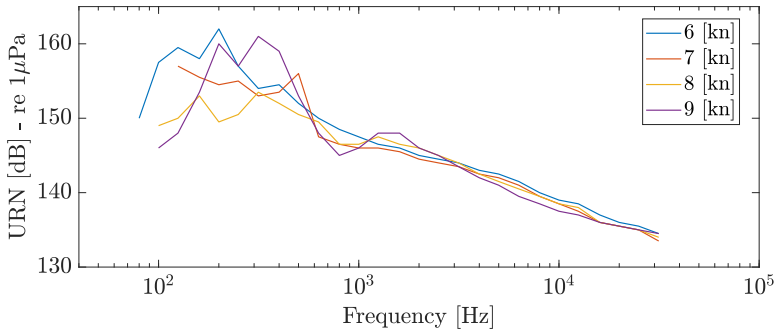

(b) Hugh R. Sharp research vessel.

Figure 2.3: Sample URN spectra of various vessels at different vessel speeds.

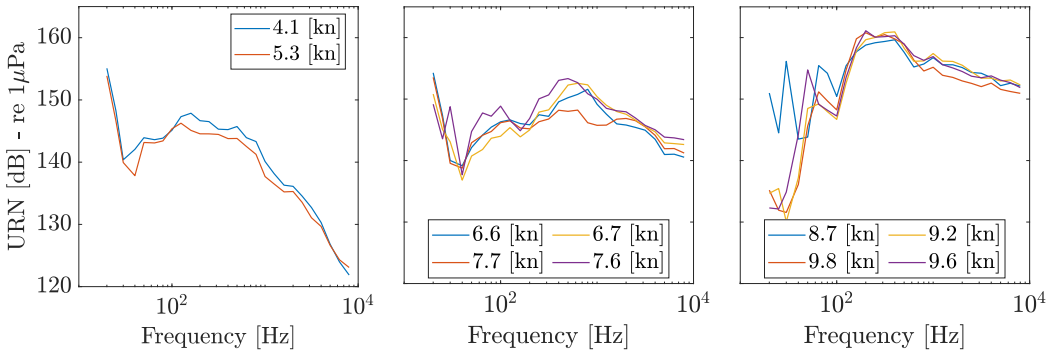

(a) No cavitation. (b) Tip vortex cavitation dominant. (c) Sheet cavitation dominant.

Figure 2.4: Sample URN spectra of the Princess Royal research vessel at various vessel speeds and cavitation conditions

A more clear example of the effects of propeller cavitation on URN is provided in Figure 2.4, which presents the URN spectra recorded by Brooker and Humphrey [75] on the 18.8[m] Princess Royal research vessel under various operating conditions. More specifically, Figure 2.4(a) presents the measured URN spectra under non-cavitating conditions, whereas the effects of Tip Vortex Cavitation (TVC) and sheet cavitation are given in Figures 2.4(b) - 2.4(c), respectively. As can be observed, for speeds lower than 6[kn] the vessel operates in non-cavitating conditions, with the overall broadband noise levels lying below 150[dB]. However, as speed increases cavitation starts to occur on the propellers, with TVC being observed for speeds between 6 - 8[kn], with a considerable increase on the noise levels, especially at the higher end of the spectrum. When speed further increases above 8[kn], sheet cavitation occurs, which clearly dominates the entire URN spectrum, highlighting the significance of propeller cavitation as a noise source.

2.4 Marine propeller noise

As discussed in Section 2.3.2, the propeller is the most significant noise contributor, especially under cavitating conditions. Naturally, it has been the subject of increased interest in academia and industry [76], and a considerable amount of effort has been spent in investigating and implementing propeller URN mitigation strategies [36–41]. Nevertheless, there is a natural tension between the need for silent yet efficient propellers that

requires finding the best trade-off for the case study under investigation [42, 46–49].

In general, the noise contribution from a propeller is divided into two types: non-cavitating, and cavitating noise. Non-cavitating propellers generate the highest noise levels at frequencies below 200[Hz] while cavitating propellers can emit noise up to frequencies of 1[MHz], dominating the audible noise spectrum [34, 35]. Until recently, propeller designers were trying to avoid cavitation for the widest possible range of operating conditions. However, the recent trends for high propeller loads have made this design philosophy practically unfeasible to achieve [34]. As such, both types of noise are important.

These types are caused by 5 physical phenomena [34]:

- The displacement of the water by the propeller blade profile,
- the pressure difference between the suction and the pressure surfaces of the propeller blade while they are rotating,
- the flow over the surface of the propeller blades,
- the periodic fluctuation of the cavity volumes caused by the operation of the blades in the non-uniform wakefield behind the vessel,
- the sudden collapse processes involved in the life of a cavitating bubble or vortex.

The first three phenomena cause the non-cavitating noise, which is always present in the operation of a marine propeller, whereas the latter two correspond to cavitation-dependent phenomena, causing the propeller to experience cavitation, and naturally emit cavitating noise.

2.4.1 Non-cavitating noise

In its non-cavitating state, propeller URN is composed of distinct tones associated with the Blade Passing Frequency (BPF) and its harmonics, also known as *tonal noise*, along with the broadband noise at higher frequencies, up to approximately 20[kHz]. Propellers normally operate behind a vessel. The presence of the vessel causes non-uniform inflow upstream of the propeller, which makes the latter operate in a circumferentially varying wakefield. This wakefield is causing fluctuations in the angle of attack of the blades, which in turn result in fluctuating loads acting on the blades. These loads

cause tonal noise, which is of dipole nature, and generally does not exceed 20[Hz] [34].

Broadband noise consists of components derived from inflow turbulence into the propeller, and various boundary layer and edge effects [34]. These sources are of quadrupole nature and their contribution to the acoustic signature of vessel is generally comparable to the contributions of rotating machinery on-board. Naturally, their relative importance may vary depending on the case study under investigation and the considered frequencies, but non-cavitating noise is less intense, and of less impact compared to a cavitating propeller.

2.4.2 Cavitating noise

When cavitation occurs on a propeller it induces low-frequency and broadband noise. Their frequency ranges between 5[Hz] - 100[kHz], with maximum noise levels occurring at approximately 50[Hz] [77]. In order to introduce the mechanisms causing cavitating noise, the phenomenon of propeller cavitation is briefly discussed.

2.4.2.1 Propeller cavitation

Cavitation is a general fluid mechanics phenomenon that refers to the rapid formation and collapse of vapour pockets in a fluid. This formation occurs due to local changes in the fluid's velocity and pressure, caused by the relative motion of a solid body. In fact, if the local pressure of the fluid reduces to values lower than its vapour tension, the vapour pockets will occur. They are generally unstable, and prone to return to the liquid phase if they pass to a higher pressure region, usually with an implosion that can generate strong pressure waves. This phenomenon affects every machine in which a fluid is used to generate forces, including pumps, turbines, bearings, and propellers [34].

Usually cavitation occurs in two different stages: cavitation inception, and cavitation development [78]. Cavitation inception can be described as the transition of a liquid into vapour due a local reduction in static pressure. It is a complex phenomenon by itself and is dependent on a number of factors, including the environment in which the propeller is operating, intimate details of its geometry, the wakefield, and local flow velocities over its sections. In simple terms, cavitation inception requires the presence

of small bubbles of gas and vapour to be present in the fluid, known as *nuclei*. If nuclei of sufficient content and size are present in the flow, and they enter a zone of low static pressure, their radii will grow [2, 79, 80]. Their growth may result in the development of various forms of cavitation, depending on the flow conditions.

2.4.2.2 Cavitation types

In the context of marine propellers, cavitation of two types occurs [34]:

- Attached cavitation, in which the interface between the liquid and vapour phases is partly attached to the surface of the propeller,
- and convected cavitation, which consists of individual bubbles that travel with the flow.

These types are further categorised in the forms depicted in Figure 2.5. These include:

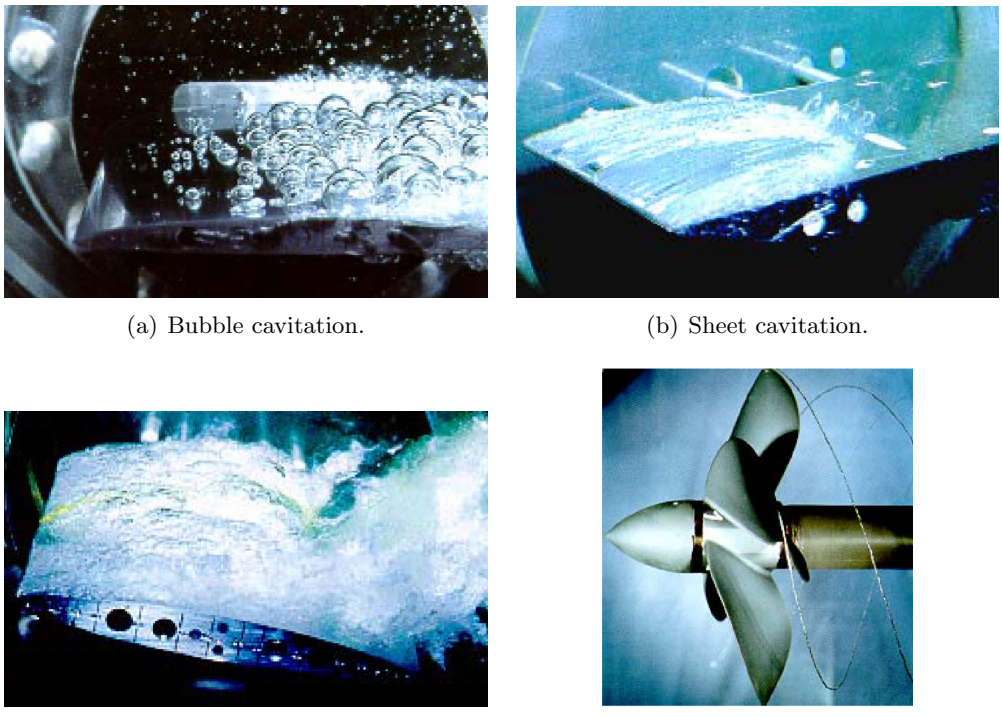

(a) Bubble cavitation. (b) Sheet cavitation.

(c) Cloud cavitation. (d) Vortex cavitation.

Figure 2.5: Types of cavitation in marine propellers [2].

- Bubble cavitation, which involves the formation of large bubbles which are subse-

quently transported downstream of the propeller, contracting rapidly over the surface of the blade. It normally occurs in the mid-chord region of the blade when the density of nuclei in the flow is relatively low. The formed bubbles that are convected downstream can collapse, potentially violently, causing significant erosion [34]. An example of bubble cavitation is presented in Figure 2.5(a).

- Sheet cavitation, which corresponds to a region of the hydrofoil completely filled with vapour. Its extent depends primarily on the design of the propeller and the inflow conditions. It is initially formed on the leading edges of the blades when enough bubbles travel through regions of low pressure, and subsequently connect with one another. It is generally stable in character, although it may become unsteady or intermittent due to non-uniform inflow. It can cause significant changes in the thrust and torque induced by the propeller [2], and generate the highest noise levels among all cavitation types [35]. An illustration of sheet cavitation is provided in Figure 2.5(b).
- Cloud cavitation, which is usually observed behind strongly developed sheet cavities, and it appears as a mist or cloud of very small bubbles. This cloud is primarily caused by the non-uniform inflow of a propeller. The non-uniformity generates periodic disturbances on the sheet cavities, causing them to detach from the surface of the blade. Subsequently, the shed cloud is convected downstream, where it undergoes collapse, possibly leading to some of the most violent erosion on the propeller [76]. An example of this cavitation type is given in Figure 2.5(c).
- Vortex cavitation, which is formed in the regions of the propeller experiencing concentrated vorticity, since the pressure in the vortex core is often much lower than in the rest of the flow, due to the high velocity gradients. If the pressure at the core drops below the vapour tension of the fluid, vortex cavitation will be formed and will travel downstream of the propeller. Regions of the propeller that experience this type of cavitation include the tip and hub of the blade. Normally, tip vortex cavitation is the very first form of cavitation to occur, and it is located some distance behind the tips of the propeller's blades, as illustrated in Figure 2.5(d). It's presence is unavoidable above a certain speed, even for properly designed propellers. Hub vortex cavitation

is formed by the combined vortices formed at the root of each blade. Normally this type of cavitation is stable and appears as a "rope with strands" corresponding to the number of blades of the propeller [34].

2.4.2.3 Noise generation

A significant amount of work has been undertaken regarding the contribution of cavitation on the URN spectra by both academia and the industry. A review of the resulting body of literature is presented and discussed in detail on Chapter 3. It suffices to state that each type of cavitation has a characteristic noise signature associated with it. Figure 2.6 provides a qualitative example of the URN spectra obtained from cavitating marine propellers. Four principal zones can be observed:

- zone I, representing low-frequency noise, with a mean power level increase proportional to f^4,
- zone II, corresponding to mid-frequency noise, with a mean power level increase of $f^{-5/2}$,
- zone III, which acts as a transition zone between Zones II and IV,
- Zone IV, corresponding to high-frequency noise, with a mean power level increase of f^{-2}, with f being the corresponding frequency.

In general, unsteady sheet cavitation on the suction side of the blades produces the highest URN levels [35], at frequencies ranging between 5[Hz] to more than 10[kHz]. The low- and mid-frequency noise, which corresponds to zones I - II of Figure 2.6, is mainly caused by the fluctuations of the sheet cavities. These fluctuations result in disturbances that take the form of acoustic waves and act as a monopole source. High-frequency noise, corresponding to zone IV, is primarily caused by the collapse of sheet cavities and the shock-waves being generated as the result of the high velocity gradients [35], as well as the oscillation of small bubbles which have the potential to induce strong pressure peaks, therefore causing broadband noise.

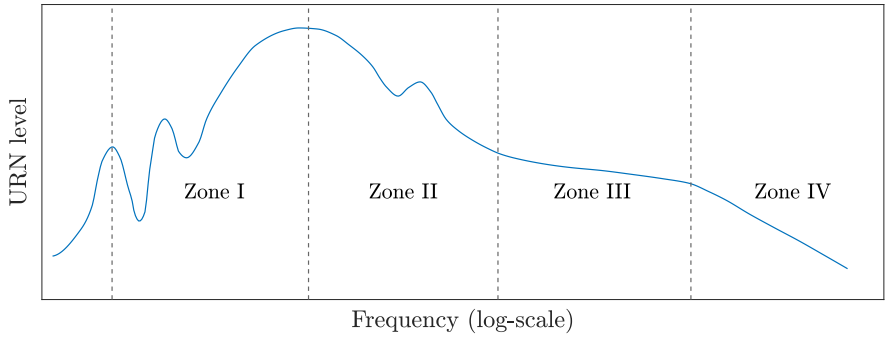

Figure 2.6: Generic noise spectrum of a cavitating propeller (adapted from [3]).

2.5 Summary

This chapter provided an overview of the problem of shipping noise, in terms of the relevant physics, societal importance, and historical perspectives. It is an important problem, as the rising levels of noise emitted by commercial shipping dominate the low-frequency ambient noise spectrum in several parts of the world. This has urged regulatory bodies, nations, and classification societies to introduce additional regulations, and issue guidelines and best practices to mitigate the problem. It has also been shown that marine propeller noise comprises a fundamental part of shipping noise, which cannot be avoided in modern vessels.

The underlying physics governing the phenomena of propeller noise generation and radiation have been summarized, starting from an introduction to the fundamentals of hydroacoustics and the idealised acoustic noise sources, up to the various types of cavitation that propellers experience and their contribution to the overall URN spectra. Through this discussion, the complexities of these phenomena have been introduced, especially under the simultaneous presence of cavitation dynamics and turbulence, which occur in every modern seagoing vessel. This discussion serves as an introduction to Chapter 3, which reviews the methods employed in academia and industry to predict URN from marine propellers.

Chapter 3

Computational Prediction of Marine Propeller Noise

Abstract

This chapter provides a comprehensive review of the state-of-the-art approaches related to the prediction of the underwater radiated noise from marine propellers in cavitating and non-cavitating conditions. The advantages and disadvantages of the various approaches is presented, and open challenges in this field are identified and discussed. This discussion justifies the selection of the methodology presented in the chapters that follow.

3.1 Introduction

This chapter provides an overview of the numerical methods employed to predict URN from marine propellers, with the aim to highlight the state-of-the-art and present the most important challenges in this field, which are abundant. According to Carlton [34] "The prediction of noise from cavitation by theoretical means is more complex than for the non-cavitating propeller... At present, the inability of many theoretical methods to take into account the detailed boundary layer and cavitation dynamics tends to limit their value". Nevertheless, theoretical approaches related to URN prediction are abundant in the available literature. In general, state-of-the-art numerical models are based on three main approaches: Physics-based models (PMs), Data-driven models (DDMs), and hybrid models (HMs). More specifically,

- PMs rely on the knowledge of the underlying physical phenomena and can be further subdivided in two main families
  - CFD models, which most commonly decouple the sound propagation from its source generation, allowing to separate the flow solution from the acoustic analysis. The viscous flow field generating the sound source is solved by means of a CFD method with an appropriate turbulence model, and the sound propagation is treated by an integral method based on acoustic analogy [81]. CFD-based models can be quite accurate and reliable at the expense of large computational requirements, which constitute their use during the early design stages inconvenient [82].
  - Empirical and semi-empirical models that utilise empirical formulas to approximate the physical phenomena with different levels of accuracy, and are always fine-tuned using available measurements [17]. These models are computationally efficient but significantly less accurate by their CFD-based counterparts [17].
- DDMs rely on Machine Learning (ML) and historical observations to build models of the underlying phenomena with no prior physics-related knowledge about them [83]. While DDMs can be computationally expensive during the model creation phase, they can be highly accurate and computationally inexpensive during the prediction phase [84]. Their main limitation lies on their accuracy, which can be high on average but not point-wise, and in some cases they are known to provide physically inconsistent predictions [85].
- HMs leverage both PMs and DDMs. They combine them to take advantage of their strengths while limiting their weaknesses. More specifically, HMs can achieve the same or higher accuracy with respect to DDMs, by fully leveraging historical data, but they also leverage prior physics-related knowledge, by exploiting computationally efficient partial outputs of various PMs to deliver physically plausible predictions [86].

The sections that follow cover the most important studies for each of these approaches. More specifically, Section 3.2 discusses CFD-based models, Section 3.3 discusses empirical and semi-empirical models, Section 3.4 presents DDMs, and Section 3.5 covers HMs. Having reviewed the state-of-the-art for all modelling approaches, Sec-

tion 3.6 discusses the advantages and disadvantages of each approach and future perspectives, while Section 3.7 concludes this chapter.

3.2 Computational fluid dynamics models

URN can be predicted through well-assessed aeroacoustics formulations, largely developed and validated during the last three decades in aeronautics, and widely employed for the analysis of the aerodynamically-generated noise from rotary wings. These are high-fidelity numerical methods that have been extended and applied to marine propellers, and require first modelling the flow field around the propeller and all the relevant dynamic phenomena that occur in order to identify the hydrodynamic sources of sound, and subsequently modelling the radiation of noise in the near- or far-field depending on the case study under consideration. The vast majority of the approaches found in literature are based on the commonly defined *hybrid approach*, in which the noise sources (hydrodynamics modelling) and sound radiation (hydroacoustics modelling) are investigated separately.

Noise sources are identified using approaches such as the Vortex Lattice Method (VLM) or Boundary Element Methods (BEM), or through CFD simulations, such as the Reynolds Averaged Navier-Stokes (RANS) solvers, LES, DES, or their hybrid variants, which are further discussed in Section 3.2.1. It should be noted that VLM and BEM do not fall into the category of CFD models, but are included in this section for discussion purposes. Sound radiation is commonly modelled with the use of acoustic analogies. Among them, the FWH equation for impermeable surfaces is widely adopted, while several studies also use the permeable FWH (p-FWH) to capture noise induced by the non-linear sources of sound. These methods are briefly discussed in Section 3.2.2. Finally, Section 3.2.3 presents several studies employing these models from the available literature. A summary of the relevant studies is provided in Table 3.1 reporting scope, employed methods, case studies, whether or not cavitating conditions were investigated, and main conclusions of each study.

3.2.1 Hydrodynamics modelling

Focusing on hydrodynamics modelling, one of the earliest approaches adopted in propeller performance analysis is the VLM [87], which is essentially a sub-class of the lifting surface methods. VLMs make use of the concept of straight line segments of vortices joined together to cover the propeller blade with a system of vortex panels. The velocities at the control points, defined in each panel over the blade, are expressed in terms of the unknown strengths of the vortices. By applying a flow tangency condition at each control point, the vortex strengths over the blade can be computed and the associated blade surface pressure field can be approximated [34].

The advantages of lifting surface methods with respect to BEM or RANS include: short computational time, enabling fast and effective assessment of propeller cavitation performance, and an established level of qualitative reliability achieved through empirical corrections developed and fine-tuned over long-term practical application. Nevertheless, several disadvantages of these methods have also been pointed out by researchers in the field, such as their inherent inaccuracy in predicting the pressure distribution near the leading and trailing edges of the propeller blades, and their limited ability for detailed modelling of complex flows dominated by viscous effects, such as the formation of vortices, and separation [88].

BEM is a more detailed flow modelling approach, and it is a well-known practical tool for the design and analysis of hydrofoils, pumps, water turbines, and marine propellers. In brief, BEM is a numerical approach that solves linear Partial Differential Equations (PDEs), if these can be formulated as integral equations, i.e. in boundary integral form [89]. BEM attempts to use given boundary conditions to fit boundary values only, rather than fitting values throughout the space defined by a PDE. Once this is accomplished, the integral equation can be utilised in the post-processing stage to numerically evaluate the solution at any desired point in the computational domain.

These methods were originally introduced by Morino and Kuo [90] and have undergone continuous developments ever since. Their application to propeller technology began in order to overcome two difficulties of the lifting surface methods: the occurrence of local errors near the blade's leading edge, and more widespread errors that occur

near the hub, where the blades are closely spaced and relatively thick. Compared to VLM, they provide more accurate results regarding the prediction of cavity patterns, and comparisons with experimental data show that sheet cavity patterns and cavity volumes for typical marine propellers can be well-predicted, except for the region near the blade tip [88].

More advanced approaches correspond to RANS, LES, and DES, which are nowadays commonly employed by most researchers and propeller designers both for cavitating, and non-cavitating flows. RANS solvers have been extensively used [24, 91–100], and they only solve averaged quantities of the Navier-Stokes equations explicitly. This lowers the computational burden, compared to DES and LES. However, it is known that their prediction capabilities can be significantly affected by the quality of the turbulence model, especially in regions of strong adverse pressure gradients, flow separation, and flow rotation [101].

LES, contrarily to RANS, resolves the largest turbulent eddies and only requires modelling of eddies smaller than the grid scale. This implies that a finer grid resolution provides a greater resolution of the turbulence effects and it also allows the broadband components of noise due to the fluid motion to be captured. Consequently, LES in general requires much denser grids than RANS, and hence, significantly higher computational effort, often considered prohibitively expensive for marine applications [39, 102–106].

To reduce the computational time requirements of LES, but still resolve the important turbulent structures, DES was proposed by Spalart [107], and has been applied in various studies in propeller design and analysis [92, 108–112]. The original version of DES was defined as "a three-dimensional unsteady numerical solution using a single turbulence model, which functions as a scale resolving model in regions where the grid density is fine enough for a large-eddy simulation, and as a Reynolds-averaged model in regions where it is not" [113]. In general, it has been found to offer a satisfactory balance between fidelity and computational cost, which is deemed necessary if these methods are to be adopted on a wider scale throughout the maritime community.

Although all methods are employed in contemporary studies, most researchers still

employ RANS to model the flow field around the propeller, with DES being considered at an increasing rate, due to the higher computational capabilities of modern computers. Nevertheless, in terms of practical propeller computations, as distinct from research studies, the application of LES and DES is more limited, due the high computational effort required to derive a solution within commercial time-frames, for which RANS solvers appear to have found most favour due to their moderate computational requirements [34].

Interesting comparisons between these methods have been conducted by major workshops, in which participants were presented with particular experimental test data that they had to reproduce using numerical methods. For instance, Salvatore et al. [114] provided a review of the submissions from the 2008 VIRTUE workshop, which involved simulations of cavitation from the INSEAN E779A propeller in uniform and non-uniform inflow conditions. Reportedly, a single submission relied on LES for turbulence modelling, whereas the other participants relied on unsteady RANS simulations. For the sake of comparison, numerical results by an inviscid-flow BEM solver including a sheet cavitation model were also presented. Most simulations required between 3 - 4 days to provide numerical results, running on multi-CPU machines, whereas the BEM code needed only 6 hours. In terms of accuracy, the conclusion of the workshop was that, while non-cavitating flows may be simulated with errors lower than 5% in terms of force coefficients, quantitative prediction of cavitation was not particularly reliable in terms of cavitation extents and pressure fluctuations.

Comparative results from the 2nd Symposium of Marine Propulsors were summarised in the work of Hoekstra et al. [115], where the Delft Twist 11 hydrofoil was simulated. Similarly to the VIRTUE workshop, from a total of five participants, two relied on LES and DES methods, whereas the other three employed RANS. The conclusions of the workshop pointed out the dependency of cavitation predictions on the grid and time-step resolution of the adopted approaches, but highlighted that a relatively good agreement in the predicted cavitation shedding frequencies. Similar results were reported by Luebke and Barkmann [116], who summarised the results of the 4th Symposium of Marine Propulsors, in which the participants were asked to simulate the

flow-field of the Potsdam Propeller Test Case (PPTC) at level and inclined shaft. Once again, LES and DES methods were still outnumbered by RANS, with the reported results revealing that the magnitudes of the pressure pulses and cavitation patterns were represented well by the participants, indicating a certain degree of maturity for all methods used.

3.2.2 Hydroacoustics modelling

The methods presented in Section 3.2.1 are utilised for the assessment of the flow field. Once the sound sources have been identified in the fluid domain, several computational approaches can be employed for the propagation of sound from the near- to the far-field, or to directly solve both problems.

Sound generation and propagation may be computed directly using the compressible set of the Navier-Stokes equations. Typically, advanced turbulence modelling techniques are utilised to capture the sound waves accurately enough, such as LES or Direct Numerical Simulations (DNS) [117, 118]. Such an approach would require the use of very fine grids to avoid dissipation and dispersion errors in order to obtain a high-quality solution. However, in many practical engineering applications, where large source-receiver distances are considered, such as for marine propeller far-field noise, this can be prohibitively expensive [76].

Substantial computational time reductions can be achieved by reducing the compressible Navier-Stokes equations to Reynolds-averaged form, and evaluating broadband noise using empirical and semi-empirical methods, as those discussed in Section 3.3. Nevertheless, these approaches are heavily limited by the availability and accuracy of appropriate empirical equations describing the noise sources for a full propeller cavitation problem [80].

Rearranging the equations of motion of a fluid into a linear wave equation, and modelling the noise sources using the mean and turbulent flow fields is another approach widely employed in the aeroacoustics field, known as Lighthill's acoustic analogy [119]. The primary advantage of this method is that it solves a volume integral of quantities dependent on the flow-field and uses them to compute sound at an arbitrary location,

which makes the method simpler and capable of working as a post-processing tool. However, Lighthill's acoustic analogy does not account for the presence of solid walls and the associated sound generation and scattering effects, rendering it of little use to a marine propeller problem [120].

Work by Curle [121] extended Lighthill's acoustic analogy to account for reflection and diffraction of sound due to the presence of solid boundaries and incorporated additional sound generation mechanisms occurring on the boundaries. Nevertheless, in the context of cavitation modelling, it suffers from the same problem as the original work of Lighthill [119]: The integration volume encompasses a non-homogeneous region filled with two fluids, complicating the formulations.

Following Curle [121], a more general formulation was developed by Williams and Hawkings [122] to account for arbitrary motion of the body for which the flow is being calculated, in which the acoustic analysis is performed by solving a surface integral for the loading and thickness terms, and a volume integral to account for the quadrupole source from the original formulation of Lighthill [119]. This formulation is known as the FWH acoustic analogy, and it has proven to be an effective and reliable numerical tool for sound radiation problems that are dominated by fluid - body interactions [123, 124]. As such it has been extensively used with different hydrodynamic solvers for the prediction of URN, under both cavitating and non-cavitating conditions, with a large body of literature dedicated in underlining the main numerical issues that arise in practical applications and the identification of potential solutions [76, 92, 125–135].

The FWH equation is a rearrangement of the Navier-Stokes equations for compressible flows, written in terms of a non-homogeneous wave equation where the force terms that account for the main sources of sound occur due to the kinematics of the body (i.e. thickness noise), the unsteady pressure fluctuations (loading noise) and the flow-field sources described by the Lighthill Tensor (quadrupole noise). Mathematically, the solution of the FWH equation is obtained through Boundary-Field Integral formulations yielding contributions due to thickness, loading, and quadrupole sources localised in the flow field around the body [136]. As will be discussed in Section 3.2.3, numerous studies provide recommendations on the correct application of the FWH,

present numerical results for the linear contributions given by the thickness and loading noise terms, and demonstrate how to include non-linear terms by the direct volume integration of the quadrupole source on the FWH equation, or by using the p-FWH formulation developed by Farassat [137].

Specifically, p-FWH allows overcoming the need for volume integration and, in principle, to evaluate the hydroacoustic behaviour of complex multi-body configurations, such as fully-appended hulls with propellers [138]. In this approach, a permeable source surface, which encloses the body of interest, is placed within the flow and is utilised as a radiating surface for the acoustic model. This surface will then allow for the monopole and dipole sources to be captured, for instance by the propeller, hull, and appendages surfaces, as well as the quadrupole sources within the flow, such as those arising from turbulence. This approach has been shown to be a robust and effective approach for marine propeller URN prediction in the work carried out by the Italian National Institute for Naval Architecture Studies and Testing (INSEAN) in [138], and has since been adopted by several researchers studying single- and multi-body problems, as will be discussed in Section 3.2.3.

3.2.3 Key studies

The methods discussed in Sections 3.2.1 - 3.2.2 have been employed in numerous studies in the fields of aero- and hydroacoustics, resulting in a vast body of literature. This section discusses several important studies focusing in marine propeller URN prediction, both under cavitating and non-cavitating conditions.

3.2.3.1 Isolated marine propellers

As will be discussed in the following, most studies studying isolated propellers operating either in open-water or non-uniform inflow conditions aim to investigate the various noise sources present, examine the prediction quality of various hydrodynamics and hydroacoustics solvers, or provide recommendations and best practices regarding their proper use.

Early studies in this field mostly employed BEM for the hydrodynamic analysis,

and the FWH acoustic analogy for the analysis of the sound radiation in the far-field, neglecting the non-linear sound sources [133, 134, 139]. For instance, authors of [133] presented a URN prediction method for non-cavitating propellers with (DTMB 4119), and without a duct (KA470), aiming to analyse the effect of the duct on the acoustic performance of propellers. The authors coupled the Farassat time-domain formulation 1A (F1A) of the FWH acoustic analogy to a BEM solver, and validated their hydrodynamic model against experimental data in terms of the thrust and torque coefficients. The predicted URN spectra for the two case-study propellers were not compared with experiments. Nevertheless, the authors concluded that the effect of a duct on the acoustic performance of the propeller is small in the far field under non-cavitating situations since the noise directivity of ducted and non-ducted propellers are almost the same, while only the noise levels of the higher order blade passage frequencies are influenced by the existence of the duct.

Authors of [134] presented a numerical study on the prediction of non-cavitating and blade sheet cavitation-induced noise of the DTMB 4119 and DTMB 4381 propellers. A potential-based panel method was employed to analyse the flow fields, whereas the far-field acoustics were predicted with the F1A formulation of the FWH acoustic analogy. Similar to [133], good agreement was reported between experimental data and the predictions of the hydrodynamic model, in terms of the thrust and torque coefficients. The circulation at the trailing edge of three blade sections and the cavity volume time-history was compared with other numerical methods, with the reported results showing minor differences. The hydroacoustics analysis was not validated against experimental data, with the authors highlighting that their numerical analysis can provide a basis for cavitation study and scaling of experimentally measured data. They furthermore concluded that the F1A formulation is a very convenient tool in embodying the time-domain analysis of the FWH equation.

An interesting comparison between the FWH and the Bernoulli equations was conducted by [139], who combined these methods with a BEM solver to predict non-cavitating and cavitating noise of the INSEAN E779A propeller in a non-homogeneous wakefield, both in an unbounded domain, as well as when operating below a horizon-

tal solid plate, inducing hull-like effects on the flow. Comparisons between the two acoustics models were conducted both in the time- and the frequency-domain, with the authors reporting a fair agreement for the results for the non-cavitating, propeller-only configuration. Nevertheless, quantitative differences were observed under cavitating conditions, which the authors attributed to potential numerical issues in the hydrodynamic solver. Focusing solely on one of the three uncertainty origins present in their simulations (i.e. input, modelling, and numerical uncertainty [140, 141]), the authors also concluded that numerical uncertainty in the evaluation of the cavity pattern can have a strong impact on the radiated noise levels and that the consistency of the solutions should be more carefully addressed in the future.

However, the inability of the Bernoulli-based solvers to evaluate pressure disturbances in the flow-field was subsequently demonstrated in a series of studies conducted by Ianniello et al. [126, 127, 128], who demonstrated that non-cavitating propeller noise in open water is an inherently non-linear problem governed mainly by the hydrodynamic sources of sound in the flow-field around the propeller vortex released at the blade tip, the vorticity, and turbulence, all of which can be very intense and persistent around and downstream of the propeller disc, and all of which are lost with Bernoulli-based solvers.

More specifically, in [126] Ianniello et al. investigated the hydroacoustic behaviour of the INSEAN E779A scaled propeller model in non-cavitating open-water conditions, by coupling a RANS solver with the p-FWH equation. Through their analysis, the authors showed that the contribution from the linear terms of the p-FWH is circumscribed to a spatially very limited region: moving far from the body, the pressure fluctuations rapidly reduce and they appear to be mainly related to non-linear sources, i.e. the vorticity and turbulence fields, regardless of the rotational speed of the blade. They further pointed out that their effects, found to be important, are even underestimated due to the numerical damping of the RANS solver on the vorticity field and on many non-linear aspects of the problem, such as the unavoidable breaking of the tip vortex far from the body, or the occurrence of cavitation phenomena. Finally, the authors underlined the inherent inadequacy of RANS solvers for hydroacoustic purposes, espe-

cially at points where the turbulent fluctuating component of the velocity field becomes relevant, and further commented on the power of the p-FWH equation to represent the main noise-generating mechanisms occurring underwater.

This study was subsequently extended in [127], where the authors utilised the same numerical methods to predict URN from a complete scaled model of a patrol vessel, equipped with 2 INSEAN E1630 Controllable Pitch Propellers (CPPs) in non-cavitating conditions. The results of both the hydrodynamics and hydroacoustics analyses were validated with experimental data, with the authors reporting very good agreement, demonstrating the capabilities and robustness of the proposed approach. More importantly, the results provided by the FWH equation once again highlighted the predominant role played by the non-linear sources underwater, where the pressure far-field is mainly affected by the velocity gradients occurring in the flow, with the dominant noise-generating source mechanism in the absence of cavitation being the vorticity released at the blade tip and shed downstream. The authors further underlined the acoustic relevance of the turbulence and vorticity fields, and the need for an accurate estimation of the velocity gradients. Unfortunately, as reported by the authors, these aspects make the direct computation of the FWH source terms very computationally demanding and, in practice, unfeasible. Nevertheless, p-FWH allows one to avoid these numerical problems when assessing the main features of the acoustic field.

Authors of [45] studied the non-cavitating noise of the DTMB 4118 propeller in non-uniform inflow conditions, utilising a DES flow solver to account for the non-linear viscous field over the rotating blades, and the F1A formulation of the FWH acoustic analogy. Numerical predictions were compared with experimental data, in terms of the unsteady forces acting on the propellers, with the authors reporting that the harmonic content of the thrust and torque of the propeller in the three-cycle wakefield, and the side-force and bending moment in the four-cycle wakefield were well-predicted. No comparison was reported with respect to the sound field. Nevertheless, the computational results revealed that noise radiation with the three-cycle wakefield has an axi-symmetric dipole-type pattern, with little scatter in different azimuth planes. Moreover, the directivity of the sound in the four-cycle wakefield demonstrated an asymmetrical character,

with obvious scatters between different azimuth planes, a result of dissipation of the distorted inflow, which can significantly contaminate the phase relation between the individual blade forces.

Authors of [142] studied the pressure fluctuations induced by propeller sheet cavitation in order to analyse and clarify this noise-generating mechanism, and to evaluate their proposed numerical method, which involved a potential based VLM for the analysis of the flow field, and the FWH equation for the acoustic analysis. To this aim, 3 different propeller scaled models were analysed, operating in 3 wakefields. Computational results were compared with experimental results obtained from a medium-size cavitation tunnel test, as well as numerical results from a potential-based BEM solver, for various configurations and operating conditions. Reportedly, the predicted flow and pressure fluctuation results were in agreement with the experiments, especially at the lower blade-rate harmonics, with the overall conclusion of the authors being that a combination of VLM with the FWH acoustic analogy can provide reasonable prediction regarding the pressure fluctuation due to propeller sheet cavitation.

Another important set of studies was conducted by Lloyd et al. [130, 131, 132], in which the authors focused on using the FWH acoustic analogy in order to evaluate the low-frequency, non-cavitating noise of the INSEAN E779A, and S6666 propellers. More specifically, the two-bladed S6666 propeller in open water conditions was the case study in [132], in which the authors employed a RANS solver for the analysis of the flow around the propeller, and the p-FWH equation for the prediction of the acoustic field, with the aim of verifying this particular implementation of the FWH equation and investigate the behavior of the permeable surface. Satisfactory agreement with the available experimental data was reported by the authors, providing a first validation of their numerical implementation. This work was subsequently extended in [131], where the authors investigated the hydroacoustic performance of the INSEAN E779A propeller model in open water conditions with RANS and the p-FWH. In this study, different grid structure configurations were analysed, in order to determine their effects on the propeller hydrodynamic and hydroacoustic performance. Major findings of this work included that typical propeller grids may not be entirely suitable for predicting pressure

fluctuations far from the propeller, and that predicting local pressure directly from a RANS computation is challenging. Moreover, the authors underlined that the FWH acoustic analogy is highly sensitive to the input data, i.e. the results of the hydrodynamic analysis, requiring a fine grid to be employed. In [130] the same group of authors examined the hydroacoustic performance of the same propeller, focusing on probes located above the wake of an open-water propeller. RANS and the p-FWH formulation were employed for two receivers located downstream with two different CFD solvers. Moreover, the effects of the permeable surface closure on the propeller's performance were also investigated. The authors, through a comparison of the obtained results with the two CFD solvers, highlighted the sensitivity of the acoustic predictions to numerical noise. They further challenged the claims of [126–128], that the contribution to the pressure signal at the receivers' locations is purely due to non-linear sources, reporting that, for open surfaces, the largest contribution to the computed pressure signals can be numerically modelled by the monopole term of the FWH equation.

Nevertheless, the importance of the non-linear quadrupole sources was once again highlighted by a series of studies from Ianniello and De Bernardis [143], Ianniello [144, 145]. More specifically, in [143], Ianniello and De Bernardis conducted a numerical investigation of the sound field of a scaled INSEAN E779A propeller model at various non-cavitating operating conditions, for which an experimental campaign was carried out through a set of standard towing tank tests. The authors employed RANS and DES models for the hydrodynamic analysis, both of which showed very good agreement with experiments concerning the main performance characteristics of the propeller, i.e. thrust, torque, and efficiency curves. The hydroacoustics analysis was carried out through a direct estimation of the linear terms, through the F1A formulation, and an overall noise prediction with the p-FWH formulation, thus accounting for the contribution of the quadrupole non-linear sources. The authors largely validated the conclusions reported on their previous studies [126–128]. Namely, that the contribution from the linear terms of the FWH is circumscribed to a spatially very limited region: moving far from the body, the pressure fluctuations rapidly reduce and they appear to be mainly related to non-linear sources, i.e. the vorticity and turbulence fields,

regardless of the rotational speed of the blade. Moreover, due to the relevant role played by the vorticity and turbulence in determining the characteristics of the acoustic field, the RANS simulation soon becomes inherently inadequate, especially at points where the turbulent fluctuating component of the velocity field becomes relevant. Finally, they underlined that a reliable hydroacoustics analysis of a marine propeller seems to require the computation of the FWH equation's non-linear quadrupole sources, and cannot neglect an accurate estimation of the three-dimensional turbulence and vorticity fields.

In [144], Ianniello studied the numerical prediction of noise from the INSEAN E779A in presence of sheet cavitation. The analysis was conducted by coupling the F1A formulation of the FWH equation to a BEM code, able to simulate the appearance and the time-evolution of a bubble on the blade surface. The numerical results indicated that, in the presence of a sheet cavity, the noise level in the far-field increases notably, the directivity of the acoustic field is altered, and, in essence, the marine propeller behaves as a true monopole source with uniform and omni-directional radiation.

In [145] the authors presented further theoretical analysis on the FWH acoustic analogy applied to a marine propeller, utilising the numerical predictions of the RANS and DES solvers employed in [143]. Through the analysis conducted, it was argued that non-linear flow phenomena, and not the blade pass frequency-related ones, are the main noise sources in the marine propeller context. Reportedly, this occurs because the relative efficiency of the rotating source becomes comparable to that of a quadrupole, unlike the stationary case, for which the low-order sources are much more efficient. For a marine propeller this is said to arise due to the low rotational speeds and the consequently low Mach numbers, as well as the multi-bladed design of propellers. Hence, the authors argued that an accurate description of the entire flow field, including the wake is needed to yield an accurate prediction of the acoustic signature of the non-linear problem. A related conclusion was that the noise due to the quadrupole sources may not be disregarded at low rotational speeds, which necessitates either the use of the p-FWH analogy, or the solution of the volume integral for the quadrupole source contribution. This occurs because the blade tip vortex persists in an extended region,

and, depending on both the operating conditions and external flow, it is inevitably destined to destabilize and break down, thus increasing vorticity and turbulence. Regarding the p-FWH approach, careful treatment of the outlet FWH integration surface was recommended, in order to avoid contamination of the far-field pressure predictions by the spurious noise source from the quadrupole sources in the wake interacting with the FWH surface. Following the authors' logic, it can be deducted that the presence of small bubbles in the wakefield of the propeller, and their interaction with the vortical structures in the wakefield may also be important for the full acoustic description of the problem [76].

Lidtke et al. [146] applied the p-FWH coupled to a RANS simulation to predicted the noise signature of the PPTC in open-water conditions. Due to the lack of available data regarding its acoustic performance, the authors conducted a validation study of their approach against other numerical solutions found in the literature. Their results indicated that such an approach can provide the means for identifying the low-frequency noise generation mechanisms in the flow, but it does not allow for the fine-scaled bubble dynamics or shock wave formations to be resolved, with the authors underlying that RANS simulations are inherently inadequate for hydroacoustics predictions. Furthermore, it was noted that, while certain modelling paths may be considered to mitigate these limitations, both in terms of cavitation and noise modelling, the use of more advanced modelling techniques, such as DES or LES, may prove vital if more in-depth studies are to be undertaken.

An interesting set of case studies was subsequently investigated by Lidtke et al. [147], in an extension of [146]. More specifically, the authors aimed to predict the noise from the PPTC, as well as from the NACA0009 hydrofoil, both under the presence of sheet cavitation. For the PPTC case study, a combination of RANS and the FWH acoustic analogy was employed with the aim to compute the tonal blade passage noise, whereas for the hydrofoil, LES with FWH are utilised. The main aim of this work was to correlate the relationships between the predicted flow features and the corresponding noise signals, to allow the authors to draw preliminary conclusions regarding the validity of their proposed method. Regarding the PPTC, good agreement was reported against

experimental data in non-cavitating conditions, with errors lower than 3.5% for the prediction of thrust coefficient. Nevertheless, the results indicated that RANS is not able to predict the unsteady behaviour of the sheet cavities particularly well, neither was it able to capture the tip vortex extending downstream of the propeller, reportedly because of the lack of appropriate refinement of the mesh away from the propeller blade, and the fact that RANS methods tend to introduce too much dissipation, causing the vortices to disappear much sooner than in reality, a finding that was also supported by the authors' earlier work [146]. As these phenomena play a significant role in the noise generation mechanisms of a marine propeller, as was concluded by Salvatore et al. [114], the authors noted that it is desirable to use higher fidelity simulations, such as LES or DES, for hydroacoustics purposes. Focusing on the numerical prediction on the hydrofoil, the authors concluded that detailed insight may be gained into the nature of the noise generation mechanisms only when high-fidelity modelling is employed, which may account for events such as cloud shedding and sheet formation.

While several researchers were investigating the capabilities of advanced CFD solvers for hydroacoustics purposes, such as LES or DES, Testa et al. conducted a set of studies [148, 149] in which the capabilities and drawbacks of employing BEM were investigated. More specifically, in [148] the authors studied the hydroacoustic performance of the INSEAN E779A propeller model in open water with three different methods. A coupled potential-based BEM, along with the Bernoulli equation, were combined with the p-FWH to yield the sound signals in the near-field, and the numerical results were compared with the pressure disturbances coming directly from a DES solver, and those predicted by a coupled DES and p-FWH model. The authors concluded that BEM hydrodynamics is adequate to capture the tonal sources of sound due to cyclic blade passages and trailing vortices convected downstream. In the near-field, the noise signatures obtained with the coupled BEM - p-FWH approach match well the results obtained with DES - p-FWH. However, moving further downstream the DES solver detects important vorticity contributions that deeply modify the overall sound pressure levels, a phenomenon completely lost by the BEM solver. Furthermore, the authors reported that in the presence of turbulence-induced noise effects, the coupled BEM -

p-FWH predictions are in good agreement with the corresponding DES - p-FWH results, or represent a sort of mean noise signal of those. However, the lack of modelling of the turbulent structures evolving in the wake further downstream makes the use of the BEM hydrodynamics analyses inadequate for any hydroacoustic investigations.

Subsequently, in [149], Testa et al. employed BEM with a specific formulation of the p-FWH acoustic analogy, referred to as Transpiration Velocity Modelling, which establishes an important correlation between URN and sheet cavitation pattern, yielding a mathematically-consistent description of blade-attached and fluctuating vapour pockets into an integral formulation for non-deformable bodies. The INSEAN E779A scaled propeller model in non-uniform flow was employed as a case study, and the hydroacoustics analysis was performed under cavitating and non-cavitating conditions. With the numerical results establishing the validity of the proposed model, the authors concluded that the proposed approach provides a more rigorous theoretical framework compared to existing formulations while requiring a reduced computation effort and data stream from hydrodynamic solvers.

Authors of [97] explored the intrinsic relations between the turbulent non-cavitating and sheet cavitating flows, and their radiated noise on marine propellers. The authors employed a RANS solver for the hydrodynamic analyses, and the FWH acoustic analogy for the prediction of the sound field. The highly-skewed propeller of the Seiun-Maru vessel was utilised as a case study. The authors reported reasonable agreement between experimental and numerical results regarding the hydrodynamic performance of the case study propeller, with discrepancies occurring in the prediction of TVC, which the authors attributed to the resolution of the tip vortex and the mesh discretisation, which will be subject to follow-up studies. In addition, the hydroacoustics analysis was not validated, due to lack of available experimental data. Nevertheless, the results showed that, for the non-cavitating case, the high sound pressure levels are mainly concentrated in the low-frequency range, and they decrease from the low-order blade passing frequency to the high-order blade passing frequency, in line with the pertinent literature [34]. The authors subsequently attributed the discrepancies observed to the inability of RANS models to accurately capture the flow dynamics, especially when the

flow field is dominated by transient vortices, stating that simulations of higher-fidelity are required to capture these phenomena, in-line with the conclusions of [76, 125, 139, 146, 147].

Flexible marine propellers were investigated in the work of [150], who analysed the interaction problems arising from the modelling of the dynamic behaviour of the flexible SVA-P1356 marine propeller designed by Schiffbau-Versuchsanstalt Potsdam (SVA). The fluid domain was simulated through a potential-based BEM, with an additional model to account for sheet cavitation. Acoustic evaluation was performed utilising the FWH acoustic analogy. A comparison between numerical predictions and experimental data was conducted for both cavitating and non-cavitating flows, with the reported results showing reasonable agreement. The authors further commented that the excitation of the blade loading heavily influences the acoustic spectrum, whereas smaller peaks are observed at the structural blade's eigenfrequency as well as the blade passage frequency.

Lidtke et al. [100] investigated the hydroacoustic behaviour of the INSEAN E779A propeller model under cavitating and non-cavitating conditions, by conducting a systematic set of simulations using a coupled viscous RANS - p-FWH approach. The aim of the authors was to understand the sensitivity of the acoustic analogy to the definition of the porous data surfaces and key simulation parameters, including the step- and grid resolutions, in order to provide guidelines for subsequent works for fully-appended vessel predictions. The authors reported differences of up to several [dB] in the far-field noise, depending on the exact definition of the porous data surface and the sampling scheme of the flow field, further stating that the main difficulties that arise from a practical perspective is the need to balance the tendency to place the porous data surfaces as close to the propeller as possible, thus minimising dissipative and dispersive losses, and avoiding spurious noise caused by incident vorticity shed by upstream geometries. They furthermore noted that as more advanced turbulence modelling techniques are employed on finer grids, this issue will worsen, with the porous surfaces being placed closer to the propeller in order to better capture the turbulence in the wake, which could make broadband noise prediction extremely difficult for practical test cases.

To the best of the author's knowledge, the latest study employing LES for hydroacoustics modelling comes from Cianferra et al. [151]. The authors modelled the small scales of motion through a dynamic Lagrangian model, and further used the FWH, to study the hydroacoustic analysis of the SVA VP1304 propeller in open water conditions. The authors reconstructed the acoustic field by integrating on the propeller - shaft - hub surface to obtain the noise contributions due to blade thickness and loading, and by integrating on a cylindrical region of the fluid to account for the quadrupole noise. By isolating the contribution of each noise source, the authors observed that the tip vortex is a considerable source of low frequency noise, as it is persistent in the downstream region and characterised by high vorticity.

More recently, Sezen et al. [152] presented a numerical study conducted for noise prediction on the propeller of the Princess Royal research vessel under cavitating conditions. The hydrodynamic flow field was solved using RANS, with sheet cavitation being modelled with the Schnerr-Sauer cavitation model, whereas the hydroacoustic analysis was conducted with the p-FWH. The authors validated their approach utilising experimental data, both in terms of the flow-field solution at 6 different loading conditions, as well as the URN predictions, at 3 loading conditions. A careful validation study was conducted, showing promising results in terms of the overall URN spectrum with several test cases in the low-frequency range, the numerical model overestimated the 1st blade passing frequency values by approximately 20[dB] in 5 out of the 6 loading conditions. Moreover, in several cases the difference between numerical predictions and experimental results was found to be in the range of 5 - 10[dB] for the frequency range between 200 - 800[Hz]. Similar to [76, 97, 125, 139, 146, 147] the authors noted that RANS is only suitable for the prediction of the low-frequency region, and more specifically to capture the blade harmonics. For the prediction of the broadband spectrum, which is strongly affected by turbulence, more advanced CFD models are required with the FWH analogy, such as LES and DES.

Authors of [153] investigated the use of the p-FWH acoustic analogy, aiming to provide guidelines and best practices for future studies. To this aim, the authors examined simple test cases that highlight the basic features of noise radiation simulations

provided by the p-FWH. Subsequently they studied the hydroacoustic behavior of a model-scale wind turbine and the INSEAN E779A propeller model in open water conditions. To capture turbulence – induced effects, the input data to the p-FWH were provided by an unsteady DES hydrodynamic solver, as well as DES data obtained by a phase-locked averaging post-processing of the unsteady hydrodynamic flow field, which detects important noise sources related to the wake vorticity contributions behind the propeller that cannot be captured by any RANS analyses. Their comparisons highlighted the crucial role of turbulence as a noise generation mechanism, and from the linear terms, namely thickness and loading noise, the noise generation mechanism is dominated by blade kinematics and loading. Regarding best practices, the authors underlined that the optimal porous surface of the p-FWH should be close to the rotor disk and the wake convected downstream, whereas Lidtke et al. [100] advised to balance the surface to minimise dissipative and dispersive losses. Furthermore, they noted that fine computational grids should be applied in the regions of the disk and the wake convected downstream to allow for an accurate prediction of vorticity and turbulence structures, and thus a reliable noise radiation prediction, as well as their observation that external noise may be affected by spurious noise and inaccuracies due to the boundary reflectional effects, whose distinction is not a trivial task.

In a series of studies [24, 91], Sezen et al. investigated the effects of grid resolution and the influence of eddy viscocity turbulence models in the predictions of the p-FWH analogy. The case study for these investigations was the INSEAN E779A propeller, with a RANS solver being used for the hydrodynamics analysis. In [91] the authors' results indicated that insufficient grid resolution reduces the numerical diffusion in the RANS solver, allowing for an extended tip vortex distribution, believed to be dominant under non-cavitating conditions. Nevertheless, an increase in tip vortex extension and intensity alongside the downstream of the propeller is not adequate by itself to make a reliable prediction of URN using RANS. Consequently, the authors underlined that realistic URN predictions require the use of more advanced models, i.e. LES and DES, together with the p-FWH, particularly if the receivers located in the region downstream of the propeller are of interest. In [24], the numerical results reported show that

the URN levels predicted by the different turbulence model are similar at low blade-loading conditions, which the authors attribute to the analogous wake structure and hydrodynamic field. For high propeller loads though, the wakefield is not stable and the coherent vortex structures break-up and evolve into the far-field. In this case, considerable differences were observed in the URN predictions and the authors cautioned on the thoughtful choice of the turbulence model.

The quality of URN predictions by the p-FWH with RANS or DES was compared by Sezen et al. [92] for a scaled model of the Princess Royal research vessel propeller, operating in the presence of TVC and sheet cavitation. The numerical predictions were compared against experimental data from cavitation tunnel tests, and the results indicated that both RANS and DES solvers can model sheet cavitation on the propeller blades, however the prediction of the TVC extension using the RANS solver was found to be insufficient with respect to DES. Finally, the authors reported that the overall URN spectra were found to be in agreement with the experimental data, nevertheless discrepancies were observed in the low- and high-frequency regions, especially in the case where the RANS solver was used for the hydrodynamics analysis.

3.2.3.2 Fully appended vessels

Studies investigating URN prediction from fully-appended vessels are far fewer than the studies examining isolated propellers. Furthermore, contrarily to the aims and conclusions of the studies discussed in the previous section, authors examining fully-appended model- or full-scale vessels focus primarily on prediction accuracy, and examine the generalisation capability of various solvers in different problems.

A complex case study was investigated by Ianniello et al. [128]. In this work, the acoustic behaviour of a full-scale fully-appended Roll-on / Roll-off Passenger (ROPAX) vessel equipped with two Contracted and Loaded Tip (CLT) propellers was investigated, utilising the same modelling approach as in [126, 127]. The approach was validated utilising measurements taken during the sea-trials of the vessel, with the predicted and measured URN spectra showing very good agreement for frequencies below 60[Hz], whereas deviations of approximately 20[dB] were reported for higher frequencies. Re-

portedly, the differences between measured and numerical results can be attributed to the large distance between the hydrophone and the vessel, which was higher than 1.5 [km], as well as distortion effects induced by sound propagation phenomena and intrinsic unsteadiness of the flow. Furthermore, the authors again underlined the dominant role played by the non-linear noise sources far from the body and the relevance of scattering effects from the hull surface, and that the FWH acoustic analogy and its variants should be employed, not only to provide deeper knowledge of a vessel as a noise source or to test possible and desirable improvements, but also as a standard approach to provide hydroacoustic characterisation at the design stage, similar to the aeronautical industry.

Authors of [129] studied the hydroacoustic behaviour of a fully-appended full-scale LNG carrier equipped with a 4-bladed ducted propeller, operating at two different rotational speeds. The hydrodynamic analysis was conducted with an unsteady RANS solver, whereas the acoustic field was predicted with the p-FWH acoustic analogy. Furthermore, a variety of modelling variables were considered, to ascertain which should be modelled for different applications and required levels of prediction accuracy. These variables included the free surface and the capturing of quadrupole noise sources, as well as a comparison of propeller representation approaches. The authors concluded that, as very good agreement between the results with and without the free surface were obtained, modelling it can be neglected, in order to reduce computational cost. Another important conclusion was that the p-FWH is highly suitable for hydroacoustics problems, and that quadrupole noise sources should not be neglected, in agreement with the conclusions of [126–128].

Özden et al. [154], Wei et al. [155] also investigated the validity of RANS as a hydrodynamics solver, in hydroacoustics analysis, but for non-cavitating conditions. More specifically, authors of [154] aimed to predict the URN of the INSEAN E1619 propeller in non-uniform, non-cavitating conditions, and behind a generic submarine model of the Defense Advanced Research Projects Agenecy (DARPA), the SUBOFF AFF8, in non-cavitating conditions, by coupling RANS with the FWH acoustic analogy. As comparisons of the acoustics predictions with experimental results were not conducted,

neither for the INSEAN E1619 propeller in open water conditions, nor for the fully-appended submarine due to the lack of experimental data, the authors validated their approach with measurements from a model-scale of a Fisheries Research Vessel (FRV), reporting relatively good agreement for frequencies between 300 - 5000[Hz]. Similar results were also reported by Wei et al. [155], who investigated the non-cavitating noise of a fully-appended DARPA SUBOFF 5470 submarine model equipped with a DTMB 5495-3 propeller model. The authors verified their proposed approach with analytical results on two case studies: the sound of a plane wave scattered by a solid sphere, and the sound of a point source scattered by a cube. Subsequently, they studied the hydroacoustic performance and scattering effects of the model-scale submarine, concluding that the scattering effect of a submarine hull has constructive interaction with the sound field directly radiated from the propeller, which in turn evidently changes the sound distribution pattern and propeller noise footprint.

LES coupled with the FWH equation was subsequently employed in the work of Bensow and Liefvendahl [125]. The authors, after validating their approach for a cylinder in cross-flow, with reportedly good agreement between numerical predictions and experimental results available in the literature, they solved the flow past the Princess Royal research vessel using a wall-modelled implicit LES and the F1A formulation of the FWH, both permeable, and surface based. Both cavitating and non-cavitating conditions were studied, with the authors noting that the flow in the aft of a vessel is highly transient, and the flow dynamics are expected to influence radiated noise, both in terms of general noise levels, and with respect to peaks in the URN spectra. Moreover, the authors argued that the results of the proposed approach reveal flow features that RANS cannot represent. Nevertheless, reportedly RANS can be expected to capture the lower harmonics of the blade passing frequency, which are often of interest for ship vibration studies and for the prediction of pressure pulses on the hull plating, but not for hydroacoustics analyses. Another interesting observation made was that no substantial differences were observed between evaluating FWH on the porous surface, or the hull shell itself, with the authors hypothesize that the lack of tip vortex cavitation may be responsible for some of the underwhelming acoustic noise results, and point to

the lack of simple, well-described in-depth validation data as a key obstacle in further developing numerical methods.

An interesting comparison was conducted by Li et al. [43], who studied the acoustic behaviour of the M/T fully-appended Olympus oil tanker combining both experimental measurements, from a on-site full-scale experimental campaign, model testing in a cavitation tunnel, and the numerical predictions of a coupled FWH - Delayed DES method. Focusing on the numerical results, the predicted sheet cavity agreed well with the one observed during the sea trials and during model tests. Tip Vortex Cavitation (TVC) was captured by the model, but its strength and extension were lower with respect to the one observed in the sea trials. The pressure pulses were reportedly in good agreement with measurements at the first 5 blade passing frequencies. Nevertheless, due to the under-resolved TVC, the numerical results under-predicted the noise levels for frequencies between 50 - 112[Hz], in which TVC is expected to have an important contribution, with a maximum deviation of 28[dB]. Higher deviations were reported for frequencies above 200[Hz]. Whereas positive results were reported overall, the authors also noted that additional validation studies are required to fully assess the validity of the proposed approach.

Authors of [108] predicted the URN due to TVC of a model scale DARPA SUBOFF 5470 submarine equipped with two highly skewed propellers: the HSP17, and the HSP38. Delayed DES, coupled with the p-FWH acoustic analogy was employed for this analysis. After a series of simulations that the authors conducted in order to represent the experimental conditions of cavitation tunnel tests as much as possible, the cavitating flows of the propellers installed on the submarine was simulated. The numerical results reported by the authors show that the predicted TVC closely follows the measurements, and that the URN spectra also show excellent agreement, confirming the experimental findings that the propeller with the highest skew angle induces lower cavitation noise.

3.3 Empirical and semi-empirical models

Empirical and semi-empirical models constitute the first attempts in predicting cavitation noise and have been investigated by several researchers over the years. Although they model limited parts of the underlying physical phenomena, they are utilised extensively in the initial design stage due to their limited computational cost [17]. This section discusses several aspects of the state-of-the-art empirical and semi-empirical models employed for URN prediction of marine cavitating propellers. Table 3.2 summarises relevant studies that are presented in this section, by reporting for each work the scope, the case study used to validate the proposed model, the main conclusions, and accuracy.

Several studies in this category utilise fully empirical formulas that are directly fitted to available experimental data. For instance [156] attempted to describe noise levels of the propeller and various rotating machinery on-board utilising only mechanical and geometrical parameters. Relatively simple equations were employed to predict URN from the propeller by relating spectral components of noise to the principal particulars of a vessel. More specifically, the authors considered vessel displacement, speed relative to cavitation inception speed, and the block coefficient as an indicator for wakefield variations. Utilising experimental data of the Hamburg Ship Model Basin (HSVA) from 5 vessels covering 3 vessel types, these parameters were related to low- and high-frequency cavitation noise by means of simple algebraic equations. Computational results were compared with experimental measurements on an oil-tanker at shallow waters, with reported deviations of ± 5[dB], with the authors concluding that, although the model can provide results of reasonable accuracy, further investigation is required to include more influencing parameters, and cover vessels with CPPs in off-design pitch.

Authors of [15] were among the first to investigate semi-empirical models for broadband noise, and proposed a simple formula to describe its upper limit for frequencies between 100[Hz] to 10[kHz] with adequate accuracy, with inputs being the propeller's number of blades and diameter, its rotational speed, and the swept cavitation area in the propeller disc. The parameters of the model were calibrated from measure-

ments taken from thruster propellers, with the authors reporting sufficient qualitative accuracy. This model has since been utilised by several researchers [157–159], who have proposed various extensions in order to improve prediction quality. More specifically, the swept cavitation area in the propeller disc was estimated by a Lifting Surface Method (LSM) in [157, 158] with both groups of authors reporting results of reasonable accuracy, whereas Takinacı and Taralp [159] modified the original model by adding a term to represent TVC, using its inception speed.

More specifically, authors of [157] applied the model of Brown [15] to the DTMB 4148, DTMB 4119, and Seium-maru HSP propellers, for which the hydrodynamic analyses were conducted with an LSM. The reported results showed sufficiently good agreement, with maximum deviation of approximately 25[dB] at low frequencies, making the proposed approach valid for the practical evaluation of propeller cavitation noise at design stage. Okamura and Asano [158] studied tonal and broadband noise from marine propellers employing the model of Brown [15] to estimate broadband noise, and a monopole model to deal with the tonal noise. Computational results were compared with full-scale measurements on a cargo liner and a training ship, with the authors reporting maximum deviations of ± 5[dB] for the tonal noise, and ± 20[dB] for the broadband noise. They concluded that the models employed are valid enough for the practical evaluation of URN, and underlined that more detailed measurements of cavitation patterns, their volume, and cavitation-induced noise are necessary to further validate their approach.

Authors of [159] proposed a semi-empirical model for the prediction of broadband noise from marine propellers, composed of two components: The empirical prediction of the broadband noise on the frequency domain based on a listing surface method, and the modulation of the noise in the time domain. As stated earlier in this section, Takinacı and Taralp [159] modified the semi-empirical model of [15] by adding a term to represent TVC, using its inception speed. In this manner, their formulation includes the effects of both sheet cavitation and TVC. Having estimated the URN spectrum, the authors generated a realistic time-domain signature of the pressure fluctuations, based on the discrete Fourier transformation and a modulation function. The proposed model was

applied to a four-bladed propeller, both at model-scale and full-scale, for two different inflow conditions. The reported results showed reasonable qualitative trends, with deviations as high as 30[dB] for certain frequency ranges, with the authors concluding that further validation is needed utilising additional experimental data.

Semi-empirical models focusing on sheet cavitation and its effects on URN have been presented in [5, 160], and have been further extended from various researchers. More specifically, authors of [160] presented a simple formulation for the noise generated by thruster propellers. Their work provided a simple relation between the amplitude of noise and the area of sheet cavitation, based on the main design characteristics of the propeller. This approach was validated utilising measurements from the 6 thrusters of the Discoverer Enterprise drill-ship, with reported results showing acceptable qualitative agreement. The same conclusions were reached by [161], who employed this model to predict URN from the propellers of the Princess Royal research vessel [75], reporting maximum deviations of approximately 30[dB].

Authors of [5] proposed a more thorough semi-empirical method to model the generation of free bubbles due to sheet cavitation. In this case the number and mean size of cavitation bubbles generated by a cavity break-off are assumed to follow a beta distribution characterised by a single parameter, and a broadband propeller-induced pressure spectrum is generated The model was verified on a number of propellers, and was validated utilising noise measurements taken on the Pasadena oil tanker at 3 different operating conditions, and 2 operating conditions of the Sydney Express coastal service vessel. The reported results showed maximum deviations of ± 20[dB] for frequencies lower than 3[kHz], whereas errors of ± 5[dB] were reported at the higher end of the URN spectra, for all cases considered. This model has since been adopted by a number of researchers: For instance, Kamiirisa and Goto [162] employed this model and estimated the behavior of sheet cavitation using an LSM, and further introduced the effect of compressibility and damping in the bubble flow to improve the prediction accuracy. Ando et al. [163] substituted the LSM for a RANS simulation, and Lafeber et al. [164], Veikonheimo et al. [165], who coupled the model of Matusiak [5] to BEM simulations for the hydrodynamic analyses.

Sources other than sheet cavitation have also been explored by several researchers, with a variety of studies being dedicated to the prediction of tip vortex induced noise. For instance, Yamada and Kawakita [166] studied URN from TVC, by combining several empirical models. The pressure profile in a tip vortex was estimated utilising the vortex strength computed from an LSM, and the vortex core size from boundary layer calculations. From this information, bubble behaviour and its noise was estimated by the Rayleigh-Plesset equation [167], and was subsequently summed with the broadband noise levels, which were estimated with the method of Brown [15]. The authors validated their approach on measurements conducted on two oceanographic research vessels and a training vessel, under various operating conditions for which TVC was observed. The reported results showed remarkably good agreement for two out of the three case study vessels, with maximum deviations of 3[dB] at low frequencies, and near-zero deviations for a large number of frequencies ranging between 2 - 11[kHz], making this approach valuable for early design stage estimations.

Raestad [168] formulated an empirical relation for the amplitude of vortex noise, known as Tip Vortex Index (TVI). This method consists of a set of empirical formulations based on experimental studies involving 15 vessels of various types. In this model, the propeller is considered as the source that transmits the noise to the vessel's hull, while the hull acts as the receiver of the pressure fluctuations. Bosschers [169] presented a formulation for the prediction of the characteristic frequency of noise generated by cavitating vortices. The authors extended the dispersion relation for perturbation waves on the cavitating core, derived by [170], to correct for viscous effects, and validated their approach utilising the experimental data of [171]. Both studies succeeded in approximating the behavior of vortex noise, with the authors reporting satisfactory qualitative results in their corresponding case studies. Nevertheless, they are both known to require extensive case-by-case tuning, as they rely on simplistic 2-dimensional vortex models, characterised by high sensitivity on several of their parameters [82, 172].

More recently, authors of [16, 173] utilised the semi-empirical vortex model of [82] to predict the hump-shaped pattern of the URN spectrum for a variety of vessels. The center frequency and level of this hump is described by an empirical model derived

by an experimental database of model-scale and full-scale hull pressure measurements. The model is based on several design characteristics of the propeller, and its principal parameter is the vortex cavity size, which was predicted by the authors utilising a combination of BEM and the vortex model of [82]. The approach was validated on a number of case studies, including a two-bladed research propeller model using the experimental data of [174], a combi freighter vessel equipped with a single CPP, and the MS Statendam cruise vessel from the experiments of [175]. The model was shown to capture the main characteristics of the measured URN spectra in most of the cases studies considered, nevertheless the variance of the prediction quality was significant, which the authors attributed to the presence of sheet cavitation and its interaction with TVC which was present in several of the case studies considered. Lafeber and Bosschers [161] also employed this model to predict URN from the propellers of the Princess Royal research vessel [75], reporting maximum deviations of approximately 20[dB] at low frequencies.

The same group of authors also extended some important aspects of [16, 173] in [176]. They investigated the effects of viscocity on a developed tip vortex cavity, and developed a semi-empirical model to describe the azimuthal velocity distribution of a cavitating vortex in a two-dimensional viscous flow. More specifically, the authors elaborated on the analytical formulation of the cavitating Lamb-Oseen vortex model [177], which had been used in [16, 173], and further extended it with an empirical relation to account for vorticity roll-up. Moreover, they proposed a new scaling relation between cavity size and cavitation number, valid for a range of vortex strengths and viscous core sizes. The parameters of the model were calibrated utilising experimental data from [178], and validated using the experiments of [179, 180]. Good agreement was obtained for small cavity sizes and when the vortex cavity is detached from the hydrofoil. For large cavity sizes, when the vortex cavity is still attached to the hydrofoil the model was reported to predict cavity sizes too small for a given cavitation number. Nevertheless, the relation between cavitation number and cavity was shown to be well predicted by the model with constant viscous core size, a phenomenon which, according to the authors, warrants further investigation. Furthermore, the authors un-

derlined that their model still needs to be extended with a relation for the axial and radial velocity distribution, but this would require more information on the vorticity roll-up and stream-wise variation of the flow.

Another approach was presented by the authors of [181] who combined RANS with bubble dynamics theory. This model is considered as semi-empirical due to the assumptions considered. More specifically, radiated noise from sheet cavitation and TVC was predicted by a theoretical method, modelling bubble collapse of the free bubbles. The authors assumed that the mean initial size of the bubbles is equal to 2.5 [μm], and adopted a normal distribution for the bubble size. Based on these assumptions, the number of bubbles was estimated from the volume of sheet cavitation, predicted by RANS. For TVC, a similar assumption for the bubble size was adopted, and the length of the TVC was assumed to be 150% of the propeller diameter. This assumption was not based on CFD results or any other theoretical method, but from observations in model tests. The validity of the proposed approach was demonstrated from experiments carried out at one of the cavitation tunnels of the HSVA on a model-scale bulk carrier, with reported results having a maximum deviation of 13[dB] with respect to the experiment.

3.4 Data-driven models

An attractive alternative to the computationally expensive CFD models, and the computationally cheap but less accurate semi-empirical models, arose relatively recently with the utilisation of DDMs. DDMs have proven to be valuable instruments in several maritime applications [83, 84, 182–194], and have also been employed by a variety of researchers in propeller design and analysis, not strictly with the aim of propeller URN prediction. Table 3.3 summarises relevant studies that are presented in this section, by reporting for each study the DDM employed, scope, input and output spaces, available data, and reported accuracy.

3.4.1 The learning problem

This section serves as an introduction to the problem of learning from data and provides a brief introduction to the most common scenarios of ML, based on which the problem of estimating URN directly from data can be properly described. Subsequently, Section 3.4.2 further formalises this problem, and introduces the basic components of the learning process and the necessary notation.

ML is a discipline concerning the study of adaptive algorithms to infer from data so as to extract critical and relevant information. It offers an effective data-driven approach to data mining and intelligent prediction. The objective of learning is to induce optimal decision rules for prediction or to extract the salient characteristics of the underlying system which generates the observed data [195]. It builds its foundations on inter-disciplinary fields including statistical learning theory, linear algebra, pattern recognition, and artificial intelligence [196–199]. In simple terms, ML exploits optimisation techniques and large amounts of data in order to devise artificial models that have the ability to automatically learn and improve from experience, without being explicitly programmed to do. Instead, an optimisation procedure is set up, commonly called as *learning* or *training* phase, that eventually leads to the artificial model, often referred to as the *learner*, without any prior knowledge about the underlying physical principles [200].

To construct the learner, a large amount of computational resources is required, and as much data as possible. More precisely, the higher the data availability, the more accurate the learner is [200] even if, in some cases, a small amount of examples could be sufficient for solving real world problems [201, 202]. Moreover, to train and optimize the performance of the learner, a large amount of computational power is always needed [200, 203, 204]. Nevertheless, once the learner is constructed, its use for making predictions, i.e. the *forward phase*, is computationally inexpensive [200, 203].

ML methods can be grouped into various categories according to different affinity principles. Several ML scenarios are encountered in practice, which mainly differ in the type of training data available to the learner, the order and method by which the training data is received, and the test data used to evaluate the learner. The most

typical ML scenarios include [205]:

- *Supervised learning*, in which the learner receives a set of labeled examples as training data, in which the output quantity that the learner aims to predict has already been measured, and makes predictions about unseen cases. This is the most common scenario, usually associated with classification, regression, and forecasting problems.
- *Unsupervised learning*, in which the learner exclusively receives unlabelled training data, and its goal is to describe the associations and patterns among the training data. This scenario is usually associated with data clustering, dimensionality reduction, or novelty detection.
- *Semi-supervised learning*, in which the learner receives a set of both labeled and unlabeled examples, with the aim to make predictions about unseen cases. This scenario is common in settings where unlabeled data is easily accessible, but measurements of the output quantities are technically or economically infeasible to obtain in large amounts. Usually, classification, regression, and forecasting problems can be framed as instances of semi-supervised learning, in which the hope is that access to the distribution of the unlabelled data can assist the learner to achieve a better performance than in the supervised learning setting.

The task of estimating URN from cavitating propellers can be mapped into a typical supervised ML regression scenario [199, 200], which is the main scenario discussed in the following.

3.4.2 The supervised learning scenario

Before presenting the ML methods utilised to estimate URN, the main components of the typical supervised scenario must be presented. As illustrated in Figure 3.1, a dataset $\mathcal{D}_n = \{(\boldsymbol{x}_1, \boldsymbol{y}_1), \cdots, (\boldsymbol{x}_n, \boldsymbol{y}_n)\}$ of n samples is available to the learner, where $\boldsymbol{x}_i \in \mathcal{X} \subseteq \mathbb{R}^\iota$ correspond to the ι inputs, also referred to as *predictors*, and $\boldsymbol{y}_i \in \mathcal{Y} \subseteq \mathbb{R}^o$ to the o outputs of the learner, also referred to as *targets*, with $i = \{1, \cdots, n\}$.

The goal of this scenario is to identify the unknown rule $\mu : \mathcal{X} \to \mathcal{Y}$ that associates an element $\boldsymbol{y} \in \mathcal{Y}$ to an element $\boldsymbol{x} \in \mathcal{X}$. μ is estimated through a learning algorithm $\mathscr{A}_\mathcal{H} : \mathcal{D}_n \times \mathcal{F} \to h$ which chooses a hypothesis $h : \mathcal{X} \to \mathcal{Y}$ in a set of hypotheses $\mathcal{F}$,

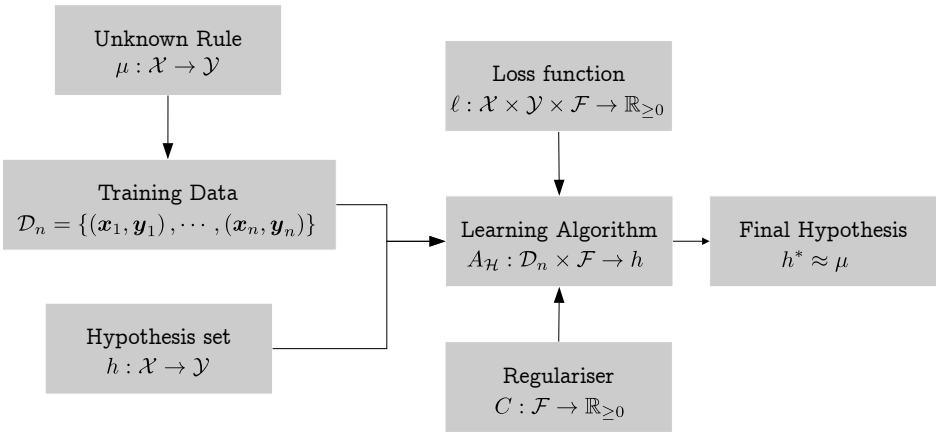

Figure 3.1: Basic components of a supervised machine learning scenario (adapted from [4]).

characterised by a set of hyperparameters $\mathcal{H}$.

The goal of $\mathscr{A}_{\mathcal{H}}$ is to find a suitable h for the case study problem. The suitability of h is measured with a prescribed loss function $\ell : \mathcal{X} \times \mathcal{Y} \times \mathcal{F} \to \mathbb{R}_{\geq 0}$, which quantifies the difference between $h(\boldsymbol{x}_i)$ and the corresponding $\boldsymbol{y}_i$. In this context, $\mathscr{A}_{\mathcal{H}}$ selects h such that the expected error,

$$\mathtt{L}(h) = \mathbb{E}_{\mu} \ell \left(h(\boldsymbol{x}, \boldsymbol{y}) \right) \tag{3.1}$$

is minimised. Unfortunately, since μ is unknown, $\mathtt{L}(h)$ cannot be computed. The only alternative is to approximate $\mathtt{L}(h)$ by $\hat{\mathtt{L}}(h)$, known as the *empirical error*, which is defined as

$$\hat{\mathtt{L}}(h) = \frac{1}{n} \sum_{\boldsymbol{x}, \boldsymbol{y} \in \mathcal{D}_n} \ell \left(h(\boldsymbol{x}), \boldsymbol{y} \right). \tag{3.2}$$

This approach is known as Empirical Risk Minimisation (ERM) [199]. Nevertheless, ERM is typically avoided in ML as it leads to severe over-fitting of h on $\mathcal{D}_n$. As a matter of fact, the training process could choose an h that is complicated enough to perfectly describe all the samples of $\mathcal{D}_n$, including noise, which afflicts them. In other words, ERM implies memorisation of data, rather than learning from it [204]. A more effective approach would be to minimise a cost function that accounts for the trade-off between the complexity of h and its ability to describe $\mathcal{D}_n$. This approach is known as

Structural Risk Minimisation (SRM) [199]. SRM considers a sequence of hypotheses families $\mathcal{F}_1 \subset \mathcal{F}_2 \subset \mathcal{F}_3 \subset \cdots$ of increasing complexity, and optimises the empirical error plus a penalty term that takes into account the complexity of the underlying hypotheses family. A smoother variant of SRM involves the adoption of regularisation techniques, and more specifically Tikhonov regularisation [206]. In this case, $\mathcal{F}$ is chosen together with a regulariser, i.e. a complexity penalising function $\mathtt{C} : \mathcal{F} \to \mathbb{R}_{\geq 0}$, which is highly dependent on the ML method employed. In this context, the output of the training procedure $h^\diamond$ is obtained as the solution to the problem

$$h^\diamond : \arg\min_{h \in \mathcal{F}} \quad \hat{\mathtt{L}}(h) + \lambda \mathtt{C}(h), \tag{3.3}$$

where $\lambda \in \mathbb{R}_{\geq 0}$ is a hyperparameter that must be set a-priori, and is not obtained as an output of the training process. It regulates the trade-off between the over-fitting tendency, related to the minimization of the empirical error, and the under-fitting tendency, related to the minimization of $\mathtt{C}$. This procedure is followed by all studies employing DDMs.

3.4.3 Hydrofoils

The applicability of DDMs that follow the above theoretical foundations in predicting the hydrodynamic performance of hydrofoils was demonstrated in a series of studies conducted by Bonfiglio et al. [207, 208, 209]. More specifically, authors of [207] studied the performance of supercavitating hydrofoils for high-performance marine vehicles utilising a multi-fidelity framework, with the aim to develop DDMs that can assess hydrodynamic performance for a wide range of operating conditions. More specifically, the authors combined simplified simulation models with a small number of experimental data and high-fidelity simulations, to develop a Gaussian Process Regressor (GPR) with the aim to predict the lift-over-drag ratio of a wedge-shaped supercavitating hydrofoil at various flow regimes. The feasibility of the approach was demonstrated against cavitation tunnel measurements, with the GPR model achieving a Mean Absolute Percentage Error (MAPE) between 1% - 5%, depending on the amount of low-

and high-fidelity simulation data utilised.

A multi-fidelity approach was also presented in [208] for the shape optimisation of three-dimensional (3D) supercavitating hydrofoils parameterised by 17 control points from 4 *b*-splines that fully define a hydrofoil's two-dimensional (2D) section. The dataset employed consisted of unsteady RANS simulations and 1D, 3D Finite Element Method (FEM) simulations, in which high-fidelity data were generated by resolving the flow at a high resolution grid, while the low fidelity data corresponded to low grid resolution simulations. The authors predicted several hydrodynamic properties of interest utilising GP. These included the lift-over-drag, lift coefficient, and cavity thickness at 25%, 50%, and 75% of the chord. Finally, the authors employed Bayesian optimisation to identify the optimal shape. The approximation errors from the GP were lower than 4% for all hydrodynamic properties, and the authors demonstrated that they could effectively use low-fidelity simulations on a very large set of design samples, reducing the overall optimization cost by several orders of magnitude while still managing a 7% performance increase in terms of lift-over-drag ratio w.r.t. a baseline design, while maintaining the required lift force and a sufficiently thick vapor cavity ensuring stability of the supercavitating flow pattern.

The work of Bonfiglio et al. [208] was further extended in [209], where the authors conducted hydro-structural optimization of super-cavitating hydrofoils. In this case study the authors developed the GP DDMs by performing multi-resolution simulations of turbulent multi-phase flows and multi-fidelity structural mechanics (combined 3D and 1D FEM simulations). A total of $1,400$ hydrofoils were simulated, out of which 400 were utilised for high-fidelity simulations, and the rest for low-fidelity simulations. Using the same input space as in [208], a set of GPRs were developed to predict the hydrodynamic performance and structural characteristics of a hydrofoil, in terms of drag-to-lift ratio, total generated lift force, maximum Von-Mises stress, and maximum deformation of the hydrofoil's tip utilising 17 control points from 4 *b*-splines that fully define a hydrofoil's 2D section. Subsequently Bayesian optimisation was employed to identify the optimal design. The authors compared the quality of the obtained solution against a benchmark case, concluding that their approach could yield the same

optimised design at a very small fraction of the computational cost. Furthermore, errors lower than 3% were reported for the GP models for all outputs.

Risk-adaptive set-based hydrofoil design under uncertainty was studied by Royset et al. [210]. The authors developed risk-adaptive DDMs that required multi-fidelity simulations, for an ultra-high speed vessel requiring hydrofoils devised to ensure high efficiency both in supercavitating and in fully wet conditions. The authors conceptualised and developed "s-risk" DDMs specifically for this case study, with the aim to predict lift-to-drag ratio, lift and negative lift. The input space of the DDMs consisted of 15 control points from 3 b-splines that fully define the shape of a hydrofoil, similar to [208, 209]. utilising high-fidelity RANS and low-fidelity potential-flow based simulations. Relative errors of approximately 2% were reported for all output quantities of the DDMs, and the computational advantages of the proposed approach were demonstrated by comparative results against a benchmark design obtained by differential evolution optimisation.

3.4.4 Isolated marine propellers

Apart from studies investigating single hydrofoil flows, there are several researchers who have utilised DDMs to investigate several phenomena of interest related to marine propellers. One of the first studies involving Artificial Neural Networks (ANNs) in propeller analysis was presented by Koushan [211]. The authors utilised an ANN to predict propeller induced pressure pulses. With this aim, the authors utilised a database of measurements from 470 model-scale tests of single screw and twin screw vessels in both cavitating and non-cavitating conditions. The input space of the ANN consisted of several quantities related to the propeller geometry and the vessels' wakefield. Regarding propeller geometry, these included the blade area ratio, ratio of pitch at the time of measurement to design pitch, skew angle, pitch, chord, thickness, and camber ratios at 3 different radial locations. Wakefields were represented by the overall average wake, average wake at 3 propeller radii, local wake at the same propeller radii at 4 angular positions. From this input space, the ANN was able to predict the 1st and 2nd harmonic pressure pulse coefficient for cavitating conditions, and the 1st harmonic

for non-cavitating conditions. The authors reported results of satisfactory accuracy, with the majority of the predictions deviating at most by ±20% from the available experimental data.

ANNs were also utilised in [212] for the prediction of propeller forces and moments during crash-back maneuvers. Measurements from 155 experiments of various maneuvers were obtained and utilised from a free-running submarine model test. These maneuvers consisted of dive jams, rise jams and deceleration runs conducted over a speed range from 8 knots to flank, for various jam angles and for two different backing profiles. During these maneuvers, time-series of several control and state variables were obtained, including the submarine's trajectory, velocities, and accelerations in 6 degrees of freedom, propeller rotational speed, and appendage deflection angles. Utilising these measurements, the authors demonstrated that the ANN was capable of accurately estimating the propeller's forces and moments, with R^2 values ranging between 0.95 - 0.99, concluding that ANNs could be a viable option for use in larger maneuvering simulation efforts.

Data-driven propeller design optimisation with ANNs was explored by Calcagni et al. [213]. More specifically, the authors utilised an ANN to describe the hydrodynamic performance of propellers, with the aim of propeller design optimisation. The authors considered two scenarios, differing on the method of generating their dataset. On the first scenario, experimental data from the original Wageningnen B-series [214] were utilised, whereas on the second scenario the experimental data were replaced by computational results from an in-house BEM model. The input space of the ANN consisted of the number of propeller blades, blade area ratio, pitch ratio at various advance ratios, whereas the open water efficiency, thrust and torque coefficients comprised the output space. MAPE lower than 4% was reported in most cases, with a few minor exceptions on samples with near-zero thrust production, characterised by the combination of low pitch ratios and high advance coefficients.

A similar method was presented in [215], where ANNs and genetic algorithms were employed to find propeller designs with minimal low-frequency discrete spectrum thrust. The scope of the ANN was to estimate the thrust coefficient, and the 1st and

2nd order discrete spectrum thrust utilising as inputs the coefficients of a 4th order polynomial describing a propeller's radial skew distribution. The authors exploited a dataset containing the results of 336,000 simulations from an in-house potential-flow based solver. Various ANN architectures were developed, with the best one having errors of 0.01%, 0.21%, and 5.71% for the thrust coefficient and the 1st, 2nd order discrete spectrum thrust, respectively. Equally impressive computational time reduction was reported for the optimisation process by the authors, with the DDM-based optimisation requiring only 0.68% of the time required for the traditional, CFD-based optimisation.

A quantitative comparison between ANNs and Kriging for data-driven propeller design optimisation was reported in [194]. More in detail, the authors compared 3 DDMs (2 Kriging variants and an ANN) on a case study involving the design optimisation of propeller blade geometries. The DDMs were constructed utilising a total of 350 numerical results from the VLM code of [216, 217], with the aim to predict propeller dynamics, as well as propeller-hull interaction effects and the necessary cavitation constraints for the optimisation process. More specifically, their input space included the span-wise chord, camber, pitch, rake, skew, and thickness distributions. To reduce the input space, the authors defined these distributions as differences from a base propeller design [218] parameterised on the basis of b-spline curves. The output space of the DDMs consisted of 4 cavity characteristics computed for the "key" blade, namely the maximum cavity volume, the cavity volume change within 1 revolution, maximum sheet thickness at the tip, and the chord-wise cavity centroid, as well as the thrust coefficient. MAPEs of approximately 1% were reported for the ANN for all outputs, whereas Kriging and its variants achieved near-zero errors for all outputs with the exception of maximum cavity volume, thrust coefficient and chord-wise cavity centroid, for which MAPEs of 0.7%, 0.3%, and 0.9% were observed, respectively. The authors also concluded that DDMs can facilitate the rapid convergence of the optimisation process, noting that the use of DDMs in optimisation reduced the computational requirements by half, even when including the time required to generate the data for the learning phase the DDMs.

Authors of [219] demonstrated the feasibility of a multi-fidelity, multi-objective design optimisation of the E779A propeller [114] with DDMs. Kriging models were developed utilising data from a varying number of low-fidelity BEM high-fidelity RANS [220] simulations, ranging between $40-640$, and $4-40$, respectively. An additional 256 RANS simulations were utilised strictly for validation purposes. The input space of the DDMs consisted solely of the radial pitch distribution of the blade, parameterised by 4 control points of a *b*-spline at fixed radial locations. The output space of the DDMs included the open water propeller efficiency, thrust coefficient, and 3 local pressure coefficients, 2 located on the leading edge of the pressure side of the propeller, near the root and tip, and one on the suction side. As a first step, the authors approximated the results of the BEM simulations, without using RANS, concluding that satisfactory performance can be obtained utilising only 160 samples, with MAPE varying between $0.3\% - 5.8\%$. Subsequently they studied the performance of the DDMs to approximate the high-fidelity RANS results, reporting MAPE between $0.06\% - 12\%$ when exploiting data from 320 BEM simulations and 40 RANS simulations.

More recently, URN prediction capabilities of ANNs were studied in [192]. The authors developed an ANN to predict the sound pressure levels at the first 3 blade passing frequencies utilising information regarding propeller geometry and wakefield, and the vessel's hullform. A dataset of hydroacoustic simulations was generated with an in-house BEM-FWH computational code, with a full-factorial design of experiments consisting for 17 propellers, 25 wakefields, 2 advance ratios and 4 cavitation numbers, for a total of 3098 simulations. The input space of the ANN consisted of a mix of time-series and scalar quantities, including propeller design parameters and inflow conditions. More specifically, time histories of the angle of attack, static pressure, and their first-order derivatives were utilised, whereas scalar inputs included the number of propeller blades, propeller diameter, rotational speed, and distances between leading edge to blade reference line at the three radial sections, 3 definitions of the cavitation index, chord length, and maximum camber to chord ratio. The output space of the ANN consisted of the sound pressure levels on the 1st, 2nd, and 3rd blade passing frequency. The authors experimented with various ANN architectures under a variety of

interpolation and extrapolation scenarios, with the best performing ANN architecture achieving an average error of 7.8 ± 1.0[dB] across all targets.

3.5 Hybrid models

HMs constitute the newest set of methods employed for URN prediction and their advantages has been demonstrated on a number of studies [85, 182, 183], including URN prediction [11, 84, 221–223]. Table 3.4 summarises these studies, by reporting for each one the DDM employed, scope, input and output spaces, available data, and main results.

The first study employing HMs in this field was presented by Cipollini et al. [221], with the aim of predicting the cavitating vortex frequency and its corresponding sound pressure level (SPL). The authors exploited a dataset of 164 cavitation tunnel model scale tests, and by combining DDMs based on the Kernel Regularised Least Squares (KRLS) algorithm Hainmueller and Hazlett [13], with the semi-empirical models of Bosschers [82], Raestad [168], they demonstrated the high potential of HMs in predicting vortex noise. In particular, the vortex frequency was predicted by the DDM with a Mean Absolute Error (MAE) of approximately 7[kHz], whereas the SPL was predicted with a MAE of 2.3[dB]. The corresponding values were even lower for the HM, with the frequency error being substantially lower and equal to 74[Hz], and the SPL being marginally improved with a MAE of 1.6[dB]. This study was further extended in [222], further demonstrating the superiority of HMs over DDMs or PMs in various interpolation and extrapolation scenarios. With the addition of more features providing information regarding the inflow conditions and cavitation phenomena, the prediction of vortex frequency and its SPL was further reduced to $(10.9, 18.1)$[%] for the DDM, whereas the same values for the HM correspond to $(6.4, 10.7)$[%]. The performance of both the DDM and HM was slightly inferior for the extrapolation scenario, with reported errors equal to $(17.6, 25.1)$[%] for the vortex frequency and SPL predictions with the DDM, whereas significantly lower errors were reported for the HM, equal to $(7.7, 12.6)$[%]. The authors commented on the ability of the HM to provide accurate predictions, and its superiority over the DDM across all scenarios, further stating

that the generalisation ability of the HM should be further validated with datasets encompassing additional propellers and wakefields.

Authors of [11] proposed HMs in order to predict an artificial simplification of URN spectra, composed by 5 two-dimensional quantities. Mindful of utilising data available strictly during the early stage propeller design process, the authors developed 3 different modelling approaches: A PM that combined BEM simulations [49, 224] with the Empirical Tip Vortex (ETV) model [82, 173], a DDM based on using KRLS and a dataset of 425 cavitation tunnel model scale tests, and an HM that takes advantage of both previous sources of information through Multi Task Learning [225, 226]. The authors carried out two sets of evaluation scenarios: In the first set (interpolation scenario), working conditions within the ones used to develop the models have been employed to test the capability of the DDMs and HMs to predict the main characteristics of the URN spectra. In the second set (extrapolation scenario) groups of working conditions were employed for which the cavitation intensity is different with respect to the intensities utilised to develop the models. An extensive error estimation analysis was carried out, with various metrics. In summary, the central peak point was approximated within $(174 \pm 10, 3.5 \pm 0.2), (114 \pm 6, 1.9 \pm 0.1), (68 \pm 3, 1.1 \pm 0.1)$ [Hz, dB] for the PM, DDM and HM, respectively. Similar errors for the remaining two break points were observed for the interpolation scenario, whereas 25% error increase was reported for the extrapolation scenario. The authors concluded that HMs showed remarkable accuracy in this task, greatly surpassing the capabilities of pure DDMs or PMs.

Authors of [223] also employed HMs to predict cavitating vortex frequency and its corresponding sound pressure level, utilising more advanced DDMs and HMs from the world of Deep Learning [203], and developed utilising a subset of the experiments from the dataset of [11]. The authors demonstrated that these advanced DDMs and HMs surpass the performance of the corresponding models presented in [11] as they can find a richer representation of the several high-dimensional parameters describing the underlying phenomena (i.e. surface pressure distributions over the blades, and bound circulation). In particular, errors of $(122.6, 2.1)$ [Hz, dB] were reported for the DDM, much lower than the errors reported by the DDMs of Miglianti et al. [11]. Even

more impressive was the prediction capability of the HM with reported errors equal to $(84.7, 1.5)$ [Hz, dB]. Despite the impressive performance of the developed models, the authors noted that model performance needs to be investigated utilising larger datasets, and under interpolation and extrapolation scenarios commonly encountered by researchers and practitioners in the field.

To the best of the author's knowledge, the latest developments are presented in the work of Miglianti et al. [84], which accounts for the extensions recommended by Oneto et al. [223], and predicts the simplification of the URN spectra proposed by Miglianti et al. [11], instead of the cavitating vortex frequency and its corresponding SPL. In this study, the authors utilised a subset of experiments from the dataset of [11] for the development of the DDMs and HMs, enriched with several quantities extracted from a BEM computational model. Instead of employing KRLS, the authors made use of recent advances in Deep Learning, to fully exploit the information incorporated in the high-dimensional tensors of several hydrodynamic quantities computed with a BEM model [49, 224, 227]. A total of 37 quantities comprised the input space of the ANNs and HMs, covering the propeller operating conditions and geometry, cavitating phenomena, and various quantities relating to the wakefield and angle of attack. The authors demonstrated that, once again, the HMs surpass the performance of the DDMs and PMs, in all interpolation and extrapolation scenarios considered. In particular, the proposed DDMs and HMs achieved average errors of $(58.7 \pm 4.3, 1.0 \pm 0.1), (48.9 \pm 3.9, 0.8 \pm 0.1)$ [Hz, dB], respectively, for the for the central peak during interpolation, with similar results for the remaining 2 break points that characterised their URN spectra. Approximately double errors were reported for the extrapolation scenario. The authors concluded that, although a larger dataset was utilised with respect to [223], it still does not allow them to verify model performance on fully unseen propeller and inflow conditions.

3.6 Open issues and future perspectives

The preceding sections provided a comprehensive overview of the literature pertaining to propeller URN prediction. Through this review several shortcomings of each family

of modelling approaches have been identified.

Focusing on high-fidelity CFD models, whereas the rapid increase in computing power makes them increasingly popular, particularly in the aeronautics industry [228, 229], in the context of marine applications, the inherently high Reynolds numbers, and the high sound velocity that governs the speed of the wave-fronts that need to be captured, make it rather challenging to use such methods on a regular basis, particularly when investigating full-scale vessels and propellers. Moreover, the nature of turbulence dictates that the largest flow scales present in the fluid domain will be of the order of the characteristic dimensions of the body. For instance, one could expect the largest eddies for a large containership to be in the order of 10 - 20[m] in size, whereas for a full-scale directly driven propeller the acoustic wavelength associated with the periodic cavitation and loading noise will be larger than 500[m]. This difference of scales implies that finding a flow solution applicable to both problems simultaneously may prove challenging due to the mesh size and fidelity requirements being different [76, 230]. These phenomena impose strict cell requirements on DES and LES and prohibit the wide use of the most sophisticated CFD methods. On the other hand, it has been demonstrated by several studies [76, 125, 139, 146, 147] that the computationally cheaper RANS solvers are inherently unable to capture the fine details of the flow-field required for a robust hydroacoustic analysis. Nevertheless, despite the shortcomings of RANS, relatively few authors employ LES or DES primarily due to their prohibitive computational cost, and the almost exclusive use of RANS when fully-appended vessels are considered is evident in current literature. This implies that the prediction of marine propeller URN is a highly complex, multi-scale phenomenon which has not been widely studied using the most modern fluid dynamics modelling techniques, primarily because fully tackling all of the complexities of the underlying flow phenomena remains computationally impractical, although not necessarily beyond the capabilities of current top-of-the-line computing systems.

Furthermore, apart from the significant computational requirements of a reliable hydroacoustics analysis, several state-of-the-art studies [24, 91, 100, 147] are still devoted to providing guidelines regarding the architectural choices that need to be considered

in a reliable CFD-based hydroacoustics analysis with the most promising p-FWH formulation. This certainly indicates an increasing maturity for these methods, however several modelling challenges still exist: The ability to accurately resolve the turbulent cavitating flow around a propeller, the accurate prediction of far-field noise propagation from near-field CFD simulations, and accounting for the wide range of frequencies affected by cavitation noise are still under investigation.

Empirical and semi-empirical models surpass the shortcoming of high computational requirements, at the expense of accuracy. Despite not accounting for most of the flow dynamics, which have shown to be of great importance for hydroacoustics purposes, comparisons between model results and model- or full-scale tests show that there is correlation between experimental and numerical results. Nevertheless, subsequent studies employing the same models on different case studies report higher discrepancy in their results. It is often the case that several semi-empirical models need to be combined to obtain the full spectra of noise, and up to now there is no clear methodology and recommendations regarding best practices for their combined usage. In this context, it is still difficult to provide quantitative conclusions on the relative performance of empirical and semi-empirical models, apart from the fact that they are commonly used in initial design stages for qualitative estimations of URN [17].

DDMs have shown promising results and have demonstrated their potential and possibility to improve the capability of empirical and semi-empirical methods, although their applicability remains rather limited in propeller design and analysis outside of academia. Nevertheless, most studies presented in Sections 3.4.3 - 3.4.4 demonstrate the ability of DDMs to provide accurate predictions by utilising databases that are carefully constructed for a very particular task. One issue encountered in the development of DDMs is the amount of data that has to be collected. In highly specialised engineering applications, it is common that the data required to develop a highly-performing DDM surpasses the experimental data that is readily available. This usually results in limited capabilities of DDMs in terms of accuracy, which can be high on average but not pointwise, and in some cases DDMs can provide physically inconsistent predictions [85].

The few studies employing HMs for propeller URN prediction report highly accu-

rate results, superior to those of pure DDMs, and far superior to empirical and semi-empirical models. Nevertheless, objective comparisons with more advanced CFD-based models have not been conducted. Researchers employing HMs generally conclude that they can be highly accurate, they require fewer historical data than DDMs as they exploit the physics-related knowledge encapsulated in PMs, and they can provide very fast results with respect to CFD-based models. Nevertheless, these studies, along with further investigation on the use of HMs outside the fields of propeller design and analysis reveals that several hybridisation schemes have been introduced in the broader literature thus far:

- A naive approach, in which the output of the PM is utilised as a new input that the DDM can use during learning [83, 84, 86],
- a more advanced approach, in which the problem is mapped in a ML Multi Task Learning framework [225, 226, 231–233] and the learning algorithm learns a function that is both close to the available data, and the predictions of the PM [11, 83, 85, 221, 222].

Unfortunately, these approaches do not allow HMs to fully achieve the true potential, since they naively join together PMs and DDMs without actually blending them: either the results of the PMs are added as new features for the DDMs, or the DDMs try to learn, simultaneously, both the data and the output of the PMs. It appears that the limitations of these approaches is threefold:

- Current studies available in the literature do not fully investigate the physical plausibility of the predictions, for instance with comparisons between the expected behaviour of the models in circumstances where physical knowledge of the phenomena is high [194].
- The current body of literature does not show the advantage of using HM in terms of the ability to better extrapolate (to be more accurate) with respect to PMs and DDM. Partially, this limitation is also due to the unavailability of large datasets covering multiple propellers and multiple working conditions [84].
- Current approaches do not show any advantages in terms of required computational effort needed in model construction, since PMs and DDMs are simply joint

together [84].

In view of the information presented thus far, a model capable of predicting URN from marine propellers based on information available at the design stage, with high accuracy and low computational cost is currently not available. Approaches based on HMs are currently the least explored, but most promising avenues for a methodology having the aims and objectives discussed in Chapter 1: They are able to generate models employing robust statistical inference procedures and data collected in past experiments, and further exploit the governing equations describing the phenomena of interest considering both theoretical and empirical aspects. For these reasons, the methodology that will be presented in Chapter 4 will focus on the development of a state-of-the-art HM.

Mindful of the accuracy and computational costs of the various PMs discussed in Sections 3.2 - 3.3, the HM will combine the following PMs:

- A panel method to estimate the hydrodynamic performance of a propeller in non-uniform inflow conditions,
- the semi-empirical model of Matusiak [5] to estimate the broadband effects of sheet cavitation,
- the Empirical Tip Vortex (ETV) model of Bosschers [82] to estimate the radiated noise due to the presence of a tip vortex cavities.

Focusing on DDMs, these can be generally grouped in two main families: shallow and deep DDMs [200, 203]. Shallow DDMs usually require handcrafting features, implicitly and/or explicitly, to be able to achieve good recognition performance [200, 234]. Usually, this feature set is designed based on classical signal processing techniques [234] and then enriched via ensemble [235, 236], kernel [237], random [238], or learned [239] representations. Deep DDMs, instead, are able to automatically learn features directly from the data [203] and over-perform state-of-the-art shallow DDMs, and in some cases also humans, in terms of recognition performance in many different applications [240–244]. Unfortunately, Deep DDMs have three main weaknesses. First, they require a huge number of samples to be trained effectively, which are usually not readily available, particularly in highly specific engineering applications such as the one considered

in this work [11]. Secondly, they are hard to interpret: It is complex to deduct what a Deep DDM has actually learned from the available data, resulting in models that are not particularly useful in practical applications where insights on the problem need to be extracted [245]. Finally, Deep DDMs are seldom able to provide physically plausible predictions, considering, for instance, the well-known problem of adversarial samples [246, 247]. With the above considerations in mind, this work will focus on Shallow DDMs. According to the discussion of Section 3.4, three main families have been identified as the most effective in practice and will be used in this work: Kernel Methods (KMs) [237, 248, 249], Ensemble Methods (EMs) [250], and ANNs [203, 239].

The PMs and DDMs will be blended in a novel HM that will leverage both theoretical knowledge of the governing physics and robust statistical inference procedures to deliver computationally cheap, physically plausible, and accurate predictions. As these PMs and DDMs are essential parts of the proposed methodology, they are further discussed in Appendices A - D.

3.7 Summary

In this chapter a thorough review of the existing literature on the field of numerical prediction of URN from marine propellers. All the common modelling approaches have been discussed, including the application of high-fidelity CFD techniques, empirical and semi-empirical models, DDMs, and HMs, and the benefits and drawbacks of each method have been presented. Finally, by identifying research gaps in the existing literature, the framework for this work has been proposed, and will be thoroughly presented in the next chapter.

Table 3.1: Overview of studies employing CFD models for propeller URN and cavitation behaviour.

Work	Scope	Method – (Hydro-) dynamics	acoustics	Cav.	Case Study	Conclusions
[24]	Investigation of the impact of eddy viscocity turbulence models in hydroacoustic performance.	RANS	FWH	✓	INSEAN E779A propeller	Vortex instability in the propeller's slipstream might be the main noise source of the URN for far-field noise estimations under non-cavitating and high blade loading conditions.
[43]	Correlation of noise spectra with observed cavitation patterns from numerical simulations, and comparison with full-scale measurements.	DES	p-FWH		M/T Olympus Oil Tanker	The numerical method underestimates the broadband noise level in frequencies where TVC has an important contribution. At frequencies above 200[Hz], broadband noise becomes increasingly under-predicted at high frequencies.
[45]	Numerical prediction of the acoustic field of a propeller interacting with non-uniform inflow, considering the effects of the interaction between the unsteady propeller loading and incoming non-uniformities.	DES	FWH	✓	DTMB 4118 propeller	Noise radiation with the three-cycle wakefield has an axi-symmetric dipole-type pattern. Directivity of sound in the four-cycle wakefield demonstrates an asymmetrical character, with scatters between different azimuth planes.
[91]	Investigation of the effects of grid resolution and the influence of eddy viscocity turbulence models in the predictions of the p-FWH analogy.	RANS	FWH	✓	INSEAN E779A propeller	Insufficient grid resolution reduces the numerical diffusion in the RANS solver. Nevertheless, an increase in tip vortex extension and intensity is not adequate by itself to make a reliable prediction of URN using RANS.
[92]	Comparison of numerical and experimental results for the URN of a model-scale propeller under the presence of TVC and sheet cavitation.	RANS, DES	p-FWH	✓	Princess Royal vessel propeller	URN spectra found to be in agreement with the experimental data. Discrepancies were observed in the low- and high-frequency regions, especially when RANS is used.

Continued on next page

Table 3.1 – *Continued from previous page*

Work	Scope	Method – (Hydro-) dynamics	acoustics	Cav.	Case Study	Conclusions
[97]	Exploration of the intrinsic relations between the turbulent non-cavitating and sheet cavitating flows, and their URN.	RANS	FWH	✓	Seiun Maru training vessel propeller	RANS is only suitable for the prediction of the low-frequency region. Prediction of the broadband spectrum requires more advanced CFD models.
[100]	Exploration of the sensitivity of the FWH for defining the porous data surfaces and key simulation parameters such as time step and grid resolution.	RANS	p-FWH	✓	INSEAN E779A propeller	Particular care must be adopted while defining the porous data surfaces to minimise the amount of upstream vorticity penetrating them while ensuring the effect of noise-generating flow features is aptly captured.
[108]	Numerical investigation of the URN due to TVC of a model scale submarine under various operating conditions	DES	FWH	✓	DARPA SUBOFF 5470 w/ HSP17, HSP38	predicted TVC closely follows the measurements, and that the URN spectra also show excellent agreement, confirming the experimental findings that the propeller with the highest skew angle induces lower cavitation noise.
[125]	Prediction of URN from cavitating propellers operating in-behind conditions.	LES	FWH	✓	Princess Royal research vessel	Results reveal flow features that RANS cannot represent, and it is not suitable for hydroacoustics analyses.
[126]	Test of the versatility and effectiveness of the numerical method in predicting URN from non-cavitating propellers.	RANS	FWH, p-FWH		INSEAN E779A propeller	RANS simulations are inadequate for hydroacoustic purposes, especially when turbulence-induced velocity fluctuations are present.
[127]	URN Prediction for a scaled ship model in a steady course.	RANS	FWH, p-FWH		Patrol vessel w/ 2 INSEAN E1630	Numerical method is able to assess URN and to identify the main generating noise mechanisms.
[128]	URN prediction for a large ROPAX. vessel.	RANS	FWH, p-FWH		Full-scale ROPAX with 2 CLTs	The numerical method can be used as a standard approach to provide hydroacoustic characterisation during the design stage.

Continued on next page

Table 3.1 – *Continued from previous page*

Work	Scope	Method – (Hydro-) dynamics	acoustics	Cav.	Case Study	Conclusions
[129]	Investigation of the hydroacoustic behaviour of an LNG carrier at different rotational speeds.	RANS	p-FWH		full-scale LNG carrier	p-FWH is highly suitable for hydroacoustics problems, and that quadrupole noise sources should not be neglected.
[130]	Analysis on the proper use of FHW for URN prediction of marine propellers, and investigation of the effects of the porous data surface on the quality of the predictions.	RANS	p-FWH		INSEAN E779A propeller	For open surfaces, the largest contribution to the computed pressure signals can be numerically modelled by the monopole term of the FWH equation.
[131]	Investigation of the effects of different grid structure configurations on the numerical results.	RANS	p-FWH		INSEAN E779A propeller	Typical propeller grids may not be suitable for predicting pressure fluctuations far from the propeller. Accurately predicting local pressures directly with RANS is challenging.
[132]	Verification of the implementation of the FWH equation and investigation of the behavior of the permeable surface.	RANS	p-FWH		S6666 propeller	The choice of an appropriate porous data surface is critical, as is the conceptual separation between the physical and numerical source terms in the porous formulation.
[133]	Investigation of the effects of duct geometry on overall URN considering sound reflection and scattering effects.	BEM	FWH		DTMB 4119, KA470 propellers	Noise generated by a marine propeller under non-cavitating conditions has a long fundamental wavelength and the effect of the duct is not so important at the far-field from the viewpoint of acoustic performance.
[134]	Investigation of URN levels and noise directivity patterns of various noise sources under the presence of sheet cavitation.	BEM	FWH	✓	DTMB 4119, DTMB 4381 propellers	In non-uniform flows noise, directivity patterns are a direct result of dipole noise under non-cavitating flows.

Continued on next page

Table 3.1 – *Continued from previous page*

Work	Scope	Method – (Hydro-) dynamics	acoustics	Cav.	Case Study	Conclusions
[139]	Prediction of the non-cavitating and cavitating URN of a model propeller under various operating conditions.	BEM	Bernoulli, FWH	✓	INSEAN E779A propeller	Numerical uncertainties in the evaluation of the cavity pattern can have a strong impact on the URN levels.
[142]	Study on the pressure fluctuations induced by propeller sheet cavitation and analysis on its effects on URN.	VLM	FHW		3 propeller models	Combination of VLM with FWH can provide reasonable prediction regarding the pressure fluctuation due to propeller sheet cavitation.
[143]	Demonstration of the potential of the numerical method for hydroacoustic analysis.	RANS, DES	p-FWH		INSEAN E779A propeller	Reliable analyses require the computation of the nonlinear quadrupole sources and the estimation of the 3D turbulence and vorticity fields.
[144]	Numerical prediction of noise from a propeller model under the presence of sheet cavitation.	BEM	FWH	✓	INSEAN E779A propeller	URN level in the far-field increases notably, the directivity of the acoustic field is altered, and, the propeller behaves as a true monopole source with uniform and omni-directional radiation.
[145]	Theoretical analysis of the FWH and investigation of how the non-linear flow phenomena affect URN.	RANS, DES	FWH		INSEAN E779A propeller	The presence of small bubbles and their interaction with the vortical structures in the wakefield is important for accurate acoustic analyses.
[146]	Analysis of the noise signature of a marine propeller model in various operating conditions.	RANS	FWH	✓	PPTC propeller	DES or LES should be employed if more in-depth studies and accurate results are required.
[147]	URN prediction of a propeller scale model and a hydrofoil, under the presence of sheet cavitation.	RANS	FWH	✓	PPTC propeller, NACA0009 hydrofoil	RANS is not able to predict the unsteady behaviour of the sheet cavities particularly well, or the tip vortex extending downstream of the propeller.

Continued on next page

Table 3.1 – *Continued from previous page*

Work	Scope	Method – (Hydro-) dynamics	acoustics	Cav.	Case Study	Conclusions
[148]	Investigation of the hydroacoustic performance of a propeller model and numerical comparison of 3 different methods.	BEM, DES	p-FWH		INSEAN E779A propeller	BEM - p-FWH predictions are in good agreement with the corresponding DES - p-FWH results. The lack of modelling of the turbulent structures evolving downstream make BEM inadequate.
[149]	Hydroacoustics analysis under cavitating and non-cavitating conditions of a propeller scale model.	BEM	FWH	✓	INSEAN E779A propeller	Proposed approach provides a rigorous theoretical framework, with reduced computational cost and data transfer from hydrodynamic solvers.
[150]	Analysis of the interaction problems arising from the modelling of the dynamic behaviour of a flexible propeller model.	BEM	FWH		P1356 propeller	Fair agreement with experimental results. Excitation of blade loading heavily influences the URN spectrum.
[151]	Investigation of the hydroacoustic analysis of a propeller model in open water conditions.	LES	FWH		SVA VP1304 propeller	Hub vortex is a considerable source of low frequency noise, as it is persistent in the downstream region and characterised by high vorticity.
[152]	Numerical prediction of URN under cavitating conditions.	RANS	p-FWH	✓	Princess Royal vessel propeller	RANS is accurate in the low-frequency region of the URN spectrum. Broadband spectrum requires using LES and DES.
[153]	Investigation of the use of the p-FWH acoustic analogy, aiming to provide guidelines and best practices for future studies.	RANS, DES	p-FWH		INSEAN E779A propeller	Turbulence is crucial as a noise generation mechanism, blade kinematics and loading are the most important linear terms.
[154]	URN prediction of a propeller model in various, non-cavitating, operating conditions.	RANS	FWH		DARPA SUBOFF AFF8, INSEAN E1619	Fair agreement on the URN levels with experiments for frequencies between 300 - 5000[Hz].

Continued on next page

Table 3.1 – *Continued from previous page*

Work	Scope	Method – (Hydro-) dynamics	acoustics	Cav.	Case Study	Conclusions
[155]	Non-cavitating URN prediction of a propeller model behind a submarine.	RANS	FWH		DARPA SUBOFF 5470 w/ DTMB 5495-3	Hull scattering effect interacts with propeller's sound field, changing the noise footprint.

Table 3.2: Overview of studies employing empirical models for propeller URN and cavitation behaviour.

Work	Scope	Case Study	Available data	Accuracy	Conclusions
[5]	Model the generation and collapse of free bubbles from sheet cavitation.	Sydney Express coastal service vessel.	Measurements from the Pasadena oil tanker.	< 20[dB]	Further validation on highly-skewed propellers, extensions to include viscous effects.
[156]	URN prediction by relating spectral components of noise to a vessel's main particulars	Oil tanker	Experiments of HSVA from 5 vessels.	± 5[dB]	Further investigation to include more input parameters, extend for vessels with CPPs.
[157]	URN due to blade sheet cavitation prediction	DTMB 4148, DTMB 4119, Seium-maru HSP propellers	Numerical experiments of [251]	± 25[dB]	Fast and reliable predictions. Validation on additional propellers required.
[158]	Prediction of tonal and broadband noise from marine propellers.	Cargo liner, training ship.	Full-scale tests.	± 5/ ± 20[dB] (tonal / broadband noise)	More detailed measurements of cavitation patterns required for validation.
[159]	Prediction of broadband noise from marine propellers.	Propeller of [252].	Experimental results of [252].	< 30[dB]	Further validation is needed utilising additional experimental data.
[160]	URN prediction of thruster propellers and reduction technologies.	Discoverer Enterprise drill-ship.	Measurements from 6 thruster propellers.	< 30[dB]	Acceptable qualitative agreement of the highest levels of cavitation noise.
[166]	URN prediction from tip vortex cavitation.	Two oceanographic research vessels.	Full-scale tests.	≤ 3[dB]	Further validation required with additional vessel types.

Continued on next page

Table 3.2 – *Continued from previous page*

Work	Scope	Available data	Case Study	Accuracy	Conclusions
[168]	Prediction of tip vortex noise and acoustic pressure.	Various twin-screw passenger vessels.	Experimental studies involving 15 vessels of various types.	≤ 25[dB]	Acceptable agreement with experimental data of model scale tests and full scale trials.
[173]	Prediction of broadband hull pressure fluctuations and URN due to propeller tip vortex cavitation.	Combi freighter vessel, MS Statendam cruise vessel [175].	Experiments from various vessels.	< 25[dB], high variance among the case studies.	Aspects influencing the shape of the hump and the high frequency slope need further investigation.
[176]	Prediction of the azimuthal velocity distribution of a cavitating vortex in a two-dimensional viscous flow.	Wing tip-vortex in cavitating and non-cavitating conditions.	Experimental azimuthal velocity data from [178].	Good qualitative agreement.	Model still needs to be extended with a relation for the axial and radial velocity distribution.
[181]	Propeller cavitation noise prediction.	Model scale bulk carrier.	Experimental data of [253].	< 13[dB]	Capabilities of the method need to be investigated further for additional vessels.

Table 3.3: Overview of studies employing DDMs in propeller design and analysis.

Work	Scope	Method	Inputs	Outputs	Available Data	Accuracy
[192]	URN prediction of blade passing frequencies.	ANN	15 quantities for propeller geometry and inflow conditions.	1^{st}, 2^{nd}, and 3^{rd} blade passing frequency URN levels.	3098 BEM-FWH simulations.	MAE: 6.8÷8.0[dB]
[194]	Hydrodynamic performance prediction.	ANN Kriging	11 quantities for propeller geometry, inflow conditions and cavitation.	4 cavity characteristics of the "key" blade.	350 VLM simulations.	ANN: $\approx 1\%$ Kriging: 0.02÷0.9[%]
[207]	Hydrodynamic performance prediction.	GP	angle of attack, cavitation index.	lift-over-drag ratio.	2D, 3D RANS simulations.	MAPE 1÷5[%]

Continued on next page

Table 3.3 – *Continued from previous page*

Work	Method	Scope	Inputs	Outputs	Available Data	Accuracy
[208]	Hydrodynamic performance prediction.	GP	17 control points of 4 b-splines.	lift-over-drag ratio, lift coeff., cavity thickness at 3 locations.	3D RANS, FEM simulations.	MAPE ≤ 4[%]
[209]	Hydrostructural performance prediction.	GP	17 control points from 4 b-splines.	drag-to-lift ratio, lift force, max. stress, tip deformation.	3D RANS, FEM simulations.	MAPE ≤ 3[%]
[210]	Hydrofoil hydrodynamic performance prediction.	"s-risk" DDM	15 control points from 3 b-splines.	lift-to-drag ratio, total lift force.	RANS and potential-flow solver simulations.	MAPE ≤ 2[%]
[211]	Propeller-induced pressure pulse prediction.	ANN	16 wakefield quantities, 19 propeller geometry quantities	1^{st}, 2^{nd} order harmonic pressure pulse coeffs.	Experimental data of 470 model-scale tests.	1^{st} order: ≤ 4 [%] 2^{nd} order: ≤ 20[%]
[212]	Propeller force and moment prediction.	ANN	16 quantities of propeller geometry and submarine control.	Forces and moments in 6 degrees of freedom.	155 experiments of submarine model tests.	R^2 0.95÷0.99[–]
[213]	Hydrodynamic performance prediction.	ANN	No. of propeller blades, blade area ratio, pitch ratio, advance coeffs.	thrust, torque coeffs, open water efficiency.	Wageningen-B series experiments, BEM simulations.	MAPE ≤ 4[%]
[215]	Discrete spectrum thrust prediction.	ANN	coeffs of a 4^{th} order polynomial for propeller skew distribution.	thrust coeff., 1st and 2nd order thrust coeffs.	$336,000$ BEM simulations.	thrust coeff: 0.01[%] 1^{st}, 2^{nd} order thrust: 0.21÷5.71[%]
[219]	Optimisation of hydrodynamic performance.	Kriging	pitch distribution.	thrust coefficient, 4 pressure coeffs.	$40-640$ BEM simulations, $4-40$ RANS simulations.	BEM: 0.3÷5.8[%] RANS: 0.06÷12[%]

Table 3.4: Overview of studies employing HMs for URN prediction.

Work	Scope	Method	Inputs	Outputs	Available Data	Accuracy
[84]	URN prediction on simplified spectra.	ANN	37 quantities for propeller geometry, inflow conditions, cavitation.	3 2-dimensional quantities of the URN spectrum.	258 cavitation tunnel tests.	DDM: 2.9÷6.1% (interp.), HM: 2.3÷4.3% (interp.), DDM: 5.8÷9.8% (extrap.), HM: 4.2÷8.1% (extrap.)
[221]	Cavitating vortex frequency and URN prediction.	KRLS	36 quantities for propeller geometry, inflow conditions, cavitation.	Cavitating vortex frequency and URN.	164 cavitation tunnel tests.	DDM: 6845[Hz], 2.3[dB], HM: 74[Hz], 1.6[dB]
[222]	Cavitating vortex frequency and URN prediction.	KRLS	39 quantities for propeller geometry, inflow conditions, cavitation.	Cavitating vortex frequency and URN.	164 cavitation tunnel tests.	DDM: 10.9÷18.1% (interp.), HM: 6.4÷10.7% (interp.), DDM: 17.6÷25.1% (extrap.), HM: 7.7÷12.6% (extrap.)
[11]	URN prediction on simplified spectra.	KRLS	39 quantities for propeller geometry, inflow conditions, cavitation.	3 2-dimensional key quantities of the URN spectrum.	425 cavitation tunnel tests.	DDM: 5.3÷140% (interp.), HM: 4.4÷10.1% (interp.), DDM: 15.2÷354% (extrap.), HM: 6.1÷12.6% (extrap.)
[223]	Cavitating vortex frequency and URN prediction.	ANN	39 quantities for propeller geometry, inflow conditions, cavitation.	Cavitating vortex frequency and URN.	258 cavitation tunnel tests.	DDM: $\approx$ 6[%], HM: 4.0÷4.7[%]

Chapter 4

Hybrid Modelling Framework

Abstract

This chapter discusses the hybridization scheme proposed in this work, with all the details needed to reproduce it. It provides information regarding the structure of the hybrid model, the parts that comprise it, it's development process, and the assessment of the physical plausibility of its predictions.

4.1 Introduction

Following the conclusions drawn from the literature study of Chapter 3, HMs are able to take advantage of the best characteristics of both PMs and DDMs by combining them together, and are widely used in contexts where "expert knowledge" regarding the problem under consideration, brought by PMs, can enhance the prediction quality of DDMs. HMs provide several advantages over PMs and DDMs. In brief:

- They can fully exploit both the knowledge of the underlying physical phenomena and historical data to deliver both accurate and physically plausible results [85].
- They can be quite efficient in making predictions, allowing to include them in software tools for design optimization [182].
- They reduce the need for historical observations, thanks to the exploitation of the prior knowledge about the phenomena, consequently reducing the computational effort needed to develop them.

The hybridisation scheme discussed in this chapter aims at enhancing these charac-

teristics even further, by truly blending PMs and DDMs and taking advantage of the knowledge of the underlying phenomena in the model's structure, learning process, and input space. In particular, it leverages the domain knowledge of the DDMs, through the design of a domain-knowledge enriched feature set, and the PMs, through their own estimates of propeller URN.

The rest of this chapter is structured as follows: Section 4.2 formalizes the proposed hybridisation scheme and clarifies the flow of information between the various parts that comprise it. Section 4.3 briefly summarizes the PMs, followed by Section 4.4 which addresses the feature engineering process, whereas Section 4.5 briefly discusses the DDMs employed. Following, Section 4.6 discusses the model selection and error estimation processes utilised to tune the PMs and DDMs, and Section 4.7 discusses the tests that can be conducted on the HM to ensure the physical plausibility of the HM's predictions. Finally, Section 4.8 summarizes this chapter.

4.2 Proposed hybridisation scheme

With these considerations in mind, this work bridges the three main gaps by developing a novel hybridization scheme that can truly blend PMs and DDMs into single HMs. With the proposed scheme, the engineering knowledge regarding the governing phenomena is exploited in model structure, model development, and model enrichment. In general, an HM can either improve the results of the PMs by exploiting available data, or improve the results of the DDMs by embedding domain knowledge into them. This process occurs either through a feature engineering process, or via the modification of the DDMs' functional form. In this work, the author considers the former approach, since the latter can be inserted under the umbrella of properly calibrated PMs or informed DDMs, as for instance PMs properly tuned with available data, or DDMs with features engineered or enriched with domain knowledge. Since one of the aims of this work is to ensure the physical plausibility of the predictions, the scope of the HM is mainly to correct the PM outputs via a DDM. To this end, the idea of recursion is used, in which for a series of iterations, the DDMs' input features are enriched with the difference between the output of the PMs and the outputs of the DDMs themselves.

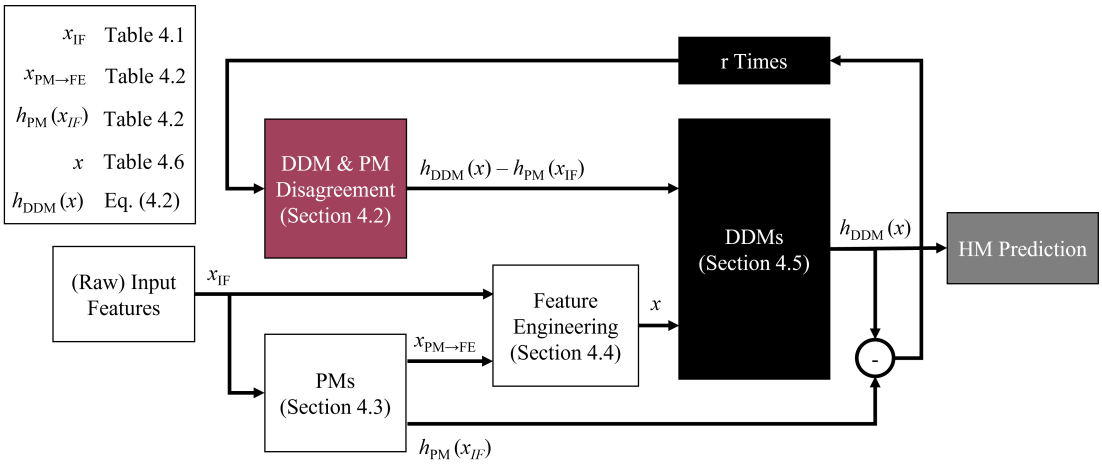

Figure 4.1: Simplified pipeline of the proposed methodology for the hybridisation scheme.

4.2.1 Hybrid model overview

More formally, the PM is defined as $h_{\mathrm{PM}}(\boldsymbol{x}_{\mathrm{IF}})$ where $\boldsymbol{x}_{\mathrm{IF}}$ is the set of quantities required by the PM, i.e. the Input Features (IF), to predict the URN spectra. Each of the DDMs that will be discussed in Section 4.5 is defined as $h_{\mathrm{DDM}}(\boldsymbol{x})$ where $\boldsymbol{x} \supseteq \boldsymbol{x}_{\mathrm{IF}}$ is the set of features required by the DDM to predict the URN spectra, as will be discussed in Section 4.4. Finally, the HM is defined as $h_{\mathrm{HM}}(\boldsymbol{x}) = h^{r}_{\mathrm{DDM}}(\boldsymbol{x})$ where

$$h^{0}_{\mathrm{DDM}}(\boldsymbol{x}) = h_{\mathrm{DDM}}(\boldsymbol{x}), \tag{4.1}$$

$$h^{i+1}_{\mathrm{DDM}}(\boldsymbol{x}) = h_{\mathrm{DDM}}(\boldsymbol{x})([\boldsymbol{x}, h^{i}_{\mathrm{DDM}}(\boldsymbol{x}) - h_{\mathrm{PM}}(\boldsymbol{x}_{\mathrm{IF}})]), \quad i \in \{1, \cdots, r\}, \tag{4.2}$$

where r is the number of recursion iterations, and is an additional hyperparameter of the HMs that needs to be tuned. In simple terms, the proposed HM is the successive application of a DDM informed by the distance from the PMs and, implicitly, by the accuracy of the previous application of the DDM. For the sake of clarity, a simplified pipeline of the proposed methodology is presented in Figure 4.1.

4.2.2 Hybrid model inputs & outputs

Model largely correspond to standard quantities required by the BEM numerical code: Namely, the propeller geometry and inflow conditions. In particular, the following

quantities describing the propeller geometry are needed:

- Skew angle (`s`), defined as the angle between the propeller reference line and a line drawn through the shaft center line and the mid-chord point of the last propeller section in the projected view,
- rake angle (`r`), which corresponds to the angle of a propeller blade face relative to its hub,
- number of propeller blades (Z),
- propeller diameter (D),
- pitch distribution (`p`), defined as the distance that a propeller advances during one revolution,
- chord distribution (`c`), defined as the distance between the leading and trailing edges of a section.
- sectional camber (`z`), defined as the locus of the midpoints between the upper and lower surfaces of the section, when measured perpendicular to the camber line.
- sectional thickness (τ), which is the distance between the upper and lower surfaces of the section measured perpendicular to the chord line.

For the quantities varying along the spanwise direction of the blade values on 8 sections from the root to the blade tip have been considered, on the locations $r/R = \{0.2, 0.35, 0.475, 0.6, 0.7, 0.8, 0.9, 0.95\}$ $[-]$. For what regards τ and `z`, which also vary along a section of the propeller on the chord-wise direction, cosinusoidal spacing is employed with 16 points on each section, equally divided on the pressure and suction sides of the blade.

In addition, the inflow conditions that the propeller experiences are needed. These correspond to the axial component of the wakefield $\boldsymbol{w}_x$, discretized on 22 radial sections and 60 angular locations, the rotational speed of the propeller n_p, advance velocity u_a, as well as the relative tunnel pressure p_{rel}. The outputs of the HM correspond to the quantities of Equation (4.2): The predicted URN levels for 31 frequencies in 1/3 octave band. For the sake of clarity, the inputs and outputs required by the HM are provided in Table 4.1.

Table 4.1: Hybrid model inputs ($\boldsymbol{x}_{\mathrm{IF}}$) and outputs.

Symbol	Description	Size*	Units
Quantities comprising $\boldsymbol{x}_{\mathrm{IF}}$			
D	Propeller diameter	-	[m]
Z	Number of blades		[–]
p	Sectional pitch	1×8	[m]
c	Sectional chord	1×8	[m]
r	Sectional total rake	1×8	[deg]
$\tau_{\max}$	Max. sectional thickness	16×8	[m]
$\mathtt{z}_{\max}$	Max. sectional camber	16×8	[m]
s	Sectional skew angle	1×8	[deg]
$\boldsymbol{w}_x$	Axial component of the wakefield	22×60	[–]
n_p	Rotational speed		[rpm]
u_a	Advance velocity		[m/s]
p_{rel}	Relative tunnel pressure		[bar]
Quantities comprising $h^r_{\mathrm{DDM}}(\boldsymbol{x}_{\mathrm{IF}})$			
$\boldsymbol{S}_{\mathrm{pl}}$	HM predicted URN levels in 1/3 octave band	1×31	[dB]

* Empty field indicates scalar quantity.

4.3 Physics-based Models

This section discusses the various PMs utilised within the framework of Section 4.2, with a focus on their integration within the HM, inputs and outputs, and their verification. More detailed information regarding theoretical considerations, assumptions, and inner workings of the PMs can be found in Appendix A.

4.3.1 Physics-based model's overview

As stated in Section 3.6, the PM employed in this work is composed of three parts:

- Unsteady hydrodynamic computations, performed through an in-house developed BEM numerical code [254, 255], to characterise the propeller's hydrodynamic field with a fair degree of accuracy,
- the semi-empirical model of Matusiak [5] to estimate the broadband effects of sheet cavitation,
- the Empirical Tip Vortex (ETV) model of Bosschers [82] to estimate the radiated noise due to the presence of a tip vortex cavities.

The raw input features largely correspond to quantities required by the BEM nu-

merical code: Namely, the propeller geometry and inflow conditions. The model of Matusiak [5] requires as an additional input the blade pressure distribution computed by BEM, along with 5 parameters that need to be estimated from any available data. The model assumes that any change in the volume rate of the generated bubbles equals the rate at which the sheet cavity volume decreases and that the bubble size follows a β distribution. In combination with a bubble dynamics model [256], this method can estimate the high-frequency broadband spectral content of the URN due to propeller cavitation with a fair degree of accuracy. Finally, the ETV model proposed by [82, 173] is employed to estimate the URN due to TVC. In particular, the ETV is a semi-empirical model based on the Tip Vortex Index (TVI) method [168], and relates the measured URN to the predicted size of the vortex cavity, using the circulation distribution of the propeller blade, also computed by BEM. It is characterised by 7 parameters that need to be estimated from available data, similar to the model of Matusiak [5]. The parameter estimation process is the topic of Section 4.6.3. Finally, the PM's inputs, which correspond to the quantities required by the BEM numerical code, are listed in Table 4.1.

4.3.2 Model outputs

In the process of evaluating the URN spectra, the PM computes a set of quantities that are subsequently processed during the feature engineering process, according to Section 4.4. These include the high-dimensional tensors of: The pressure coefficient on the key-blade, the blade circulation at the propeller tip, angle of attack, as well as a set of non-dimensional scalar quantities that relate to the operating condition of a propeller in a uniform fluid stream. These quantities are defined according to the guidelines of ITTC [17], and they correspond to the advance coefficient J, the thrust K_t and torque K_q coefficients, as well as the open water efficiency of the propeller η_o. These are given by Equations (4.3) - (4.6), respectively.

$$J = \frac{u_a}{\mathtt{n}D}, \tag{4.3}$$

$$K_t = \frac{T}{\rho \mathtt{n}^2 D^4}, \tag{4.4}$$

$$K_q = \frac{Q}{\rho \mathtt{n}^2 D^5}, \tag{4.5}$$

$$\eta_o = \frac{J}{2\pi}\frac{K_t}{K_q}, \tag{4.6}$$

with Q being the torque generated by the propeller.

Another important quantity that is also evaluated is the cavitation index σ, which refers to the ratio of the static to dynamic head of the flow, and represents the flow's tendency to cavitate [7]. It is evaluated according to Equation (4.7).

$$\sigma = \frac{p_{\text{static,ref}} - p_v}{\frac{1}{2}\rho u_{\text{ref}}^2}, \tag{4.7}$$

$$p_{\text{static,ref}} = p_{\text{atm}} + \rho g \mathtt{h} \tag{4.8}$$

with u_{ref} being a reference velocity, $p_{\text{static,ref}}$ the static reference pressure, p_{atm}, the atmospheric pressure, and $\mathtt{h}$ the shaft immersion at the center disc of the propeller. For the sake of completeness, all 4 different formulations of σ have been considered

- σ_u, which refers to the cavitation index evaluated at the shaft line and is based on the advance velocity of the propeller. For this formulation, $u_{\text{ref}} = u_a$.
- $\sigma_{\mathtt{n}}$, which is also evaluated at the shaft line, but is based on the peripheral velocity of the propeller, i.e. $u_{\text{ref}} = \mathtt{n}D$.
- $\sigma_{\text{u,tip}}$, which is based on the resultant velocity at the blade tip, equal to $u_{\text{ref}} = \sqrt{u_a^2 + (\pi \mathtt{n} D)^2}$, with respect to the static pressure at the blade tip.
- $\sigma_{\text{n,tip}}$, which is based on the peripheral velocity of the propeller, i.e. $u_{\text{ref}} = \mathtt{n}D$, with respect to the static pressure at the blade tip.

For the sake of readability, Table 4.2 lists the outputs of the PM.

4.3.3 Model verification & validation

To verify the implementation of the PMs, a set of verification and validation studies was conducted. More formally, the following processes are followed, as defined in Schwer [257], Oberkampf et al. [258]:

Verification. *The process of determining that a model implementation accurately rep-*

Table 4.2: Physics-based model outputs ($\boldsymbol{x}_{\mathrm{PM}\to\mathrm{FE}}$, $h_{\mathrm{PM}}(\boldsymbol{x}_{\mathrm{IF}})$).

Symbol	Description	Size*	Units
Quantities comprising $\boldsymbol{x}_{\mathrm{PM}\to\mathrm{FE}}$			
$\boldsymbol{C}_{\mathrm{p}}$	Pressure coefficient	$44 \times 22 \times 60$	[–]
$\boldsymbol{\Gamma}$	Blade Circulation	22×60	[–]
$\boldsymbol{\alpha}_{G,atk}$	Angle of attack	22×60	[–]
J	Advance coefficient		[–]
K_t	Thrust coefficient		[–]
K_q	Torque coefficient		[–]
η_o	Propeller open-water efficiency		[–]
σ_u	Cavitation index based on u_a		[–]
$\sigma_{\mathtt{n}}$	Cavitation index based on $\mathtt{n}D$		[–]
$\sigma_{\mathrm{u,tip}}$	Cavitation index based on $\sqrt{u_a^2 + (\pi \mathtt{n} D)^2}$		[–]
$\sigma_{\mathtt{n},\mathrm{tip}}$	Cavitation index based on $\mathtt{n}D$ at blade tip		[–]
Quantities comprising $h_{\mathrm{PM}}(\boldsymbol{x}_{\mathrm{IF}})$			
$\boldsymbol{S}_{\mathrm{pl}}$	PM predicted URN levels in 1/3 octave band	1×31	[dB]

* Empty field indicates scalar quantity.

resents the developer's conceptual description of the model and the solution to the model.

Validation. *The process of determining the degree to which a model is an accurate representation of the real world from the perspective of the intended uses of the model.*

According to Oberkampf et al. [258], verification is ideally carried out by comparison of the numerical results against analytical solutions, thereby providing evidence that the computational model is solved correctly and accurately. On the other hand, validation provides evidence that the mathematical model accurately relates to experimental measurements. Contrarily to more generic hydrodynamic or acoustic CFD-based numerical codes that can be applied to simpler cases for the purpose of verification, such as flows over isolated hydrofoils or idealised noise sources, the PMs discussed in Section 4.3 are semi-empirical. This means that they are strictly applicable to problems involving the fluid flow and the acoustics analysis of marine propellers. Unfortunately, analytical solutions for these problems are not available. In addition, as stated in [258], verification and validation experiments must be designed purposefully and be linked to the problem under consideration. In the context of this work, these processes should ideally be conducted with a broad set of propeller types, operating under an equally broad set of conditions that encompass various cavitation types. Unfortunately, such

a broad set of experimental data is also not available for model verification and validation. In fact, this is a recurring problem in the field of hydroacoustics and has been discussed by several researchers in the past [11, 84, 145, 169].

For these reasons, a less formal verification and validation process will be conducted for the majority of the models. In the absence of analytical solutions, model predictions will be compared with numerical experiments conducted by past studies, thereby skipping the verification process. Furthermore, it should be noted that any simulation model cannot fully capture the phenomena that contribute to the behaviour of a complex physical process such as the one studied in this work. As a result, the predictions will most likely show deviations, in the sense that they are not expected to fully agree with reality. Nonetheless, past studies involving the models employed in this work can provide an indication of how well each model's predictions are expected to agree with reality. With these considerations in mind, the model verification process on several occasions will compare the quality of the obtained predictions, to the quality reported in the pertinent literature. Finally, the domain of the experiments used for the verification process will, on occasion, have a small but unavoidable overlap with the case studies used to demonstrate the feasibility of the proposed methodology discussed in Chapter 5.

Table 4.3 summarises the PMs that will be verified, and lists the sources of the numerical or experimental data that will be utilised for these purposes. For these models, custom *Matlab* [259] implementations have been developed. As can be seen from Table 4.3, only a subset of the models used in this work will be verified. The models that have not been verified include:

- The BEM numerical code of Section A.2, which has been verified and validated for a variety of propeller types, including supercavitating [227], ducted [224], and tip loaded propellers [49], for cavitating flows in both steady [260] and unsteady conditions [255], and for strongly non-homogeneous wakefields in [254, 261], and off-design conditions in [262].
- The PSO algorithm used for the parameter calibration of the ETV and the Matusiak models, for which the Matlab *Global Optimisation Toolbox* [263] is utilised.

Table 4.3: Physics-based models verification and validation experiments.

Model	Section	Sources of numerical or experimental data.
Matusiak model	A.3	Matusiak [5], Ohl et al. [264], Johansen et al. [265], Aktas [7], Aktas et al. [8]
ETV model	A.4	Aktas [7], Aktas et al. [8], Pennings et al. [178]

4.3.3.1 Verification of the Matusiak model

The model of Matusiak that was presented in Section A.3 is largely based on the Gilmore equation (A.11) - (A.14) to account for bubble dynamics. To ensure that the implementation of the Gilmore equation is correct, three simulations have been conducted.

The first simulation replicates the case study used by Matusiak [5], who presents numerical results of the simulation of one bubble with a radius of 1[mm] that breaks-off from the sheet cavity of a partially cavitating hydrofoil, which has been used to verify the implementation of the author. The simulation is characteristic of a full-scale propeller with a diameter of 5[m], for which the hydrofoil lies at a radial position of 2[m], with a distance of 1[m] between the point of break-off of the cavity and the trailing edge. The blade is considered to be in the upright position, the propeller is rotating at 118[rpm] and its submergence is equal to 3.5[m].

Whereas most quantities needed to reproduce the numerical experiment are given in [5], there are several unknowns that need to be inferred. Table 4.4 lists all the quantities required to set up the simulation, the values specified by Matusiak, and the values that were inferred from the author. Focusing on the inferred values, the value for the surface tension coefficient corresponds to the reference temperature of 21.5[^{o}C] for water-air interface, and the same reference temperature has been used for the value of the fluid density, according to the recommendations of [266]. Furthermore, the adiabatic value for the polytropic index was assumed. In addition, the assumption of linear pressure growth has been made in [5], with the ambient pressure at the location of the bubble being approximated according to Equation (A.10), which requires as inputs

- the duration that the bubble needs to travel from the point of break-off to the trailing edge of the hydrofoil,

Table 4.4: Constants used in the first verification study of the Gilmore equation.

Quantity	Symbol	Value	Units	Specified in [5]	Inferred
Initial bubble radius	$r_b(t=0)$	1	[mm]	✓	
Initial bubble velocity	$\dot{r}_b(t=0)$	0	[m/s]	✓	
Tait's law constant	$c_{\mathrm{T}}^{(0)}$	3×10^8	[Pa]	✓	
Tait's law constant	$c_{\mathrm{T}}^{(1)}$	7	[–]	✓	
Sound velocity	u_s	1450	[m/s]	✓	
Atmospheric pressure	p_{atm}	98	[kPa]	✓	
Vapour pressure	p_v	1005	[Pa]		✓
Surface tension coefficient	c_{st}	0.0725	[N/m]		✓
Fluid density	ρ	1025.5	[kg/m^3]		✓
Polytropic index	c_{pi}	1.4	[–]		✓

- the pressure on the trailing edge,
- and the local inflow velocity, which is assumed constant.

Reasonable ranges for those can be inferred given the geometric characteristics of the propeller and the cavity size, which are specified, or calibrated. For instance local inflow velocity can be fine-tuned so that the bubble would approximately travel the entire distance from the point of break-off to the trailing edge of the hydrofoil, corresponding to 1[m]. Regarding the vapour pressure, Matusiak [5] mentions that $p_v = p_{g,0}$, but the corresponding value is not specified. For this reason, a calibration process was employed in an effort to replicate the results provided, using values ranging between $600 \div 4180$[Pa], which correspond to sea water temperatures ranging between $0 \div 30$[^{o}C] for a salinity approximately equal to 35[g/kg] as recommended by [266]. The best results for the simulation of a single bubble are presented in Figure 4.2, which closely resemble the computations of [5]. These were obtained for $p_v = 1005$[Pa], corresponding to a sea water temperature of approximately 7.5[^{o}C]. Nevertheless, the additional degrees of freedom related to the linear pressure growth are not easy to estimate, and they affect the results of the simulations significantly.

Given the uncertainties of this verification process, additional simulations have been conducted, with the aim of approximating the experimental data of Ohl et al. [264], Johansen et al. [265]. More specifically, authors of [264] studied sound and light emissions from bubbles experimentally, using high-speed photography in combination with hydrophones, whereas the authors of [265] studied experimentally the shock waves

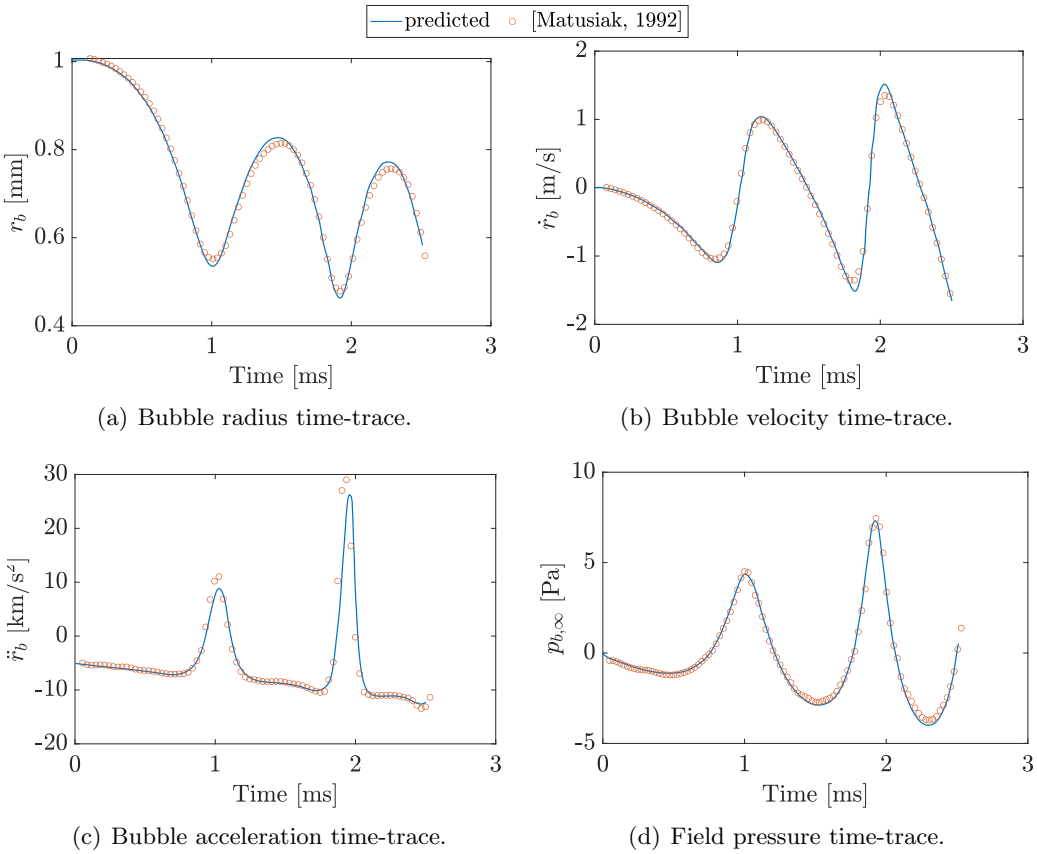

(a) Bubble radius time-trace.

(b) Bubble velocity time-trace.

(c) Bubble acceleration time-trace.

(d) Field pressure time-trace.

Figure 4.2: Verification of the implementation of the Gilmore equation according to the numerical results of Matusiak [5].

emitted by the collapse of laser-induced bubbles. Experiments were conducted with a single spherical oscillating bubble excited by sinusoidal pressure fields which were subsequently analysed towards the aims of each work. The parameters of the numerical simulations conducted are provided in Table 4.5, and the obtained results are compared with the experimental data in Figure 4.3. Similar to the previous verification study, not all quantities needed for the simulations were provided by the authors, and a small subset of parameters had to be calibrated to obtain the results of Figure 4.3. It can be seen that in both simulations the numerical and experimental data agree relatively well. The radii of the bubbles are captured both in terms of magnitudes and phases, and equally important is the fact that the obtained signals follow the bubble collapse, which is the primary source of radiated pressure waves.

Table 4.5: Constants used in the additional verification studies of the Gilmore equation.

Quantity	Symbol	Units	Ohl et al. [264]	Johansen et al. [265]
Initial bubble radius	$r_b(t=0)$	[μm]	8.1	61
Initial bubble velocity	$\dot{r}_b(t=0)$	[m/s]	0	0
Tait's law constant	$c_{\mathrm{T}}^{(0)}$	[Pa]	2.98×10^8	3.05×10^8
Tait's law constant	$c_{\mathrm{T}}^{(1)}$	[–]	7.06	7.15
Sound velocity	u_s	[m/s]	1500	1484
Atmospheric pressure	p_{atm}	[kPa]	100	101
Vapour pressure	p_v	[Pa]	2500	2330
Surface tension coeff.	c_{st}	[N/m]	0.07	0.072
Fluid density	ρ	[kg/m^3]	1000	998
Polytropic index	c_{pi}	[–]	1.4	1.33

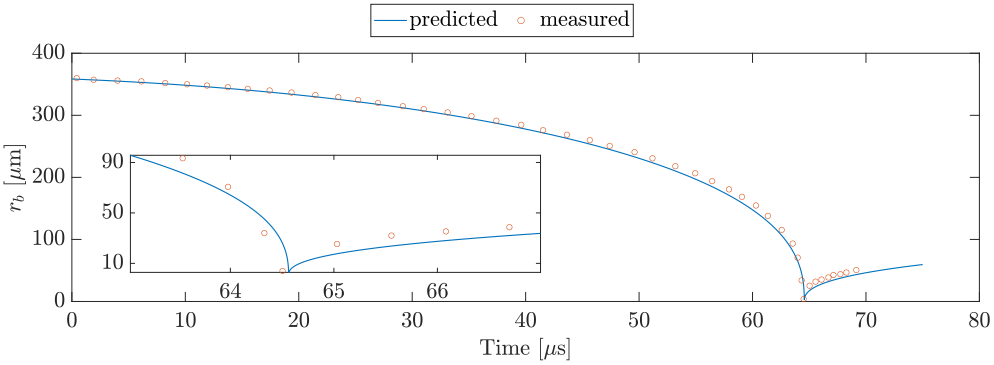

(a) Experiments of Ohl et al. [264].

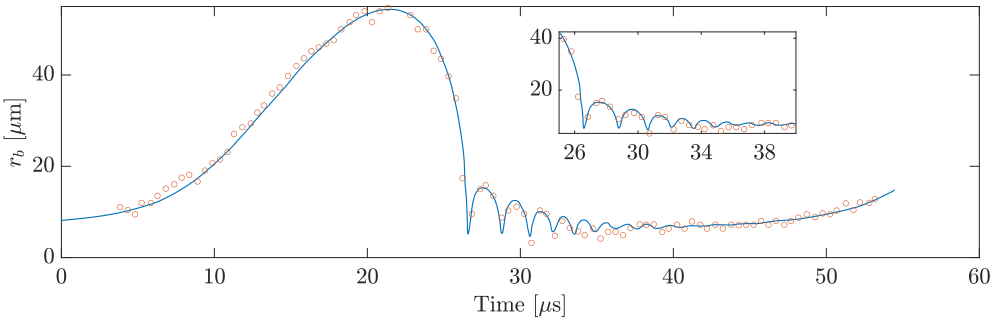

(b) Experiments of Johansen et al. [265].

Figure 4.3: Validation study for the implementation of the Gilmore equation (A.11) - (A.14)

.

Additional results are provided in [5] regarding the pressure time-trace induced by a collapsing cloud of 100 cavitation bubbles with a radius of 1[mm], for the same partially cavitating hydrofoil, and are compared with the implementation of the present study

in Figure 4.4. Whereas the results obtained are physically credible, the random time shifts at which the bubbles are being shed makes it impossible to exactly reproduce the results. To assess the effects of these shifts on the noise predictions, one of the experiments conducted by [6, 7] has also been simulated. This is just one out of the 432 experiments that will be used to assess the feasibility of the proposed methodology, and the experimental campaign of [6, 7] is more thoroughly discussed in Chapter 5. For now, it suffices to state that this experiment involves a propeller model of the Meridian Standard Propeller Series operating in non-uniform wakefield, for which the simulation has been repeated 100 times. Small variations of the parameter values provided in Table 4.9 have been used for the simulations, in an attempt to decrease the discrepancy between the predicted and measured noise. Figure 4.5 compares the experimental and numerical results, with the shaded area corresponding to the 95% confidence interval of the noise levels in the frequency range between $800 \div 20000$[Hz]. The model overestimates the actual URN levels by approximately 15[dB] on average, with discrepancies between $8 \div 20$[dB]. The predictions are credible, and the random time shifts of the cavity break-off affect mostly the region between $800 \div 2500$[Hz], with maximum variations of roughly 10[dB], which tend to diminish for higher frequencies. This behaviour also confirms the findings of [164], who employed the model of Matusiak to predict the URN emitted from the propeller of a 3600 TEU container ship scale model in the cavitation tunnel of HSVA. Discrepancies of the same magnitude have also been reported by [5], for the prediction of URN of an oil tanker and a container ship. Overall, physically plausible trends are obtained, and the quality of the predictions obtained agree with the findings of previous studies employing this model, without any calibration effort from the author.

4.3.3.2 Verification of the Empirical Tip Vortex model

The ETV model of Section A.4 is based on the Proctor vortex model of Equation A.19, for the estimation of the vortex cavity size. The latter was verified utilising the experimental results of Pennings et al. [178], who conducted stereoscopic particle image velocimetry measurements on a half-wing model with a NACA $66_2 - 415$ cross section.

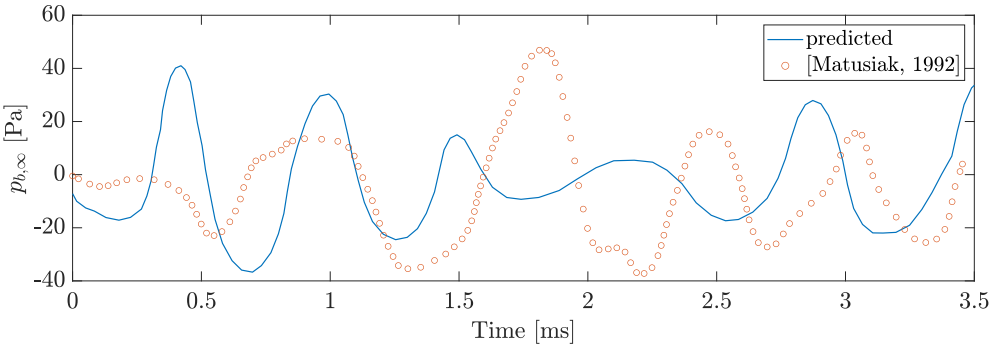

Figure 4.4: Part of the pressure time-trace obtained from the simulation of 100 bubbles.

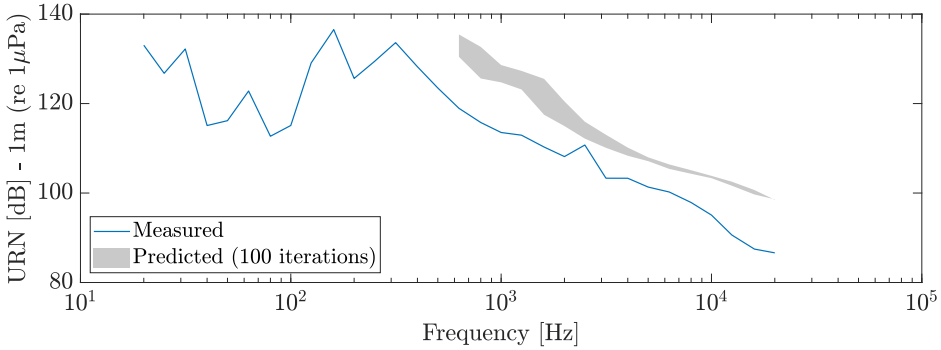

Figure 4.5: Measured URN and Matusiak model predictions for one of the experiments of [6, 7]. The simulation has been repeated 100 times to illustrate the effects of the random time shifts at which the bubbles are being shed.

The wing had a half-span of 0.15[m] and a chord length of 0.1256[m] at the root, for which measurements were performed in a cavitation tunnel at a free-steam velocity of 6.7[m/s], with typical viscous core radii of approximately 1[mm]. Whereas the velocity fields were measured for various lift coefficients and angles of attack at several cross-flow panes downstream of the trailing edge, focus is given on one of those experiments, corresponding to lift coefficient of 0.66[–], angle of attack equal to 9[deg], Reynolds number of 0.9×10^5[–], and dissolved oxygen level equal to 2.5[mg/l], at a distance of approximately a root chord length behind the tip. For this particular experiment, the vortex circulation was equal to 0.22[m^2/s], and the parameters of the Proctor vortex model were manually calibrated. Figure 4.6 presents the experimental results and the predictions of the Proctor vortex model, which shows good agreement with the measurements for the following values: $c_P^{(0)} = 1.2575$[–], $c_P^{(1)} = 0.75$[–], $c_P^{(2)} = 16.035$[–]. In

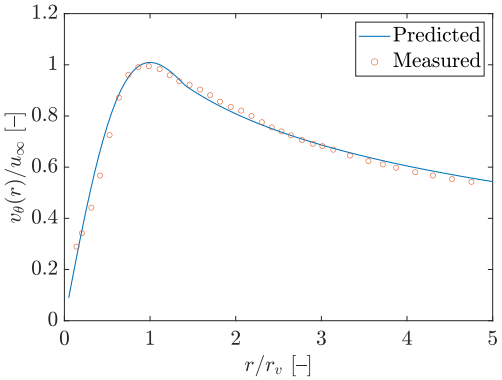

Figure 4.6: Comparison between measured and predicted azimuthal velocity distribution of a cavitating tip vortex on an elliptic platform wing with a NACA $66_2 - 415$ cross section.

Figure 4.6 the radius is normalised with respect to the wetted viscous core radius, equal to 1.1[mm], and the azimuthal velocity is normalised with respect to the free-stream velocity. Although not presented for the sake of brevity, results of comparable accuracy were obtained for several experiments.

For what regards the verification of the ETV model in its entirety, unfortunately a direct comparison with results from past studies has not been performed, as it was not possible to obtain the experimental data necessary to replicate them. For this reason, a randomly chosen subset of the experiments discussed in Chapter 5 was chosen, for which the strength of the tip vortex is obtained from the BEM computations of Section A.2, using the average circulation over a complete propeller revolution at 95% of the radius. Subsequently, a manual calibration process was performed for the parameters of Table 4.9. The final predictions of the ETV model are compared with the experimental results of [7, 8] in Figure 4.7. More specifically, Figure 4.7(a) provides the measured and predicted resonance frequencies, and Figure 4.7(b) presents the corresponding noise levels. The MAPE observed corresponds to 18.3 ± 3.4[%], and 19.3 ± 4.2[%] for the center frequencies and noise levels, respectively.

Overall, model predictions correlate with the experimental results, although significant variance is observed. This confirms the findings of several works employing this model [11, 82, 173]. One interesting aspect is that the predicted resonance frequencies are well-centered around the measured ones. This contradicts the findings of Bosschers

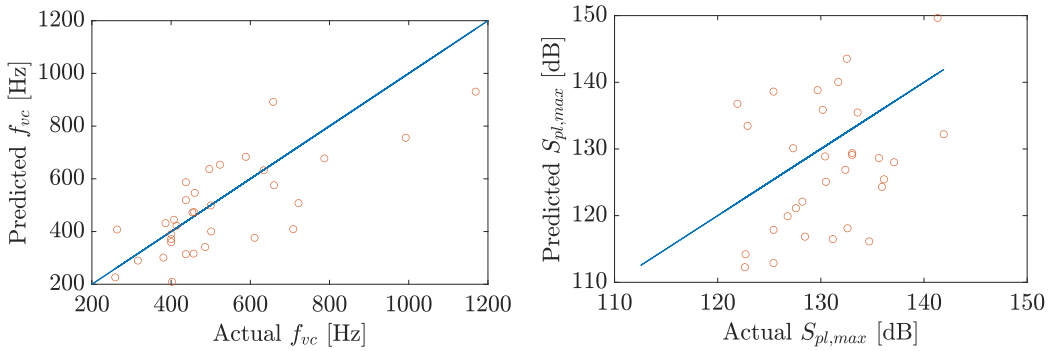

(a) Measured and predicted resonance frequency. (b) Measured and predicted sound pressure level.

Figure 4.7: Comparison between experimental results and predictions of the ETV model for a subset of experiments of Aktas [7], Aktas et al. [8].

[82], who reported that better results could be obtained if a constant was added to the right hand side of Equation (A.26) for several of his experiments. This constant does not seem to be necessary for the experiments of Figure 4.7, however this has not been investigated further.

4.4 Feature Engineering

As stated in Sections 3.4.2 - 3.6, one factor with significant impact to the performance of a learning algorithm $\mathscr{A}_{\mathcal{H}}$ in any given problem is the input space $\mathcal{X}$. An appropriate choice of the quantities comprising $\mathcal{X}$ cannot only improve predictive performance, but also reduce computational time during the learning phase. In fact, DDMs can be very effective under a strict assumption: the available dataset $\mathcal{D}_n$ should contain information that is rich enough to allow $\mathscr{A}_{\mathcal{H}}$ to find a good approximation of the rule μ, but it should also be characterised by an input space with cardinality that is not too high with respect to the number of samples in the dataset n [200, 203]. Feature engineering addresses the problem of finding a compact and informative set of features that improves the accuracy and computational efficiency of $\mathscr{A}_{\mathcal{H}}$.

In the context of this work, the feature engineering process should ideally provide an informative representation comprising all the relevant aspects that contribute to the formation of a URN spectrum. Furthermore, the features extracted must originate

only from quantities that are available during the early design process, or can be easily estimated utilising computationally efficient PMs, as the ones presented in Section 4.3. These aspects include:

- propeller geometry,
- inflow conditions,
- cavitation type.

In the following, the process of extracting informative quantities (features) from all these groups is presented. More specifically, Section 4.4.1 discusses the quantities extracted from the propeller geometry, Section 4.4.2 presents the quantities that describe the inflow conditions of the propeller, and Section 4.4.3 discusses the quantities employed to provide further information regarding the cavitating phenomena the propeller is experiencing.

4.4.1 Propeller geometry

In theory, the entire propeller geometry could be provided to the DDMs, as a set of points in 3D space. However, as per common practice, the geometry of the propeller can be distilled in a much lower dimensional-space in the form of tables, providing key design parameters on a limited set of sections. Often, small variations exist in the definition of these design parameters. Nevertheless, the differences commonly encountered concern matters of presentation rather than fundamental changes of definition [34]. As such, this section is focused on considering propeller geometry in general terms, acting as an adequate basis for most applications.

Naturally, a propeller design has various parameters that influence its efficiency, the development of cavitation, and consequently the emitted noise. One of the most important factors in propeller noise generation is the pressure fluctuation on the blades, and decreasing this fluctuation is considered as one of the most effective ways to decrease URN generation [267]. Several geometric characteristics of the propeller influence the pressure distribution, including

- the Blade Area Ratio (BAR), defined as the ratio of the blade area, either in the projected, developed, or expanded view, divided by the propeller disc area. It regu-

lates the load along the blades, affecting the probability of cavitation occurrence and propeller efficiency [34].

- Skew angle, which affects the stability of the unsteady forces produced [268, 269].
- Rake angle, which affects cavitation performance indirectly: it increases or decreases the clearance of the blade tip from the hull, allowing the propeller designer to select propellers with smaller or larger diameter and varying rotational speed [270].
- Number of propeller blades, as according to Asimakopoulos et al. [271], cavity volume can be significantly reduced with an increasing number of blades, as it leads to a larger expanded area of the propeller. The larger expanded area in turn reduces the pressure difference between the back- and face- sides of the blade, thereby decreasing cavitation volume.
- Propeller diameter, which has been shown to affect the acoustic behaviour of the propeller, with studies showing that cavity volume increases quadratically with respect to propeller diameter [271].
- Pitch, which also affects the developed cavity volume [271].
- Section chord, which affects the circulation distribution, with subsequent effects in the development of vortex cavities [270].
- Section camber, for which high values in the mid-chord region of the section are known to increase the probability of bubble cavitation development [272].
- Section thickness, as it is critical with respect to cavitation development, especially in the leading edge region on a section, due to its effect on the local flow curvature [7].

All these quantities provide an extensive description of the propeller geometry, and they are utilised as geometry-related quantities for the DDMs. Similar to the PM, for the quantities varying along the spanwise direction of the blade, values on 8 sections from the root to the blade tip have been included on the input space, on the locations $^{r}/_{R} = \{0.2, 0.35, 0.475, 0.6, 0.7, 0.8, 0.9, 0.95\}$ [−]. Regarding the quantities τ and $\mathtt{z}$ which also vary along a section of the propeller on the chord-wise direction, only their maximum values on each section have been considered, to further reduce the cardinality of the input space. For the sake of clarity, these quantities are illustrated in Figure 4.8 .

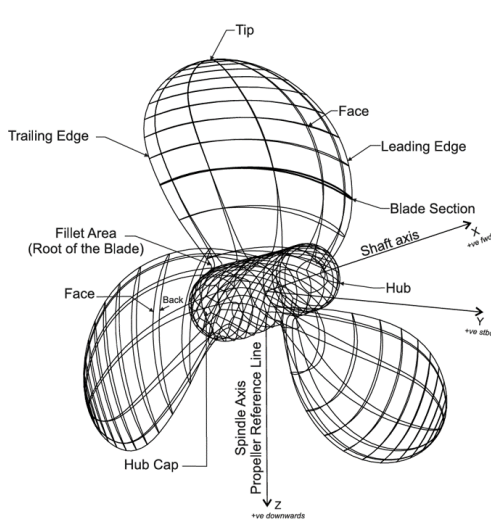

(a) Propeller main dimensions.

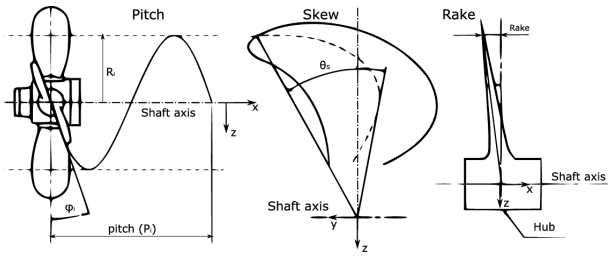

(b) Pitch, skew and rake.

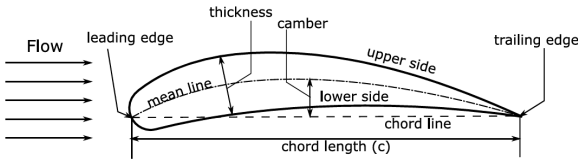

(c) Hydrofoil geometry.

Figure 4.8: Propeller and blade geometry [9].

4.4.2 Inflow conditions

Cavitation inception and development, and therefore URN, is affected by several performance characteristics that relate to the operating conditions the propeller is experiencing. In general, these characteristics are divided into open water and the behind-hull characteristics. More in detail, the open water characteristics relate to the description of the forces and moments acting on a propeller when operating in a uniform fluid stream, hence by definition they correspond to steady loadings, and are scalar quantities. On the other hand, behind-hull characteristics refer to the performance characteristics generated when the propeller is operating in a non-uniform inflow, i.e. in a wakefield generated by the presence of a solid body upstream of the propeller. Naturally, these characteristics have an unsteady component [34], and are generally high-dimensional tensors. These differences require that the two groups be treated separately: Specifically, open water characteristics are evaluated within the PM, according to Section 4.3 and are not altered within the feature engineering process. On the other hand, the behind-hull characteristics vary both in the chord- and span-wise directions of a blade, as well as its angular position during one revolution. These characteristics correspond to the wakefield, and the angle of attack. Both of these are high-dimensional

tensor quantities, and they require additional treatment if the cardinality of the input space has to be reduced.

4.4.2.1 Wakefield

The wakefield provides highly useful information for the DDMs. More specifically, it is known to have a high influence on the dynamics of propeller cavitation and URN behaviour [8, 35]. In the following, any and all references to the wakefield of the propeller refer to the nominal wakefield, i.e. the wakefield measured behind a hull-form during during model tests, without the propeller present. In its most general form, it consists of three components: axial, radial, and tangential. Each component is represented by a 2D dimensional tensor, describing its distribution in a polar coordinate system, centered on the propeller's disc. Although all three components are important, the axial wake is the dominant component with respect to the propeller's loading characteristics [34, 35, 273]. Therefore, with an acceptable loss of information the radial and tangential components can be neglected.

Focusing on the axial component of the wakefield $\boldsymbol{w}_x$, the main aspects that influence cavitation dynamics include its global intensity, and its variations at different angular positions. This has been highlighted by Konno et al. [274], who observed that altering the gradient of the wake distribution has a strong effect on cavity collapse events, and that wakes with stepper velocity gradients produce higher tonal amplitudes of pressure fluctuations, as well as high-frequency contributions from increased dynamic cavity collapses. The global intensity of w_x can be described by the mean wake fraction, by integration on a volumetric basis

$$\bar{w}_x = \frac{1}{\frac{\pi}{4}\left(D^2 - D_h^2\right)} \int_{r_h}^{D/2} r \int_0^{2\pi} w_x d\theta dr. \tag{4.9}$$

To approximate the variations of w_x, the quantities defined by Odabasi and Fitzsimmons [10] have been employed, similar to the work of Miglianti et al. [11]. An example of these quantities is given in Figure 4.9 illustrated for one propeller section, and they include

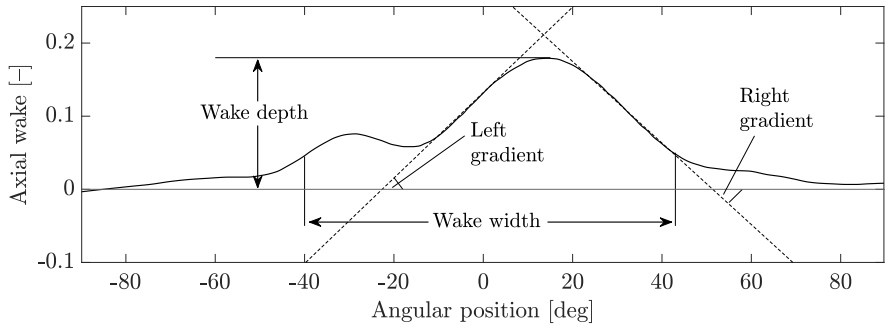

Figure 4.9: Wakefield parameters defined by Odabasi and Fitzsimmons [10] (adapted from [11]).

- the wakefield depth, which corresponds to the maximum value of w_x with respect to $w_x = 0$,
- wakefield width, corresponding to the angular sector for which $w_x \geq 0.5$,
- left wakefield gradient, which refers to the maximum value of $^{dw_x}/_{d\theta}$,
- right wakefield gradient, referring to the minimum value of $^{dw_x}/_{d\theta}$.

These scalar quantities can summarise the variation of w_x at any given propeller section. In this work, they are evaluated for two propeller radial locations, namely at 70% and 90% of the propeller radius. These specific locations have been chosen as they are considered to be the most representative for sheet and tip vortex cavitation [10].

To further enrich the representation of w_x a Fourier analysis has been conducted to decompose the total fluctuating component of w_x at any radial location into a finite set of sinusoidal components of various harmonic orders. The number of harmonic orders depends on the particular w_x under consideration and the number of blades of the case study propeller. Typically, the first $n_F = 8$ - 10 harmonics are the ones being used [34]. Using this basis, the general approximation of $\boldsymbol{w}_x$ at a particular radial location $\mathtt{r}$ of the propeller is given by

$$w_x(\theta)|_{\mathtt{r}} = \frac{1}{2}\mathtt{a}_w^{(0,r)} + \sum_{k=1}^{n_F} \mathtt{a}_w^{(k,r)} \cos(k\theta) + \mathtt{b}_w^{(k,r)} \sin(k\theta), \tag{4.10}$$

$$\mathtt{a}_w^{(0,r)} = \frac{1}{\pi}\int_0^{2\pi} w_x(\theta)|_{\mathtt{r}} d\theta \tag{4.11}$$

$$\mathtt{a}_w^{(k,\mathtt{r})} = \frac{1}{\pi}\int_0^{2\pi} w_x(\theta)|_{\mathtt{r}} \cos(k\theta)\, d\theta, \tag{4.12}$$

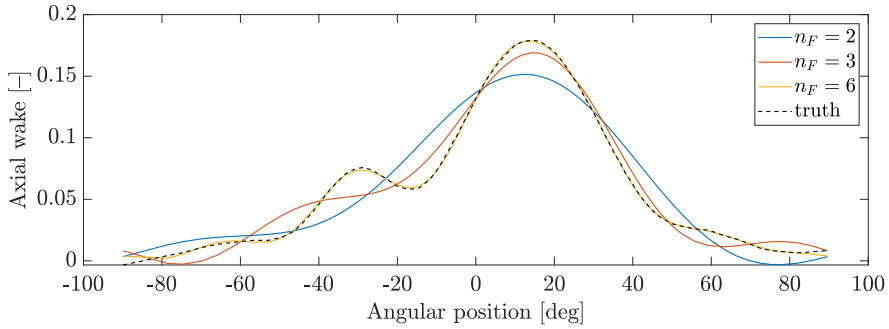

Figure 4.10: Wakefield approximations with Fourier series of various orders.

$$\mathtt{b}_w^{(k,\mathtt{r})} = \frac{1}{\pi}\int_0^{2\pi} w_x(\theta)|_{\mathtt{r}} \sin(k\theta)\, d\theta, \tag{4.13}$$

with $\mathtt{a}_w^{(k,r)}$, $k = \{0, \cdots, n_{\mathrm{F,w}}\}$, and $\mathtt{b}_w^{(k,r)}$, $k = \{1, \cdots, n_{\mathrm{F,w}}\}$ being the Fourier coefficients utilised in the input space of the DDMs. Examples of the approximations that can be obtained with Fourier series of various orders for the wakefield of Figure 4.9 are illustrated in Figure 4.10. For this particular example, the first $n_{\mathrm{F,w}} = 6$ harmonics are enough to approximate w_x with negligible errors.

4.4.2.2 Geometric angle of attack

The angle of attack is another important aspect with respect to cavitation occurrence, and more specifically the presence of sheet cavities on the suction sides of the blades. More specifically, it is known to affect the volume and period of cavity collapse, and the growth and development of the attached cavity on the propeller sections' leading edge [275]. Furthermore, it further underlines the combined effect of the non-uniformity of w_x, oblique flow, and the propeller's pitch distribution. It should be noted that the evaluation of the angle of attack requires the propeller's self-induced velocities to be known, and these can be straightforwardly evaluated using a BEM or lifting surface numerical code. In addition, the information it contains is implicitly included in w_x [11], the geometric angle of attack $\alpha_{\mathrm{G,atk}}$ is used instead, for simplicity. $\alpha_{\mathrm{G,atk}}$ is defined as the difference between the advance angle of a blade section $\alpha_a(r, \theta)$ and its local pitch

angle $\mathtt{p}(r)$ [276], and it can be evaluated as

$$\alpha_{\mathrm{G,atk}}(r,\theta) = \mathtt{p}(r) - \frac{u_a}{r\omega_p}\left[1 - w_x\left(r,\theta\right)\right]. \tag{4.14}$$

As can be seen from Equation (4.14), $\alpha_{\mathrm{G,atk}}$ is a 2D tensor. Similar to w_x a limited set of quantities have been employed to summarise it. For the same radial locations of the blade, namely at 70% and 90% of the propeller radius, these include

- the average value of $\alpha_{\mathrm{G,atk}}$, denoted as $\bar{\alpha}_{\mathrm{G,atk}}$,
- its minimum value $\alpha^{\mathrm{min}}_{\mathrm{G,atk}}$ and the corresponding angular location $\theta^{\mathrm{min}}_{\mathrm{G,atk}}$,
- its maximum value $\alpha^{\mathrm{max}}_{\mathrm{G,atk}}$ and the corresponding angular location $\theta^{\mathrm{max}}_{\mathrm{G,atk}}$,
- and the coefficients $\mathtt{a}^{(k)}_{\mathrm{G,atk}}$, $\mathtt{b}^{(k)}_{\mathrm{G,atk}}$ resulting from a Fourier analysis, for a finite number of harmonic components. Similar to w_x, the number of harmonics utilised depends on the shape of $\alpha_{\mathrm{G,atk}}$ that arises from Equation (4.14), and should be appropriately chosen for the case study under consideration.

4.4.3 Cavitating phenomena

As stated in Section 4.3, a set of high-dimensional quantities are computed by the PM in the process of evaluating the URN levels. These can be further processed during the feature engineering phase to provide summarized yet rich information towards the DDMs of Section 4.5. These quantities include:

- A tensor of pressure coefficients $\boldsymbol{C}_p$, evaluated for each panel and time-step. This is chose as it directly relates to the occurrence of blade surface cavitation and can provide an estimation of cavitation inception.
- and a tensor of the blade circulation $\boldsymbol{\Gamma}$ for every radial section and time-step. $\boldsymbol{\Gamma}$ is related to the forces acting on the hydrofoil, and in particular to the lift, according to the well known Kutta–Joukowski theorem and correlates with the load acting on the blades and its distribution, which in turn is strictly related to the strength of the shed vortices and the occurrence of vortex cavitation.

From these variables a smaller set of quantities has been extracted according to Sections 4.4.3.1 - 4.4.3.2.

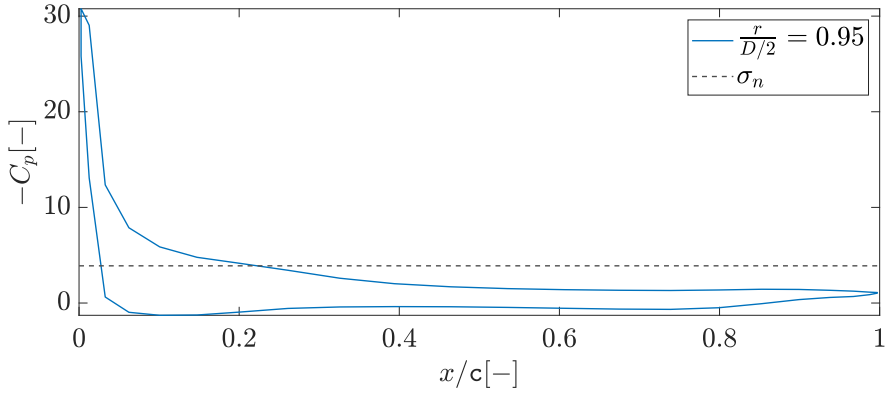

Figure 4.11: Example of cavity area estimation on a case-study hydrofoil.

4.4.3.1 Cavity area estimation

Cavitation inception and development is a very complex phenomenon that cannot be reliably modelled by BEM [145]. Nevertheless, the computed pressure distribution can provide a good approximation regarding the presence of cavitation under one assumption: that cavitation occurs when $-\boldsymbol{C}_p > \sigma_n$, meaning that the local pressure is lower than the vapour pressure. This cavitation inception criterion has been applied for the design of conventional and unconventional propellers, and it allows to estimate the occurrence of cavitation on the blades, its location, and to guess its extent [260, 277]. This only corresponds to a rough approximation of the true cavity area and does not consider the development of cavitation, which results in an enlargement of the cavitating area on the blade. Nevertheless, including this approximation in the input space can allow the DDMs to better discriminate between different conditions. An example of this criterion being applied on a single hydrofoil is illustrated in Figure 4.11. Results arising from this process for an entire propeller are provided in Figure 4.12, for 4 consecutive time-steps. The examples of Figures 4.11 - 4.12 correspond to one of the case-study propellers, which are more extensively discussed in Chapter 5.

With these considerations in mind, the area for which $p(r, \theta) < p_v$ is evaluated for the suction ($\boldsymbol{a}_{\mathrm{c,suc.}}$) and pressure ($\boldsymbol{a}_{\mathrm{c,pre.}}$) sides of the key blade, as an indication of cavitation extent. This allows for a first reduction of the information contained in the $\boldsymbol{C}_p$ tensor in the form of two vectors containing the estimated cavity areas for each side and angular position of the key blade. Subsequently, the following quantities have

been evaluated from these vectors:

- Fourier coefficients $\mathtt{a}_{\text{c,pre.}}$, $\mathtt{a}_{\text{c,suc.}}$, $\mathtt{b}_{\text{c,pre.}}$, $\mathtt{b}_{\text{c,suc.}}$,
- the minimum cavity areas on each side of the blade $a^{\min}_{\text{c,suc.}}$, $a^{\min}_{\text{c,pre.}}$,
- their corresponding angular positions $\theta^{\min}_{\text{c,suc.}}$, $\theta^{\min}_{\text{c,pre.}}$,
- the maximum cavity areas on each side of the blade $a^{\max}_{\text{c,suc.}}$, $a^{\max}_{\text{c,pre.}}$,
- and their corresponding angular positions $\theta^{\max}_{\text{c,suc.}}$, $\theta^{\max}_{\text{c,pre.}}$.

4.4.3.2 Cavitation type

Furthermore, to include information regarding the cavitation type, the blade has been subdivided into 4 panels, as illustrated in Figure 4.13. These include:

- Panel 1 (P1): From 70% of the propeller radius to the tip of the blade, and from the leading edge to 20% of the chord,
- Panel 2 (P2): From 70% of the propeller radius to the tip of the blade, and from 20% to 60% of the chord.
- Panel 3 (P3): From blade root to 70% of the propeller radius, and from the leading edge to 20% of the chord,
- Panel 4 (P4): From blade root to 70% of the propeller radius, and from 20% to 60% of the chord.

This subdivision was chosen in order to indicate the occurrence of sheet cavitation near the leading edge of the blade and bubble cavitation round the mid-chord region of the blade. Subsequently, for panels P1, P3 on the pressure side of the blade, and for all panels on the suction side, a vector containing the maximum value of $-\boldsymbol{C}_p$ as a function of the angular position of the key blade has been evaluated. Finally, to further compress the information, a Fourier analysis is performed on the resulting vectors and values of the Fourier coefficients for a finite number of harmonic orders have been added to the input space of the DDMs. Naturally, the number of harmonics, and therefore the number of coefficients, is dependent on the shape of the resulting vectors.

A qualitative visualisation of this representation is provided in Figure 4.14, which illustrates the 6 curves obtained as a function of the angular position, along with their approximations as Fourier series. In this particular example, 4 harmonic orders were

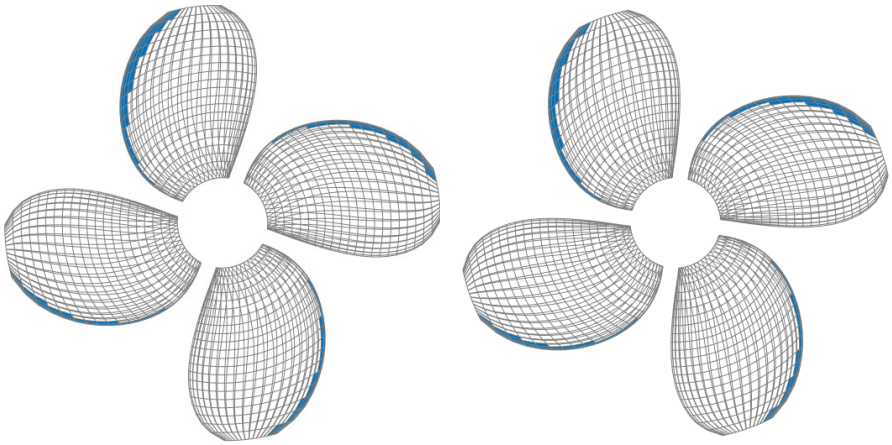

(a) t_1.

(b) $t_2 > t_1$.

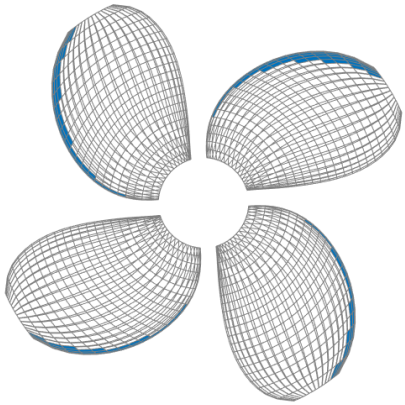

(c) $t_3 > t_2$.

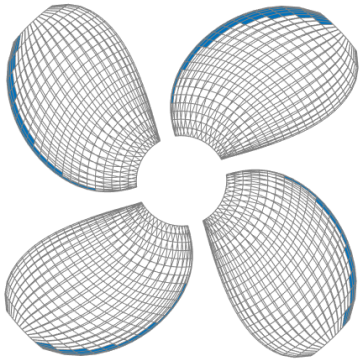

(d) $t_4 > t_3$.

Figure 4.12: Example of cavity area estimation on a case-study propeller.

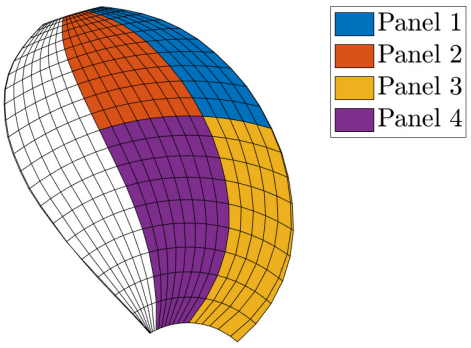

Figure 4.13: Blade subdivision in panels.

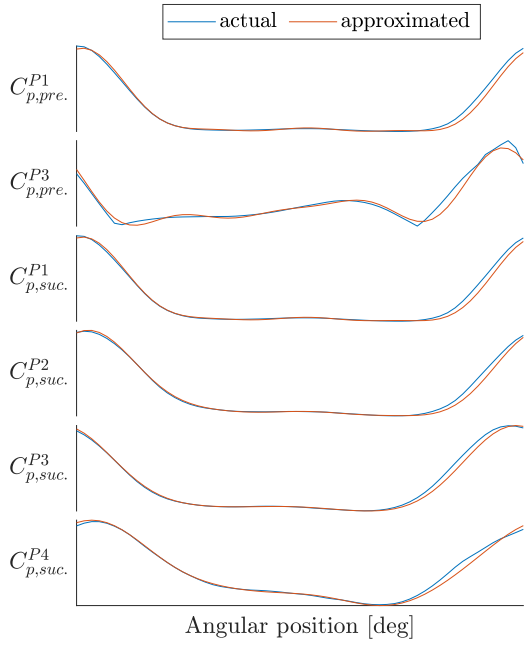

Figure 4.14: Representation of the pressure coefficients on $\mathcal{X}$.

sufficient to reconstruct the curves, for a total of 54 coefficients. Considering that $\boldsymbol{C}_p \in \mathbb{R}^{u \times s \times q}$ according to the discretisation discussed in Section A.2, it can be safely stated that this process encodes rich information in a much more compact manner.

Finally, the strength of the vortex shed in the wake at 95% of the propeller radius is evaluated from $\boldsymbol{\Gamma}$ for every angular position of the key blade, as it is known to correlate with the occurrence of TVC [256]. From this vector, the following quantities have been included in the input space:

- The minimum strength of the shed vortex $\Gamma^{\min(0.95)}$,
- its corresponding angular location $\theta_{\Gamma}^{\min(0.95)}$,
- the maximum strength of the shed vortex $\Gamma^{\max(0.95)}$,
- its corresponding angular location $\theta_{\Gamma}^{\max(0.95)}$,
- and the coefficients $\mathtt{a}_{\Gamma^{0.95}}^{(k)}$, $\mathtt{b}_{\Gamma^{0.95}}^{(k)}$ resulting from a Fourier analysis for a finite number of harmonic components.

For the sake of completeness, a summary of the output quantities of the feature engineering process is provided in Figure 4.6. The inputs of the process have been listed in Tables 4.1 - 4.2.

Table 4.6: Outputs ($\boldsymbol{x}$) of the feature engineering process.

Symbol	Description	Size	Units
$\mathtt{a}_{\mathrm{c,pre.}}$	Cosine Fourier coeffs. of $a_{\mathrm{c,pre.}}$	$1 \times (n_{F,\mathtt{a}_G} + 1)$	[m]
$\mathtt{b}_{\mathrm{c,pre.}}$	Sine Fourier coeffs. of $a_{\mathrm{c,pre.}}$	$1 \times n_{F,\mathtt{a}_G}$	[m]
$\mathtt{a}_{\mathrm{c,suc.}}$	Cosine Fourier coeffs. of $a_{\mathrm{c,suc.}}$	$1 \times (n_{F,\mathtt{a}_G} + 1)$	[m]
$\mathtt{b}_{\mathrm{c,pre.}}$	Sine Fourier coeffs. of $a_{\mathrm{c,pre.}}$	$1 \times n_{F,\mathtt{a}_G}$	[m]
$a^{\min}_{\mathrm{c,pre.}}$	Minimum value of $a_{\mathrm{c,pre.}}$		[m]
$a^{\min}_{\mathrm{c,suc.}}$	Minimum value of $a_{\mathrm{c,suc.}}$		[m]
$\theta^{\min}_{\mathrm{c,pre.}}$	Angular position of $a^{\min}_{\mathrm{c,pre.}}$		[deg]
$\theta^{\min}_{\mathrm{c,suc.}}$	Angular position of $a^{\min}_{\mathrm{c,suc.}}$		[deg]
$a^{\max}_{\mathrm{c,pre.}}$	Maximum value of $a_{\mathrm{c,pre.}}$		[m]
$a^{\max}_{\mathrm{c,suc.}}$	Maximum value of $a_{\mathrm{c,suc.}}$		[m]
$\theta^{\max}_{\mathrm{c,pre.}}$	Angular position of $a^{\max}_{\mathrm{c,pre.}}$		[deg]
$\theta^{\max}_{\mathrm{c,suc.}}$	Angular position of $a^{\max}_{\mathrm{c,suc.}}$		[deg]
$\mathtt{a}^{P1}_{C_{\mathrm{p,pre.}}}$	Cosine Fourier coeffs. of $C^{P1}_{\mathrm{p,pre.}}$	$1 \times (n^{P1}_{F,C_{\mathrm{p,pre.}}} + 1)$	[m]
$\mathtt{b}^{P1}_{C_{\mathrm{p,pre.}}}$	Sine Fourier coeffs. of $C^{P1}_{\mathrm{p,pre.}}$	$1 \times n^{P1}_{F,C_{\mathrm{p,pre.}}}$	[m]
$\mathtt{a}^{P3}_{C_{\mathrm{p,pre.}}}$	Cosine Fourier coeffs. of $C^{P3}_{\mathrm{p,pre.}}$	$1 \times (n^{P3}_{F,C_{\mathrm{p,pre.}}} + 1)$	[m]
$\mathtt{b}^{P3}_{C_{\mathrm{p,pre.}}}$	Sine Fourier coeffs. of $C^{P3}_{\mathrm{p,pre.}}$	$1 \times n^{P3}_{F,C_{\mathrm{p,pre.}}}$	[m]
$\mathtt{a}^{P1}_{C_{\mathrm{p,suc.}}}$	Cosine Fourier coeffs. of $C^{P1}_{\mathrm{p,suc.}}$	$1 \times (n^{P1}_{F,C_{\mathrm{p,suc.}}} + 1)$	[m]
$\mathtt{b}^{P1}_{C_{\mathrm{p,suc.}}}$	Sine Fourier coeffs. of $C^{P1}_{\mathrm{p,suc.}}$	$1 \times n^{P1}_{F,C_{\mathrm{p,suc.}}}$	[m]
$\mathtt{a}^{P2}_{C_{\mathrm{p,suc.}}}$	Cosine Fourier coeffs. of $C^{P2}_{\mathrm{p,suc.}}$	$1 \times (n^{P2}_{F,C_{\mathrm{p,suc.}}} + 1)$	[m]
$\mathtt{b}^{P2}_{C_{\mathrm{p,suc.}}}$	Sine Fourier coeffs. of $C^{P2}_{\mathrm{p,suc.}}$	$1 \times n^{P2}_{F,C_{\mathrm{p,suc.}}}$	[m]
$\mathtt{a}^{P3}_{C_{\mathrm{p,suc.}}}$	Cosine Fourier coeffs. of $C^{P3}_{\mathrm{p,suc.}}$	$1 \times (n^{P3}_{F,C_{\mathrm{p,suc.}}} + 1)$	[m]
$\mathtt{b}^{P3}_{C_{\mathrm{p,suc.}}}$	Sine Fourier coeffs. of $C^{P3}_{\mathrm{p,suc.}}$	$1 \times n^{P3}_{F,C_{\mathrm{p,suc.}}}$	[m]
$\mathtt{a}^{P4}_{C_{\mathrm{p,suc.}}}$	Cosine Fourier coeffs. of $C^{P4}_{\mathrm{p,suc.}}$	$1 \times (n^{P4}_{F,C_{\mathrm{p,suc.}}} + 1)$	[m]
$\mathtt{b}^{P4}_{C_{\mathrm{p,suc.}}}$	Sine Fourier coeffs. of $C^{P4}_{\mathrm{p,suc.}}$	$1 \times n^{P4}_{F,C_{\mathrm{p,suc.}}}$	[m]
$\Gamma^{\min(0.95)}$	Minimum value of $\Gamma^{(0.95)}$		[m^2/s]
$\theta^{\min(0.95)}_{\Gamma}$	Angular position of $\Gamma^{\min(0.95)}$		[deg]
$\Gamma^{\max(0.95)}$	Maximum value of $\Gamma^{(0.95)}$		[m^2/s]
$\theta^{\max(0.95)}_{\Gamma}$	Angular position of $\Gamma^{\max(0.95)}$		[deg]
$\mathtt{a}_{\Gamma^{0.95}}$	Cosine Fourier coeffs. of $\Gamma^{(0.95)}$	$1 \times (n_{F,\Gamma^{(0.95)}} + 1)$	[m^2/s]

Continued on next page

Table 4.6 – *Continued from previous page*

Symbol	Description	Size	Units
$\mathtt{b}_{\Gamma^{0.95}}$	Sine Fourier coeffs. of $\Gamma^{(0.95)}$	$1 \times n_{F,\Gamma^{(0.95)}}$	[m^2/s]
$\mathtt{n}$	Rotational speed of the propeller		[Hz]
u_a	Advance velocity of the propeller		[m/s]
p_{rel}	Relative tunnel pressure		[mbar]
J	Advance coefficient		[–]
K_t	Thrust coefficient		[–]
K_q	Torque coefficient		[–]
η_o	Propeller open-water efficiency		[–]
σ_u	Cavitation index based on u_a		[–]
$\sigma_{\mathtt{n}}$	Cavitation index based on $\mathtt{n}D$		[–]
$\sigma_{\text{u,tip}}$	Cavitation index based on $\sqrt{u_a^2 + (\pi \mathtt{n} D)^2}$		[–]
$\sigma_{\mathtt{n},\text{tip}}$	Cavitation index based on $\mathtt{n}D$ at blade tip		[–]
$\bar{w}_x^{(0.7)}$	Average w_x at 70% of $D/2$		[–]
$\bar{w}_{\text{depth}}^{(0.7)}$	Depth of w_x at 70% of $D/2$		[–]
$\bar{w}_{\text{width}}^{(0.7)}$	Depth of w_x at 70% of $D/2$		[–]
$\bar{w}_{\text{depth}}^{(0.7)}$	Depth of w_x at 70% of $D/2$		[–]
$d\theta/dw_x\vert_{\text{left}}^{(0.7)}$	Left gradient of w_x at 70% of $D/2$		[deg]
$d\theta/dw_x\vert_{\text{right}}^{(0.7)}$	Right gradient of w_x at 70% of $D/2$		[deg]
$\mathtt{a}_w^{(0.7)}$	Cosine Fourier coeffs. of w_x at 70% of $D/2$	$1 \times (n_{\text{F,w}} + 1)$	[–]
$\mathtt{b}_w^{(0.7)}$	Sine Fourier coeffs. of w_x at 70% of $D/2$	$1 \times n_{\text{F,w}}$	[–]
$\bar{w}_x^{(0.9)}$	Average w_x at 90% of $D/2$		[–]
$\bar{w}_{\text{depth}}^{(0.9)}$	Depth of w_x at 90% of $D/2$		[–]
$\bar{w}_{\text{width}}^{(0.9)}$	Depth of w_x at 90% of $D/2$		[–]
$\bar{w}_{\text{depth}}^{(0.9)}$	Depth of w_x at 90% of $D/2$		[–]
$d\theta/dw_x\vert_{\text{left}}^{(0.9)}$	Left gradient of w_x at 90% of $D/2$		[deg]
$d\theta/dw_x\vert_{\text{right}}^{(0.9)}$	Right gradient of w_x at 90% of $D/2$		[deg]
$\mathtt{a}_w^{(0.9)}$	Cosine Fourier coeffs. of w_x at 90% of $D/2$	$1 \times (n_{\text{F,w}} + 1)$	[–]
$\mathtt{b}_w^{(0.9)}$	Sine Fourier coeffs. of w_x at 90% of $D/2$	$1 \times n_{\text{F,w}}$	[–]
$\bar{\alpha}_{\text{G,atk}}^{0.7}$	Average $\alpha_{\text{G,atk}}$ at 70% of $D/2$		[deg]
$\alpha_{\text{G,atk}}^{\min(0.7)}$	Minimum $\alpha_{\text{G,atk}}$ at 70% of $D/2$		[deg]

Continued on next page

Table 4.6 – *Continued from previous page*

Symbol	Description	Size	Units
$\theta_{\mathrm{G,atk}}^{\min(0.7)}$	Angular position of $\alpha_{\mathrm{G,atk}}^{\min(0.7)}$ at 70% of $D/2$		[deg]
$\alpha_{\mathrm{G,atk}}^{\max(0.7)}$	Maximum $\alpha_{\mathrm{G,atk}}$ at 70% of $D/2$		[deg]
$\theta_{\mathrm{G,atk}}^{\max(0.7)}$	Angular position of $\alpha_{\mathrm{G,atk}}^{\max(0.7)}$ at 70% of $D/2$		[deg]
$\mathtt{a}_{G,atk}^{(0.7)}$	Cosine Fourier coeffs. of $\alpha_{\mathrm{G,atk}}$ at 70% of $D/2$	$1 \times (n_{F,\mathtt{a}_G} + 1)$	[deg]
$\mathtt{b}_{G,atk}^{(0.7)}$	Sine Fourier coeffs. of $\alpha_{\mathrm{G,atk}}$ at 70% of $D/2$	$1 \times n_{F,\mathtt{a}_G}$	[deg]
$\bar{\alpha}_{\mathrm{G,atk}}^{0.9}$	Average $\alpha_{\mathrm{G,atk}}$ at 90% of $D/2$		[deg]
$\alpha_{\mathrm{G,atk}}^{\min(0.9)}$	Minimum $\alpha_{\mathrm{G,atk}}$ at 90% of $D/2$		[deg]
$\theta_{\mathrm{G,atk}}^{\min(0.9)}$	Angular position of $\alpha_{\mathrm{G,atk}}^{\min(0.7)}$ at 90% of $D/2$		[deg]
$\alpha_{\mathrm{G,atk}}^{\max(0.9)}$	Maximum $\alpha_{\mathrm{G,atk}}$ at 90% of $D/2$		[deg]
$\theta_{\mathrm{G,atk}}^{\max(0.9)}$	Angular position of $\alpha_{\mathrm{G,atk}}^{\max(0.9)}$ at 90% of $D/2$		[deg]
$\mathtt{a}_{G,atk}^{(0.9)}$	Cosine Fourier coeffs. of $\alpha_{\mathrm{G,atk}}$ at 90% of $D/2$	$1 \times (n_{F,\mathtt{a}_G} + 1)$	[deg]
$\mathtt{b}_{G,atk}^{(0.9)}$	Sine Fourier coeffs. of $\alpha_{\mathrm{G,atk}}$ at 90% of $D/2$	$1 \times n_{F,\mathtt{a}_G}$	[deg]

*Empty field indicates scalar quantity.

4.5 Data-driven Models

As stated in Section 3.6, DDMs can be grouped into two main families: shallow and deep DDMs. In light of the main weaknesses of deep DDMs, namely high data requirements, and lack of interpretability, this work focuses on shallow DDMs. According to the no-free-lunch theorem [278], in order to find the best algorithm for a particular application, it is necessary to test multiple algorithms. Given that the problem of predicting the URN spectra based on the predictive features reported in Table 4.6 corresponds to the typical multi-output regression problem in ML [200, 237], 5 algorithms from the families of KMs, EMs, and ANNs are utilised, as reported in Section 3.6. These correspond to: Kernel Regularised Least Squares (KRLS) [237], Random Forests (RFs) [235], a Single Layered Neural Network (ANN) [239], and Extreme Learning Machines (ELMs) [12]. Only a brief description of these algorithms is provided in Section 4.5.1, with special attention to the relevant architectural choices of these algorithms, along with their hyperparameters that need to be tuned from the available training data. In addition,

their verification process is subsequently discussed in Section 4.5.2. The evaluation of appropriate hyperparameter values is a major topic by itself, and is further discussed in Section 4.6. More information about these algorithms is provided in Appendix D. Finally, the DDMs' inputs and outputs have been largely discussed in the previous sections, therefore they are omitted in the following. In particular, their inputs correspond to the quantities listed in Table 4.6 and the recursive difference between DDM and PM URN spectra predictions, as provided by Equations (4.1) - (4.2) of Section 4.2.

4.5.1 Models' overview

KRLS [13] is one of the most effective algorithms in the family of KMs [184]. Similar to all KMs, it exploits the "Kernel trick" for distances in order to extend linear techniques to solve non-linear problems [248, 279], and they provide a flexible and expressive learning frame- work that has been successfully applied to a wide range of real world problems. The hyperparameters of KRLS include the choice of the kernel, which is fixed to the Gaussian Kernel in this work because of the theoretical reasons described in [280] and its effectiveness [281, 282]. In KRLS two hyperparameters need to be tuned. The parameter γ that characterizes the Gaussian kernel, along with the regularization parameter λ, which was discussed in Section 3.4.2.

RFs rely on the "wisdom of crowds" principle, i.e. the fact that combining the output of several classifiers or regressor results in a much better performance than using any single one of them [235, 283]. They are a popular and widely adopted method, which combines many decision trees in order to obtain effective predictors that have limited hyperparameter sensitivity and high numerical robustness [235]. RFs were first introduced by Breiman [235] who, inspired by the earlier work of Amit and Geman [284], extended the bagging strategy of Breiman [285], in an attempt to optimise the generalisation performance of a model that combines several classifiers. With this idea, Breiman developed a robust learning algorithm that turns out to perform very well compared to many other approaches, is suitable for both regression and classification problems, and it has a computationally efficient forward phase. The hyperparameters of the RF include: The number of trees n_{RF}, the number of samples to extract during

the Bootstrap (BTS) procedure *bn* for each BDT, the number of samples in the terminal nodes of each BDT n_{BDT}, and the number of predictors utilised in each subset during the growth of each BDT ι_{BDT}. In [235], Breiman suggested to set $b = 1$, and $\iota_{\mathrm{BDT}} = \sqrt{\iota}$ for regression problems, while n_{RF} can be chosen according to some consistency measure, or based on the out-of-bag error [235]. Several other hyperparameters exist, but they are set to default values, since they are not as influential, according to some recent work in the field [286, 287].

ANNs combine together many simple models of a human brain neuron, called perceptrons [288], in order to build a complex network. The neurons can be organised in one (shallow ANNs) or multiple stacked (deep ANNs) layers, connected together by weights, which are "learned" from the available data via back-propagation [289]. In this work, shallow ANNs have been employed for the reasons discussed in Section 3.6, with the hyperbolic tangent activation function due to its approximation properties [290]. The hyperparameters required to define the architecture of the ANN is the number of neurons of the single hidden layer $\mathtt{h}_1$, the regularization trade-off parameter λ, and the learning rate ϵ.

Finally, ELMs represent a state-of-the-art method [12, 238, 291, 292] that was introduced to overcome the problems posed by the back-propagation algorithm [293, 294]: potentially slow convergence rates, sensitivity to some optimisation parameters, and the presence of local minima that call for multi-start and retraining strategies. Originally, ELMs were developed as single-hidden-layer feedforward ANNs [295–297], and were later extended to their deep version [298–300], in order to cope with problems intractable by shallow architectures [301–303]. In this work, shallow ELMs have been employed, characterized by the following hyperparameters: the number of neurons in the hidden layer $\mathtt{h}$, and λ.

4.5.2 Verification of the data-driven models

Similar to the PMs, only a subset of DDMs used in this work are verified and are listed in Table 4.7. The models that have not been verified include:

- The RF, for which the Python *scikit-learn* [304] library is utilised.

Table 4.7: Data-driven models' verification and validation experiments.

Model	Section	Sources of numerical or experimental data.
KRLS	D.2	Hainmueller and Hazlett [13]
ELM	D.4.3	Huang et al. [291]

- The ANN of Section D.4.1, for which the Python *PyTorch* [305] library is employed.

To validate the ELM and KRLS implementations, various case studies have been considered, involving datasets for regression tasks hosted on common repositories [306]. The results have been satisfactory on all datasets considered. However, for the sake of brevity, only some illustrative examples are presented in this section, which correspond to mono-dimensional cases studies presented in the works from which the DDMs originate.

4.5.2.1 Extreme Learning Machine

To verify the ELM, the simplest example of Huang et al. [12] is presented. In this example the ELM approximates a function commonly employed to illustrate the application of support vector machines for regression problems [307]. The function is known as the normalised *sinc* function, and is given by

$$\text{sinc}(x) = \begin{cases} \frac{sin(x)}{x}, & \text{for } x \neq 0 \\ 1, & \text{for } x = 0. \end{cases} \tag{4.15}$$

Similar to [12], a dataset is created, consisting of 5000 points with $x \sim \mathcal{U}(-10, 10)$, and additive noise of $\epsilon \sim \mathcal{U}(-0.2, 0.2)$. Assigning 20 hidden nodes to the ELM, and retaining 10% of the dataset for testing (randomly selected), 50 trials have been conducted, for which the observed MAPE corresponds to 3.42 ± 0.65[–] at the 95% confidence level. The authors of [12] reported the root mean square error, equal to 0.0097 ± 0.0028[–]. The corresponding value of the numerical experiments conducted by the author equals 0.0101 ± 0.0024[–]. For reference, the predictions obtained by the ELM during one of these experiments is provided in Figure 4.15.

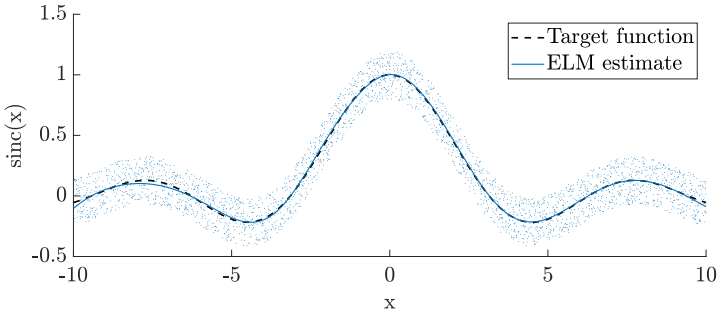

Figure 4.15: Verification of the ELM implementation with one case study from Huang et al. [12].

4.5.2.2 Kernel Regularised Least Squares

To verify the implementation of KRLS, one of the examples provided by Hainmueller and Hazlett [13] is employed, chosen by Hainmueller and Hazlett to demonstrate that regularisation helps prevent over-fitting. To demonstrate this point, the authors considered a high-frequency function given by

$$f(x) = 0.2\sin(12\pi x) + \sin(2\pi x). \tag{4.16}$$

Two simulations were conducted with sample sizes $n = 40, 400$, for which $x \sim \mathcal{U}(0, 1)$, and $\epsilon \sim \mathcal{N}(0, 0.2)$. The results of these simulations are provided in Figure 4.16, and confirm the findings of Hainmueller and Hazlett. Namely, that KRLS approximates the high-frequency target function well, with a smooth low-frequency approximation. Furthermore, the approximation remains stable, even with the largest sample size, indicating that KRLS is not prone to overfitting the function. The authors indicate that this behavior depends on the appropriate choice of the hyperparameter λ, discussed in Section 3.4.2. For the results of Figure 4.16, $\lambda = 0.923$ for $n = 40$, and $\lambda = 3.29$ for $n = 400$.

4.6 Model selection and error estimation

Sections 4.3 - 4.5 introduced a variety of PMs and DDMs (and implicitly HMs) that can be employed to solve the problem under consideration. Having multiple models

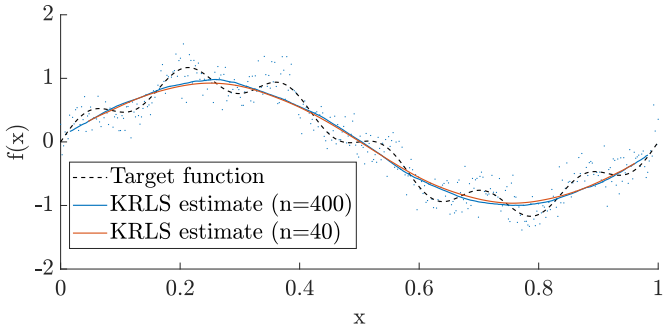

Figure 4.16: Verification of the KRLS implementation with one case study from Hainmueller and Hazlett [13].

available gives rise to two very important questions: How can the best model be selected? How can its generalisation error be estimated? Both of which are answered in this section.

4.6.1 Overview

Both questions have received solid answers from the field of statistical inference [308–310]: In ML, the problem of selecting the DDM with the highest accuracy is known as the *Model Selection* (MS) problem, whereas the problem of estimating the generalisation error of the model, i.e. the error it will exhibit on previously unseen data, is referred to as the *Error Estimation* (EE) problem. Various methodologies are available for the MS and EE phases [204, 310]. In this work, Resampling Methods (RMs) are utilised, since they are known to perform well in most problems, and are most commonly used by researchers and practitioners in the field of ML [204].

RMs [204, 311–313] allow for the application of simple statistical techniques to estimate the quantities of interest, and include the hold-out (HO) method, the well-known k-fold Cross Validation (kCV) method [312, 314], the leave-one-out (LOO) [315], and the BTS [316]. The idea behind these methods is rather simple: If a rule μ performs well on data that have not been used for selecting μ itself, probably μ will generalise well, namely it will have a small generalisation error. However, this idea is valid only if the following assumption is satisfied: The data must come from a phenomenon that does not change in time. Plainly, it is assumed that the available data and the future-

sampled data must be independent and identically distributed.

In RMs the original dataset $\mathcal{D}_n$ is resampled one or many (n_r) times, with or without replacement, to build three independent datasets called learning ($\mathcal{L}_\ell^r$), validation ($\mathcal{V}_v^r$) and test ($\mathcal{T}_t^r$) sets containing ℓ, v, and t experiments respectively, with $\mathcal{L}_\ell^r \cap \mathcal{V}_v^r = \oslash$, $\mathcal{L}_\ell^r \cap \mathcal{T}_t^r = \oslash$, $\mathcal{V}_v^r \cap \mathcal{T}_t^r = \oslash$, and $\mathcal{L}_\ell^r \cup \mathcal{V}_v^r \cup \mathcal{T}_t^r = \mathcal{D}_n$ for all $r \in \{1, \cdots, n_r\}$. To select the best combination of hyperparameters $\mathcal{H}^\diamond$ in a set of possible ones $\mathfrak{H} = \{\mathcal{H}_1, \mathcal{H}_2, \cdots\}$ for the algorithm $\mathscr{A}_\mathcal{H}$, i.e. to perform the MS phase, the following procedure must be applied

$$\mathcal{H}^\diamond : \quad \arg\min_{\mathcal{H}\in\mathfrak{H}} \sum_{r=1}^{n_r} \mathtt{M}(\mathscr{A}_\mathcal{H}(\mathcal{L}_\ell^r), \mathcal{V}_v^r), \tag{4.17}$$

where $\mathscr{A}_\mathcal{H}(\mathcal{L}_\ell^r)$ is a model developed with the algorithm $\mathscr{A}$ and the set of hyperparameters $\mathcal{H}$ utilising the data $\mathcal{L}_\ell^r$. Since the data sets $\mathcal{L}_\ell^r$ and $\mathcal{V}_v^r$ are independent, $\mathcal{H}^\diamond$ should be the set of hyperparameters that allows the model to achieve a small error on a dataset that is independent from $\mathcal{L}_\ell^r$.

To evaluate the performance of the optimal model $h_\mathscr{A}^\diamond = \mathscr{A}_{\mathcal{H}^\diamond}(\mathcal{D}_n)$, i.e. to perform the EE phase, a separate set of data $\mathcal{T}_t$ is needed, since the error that the $h_\mathscr{A}^\diamond$ commits over $\mathcal{D}_n$ would be optimistically biased, as $\mathcal{D}_n$ has been used to learn it. For this reason

$$\mathtt{M}(\mathscr{A}_{\mathcal{H}^\diamond}(\mathcal{L}_\ell^r \cup \mathcal{V}_v^r), \mathcal{T}_t^r) \tag{4.18}$$

is evaluated. Since the data in $\mathcal{L}_\ell^r \cup \mathcal{V}_v^r$ is independent from the data in $\mathcal{T}_t^r$, the metric of Equation (4.18) is an unbiased estimator of the true performance of the final model [204].

The average error $\bar{\mathtt{M}}$ that the model commits over all $\mathcal{T}_t^r$, $r = \{1, \cdots, n_r\}$ is evaluated as

$$\bar{\mathtt{M}}(\mathscr{A}_{\mathcal{H}^\diamond}, \mathcal{T}_t) = \frac{1}{n_r} \sum_{r=1}^{n_r} \mathtt{M}(\mathscr{A}_{\mathcal{H}^\diamond}(\mathcal{L}_\ell^r \cup \mathcal{V}_v^r), \mathcal{T}_t^r), \tag{4.19}$$

and the standard deviation of $\mathtt{M}$ is given by

$$\sigma_\mathtt{M}(\mathscr{A}_{\mathcal{H}^\diamond}, \mathcal{T}_t) = \left[\frac{1}{n_r - 1} \sum_{r=1}^{n_r} \left[\mathtt{M}(\mathscr{A}_{\mathcal{H}^\diamond}(\mathcal{L}_\ell^r \cup \mathcal{V}_v^r), \mathcal{T}_t^r) - \bar{\mathtt{M}}\left(\mathscr{A}_{\mathcal{H}^\diamond}, \mathcal{T}_t\right) \right]^2 \right]^{\frac{1}{2}}. \tag{4.20}$$

Given a confidence level α, and thus the value $\mathtt{t}(\alpha)$ of the cumulative Student's t-distribution, from Equations (4.19) - (4.20) the confidence interval $\mathtt{CI}$ at the α^{th} level of confidence can be evaluated as

$$\mathtt{CI}_{\mathtt{M}}(\alpha, \mathscr{A}_{\mathcal{H}^\diamond}, \mathcal{T}_t) = \bar{\mathtt{M}}(\mathscr{A}_{\mathcal{H}^\diamond}, \mathcal{T}_t) \pm \mathtt{t}(\alpha) \frac{\sigma_{\mathtt{M}}(\mathscr{A}_{\mathcal{H}^\diamond}, \mathcal{T}_t)}{(n_r)^{\frac{1}{2}}}. \tag{4.21}$$

If $n_r = 1$, and ℓ, v, and t are aprioristically set such that $n = \ell + v + t$, and if the resampling procedure is performed without replacement, the hold out method is obtained [204]. To implement the complete nested kCV, the following must be set

$$n_r \leq \binom{n}{k}\binom{n - \frac{n}{k}}{k}, \tag{4.22}$$

$$\ell = (k-2)\frac{n}{k}, \tag{4.23}$$

$$v = \frac{n}{k}, \tag{4.24}$$

$$t = \frac{n}{k}, \tag{4.25}$$

and resampling must be done without replacement [314].

Finally, for the implementation of the nested non-parametric BTS, $\ell = n$ and $\mathcal{L}_\ell^r$ must be sampled with replacement from $\mathcal{D}_n$, while $\mathcal{V}_v^r$ and $\mathcal{T}_t^r$ are sampled without replacement from the sample of $\mathcal{D}_n$ that has not been sampled in $\mathcal{L}_\ell^r$ [314]. It should be noted that for BTS $n_r \leq \binom{2n-1}{n}$. In this work, the complete nested kCV is employed, as it represents the state-of-the-art approach [204, 314]. Algorithm (4.1) presents a simplified version of the pseudo-code for the resampling-based MS and EE process [204].

As stated in Section 3.4.2, the error that each DDM or HM commits when approximating μ is measured with reference to a loss function $\ell : \mathcal{X} \times \mathcal{Y} \times \mathcal{F} \to \mathbb{R}_{\geq 0}$ through the empirical error. Generally, for regression problems typically two loss functions are employed: the absolute loss $\ell_1(h(\boldsymbol{x}), y) = |h(\boldsymbol{x}) - y|$ and the squared loss $\ell_2\left(h(\boldsymbol{x}), y\right) = \left(h(\boldsymbol{x}) - y\right)^2$ [317]. Based on these losses, it is possible to define different $\mathtt{M}$, which weigh differently the distance between $\boldsymbol{y}_i$, and $h(\boldsymbol{x}_i)$, $i = \{1, \cdots, n\}$. It should be noted that it is not required to utilise the same metric to evaluate the performance of each DDM or HM during the MS phase, and during the EE phase [200, 317].

Algorithm 4.1: Model Selection and Error Estimation utilising Resampling Methods.

Input: $\mathcal{D}_n$, $\mathscr{A}_{\mathfrak{H}}$, n_r, ℓ, v, t, Resampling method (HO, LOO, kCV, BTS)
Result: $\mathscr{A}_{\mathcal{H}^\diamond}$, $\hat{\mathtt{L}}\left(\mathscr{A}_{\mathcal{H}^\diamond}\right)$
$\mathtt{L}_{\mathrm{MS}}^{\diamond} \leftarrow +\infty$
for $\mathscr{A}_{\mathcal{H}} \in \mathscr{A}_{\mathfrak{H}}$ **do**
  $\mathtt{L}_{\mathrm{MS}} \leftarrow 0$
  $\mathtt{L}_{\mathrm{EE}} \leftarrow 0$
  for $r \leftarrow 1$ **to** n_r **do**
    Split $\mathcal{D}_n$ in $\mathcal{L}_\ell^r$, $\mathcal{V}_v^r$ and $\mathcal{T}_t^r$ according to the selected method
    $\mathtt{L}_{\mathrm{MS}} \leftarrow \mathtt{L}_{\mathrm{MS}} + {}^1\!/_{n_r}\, \mathtt{M}(\mathscr{A}_{\mathcal{H}}(\mathcal{L}_\ell^r), \mathcal{V}_v^r)$
    $\mathtt{L}_{\mathrm{EE}} \leftarrow \mathtt{L}_{\mathrm{EE}} + {}^1\!/_{n_r}\, \mathtt{M}(\mathscr{A}_{\mathcal{H}^\diamond}(\mathcal{L}_\ell^r \cup \mathcal{V}_v^r), \mathcal{T}_t^r)$
  end
  if $L_{MS}^{\diamond} > L_{MS}$ **then**
    $L_{\mathrm{MS}}^{\diamond} \leftarrow L_{\mathrm{MS}}$
    $\mathscr{A}_{\mathcal{H}^\diamond} \leftarrow \mathscr{A}_{\mathcal{H}}$
    $\hat{\mathtt{L}}\left(\mathscr{A}_{\mathcal{H}^\diamond}\right) \leftarrow \mathtt{L}_{\mathrm{EE}}$
end

In this work, the MAE, MAPE, and the Pearson Product-Moment Correlation Coefficient (PPMCC) will be utilised [318]. Assuming that $\mathcal{Y}$ is mono-dimensional, the MAPE is computed as the absolute loss value of h over $\mathcal{T}_t^r$ in percentage, according to

$$\mathrm{MAPE}(h, \mathcal{T}_t^r) = \frac{1}{t} \sum_{i=1}^{t} \left| \frac{y_i^t - h(\boldsymbol{x}_i^t)}{y_i^t} \right|. \tag{4.26}$$

The MAE is evaluated as the absolute loss of h over $\mathcal{T}_t^r$

$$\mathrm{MAE}(h, \mathcal{T}_t^r) = \frac{1}{t} \sum_{i=1}^{t} \left| y_i^t - h(\boldsymbol{x}_i^t) \right|. \tag{4.27}$$

The PPMCC measures the linear dependency between $h(\boldsymbol{x}_i^t)$ and y_i^t, and is given by

$$\mathrm{PPMCC}(h, \mathcal{T}_t^r) = \frac{\sum_{i=1}^{t} \left(y_i^t - \bar{y}\right) \left(h(\boldsymbol{x}_i^t) - \hat{\bar{y}}\right)}{\sqrt{\sum_{i=1}^{t} \left(y_i^t - \bar{y}\right)^2} \sqrt{\sum_{i=1}^{t} \left(h(\boldsymbol{x}_i^t) - \hat{\bar{y}}\right)^2}}, \tag{4.28}$$

where the following notation is utilised

$$\bar{y} = \frac{1}{t} \sum_{i=1}^{t} y_i^t \tag{4.29}$$

$$\hat{\bar{y}} = \frac{1}{t}\sum_{i=1}^{t} h(\boldsymbol{x}_i) \tag{4.30}$$

Other state-of-the-art error metrics exist, but from a physical point of view, the ones mentioned already give a complete description of the quality of the various models, therefore only these will be reported. For the scope of this work $\mathcal{Y} \subseteq \mathbb{R}^o$ is multidimensional, and represents the measured noise levels at the different frequencies that compose the URN spectra. As such, the error metrics of Equations (4.26) - (4.28) are redefined as the average metrics among the predicted and measured noise levels that compose the spectra. This is possible since the spectra represent homogeneous quantities, and the average values of the MAE, MAPE, and PPMCC describe adequately the differences between the measured and predicted spectra [84]. Finally, since in regression it is quite hard to synthesise the quality of a model in a limited set of metrics, visualisation techniques like scatter plots and histograms will be utilised to visualise the performance of the various models [319]. Sections 4.6.2 - 4.6.3 discuss the methodology utilised in this work to obtain $h^\diamond$

4.6.2 Data-driven and Hybrid Models

For what regards the DDMs and HMs, the optimal model $h^\diamond$ is obtained by employing a grid search, i.e. trying all possible combinations of the hyperparameters listed in Table 4.8.

4.6.3 Physics-based Models

The PMs also have a set $\mathcal{S}$ of calibration constants. The values of these constants arise either from theoretical considerations, or they have to be estimated from experimental data, and are summarised in Table 4.9.

The Matusiak model requires the calibration of 5 constants. Matusiak [5] performed a detailed calibration study and thoroughly discussed the choice of certain values along with their interpretation. However, the calibration process was performed using limited measurements, and certain values were chosen for reasons of computational cost that

Table 4.8: Hyperparameters and hyperparameters search space for all algorithms tested in this work.

Model	Algorithm	Hyperparameters
PMs	None	
DDMs	ANN	$\epsilon : \{0.0001, 0.0005, 0.001, 0.005, 0.01\}$
		$h_1 : \{32, 64, 128, \cdots, 65536\}$
		$\lambda : \{10^{-6}, 10^{-5.8}, \cdots, 10^{3}\}$
	KRLS	$\lambda : \{10^{-6}, 10^{-5.8}, \cdots, 10^{3}\}$
		$\gamma : \{10^{-6}, 10^{-5.8}, \cdots, 10^{3}\}$
	ELM	$m : \{32, 64, 128, \cdots, 65536\}$
		$\lambda : \{10^{-6}, 10^{-5.8}, \cdots, 10^{3}\}$
	RF	$n_f : \{d^{1/3}, d^{1/2}, d^{3/4}\}$
		$n_l : \{1, 3, 5, 10\}$
		$n_t : \{1000\}$
HMs	As per the DDMs	As per the DDMs
		$r : \{1, 2, 4, 8\}$

do not apply anymore. For the ETV model, 7 constants have to be calibrated, for which Bosschers [82] performed an extensive analysis on several datasets, both in model-scale and full-scale data, under a variety of operating conditions. Nevertheless, the nature of the method requires the implementation of a calibration procedure in order to provide plausible predictions. Certain parameters of the Gilmore [320] equation could have also been treated as calibration constants. For instance, by modifying the value of the polytropic index c_{pi}, which determines if the process is adiabatic ($c_{\text{pi}} = 1.4$) or isothermal ($c_{\text{pi}} = 1$). Nevertheless, their values have been kept constant according to Table A.1 to simplify the calibration process.

4.6.3.1 Problem Formulation

The calibration process is formulated as an optimisation problem. Let $\boldsymbol{x}_i \in \mathcal{X} \subseteq \mathbb{R}^d$ be the d inputs of the model, i.e. all quantities related to the propeller geometry, wakefield, and inflow conditions for the corresponding experiment, and $\boldsymbol{y}_i \in \mathcal{Y} \subseteq \mathbb{R}^o$

Table 4.9: Parameter set $\mathcal{S}$ of the semi-empirical models.

Method	Symbol	Equation	Value*	Symbol	Equation	Value*
Matusiak Model (Section A.3)	β_f	Eq. (A.5)	0.8	m	Eq. (A.6)	9
	n_b^C	Eq. (A.5)	5	c_b	Eq. (A.6)	1.8
	n_{bo}	Eq. (A.11)	3.5			
ETV Model (Section A.4)	$c_P^{(2)}$	Eq. (A.19)	10	c_f	Eq. (A.36)	–
	c_{lo}	Eq. (A.37)	4	c_{hi}	Eq. (A.37)	-2
	c_{fc}	Eq. (A.26)	0.45	c_s	Eq. (A.38)	0.8
	c_a	Eq. (A.35)	–			

* [–] indicates that the constant has no recommended value, implying that a curve-fitting procedure must be used.

be the o sound pressure levels characterising $\boldsymbol{S}_{\mathrm{pl}}$. Also, let $\boldsymbol{s} \in \mathcal{S}^p$ be a vector of p constants of to be calibrated, with admissible values lying between lower and upper bounds $\boldsymbol{s}_{\mathrm{min}}$, and $\boldsymbol{s}_{\mathrm{max}}$, respectively. Furthermore, let $g_{\mathrm{obj}} : \mathbb{R}^p \to \mathbb{R}$ be a function that quantifies the error between

- the measured $\boldsymbol{S}_{\mathrm{pl}}$ contained on a dataset $\mathcal{D}_n = \{(\boldsymbol{x}_1, \boldsymbol{y}_1), ..., (\boldsymbol{x}_n, \boldsymbol{y}_n)\}$ of n experiments,
- and the corresponding predictions of the model $h : \mathcal{X} \to \mathcal{Y}$ characterised by the constants $\boldsymbol{s}$,

measured according to a loss function $\ell : \mathbb{R}^o \to \mathbb{R}$. Regarding ℓ, the mean squared error averaged over all o outputs has been adopted, according to

$$\ell\left(h\right) = \frac{1}{o} \sum_{i=1}^{o} \left[h_i\left(\boldsymbol{x}; \boldsymbol{s}\right) - y_i\right]^2 . \tag{4.31}$$

This error metric has been chosen as it is one of the most effective, differentiable, and convex metrics for regression [307, 317]. Averaging the errors between sound pressure levels of different frequencies is possible since they all represent homogeneous quantities, and the average difference can describe the quality of h in a satisfactory manner.

Subsequently, g_{obj} can be considered as the average error h commits on the measured $\boldsymbol{S}_{\mathrm{pl}}$ of $\mathcal{D}_n$, defined as

$$g_{\mathrm{obj}}(\boldsymbol{s}, \mathcal{D}_n) = \frac{1}{n} \sum_{i=1}^{n} l\left[h\left(\boldsymbol{x}_i; \boldsymbol{s}\right), \boldsymbol{y}_i\right], \tag{4.32}$$

Table 4.10: Bounded space of $\mathcal{S}$ used during the calibration process.

Method	Symbol	$s_{\min}$	$s_{\max}$
Matusiak Model (Section A.3)	β_f	0.1	1.0
	m	1	9
	n_b^C	2	50
	c_b	0.6	3.0
	n_{bo}	2	300
ETV Model (Section A.4)	$c_P^{(2)}$	-0.1	0.6
	c_f	5	15
	c_{lo}	1	10
	c_{hi}	-10	-1
	c_{fc}	0.3	0.6
	c_s	0	1
	c_a	50	150

It should be noted that this metric is susceptible to the differences in the orders of magnitude of each output. For this reason, by employing a simple normalisation and combining the definitions, g_{obj} can be written as

$$g_{\text{obj}}(\boldsymbol{s}, \mathcal{D}_n) = \frac{1}{o}\frac{1}{n}\sum_{i=1}^{n}\sum_{j=1}^{o}\left[\frac{h_j\left(\boldsymbol{x}_i;\boldsymbol{s}\right) - y_{i,j}}{\left(\frac{1}{n}\sum_{k=1}^{n} y_{k,j}^2 - \left(\frac{1}{n}\sum_{k=1}^{n} y_{k,j}\right)^2\right)^{1/2}}\right]^2. \tag{4.33}$$

Thus, the solution to the following continuous problem is required

$$\begin{aligned} \boldsymbol{s}^{\diamond} : \arg\min_{\boldsymbol{s}\in\mathcal{S}} \quad & g_{\text{obj}}(\boldsymbol{s}, \mathcal{D}_n) = \frac{1}{o}\frac{1}{n}\sum_{i=1}^{n}\sum_{j=1}^{o}\left[\frac{h_j\left(\boldsymbol{x}_i;\boldsymbol{s}\right) - y_{i,j}}{\left(\frac{1}{n}\sum_{k=1}^{n} y_{k,j}^2 - \left(\frac{1}{n}\sum_{k=1}^{n} y_{k,j}\right)^2\right)^{1/2}}\right]^2 \\ \text{subject to} \quad & \boldsymbol{s}_{min} \leq \boldsymbol{s} \leq \boldsymbol{s}_{max}. \end{aligned} \tag{4.34}$$

4.6.3.2 Solution Method

Problem (4.34) is characterised by an Objective Function (OF) which is non-convex [321] with respect to $\boldsymbol{s}$. Furthermore, obtaining or estimating the derivatives of h with respect to $\boldsymbol{s}$ is a cumbersome and time-intensive procedure. Therefore, a Black Box Optimisation (BBO) method is employed to solve Problem (4.34). BBO refers to all optimisation algorithms that do not use derivative information to minimise an OF, and

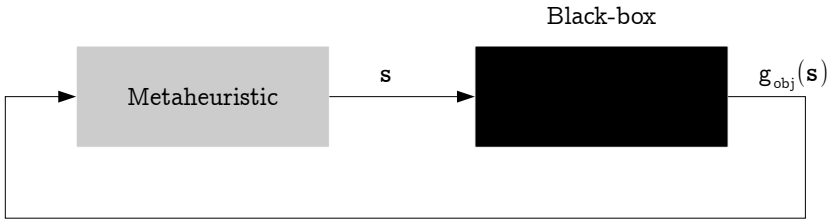

Figure 4.17: Black-box scenario for the objective function (adapted from [14]).

are commonly used in applications that involve obtaining minima of computer simulations whose outputs do not include derivatives [14]. Their main advantage is the lack of any restrictive assumptions regarding the functional form of the problem, and the OF is treated as a black-box, as illustrated in Figure 4.17.

The literature on BBO methods is quite large, with a variety of algorithms that can solve a very diverse class of problems [322–324]. As such, they have been exploited in several branches of science and engineering, for instance engineering design [325–327], materials science [328, 329], oil and gas sector [330, 331], as well as maritime operations [332, 333], and the shipbuilding industry [334, 335]. Among the available algorithms, a method from the *approximate* family of algorithms will be utilised, belonging to the class of *metaheuristics*. Metaheuristics are general-purpose algorithms that can be applied to solve almost any optimisation problem and can deliver satisfactory solutions in a reasonable time, even in large-size problem instances. One disadvantage of metaheuristics is that they have their own set of parameters that need calibration. These parameters allow for greater flexibility and robustness, but require careful initialisation as they may have great influence on the efficiency and effectiveness of the search towards the minimum, and their values depend mainly on the problem at hand.

From the available metaheuristics algorithms, a stochastic, population-based approach is utilised, known as Particle Swarm Optimisation (PSO). This choice was made for a variety of reasons, including [336–339]:

- the reduced number of parameters that require calibration,
- fast convergence and high accuracy,
- reduced computation burden in comparison with most other heuristics,
- robustness to initial solutions,

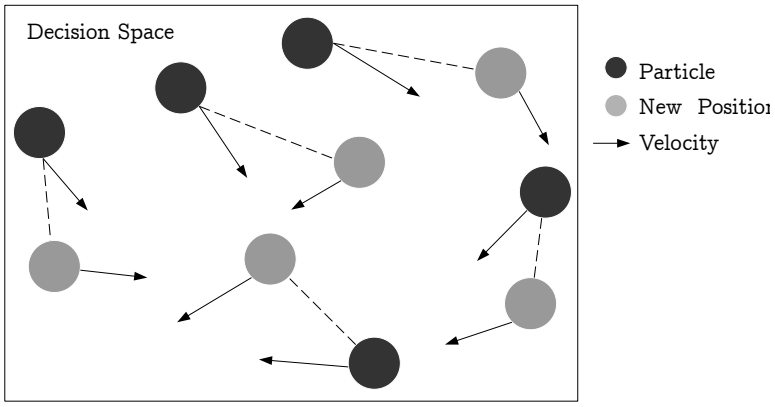

Figure 4.18: Particle swarm with their associated positions and velocities. At each iteration, a particle moves from one position to another in the decision space (adapted from [14]).

- behavior not highly affected by increase in dimensionality,
- incorporation of efficient strategies to mitigate premature convergence,
- ability to handle non-linear, non-convex search spaces with discontinuities,
- availability in most numerical platforms,
- existence of stochastic properties, which allow for solution variability and thorough exploration of the search space in the initial iterations, with a local search behaviour during the final iterations.

In brief, PSO is inspired from swarm intelligence and mimics the social behaviour of organisms in groups, emulating the interactions between members of the group in order to share information. In those groups, a coordinated behavior using local movements emerges without any central control [340]. Originally, PSO was successfully designed for continuous optimisation problems, with its first application being proposed in Eberhart and Kennedy [341].

The search for the optimal solution is performed through agents, referred to as particles, whose trajectories are adjusted by a stochastic and a deterministic component. Initially, the PSO algorithm generates a random population of n_e particles moving in a p dimensional space. Each particle i is a candidate solution to the problem, characterised by its position $\boldsymbol{z}_e^{(i)} \in \mathbb{R}^p$ and velocity $\boldsymbol{u}_e^{(i)} \in \mathbb{R}^p,\ i = \{1, \cdots, n_e\}$ in the decision space, and an OF value $g_{\mathrm{e}}^{(i)} = g_{\mathrm{obj}}(\boldsymbol{z}_{\mathrm{e}}^{(i)})$, as illustrated in Figure 4.18. The optimisation

process takes advantage of the cooperation between the particles, in the sense that the "success" of some particles, i.e. their lower OF value, will influence the behavior of their peers. The movement of the particles in the group is controlled by 3 factors:

- the cognitive learning factor $\mathrm{c_{co}} \in \mathbb{R}_{>0}$, which indicates the confidence of the particle in itself, determined by the best position visited by it ($\boldsymbol{z}_{\mathrm{e}}^{\diamond(i)}$), with the corresponding OF value $g_{\mathrm{e}}^{\diamond(i)} = g_{\mathrm{obj}}(\boldsymbol{z}_{\mathrm{e}}^{\diamond(i)})$,
- the social learning factor $\mathrm{c_{so}} \in \mathbb{R}_{>0}$ that indicates the confidence of the particle in the swarm, determined by the best position visited by the entire swarm or a smaller neighborhood around particle i ($\boldsymbol{z}_{\mathrm{sw}} \in \mathbb{R}^p$) with the corresponding OF value being $g_{\mathrm{sw}} = g_{\mathrm{obj}}(\boldsymbol{z}_{\mathrm{sw}})$,
- and the inertial weight $\mathrm{c_{iw}} \in \mathbb{R}_{>0}$ that influences the convergence behaviour by increasing the distance that the particle will traverse from its current position.

There are many possibilities to define the number of particles n_{en} in the neighborhood for each particle. Most common include the global best method, in which the neighborhood is defined as the entire swarm, and the local best method where the neighborhood is a smaller set of directly connected particles, with a "leader" guiding the search of the connected particles towards better regions of the decision space.

At each iteration, or time-step $t_j,\ j = \{1, \cdots n_{\mathrm{ts}}\}$, each particle applies the following operations: A velocity update, which defines the direction and the distance each particle should traverse according to

$$\boldsymbol{u}_e^{(i)}(t_j) = c_{\mathrm{iw}}\boldsymbol{u}_e^{(i)}(t_j) + \boldsymbol{u}_e^{(i)}(t_{j-1}) + \mathfrak{r}_1 c_{\mathrm{co}}\left(\boldsymbol{z}_{\mathrm{e}}^{\diamond(i)} - \boldsymbol{z}_e^{(i)}(t_{j-1})\right) + \\ + \mathfrak{r}_2 c_{\mathrm{so}}\left(\boldsymbol{z}_{\mathrm{sw}}^{\diamond} - \boldsymbol{z}_e^{(i)}(t_{j-1})\right), \quad (4.35)$$

with $\mathfrak{r}_i = \mathcal{U}(0,1)$. Subsequently, a position update follows, according to

$$\boldsymbol{z}_e^{(i)}(t_j) = \boldsymbol{z}_e^{(i)}(t_{j-1}) + \boldsymbol{u}_e^{(i)}(t_j), \quad (4.36)$$

followed by the best swarm (or neighborhood) position update, where each particle updates (potentially) its current best OF value. By performing this process, each

Table 4.11: Parameters of the PSO algorithm.

Parameter	Description	Common range*	Value
n_{ts}	Number of iterations	$[50, 350] \cdot \dim \boldsymbol{s}$	$200 \cdot \dim \boldsymbol{s}$
n_{e}	Number of particles	$[10, 100] \cdot \dim \boldsymbol{s}$	$100 \cdot \dim \boldsymbol{s}$
n_{en}	Neighborhood size	$[0.2, 1] \cdot n_{\text{e}}$	$0.9 \cdot n_{\text{e}}$
c_{co}	Cognitive learning factor	$[1.2, 2.0]$	1.5
c_{so}	Social learning factor	$[1.2, 2.0]$	1.5
c_{iw}	Inertial weight	$[0.3, 1.1]$	0.7

* Discussed or proposed in [336–339, 342–352].

particle changes its position according to its own experience and the experience of the neighboring particles [340]. An overview of the PSO optimisation process is provided in Algorithm 4.2, and the parameter values utilised in this work, along with commonly used values, are presented in Table 4.11.

4.7 Physical Plausibility

As discussed in Section 3.6, one limitation of current approaches is the lack of investigation of the physical plausibility of the predictions. To verify if the plausibility of the predictions is ensured, two approaches have been employed: the Feature Ranking (FR) procedure of Section 4.7.1, which originates from the field of DDMs, and the Test against Prior Knowledge (TPK) of Section 4.7.2 that originates from the field of PMs.

4.7.1 Feature ranking

Once the DDMs and HMs have been developed, it is possible to investigate how each quantity in $\mathcal{X}$ affects the predictions of each model. This investigation helps to understand if the resulting predictions rely on the true underlying physical phenomena, or if the models just capture spurious relations. More formally, this procedure allows to detect if the importance of features, already known to be relevant from a physical perspective, is appropriately taken into account by the learned models [353, 354]. Failure of the learned models to properly account for the relevant features might indicate poor quality in the measurements, or spurious correlations. FR therefore represents an important step in the model verification process, since it examines whether the learned

Algorithm 4.2: Particle Swarm Optimisation

Input: $c_{\mathrm{co}}, c_{\mathrm{so}}, c_{\mathrm{iw}}, n_{\mathrm{ts}}, n_{\mathrm{e}}, n_{\mathrm{en}}, \boldsymbol{s}_{\min}, \boldsymbol{s}_{\max}$
Result: $\boldsymbol{z}_{\mathrm{sw}}, g_{\mathrm{sw}}$
`/* Random initialisation of` n_e `particles in` $\mathcal{S}$ `*/`
for $i \leftarrow 1$ **to** n_e **do**
  $\boldsymbol{u}_e^{(i)}(t_0) \leftarrow \mathbf{0}$
  $\boldsymbol{z}_e^{(i)}(t_0) \leftarrow (Z_1, \cdots Z_p)$ where $Z_j = \mathcal{U}\left(s_{\min}^{(j)}, s_{\max}^{(j)}\right)$, $j \in \{1, \cdots, p\}$
  $\boldsymbol{z}_{\mathrm{e}}^{\diamond(i)} \leftarrow \boldsymbol{z}_e^{(i)}(t_0)$
  $g_{\mathrm{e}}^{\diamond(i)} \leftarrow g_{\mathrm{obj}}\left(\boldsymbol{z}_e^{(i)}(t_0)\right)$
end
$g_{\mathrm{sw}} \leftarrow \min_i g_{\mathrm{e}}^{\diamond(i)}$
$\boldsymbol{z}_{\mathrm{sw}} \leftarrow \arg\min_i g_{\mathrm{e}}^{\diamond(i)}$
`/* Iterations */`
while $j \leq n_{ts}$ **do**
  for $i \leftarrow 1$ **to** n_e **do**
    `/* Update position and velocity of particle` i `*/`
    Evaluate $\boldsymbol{u}_e^{(i)}(t_j)$ according to Eq. (4.35)
    Evaluate $\boldsymbol{z}_e^{(i)}(t_j)$ according to Eq. (4.36)
    Evaluate $g_e^{(i)}(t_j) = g_{\mathrm{obj}}\left(\boldsymbol{z}_e^{(i)}(t_j)\right)$
    `/* Best position and OF value update */`
    if $g_e^{\diamond(i)} > g_e^{(i)}(t_j)$ **then**
      $g_{\mathrm{e}}^{\diamond(i)} \leftarrow g_{\mathrm{e}}^{(i)}(t_j)$
      $\boldsymbol{z}_{\mathrm{e}}^{\diamond(i)} \leftarrow \boldsymbol{z}_e^{(i)}(t_j)$
    if $g_{sw} > g_e^{\diamond(i)}$ **then**
      $g_{\mathrm{sw}} \leftarrow g_{\mathrm{e}}^{\diamond(i)}$
      $\boldsymbol{z}_{\mathrm{sw}} \leftarrow \boldsymbol{z}_{\mathrm{e}}^{\diamond(i)}$
  end
  $j \leftarrow j + 1$
end

models generate results that are consistent with prior knowledge of the phenomena under consideration.

For this purpose, a statistically sound and robust approach has been employed, which combines the development of a DDM (or HM) together with the permutation test [355–357], and was first applied in RFs by Breiman [235], using the mean decrease in MAE as a metric. The concept behind this approach is the following: The importance of a feature is estimated by computing the increase of the model's prediction error after permuting the feature. The feature is deemed important if the permutation of its values increases the model's error, which implies that the model relied on the feature for its

predictions. On the other hand, a feature is considered unimportant if the permutation of its values does not significantly alter the error of the model, implying that the model practically ignored that feature for its predictions. This approach is summarised and simplified in Algorithm 4.3, which shows that it is repeated n_{rep} times for every feature in $\mathcal{X}$. The final rankings $\boldsymbol{I} \in \mathbb{R}^{\iota}_{>0}$ of the features are subsequently obtained by averaging the importance of each feature over all model outputs, and sorting the results accordingly.

Algorithm 4.3: Permutation Feature Importance

Input: $\mathscr{A}_{\mathcal{H}}$, $\mathcal{D}_n$, $M(\cdot,\cdot)$, n_{rep}
Result: Feature importance vector $\boldsymbol{I} = \{I_1, \cdots, I_\iota\}$
Compute the reference error $\epsilon_{\text{ref}} = M(\mathscr{A}_{\mathcal{H}}, \mathcal{D}_n)$
for *each input feature* $j \in \{1, \cdots, \iota\}$ **do**
  for *each repetition* $k \in \{1, \cdots, n_{rep}\}$ **do**
    Permute feature $\boldsymbol{x}^{(j)}$ to generate a corrupted version $\hat{\mathcal{D}}_n^{(k)}$ of $\mathcal{D}_n$
    Compute the error $\epsilon_j^{(k)} = M(\mathscr{A}_{\mathcal{H}}, \hat{\mathcal{D}}_n^{(k)})$
  end
  Calculate feature importance $I_j = \epsilon_{\text{ref}} - \frac{1}{N_r}\sum_{k=1}^{N_r} \epsilon_j^{(k)}$
end

4.7.2 Test against prior knowledge

To conduct the TPK, a set of numerical experiments can be conducted that assess the physical plausibility of the predicted URN spectra. These experiments must be carefully designed to assess if the predictions of the DDMs and HMs are aligned with the knowledge of the phenomena under consideration. This analysis is critical in cases for which poor predictions can have major impact [358]. In fact, classical PMs are still preferred in most engineering applications, despite higher modelling and computational effort: They ensure physical plausibility, and are guaranteed to extrapolate to new samples, whereas DDMs only guarantee high performance in the vicinity of the data used to develop them [359].

This assessment is especially critical for DDMs as, contrarily to PMs and HMs, they do not rely on any prior knowledge regarding the phenomena under consideration. Whereas there is a multitude of experiment designs that can be employed, the simplest

approach involves testing the models' predictions in various loading conditions, which can be introduced by varying `n` and p_{tunnel}. Selecting values that do not appear in the dataset that was used to develop the models allows to investigate how the cavitating area and the vortex strength affect model predictions. The predictions of the models will be compared with general theory on cavitation noise. More specifically

- for the effect of the cavitation area, the relative differences between:
  - the noise increment corresponding to increased or decreased cavitation area as predicted by the method of Brown [15],
  - and the noise increment according to the HMs, estimated on the frequency band between 4 - 20 [kHz],

  is evaluated.
- For the effect of the vortex strength, the relative differences between:
  - the URN peak level corresponding to increased or decreased cavitating tip vortex radius, as predicted by the model of Bosschers [16],
  - and the URN peak level according to the HMs

  is evaluated.

4.8 Summary

This chapter provided an overview of the hybridization scheme proposed in this work to estimate the noise spectra from cavitating marine propellers. A detailed description of the mathematical framework and all necessary components have been addressed and presented: A set of PMs to provide a first estimate of the URN spectra, a set of DDMs originating from the three main families of ML algorithms, to correct the URN spectra estimated from the PMs, and a comprehensive feature engineering process to provide the DDMs with a summarized, yet rich, representation of the main aspects that govern the underlying physical phenomena. In addition, the process of estimating the (hyper-) parameters of the DDMs and HMs is presented, along with the process of evaluating the errors they commit on new, unseen, geometries and conditions, as well as the assessments that can be conducted to assess the physical plausibility of the predictions.

Chapter 5

Dataset Description

Abstract

This chapter discusses the dataset used to demonstrate the feasibility of the proposed methodology, and to quantify the accuracy of the proposed models. Whereas most studies in the literature conduct comparisons between experimental and numerical data on a limited set of cases, more than 430 experiments from two universities have been made available and are utilised to assess the capabilities of the proposed approach.

5.1 Introduction

Due to the nature of the DDMs and HMs, availability of experimental data is necessary for their development. This chapter discusses the dataset employed, not only to develop them, but also to test the methodology proposed in Chapter 4. To this aim, an excess of 430 numerical experiments are conducted, all of which are compared with experimental data. These comparisons allow to fully assess the performance of the models, and reveal any potential weaknesses in the proposed methodology. In addition, the large number of available experiments allows the author to learn the models on various subsets of the data, and perform a set of analyses that can assess the ability of all models to extrapolate on various scenarios.

In particular, the dataset generated in the extensive measurement campaign of [7, 8] is utilised. The authors of these studies conducted systematic cavitation tunnel tests at the Emerson Cavitation Tunnel (ECT) of Newcastle University [360]. A total of

432 tests were conducted, involving 6 propeller scaled models of the Meridian Standard Propeller Series and 3 wakefields at various loading conditions, induced by varying the propellers' rotational speed, and the relative pressure of the cavitation tunnel. This dataset will serve as a basis for the learning phase of the model presented in Chapter 4. In addition, data from a moderately loaded propeller model operating in uniform inflow conditions is also available, for which experimental analyses were carried out in the framework of the EU funded project PIAQUO [361] in the cavitation tunnel of the University of Genoa.

Further details regarding the propellers composing the available data are provided in Section 5.2, whereas Section 5.3 discusses the 3 wakefields. Section 5.4 provides further details regarding the design of experiments which resulted in the dataset of [7, 8]. Finally, Section 5.5 discusses the additional set of numerical experiments conducted for the TPK, according to Section 4.7.2. It should be noted that experimental data corresponding to the numerical experiments of Section 5.5 is not available. Nevertheless, the numerical predictions will be compared with general theory on cavitation noise, which is adequate for the physical plausibility assessment.

5.2 Propeller Models

Aktas [7], Aktas et al. [8] chose the Meridian Standard Propeller Series with the aim to generate a representative systematic body of URN data. The Meridian series was chosen as it provides the best coverage in terms of the major propeller design parameters for acoustic testing [362]. This series is derived from the proprietary propeller designs of Stone Manganese Marine Ltd., and constitutes a unique standard series based solely on practical propeller designs with standardised variations in Pitch-to-Diameter Ratio (PDR), BAR and Z. Initially, the series comprised 5 parent models having a combination of 4 distinct BARs $\in \{0.45, 0.65, 0.85, 1.05\}$[–], and 5 mean PDRs $\in \{0.4, 0.6, 0.8, 1.0, 1.2\}$[–], with $D = 304.8$[mm] and 6 blades. Currently there are 60 propellers in the series, with $Z \in \{4, 5, 6\}$[–], BAR $\in [0.45 - 1.05]$[–] and mean PDR $\in [0.4 - 1.2]$[–] [34].

The subset utilised in this work includes the propeller models: KCD 65, KCD 74,

Table 5.1: Key design parameters of the propellers in $\mathcal{D}_n$.

Model	Z [–]	BAR [–]	PDR [–]	Model	Z [–]	BAR [–]	PDR [–]
KCD 65	6	0.85	0.8	KCD 74	6	1.05	0.8
KCD 129	5	0.85	0.8	KCD 191	4	0.65	0.6
KCD 192	4	0.65	0.8	KCD 193	4	0.65	1.0

KCD 129, KCD 191, KCD 192, and KCD 193. According to Aktas [7], these models were chosen as their geometry allows to test significant propeller design parameters in relation to URN. More specifically, models KCD 191, KCD 192, and KCD 193 were chosen to assess the effect of pitch to URN, while models KCD 65, and KCD 74 were selected to assess the effect of the BAR. These propeller models are illustrated in Figure 5.1, whereas their main design characteristics are provided in Table 5.1. For the sake of completeness, additional geometric details are given in Appendix E.

For what regards the additional Moderately Loaded Propeller (MLP), compared to the Meridian propellers, its geometry has a rather modern design having a skew at the tip greater than 40[deg]. The operating point defines this geometry as a moderately loaded propeller since it was designed for a semi-displacement small passenger vessel with a reference displacement of 60[tons] operating at a design speed of 20[kn]. In these conditions, the cavitation index is approximately equal to 1.4[–] and lower than 1.2[–] at the maximum vessel speed of 25[kn]. These characteristics, which indicate serious risk of sheet and tip vortex cavitation, together with the possible operation of the vessel in restricted areas, made this propeller the ideal candidate for detailed numerical and experimental analyses that were carried out in the framework of the EU funded project PIAQUO [361], specifically devoted to vessel noise prediction and mitigation. A visual impression of this propeller is provided in Figure 5.2. Detailed information regarding its geometry is not provided due to confidentiality constraints.

5.3 Wakefields

The wakefields selected by Aktas were largely chosen following the conclusions of Konno et al. [274], who observed that cavity collapse events increase the amplitude and com-

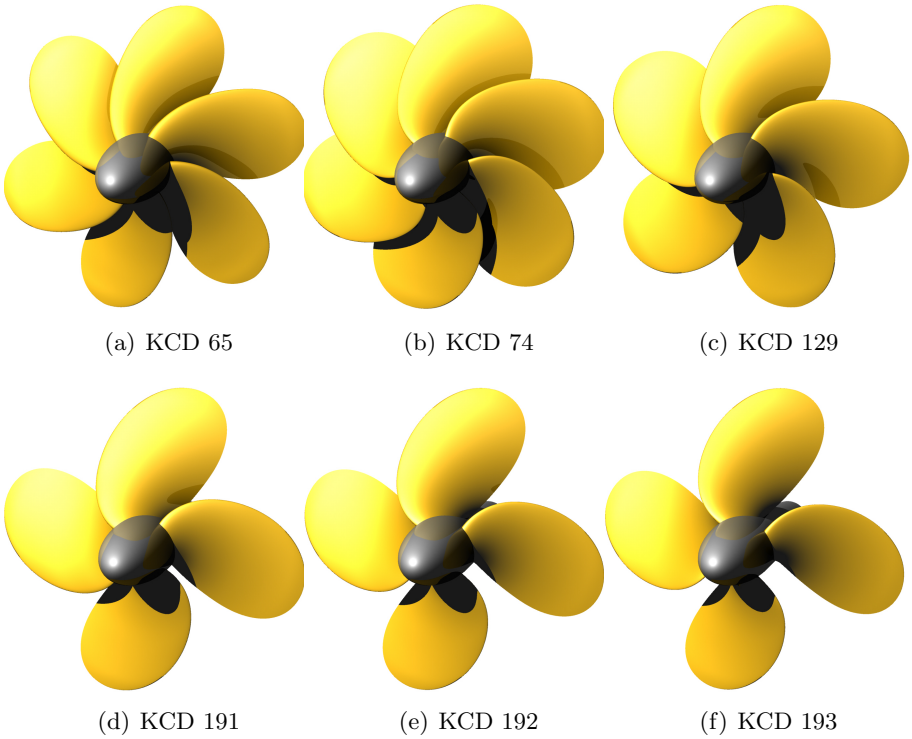

(a) KCD 65 (b) KCD 74 (c) KCD 129

(d) KCD 191 (e) KCD 192 (f) KCD 193

Figure 5.1: Visual impression of the Meridian propellers available in the dataset.

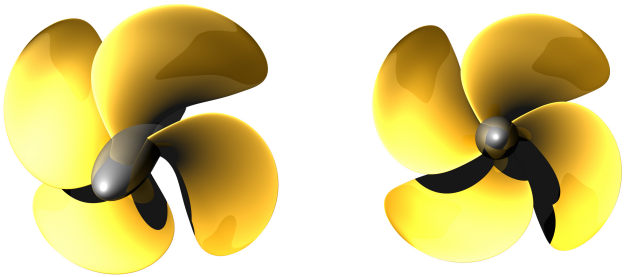

(a) 3D view. (b) Front view.

Figure 5.2: Visual impression of the moderately loaded propeller available in the dataset.

plexity of the pressure pulses, and highlighted the effects of altering the gradient of the wake distribution. More specifically, wakefields with steeper velocity changes were shown to produce higher tonal amplitudes of pressures, as well as high frequency contributions from the increased dynamic cavity collapses, both on and off the blade surface.

Inspired by Konno et al., Aktas utilised the criteria of the British Ship Research

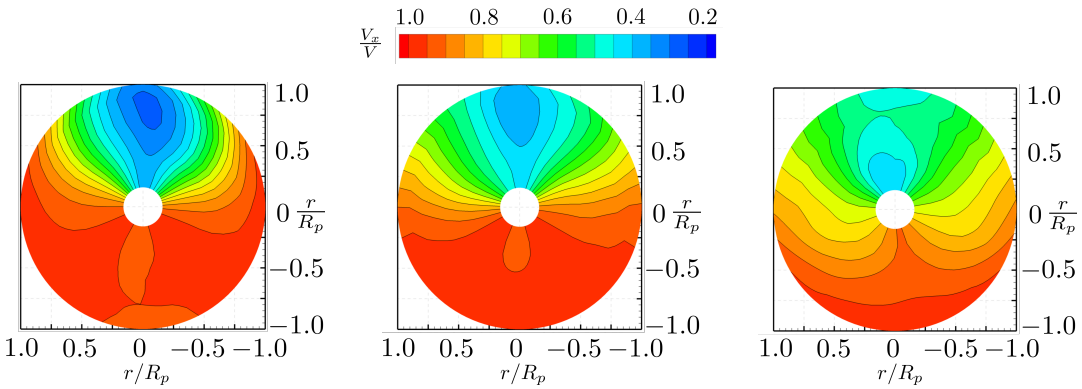

(a) W1 (b) W2 (c) W3

Figure 5.3: Contour plots of axial velocity distributions of the wakefields in the dataset.

Table 5.2: Main parameters of the wakefields in $\mathcal{D}_n$.

Name	Units	W1	W2	W3
Wake depth	[–]	0.71	0.64	0.50
Half wake width	[deg]	60	95	132
Mean wake	[–]	0.16	0.20	0.195
Wake non-uniformity	[–]	0.86	0.81	0.63

Association suggested by [10, 363] to develop a family of 3 representative wakefields that complement the parametric variations of the propeller models. These wakefields were generated by varying the wake non-uniformity, mean wake, half-wake width and wake depth, in order to induce variations of the inflow velocities of varying severity. The wakefield with the narrowest wake width and highest wake depth is the most severe, and is referred to as W1, the wakefield with lowest wake depth and largest half wake width is the mildest one and is referred to as W3, whereas W2, with parameters lying between W1 and W3 is of intermediate severity. Table 5.2 presents the main parameters of the three wakefields, and Figure 5.3 provides a visual impression.

5.4 Experimental campaign

Utilising the propeller models of Section 5.2 and the wakefields of Section 5.3, a full factorial design of experiments was conducted by Aktas [7] by varying the rotational speed of the propellers and the tunnel vacuum pressure. More specifically,

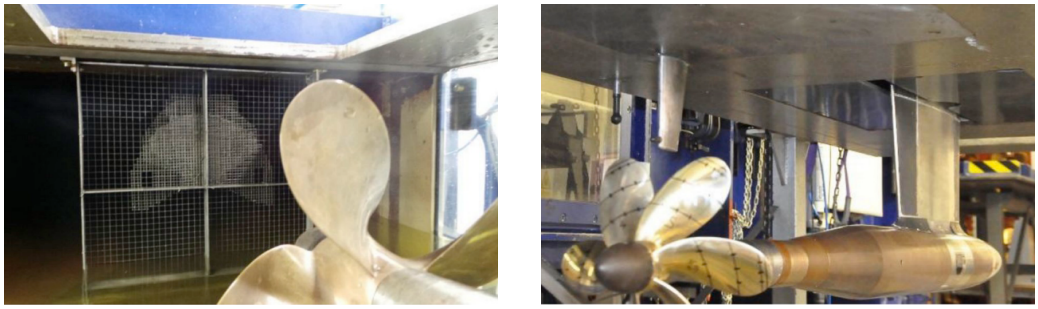

(a) Test set-up of a model propeller behind a wake screen [7].

(b) Location of the hydrophone relative to a model propeller [8].

Figure 5.4: Experimental Setup.

- 8 discrete rotational speeds were considered: {600, 800, 1000, 1200, 1400, 1500, 1750, 2000} [rpm],
- and 3 tunnel vacuum pressures p_{tunnel}: atmospheric, 150[mmHg], and 300[mmHg],

at a constant inflow velocity of 3[m/s]. This experimental design provided a set of cavitation tunnel tests that cover both TVC and sheet cavitation conditions.

To ensure the consistency of the results, constant monitoring of the water quality inside the tunnel was also performed, and background noise was removed by measured transfer functions, as suggested in [276]. URN was measured by one hydrophone placed in the tunnel test section, and was acquired in the form of pressure time-traces. These were subsequently transformed to the frequency domain by applying the Fast Fourier Transformation (FFT), and the measured URN values were converted to 1/3 octave band relative to 1[μPa], and corrected to a standard measuring distance of 1[m], according to the recommendations of [276].

A visual impression of the experimental setup is presented in Figure 5.4, illustrating a model propeller behind one of the wake screens, and the location of the hydrophone relative to a model propeller. Further details regarding the equipment utilised for the measurements can be found in [7]. Naturally, the size of the dataset does not allow for a full presentation of all the experiments and simulated BEM results. Nevertheless, some characteristic examples of URN spectra and related measurements are analysed in the present section. All the considerations reported are valid for the entire dataset.

To provide a visual impression of the operating conditions covered in the dataset,

Figures 5.5-5.6 report the open water diagrams, operating points and cavitation indices (based on rotational speed at the blade tip) of all the propellers in the dataset. As can be seen, the dataset covers a broad operating region for all propellers, with $J \in [0.3-0.8)[-]$ and $\sigma_{n,tip} \in [0.15, 1.4][-]$ for propellers KCD 65, KCD 74, KCD 129, and KCD 191, and $J \in [0.3-1.0)[-]$, $\sigma_{n,tip} \in [0.25, 2.2][-]$ for propellers KCD 192, and KCD 193. The effect of the various wakes is also visible, with the most severe wakefield $W1$, characterised by the narrowest wake width and the highest wake depth, causing the lowest K_t, K_q values to occur for a fixed J across all propellers. Wakefield W3, being the mildest one, results in the highest average values for K_t, K_q for a fixed J and propeller, and wakefield W2 provides intermediate K_t, K_q values that lie closer to the ones arising from W3.

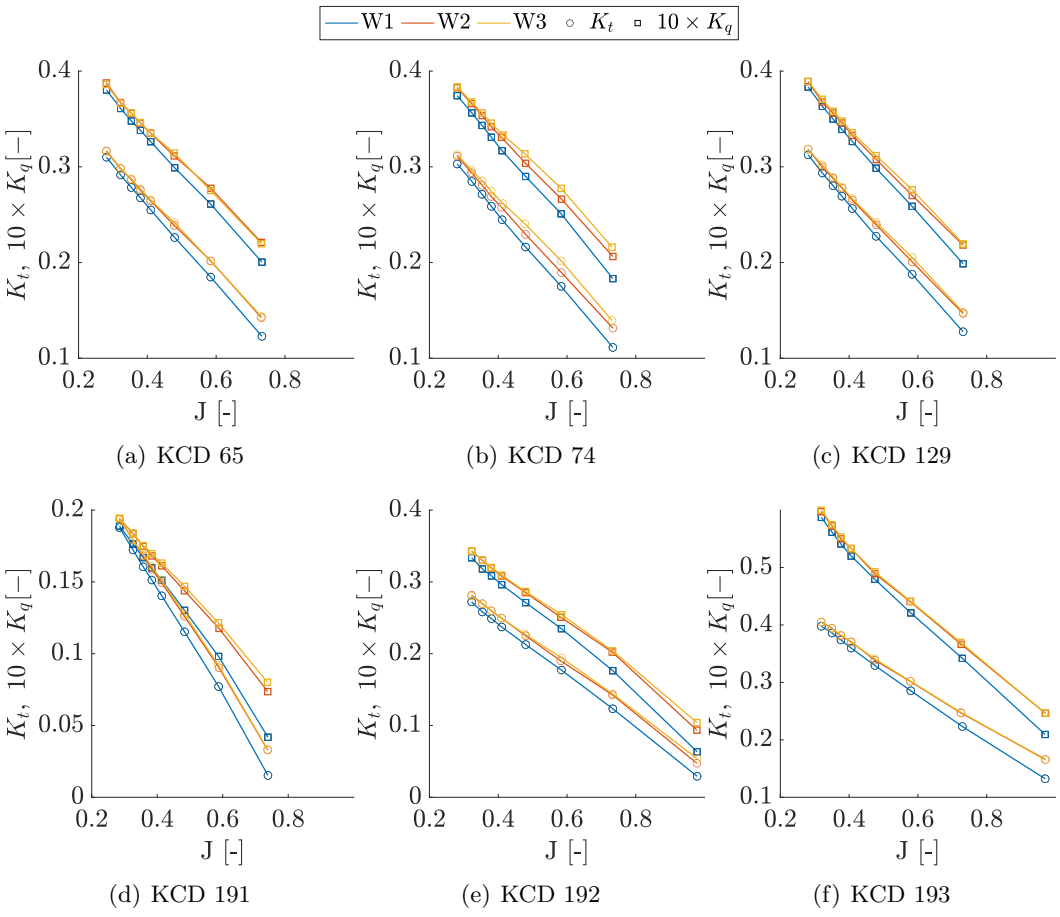

(a) KCD 65 (b) KCD 74 (c) KCD 129

(d) KCD 191 (e) KCD 192 (f) KCD 193

Figure 5.5: Open water diagrams and operating points of the propellers in $\mathcal{D}_n$.

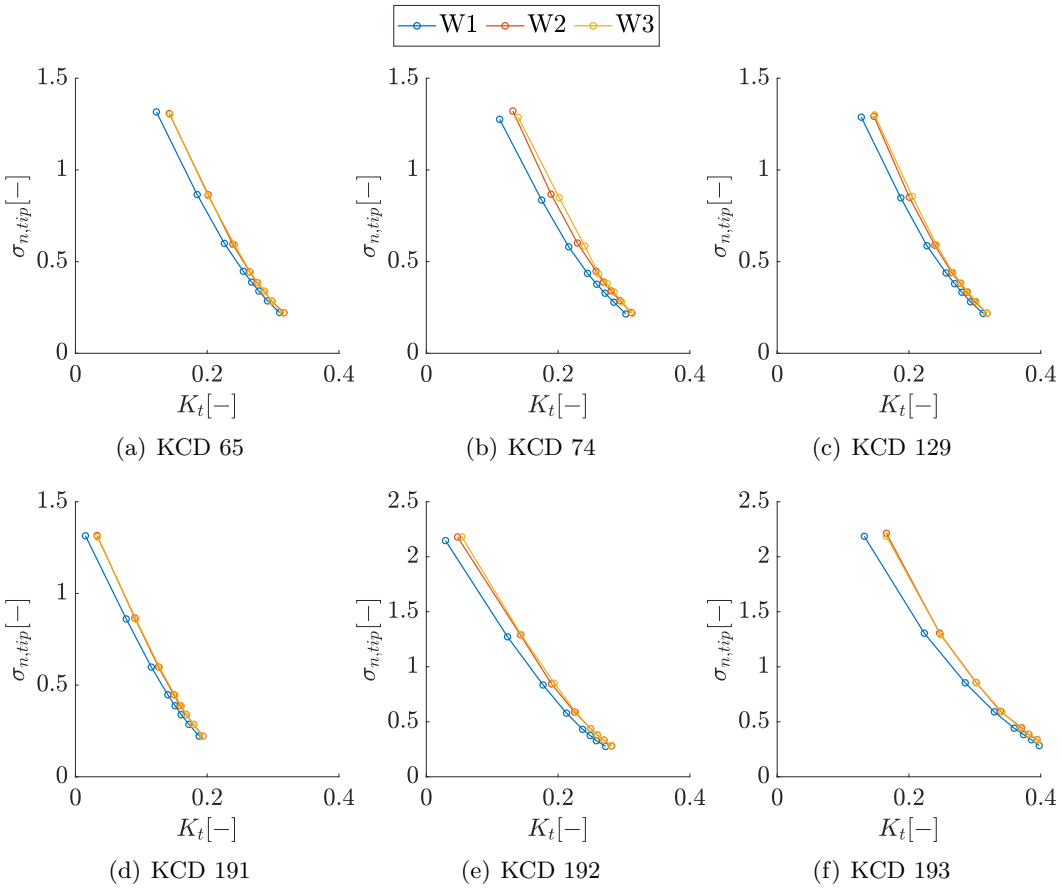

(a) KCD 65 (b) KCD 74 (c) KCD 129

(d) KCD 191 (e) KCD 192 (f) KCD 193

Figure 5.6: Cavitation indices of the experiments in $\mathcal{D}_n$.

A demonstrative example of the cavitating conditions included in the dataset is provided in Figure 5.7, which focuses on propeller KCD 193, operating on wakefield W1 under (fixed) rotational and inflow velocities. The specific conditions corresponding to these experiments are provided in Table 5.7. More specifically, Figure 5.7 illustrates the effect of the variation of p_{tunnel}, which is causing variations on the cavitation index, thus affecting the detected cavitating areas, illustrated in Figure 5.7(a), and the formation of the URN spectra, shown in Figure 5.7(b).

Furthermore, Figure 5.8 presents the computed C_p values from the BEM code for the pressure and suction sides of the propeller. As stated in Section 4.2.2, C_p is evaluated for 44 locations in the chord-wise direction, and 22 radial sections that represent approximately 1000 panels per blade. For these panels, 60 angular positions are consid-

Table 5.3: Sample experiments in $\mathcal{D}_n$.

Experiment	Propeller	Wakefield	J [–]	ω_p [rad/s]	σ_n [–]
A					3.06
B	KCD 193	W1	0.319	183.47	2.35
C					1.85

ered, corresponding to an equivalent time-step of 6 [deg]. From these examples typical characteristics of C_p can be observed. More in detail, the yellow areas on the pressure sides correspond to high pressure regions near the leading edge of the blades, while the dark blue areas are associated with the typical negative pressure peaks. Although not easily distinguishable from these graphs, the pressure distributions on the blades are not identical. The non-uniform inflow conditions cause each blade to operate in a locally different flow field. Although cavitation inception and development are highly complex phenomena that cannot be reliably modelled by BEM, the approximation that cavitation occurs when the local pressure is lower than the vapour pressure does highlight the differences between these 3 experiments. This also demonstrates the importance of the feature engineering process described in Section 4.4: whereas the pressure distributions appear to be similar across all 3 experiments, the differences are amplified by the estimation of the cavitating area in Figure 5.7(a), facilitating the ability of the DDMs and HMs to distinguish between similar cases that appear in the dataset.

Figure 5.9 provides the URN spectra for two Meridian propellers in the dataset, operating at different wakefields, for various values of the cavitation index. These spectra provide a small but representative example of the URN measurements on the dataset. As can be observed, the spectra are characterised by some common characteristics. The peaks appearing at low frequencies largely correspond to the tonal components located at the blade passage frequency and its multitudes. At higher frequencies, the part of the spectrum associated with cavitation is visible, characterised by a maximum SPL at the lower end, and another peak at the higher end, after which the pressure levels decay, at an approximately constant decay rate. Depending on the cavitation type, these peaks are typically associated with the noise generated by the pulsation of the TVC, or other phenomena like sheet and bubble cavitation, which tend to dominate a

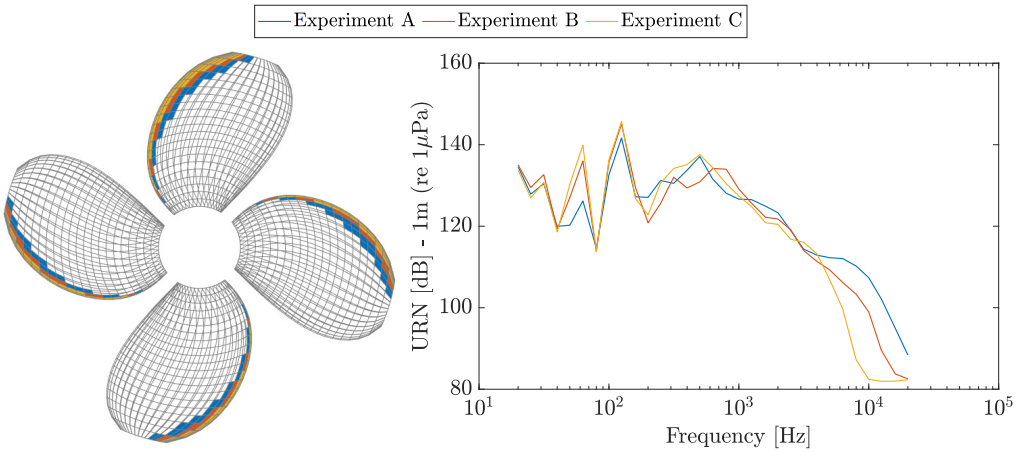

(a) Computed cavitation areas. (b) Recorded URN spectra.

Figure 5.7: Samples of recorded URN spectra and cavitation area computed with BEM for the experiments of Table 5.3.

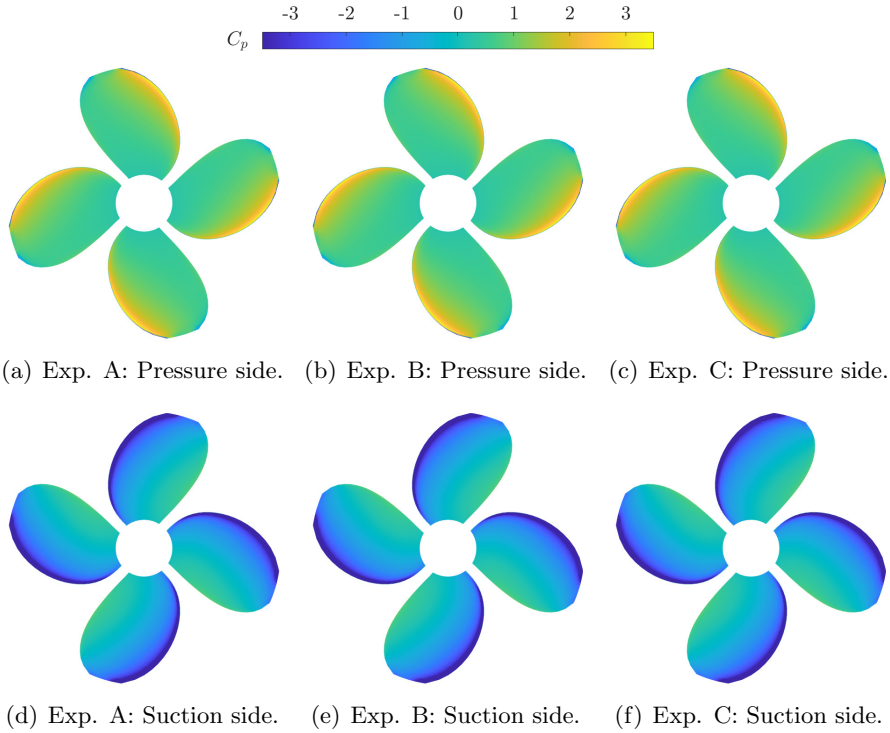

(a) Exp. A: Pressure side. (b) Exp. B: Pressure side. (c) Exp. C: Pressure side.

(d) Exp. A: Suction side. (e) Exp. B: Suction side. (f) Exp. C: Suction side.

Figure 5.8: C_p values computed with BEM for the experiments of Table 5.3.

URN spectrum if present. These phenomena are highly important in studies related to URN from full-scale vessels, as they tend to dominate the URN signature of the vessel [130].

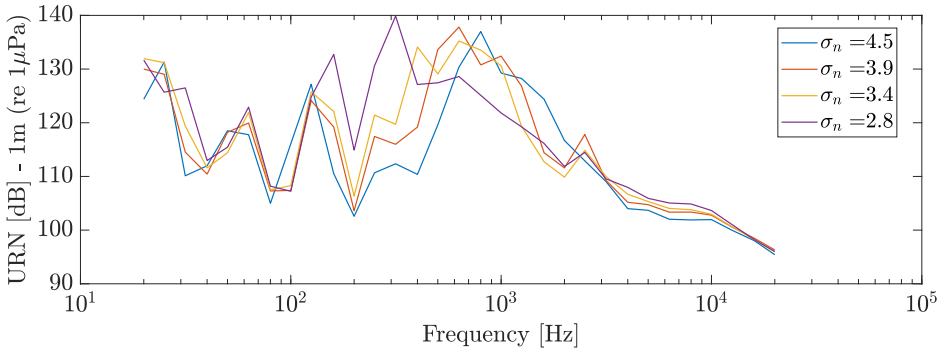

(a) Propeller KCD 129 on wakefield W1.

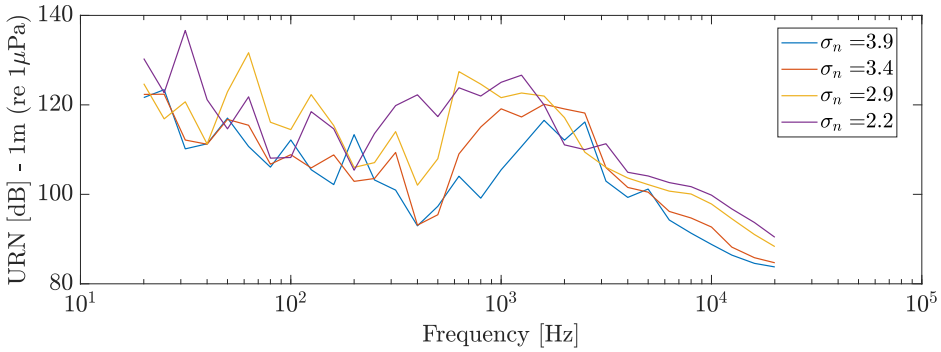

(b) Propeller KCD 191 on wakefield W2.

Figure 5.9: Sample URN spectra recorded for two propellers at different loading conditions.

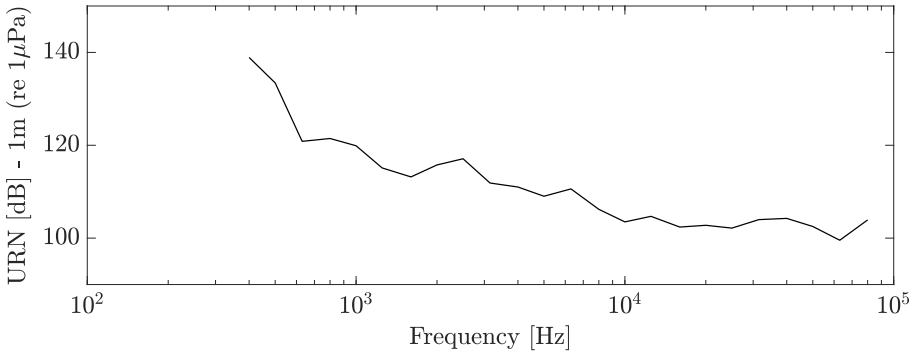

Figure 5.10: Sample URN spectra recorded for the moderately loaded propeller of Figure 5.2.

For what regards the experiments of the propeller model presented in Figure 5.2, the experimental measurements were made available by the cavitation tunnel of the University of Genoa, following the same standard procedure used to process the signals of the Meridian series propellers (pressure time traces converted to 1[m] reference

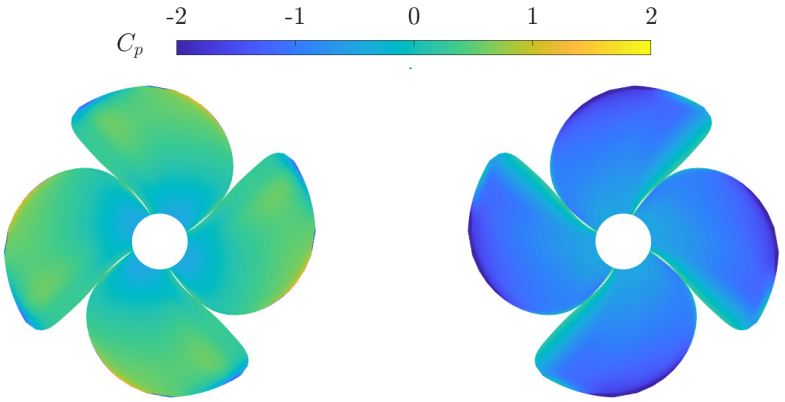

(a) Pressure side. (b) Suction side.

Figure 5.11: C_p values computed with BEM for one time-step of the propeller presented in Figure 5.2.

distance). Usual propeller performance and high-speed visualization of the cavitation process revealed the expected cavitation of the tip vortex and the occurrence of both suction and pressure side sheet cavitation, making this geometry a challenging test case for the models under investigation. Figure 5.10 presents the measured URN spectrum on the investigated operating conditions, and Figure 5.11 provides a sample of the $\boldsymbol{C}_p$ values computed with unsteady non-cavitating BEM simulations for one time-step.

5.5 Test against prior knowledge numerical experiments

As discussed in Section 4.7.2, to further assess the accuracy of the models and demonstrate their applicability and generalisation capabilities, a set of numerical experiments can be conducted, with the aim of evaluating the physical plausibility of the predicted URN spectra. The experiments performed in this work still involve the Meridian propellers and wakefields of Figure 5.3 but at different loading conditions, introduced by varying $\mathtt{n}$ and p_{tunnel}, and listed in Table 5.4.

To better appreciate the cavitating conditions occurring in these experiments, apart from the unsteady non-cavitating BEM simulations that provide the necessary inputs for all the models, unsteady cavitating BEM simulations have also been performed. A visual impression of the cavities formed on the blade surfaces for all experiments

Table 5.4: Numerical experiments conducted to assess the physical plausibility of the model predictions.

Case	Propeller	Wakefield	n [Hz]	p_{tunnel} [mmHg]	J [–]	σ_n [–]
C_1	KCD 191	W3	22.0	300	0.44	3.75
C_2	KCD 191	W2	25.5	100	0.38	3.42
C_3	KCD 129	W3	20.7	80	0.46	5.18
C_4	KCD 192	W3	22.5	0	0.43	4.74
C_5	KCD 74	W3	24.5	0	0.39	4.07

of Table 5.4 is provided in Figure 5.12, at two different time-steps of the simulations. In these figures, the color of the cavity bubble corresponds to the estimated thickness from the cavitating BEM conditions. The range of the thickness values is consistent among all experiments, to facilitate a qualitative visual comparison in terms of both cavitation area and cavitation thickness.

5.6 Summary

This chapter discussed the dataset employed to test the approach proposed in this work. An excess of 430 cavitation tunnel tests has been made available for this purpose. These tests include 6 propellers of the Meridian standard series operating at various inflow conditions on 3 different wakefields, as well as an moderately loaded propeller operating in uniform wakefield. Based on this experimental data, 4 extrapolation scenarios will be conducted to test the prediction capabilities of all models, and assess their strengths and weaknesses. More specifically, all models will be tested in extrapolating on unseen geometries, wakefields, and rotational speeds. These comparisons allow the author to fully assess the performance of all the models, and reveal any potential weaknesses in the proposed approach. Extensive analysis and comparisons between numerical and experimental data for all case studies discussed so far will be carried out in Chapter 6.

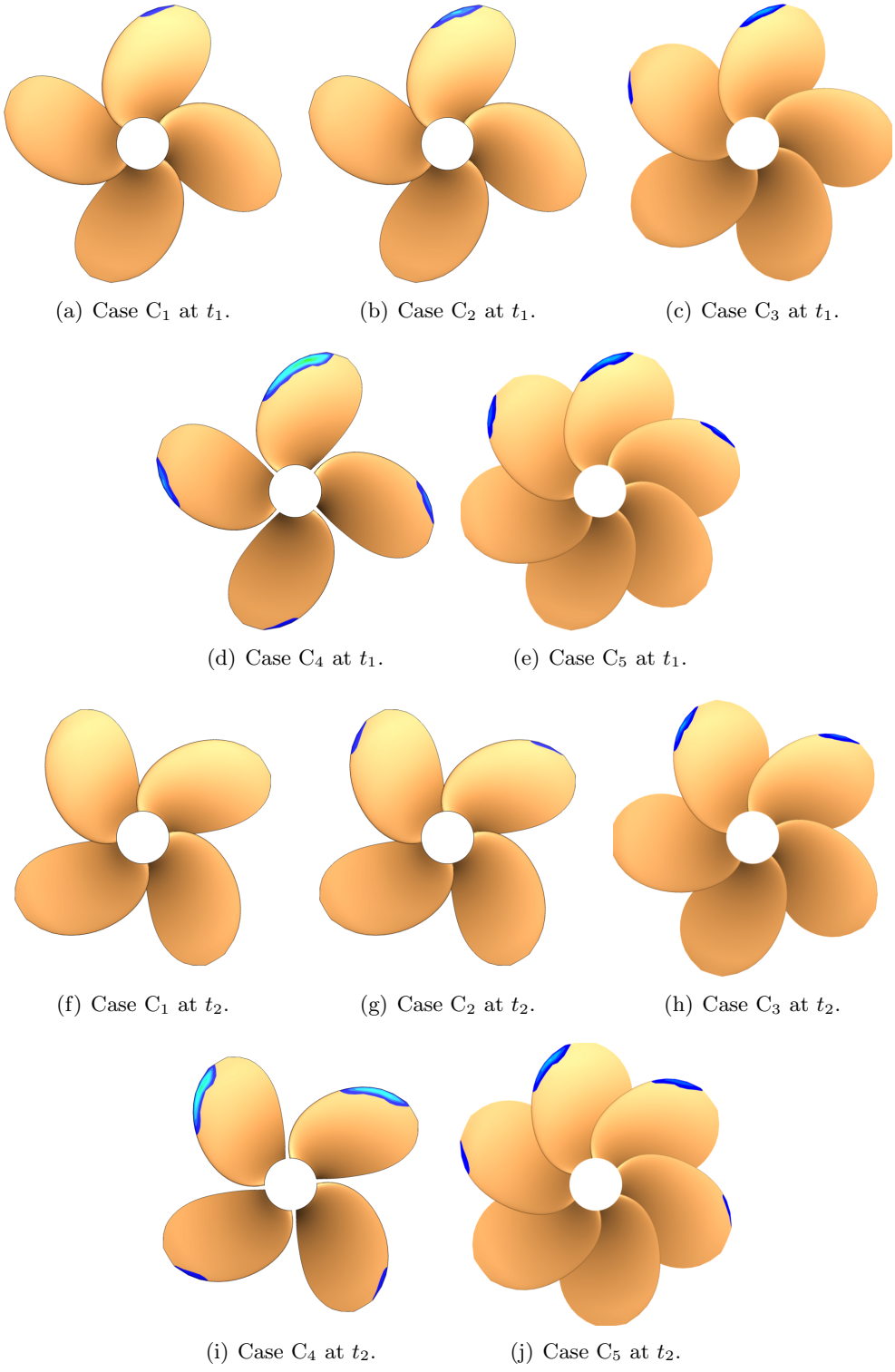

(a) Case C_1 at t_1. (b) Case C_2 at t_1. (c) Case C_3 at t_1.

(d) Case C_4 at t_1. (e) Case C_5 at t_1.

(f) Case C_1 at t_2. (g) Case C_2 at t_2. (h) Case C_3 at t_2.

(i) Case C_4 at t_2. (j) Case C_5 at t_2.

Figure 5.12: Cavitation occurrence computed by cavitating BEM for the case studies of Table 5.4 at two different time-steps. Isocolours indicate the thickness of the cavity.

Chapter 6

Results

Abstract

This chapter provides a detailed analysis and comparison of the model predictions against the experimental results of the datasets presented in Chapter 5. A series of analyses are conducted with the aim of identifying and quantifying the strengths and weaknesses of the proposed approach.

6.1 Introduction

This chapter discusses the performance of the approach presented in Chapter 4 on the dataset of Chapter 5 on the extrapolation scenarios discussed in Section 6.2. In addition, the physical plausibility of the models' predictions are assessed according to Section 5.5. As discussed in Section 4.2.2, the aim of the various models is to predict the measured URN levels at 31 frequencies in 1/3 octave band. Throughout this chapter, their prediction abilities are measured according to the error metrics described in Section 4.6, and average results together with their t-student 95% confidence interval are reported. For the sake of brevity, individual results on every experiment are not provided due to the size of the dataset and the number of numerical experiments performed.

The rest of this chapter is organised as follows. Section 6.2 describes the numerical experiments performed to obtain the results presented in the rest of this chapter, and introduces the extrapolation scenarios conducted in this work. Sections 6.3 - 6.5 report the results of the models on scenarios I - III of Section 6.2. Section 6.6 compares the

performance of the best PM, DDM, and HM on scenarios I - III. Section 6.7 compares the performance of the best PM, DDM, and HM, as identified in Section 6.6, on scenario IV. Section 6.8 discusses the results of the physical plausibility analysis conducted for the DDMs and HMs that was presented in Section 5.5. Section 6.9 discusses the best values of the parameters identified through the calibration process of Section 4.6.3 for the PM. Finally, Section 6.10 summarises this chapter.

6.2 Experimental setting

As stated in Section 4.6.2, to obtain the results discussed in this chapter, the hyperparameters of Table 4.8 have been tested for the MS procedure for every DDM and HM. The Python *scikit-learn* [304] library is utilised for the RF, the Python *PyTorch* [305] library is employed for the ANN, whereas custom *Matlab* [259] implementations have been developed for the KRLS and ELM algorithms. The experiments were performed on a machine equipped with two Intel Xeon Silver 4216, 128 GB of RAM, and 512 GB SSD running Windows Server 2019.

Four scenarios are considered to test the extrapolation capabilities of the proposed models, and they are listed in Table 6.1. They differ only in the way $\mathcal{D}_n$ is split on $\mathcal{L}_l^r \cup \mathcal{V}_v^r$ and $\mathcal{T}_t^r$ according to the principles of Section 4.6:

- Scenario I - LOGO: In this scenario the models have been trained with all data except experiments referring to a particular propeller geometry, which are used to assess the model's predictions.
- Scenario II - LOWO: In this scenario the models have been trained with all data except the experiments referring to a particular wakefield, which are used to assess the model's predictions.
- Scenario III - LORSO: In this scenario the models have been trained with all data except the experiments referring to a particular rotational speed, which are used to assess the model's predictions.
- Scenario IV: in this scenario the models have been trained on all the data, apart from the experiment referring to the MLP of Figure 5.2, with the aim to predict the URN spectrum of Figure 5.10. This scenario allows the author to test the capability of the

Table 6.1: Extrapolation scenarios and corresponding $\mathcal{T}_t^r$ sets.

Scenario		Test set
I	Leave One Geometry Out (LOGO)	$\mathcal{T}_t^r$ refers to experiments of a particular geometry.
II	Leave One Wakefield Out (LOWO)	$\mathcal{T}_t^r$ refers to experiments of a particular wakefield.
III	Leave One Rotational Speed Out (LORSO)	$\mathcal{T}_t^r$ refers to experiments of a particular speed.
IV	Simultaneous extrapolation	$\mathcal{T}_t^r$ corresponds to the MLP of Figure 5.2, with the URN spectrum of Figure 5.10.

models to extrapolate in conditions for which the propeller geometry, wakefield, and operating conditions vary simultaneously. Strictly for this scenario, all models have been learned on all data, apart from the data corresponding to the MLP.

Based on the different scenarios, $\mathcal{D}_n$ is split in a test set $\mathcal{T}_t^r$ and the learning and validation sets $\mathcal{L}_l^r \cup \mathcal{V}_v^r$. $\mathcal{T}_t^r$ is used to assess the performance of the models on unseen data (i.e. the EE phase), as measured with the MAE, MAPE, and PPMCC. The average model's performance can be evaluated when this process is repeated multiple times, by swapping (based on the scenario) different propellers, wakefields, etc. between $\mathcal{T}_t^r$ and $\mathcal{L}_l^r \cup \mathcal{V}_v^r$.

For what regards the MS phase, $\mathcal{L}_l^r \cup \mathcal{V}_v^r$ is further split into $\mathcal{L}_l^r$ and $\mathcal{V}_v^r$. The models are trained on $\mathcal{L}_l^r$ with the hyperparameter sets of Table 4.8, and their performance is measured on $\mathcal{V}_v^r$ according to the MAE. This procedure is repeated multiple times, and the hyperparameter configuration with the lowest average MAE is selected. Finally, the model with the best hyperparameter configuration is retrained on $\mathcal{L}_l^r \cup \mathcal{V}_v^r$ and is used for testing purposes, according to the previous paragraph.

For the sake of clarity, Figure 6.1 provides a visual impression of the intrinsic hierarchy of the dataset and the first three scenarios, in which data not seen by the models during the learning phase is highlighted. Furthermore, when results are reported in Sections 6.3 - 6.5, they are always accompanied by the corresponding $\mathcal{T}_t^r$.

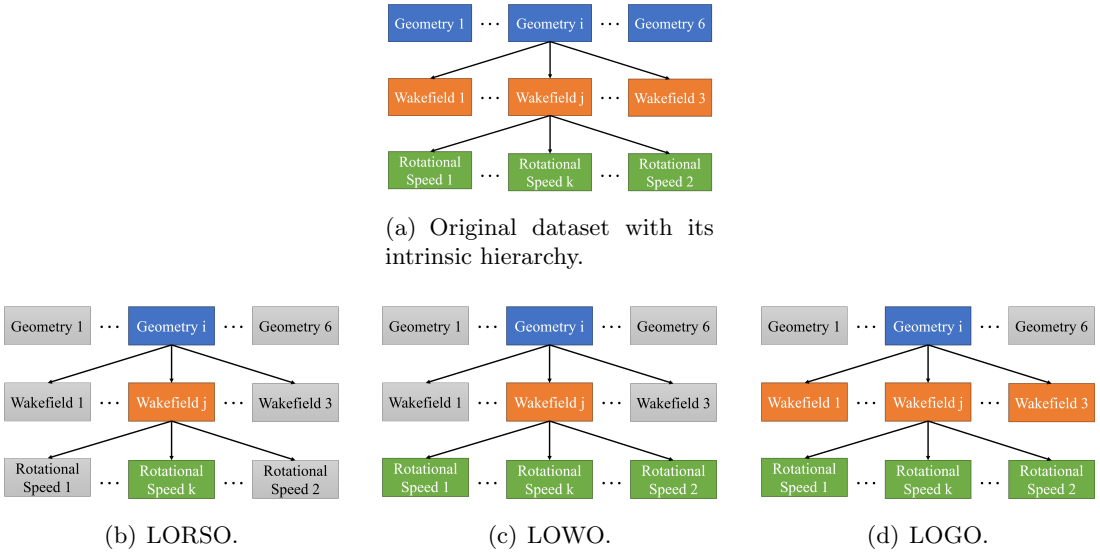

(a) Original dataset with its intrinsic hierarchy.

(b) LORSO.

(c) LOWO.

(d) LOGO.

Figure 6.1: Visual representation of the intrinsic hierarchy of the dataset and the three extrapolating scenarios. Data withheld during learning, i.e. strictly used for testing purposes, is colored.

6.3 Results of Scenario I

As discussed in Section 6.2, this is the LOGO scenario, in which the models have been trained with all data except the experiments referring to a particular propeller geometry. Each $\mathcal{T}_t^r$ consists of all experiments conducted with one of the 6 propellers of Section 5.2. The most important findings for each model type (PMs, DDMs, HMs) are extensively discussed in Sections 6.3.1 - Section 6.3.3. Specifically, Section 6.3.1 discusses the results of the PMs, Section 6.3.2 presents the results of the DDMs, and Section 6.3.3 discusses the results of the HMs. Finally, Section 6.3.4 summarises the performance of all models for this scenario.

6.3.1 Physics-based model results

Table 6.2 reports the various error metrics on this scenario for the PM calibrated with PSO according to Section 4.6.3, and the PM with the parameter values reported in Table 4.9 as suggested in [5, 82].

It is observed that the accuracy of both PMs is fairly consistent for all metrics and across all propellers, with no significant variance. On average, the PSO-calibrated

Table 6.2: PM performance measured with the MAE, MAPE and PPMCC on Scenario I (average value and 95% confidence interval).

	Calibrated Parameters			Initial Parameters		
Propeller	MAE	MAPE	PPMCC	MAE	MAPE	PPMCC
KCD 65	7.99 ± 1.10	7.70 ± 1.04	0.80 ± 0.12	18.53 ± 2.34	17.01 ± 2.33	0.41 ± 0.17
KCD 74	7.48 ± 1.02	7.10 ± 0.96	0.85 ± 0.08	19.71 ± 3.11	19.14 ± 3.41	0.28 ± 0.24
KCD 129	7.70 ± 1.04	7.28 ± 0.97	0.84 ± 0.08	19.27 ± 3.06	18.20 ± 3.52	0.32 ± 0.22
KCD 191	7.67 ± 1.02	7.14 ± 0.94	0.82 ± 0.11	19.24 ± 3.01	18.19 ± 3.58	0.34 ± 0.21
KCD 192	7.82 ± 1.04	7.31 ± 0.96	0.80 ± 0.10	18.83 ± 2.95	17.99 ± 2.36	0.31 ± 0.19
KCD 193	7.53 ± 1.02	7.00 ± 0.95	0.83 ± 0.09	19.35 ± 2.75	17.76 ± 3.19	0.30 ± 0.26
all	7.70 ± 1.03	7.20 ± 0.97	0.82 ± 0.10	19.35 ± 2.98	18.03 ± 3.06	0.33 ± 0.22

PM provides predictions of sufficient quality, with an overall MAE of 7.70 ± 1.03[dB], a MAPE of 7.20 ± 0.97[%], and PPMCC equal to 0.82 ± 0.10[–]. On the other hand, when the parameter values of [5, 82] are employed, significantly higher errors are observed, approximately equal to 19.35 ± 2.98[dB] or 18.03 ± 3.06[%] with relatively weak linear associations between the measured and predicted URN spectra, as shown by the low values of PPMCC. Overall, these results suggest that with a proper calibration process, the PM by itself can achieve satisfactory accuracy, comparable with some of the more sophisticated CFD-based models discussed in Section 3.2, which is a surprising result.

6.3.2 Data-driven models results

Table 6.3 reports the results obtained with the DDMs of Chapter D on this scenario. It is observed that, compared to the PMs discussed in Section 6.3.1, results of higher accuracy are obtained regardless of the DDM considered.

For what regards the ANN, overall errors of 5.35 ± 1.72[dB], 5.09 ± 1.68[%], and 0.85 ± 0.07[–] are reported for the MAE, MAPE and PPMCC, respectively. Although the results are impressive, these errors are, on average, the highest ones amongst all DDMs. The ELM commits slightly lower errors of 5.26 ± 0.88[dB], 4.97 ± 0.87[%], and 0.87 ± 0.06[–] for the MAE, MAPE, and PPMCC, respectively. Slightly performance is observed for the RF, with errors of 4.75 ± 0.85[dB], 4.57 ± 0.82[%], and 0.87 ± 0.06[–] for the MAE, MAPE, and PPMCC, respectively. Even more impressive is the performance

of KRLS, with average errors equal to 4.48 ± 0.69[dB] for the MAE, 4.12 ± 0.66[%] for the MAPE, and 0.88 ± 0.06[–] for the PPMCC. It should be noted that, although the average errors of KRLS are seemingly lower, the 95[%] confidence intervals show partial overlap between the rest of the DDMs, which does not allow the author to draw statistically significant conclusions regarding the choice of a specific DDM.

Furthermore, considerable deviations are observed on the average performance with respect to the various propellers. Whereas the error variance of each DDM within each propeller is high enough not to allow statistically significant conclusions to be drawn, these findings warrant some attention. More in detail, the smallest deviations are observed for the ANN, with a maximum relative performance difference of 12[%], occurring for the predictions on the propellers KCD 65 with a MAE of 5.62 ± 1.70[dB], and KCD 191 with a MAE of 5.17 ± 1.72[dB]. Differences as large as 40% are observed for the ELM, with the lowest and highest errors occurring for propellers KCD 192, and KCD 129, respectively. For the RF and KRLS, these deviations are equal to 27[%] and 24[%], respectively. Overall, these results indicate that the URN spectra can be predicted with satisfactory accuracy by all DDMs for this scenario, and provide a first validation that the feature engineering process discussed in Section 4.4 is effective.

6.3.3 Hybrid model results

Table 6.4 reports the results obtained with the HMs for this scenario. Overall, it is observed that the relative performance of the HMs closely follows the performance of the DDMs reported in Section 6.3.2, with the hybrid ANN (H-ANN) committing the highest average errors among all HMs, closely followed by the H-ELM, H-RF, and H-KRLS, which is, on average, the most accurate HM.

More specifically, the hybrid ANN (H-ANN) commits average errors of 4.48 ± 1.53[dB], 4.16 ± 1.25[%], and 0.89 ± 0.04[–] for the MAE, MAPE, and PPMCC, respectively. In contrast to the PMs or DDMs, the HMs show higher error variance among different propellers. For instance, considering KCD 193, the H-ANN commits a MAE of 4.04 ± 1.46[dB], whereas for propeller KCD 65 the MAE equals 5.15 ± 1.67[dB], roughly a 20[%] difference. This could be explained by the relative performance of the

Table 6.3: DDMs performance measured with the MAE, MAPE, and PPMCC on Scenario I (average value and 95% confidence interval).

Metric	Propeller	ANN	KRLS	ELM	RF
MAE [dB]	KCD 65	5.62 ± 1.70	4.58 ± 0.69	4.93 ± 0.78	4.87 ± 0.81
	KCD 74	4.91 ± 1.63	4.66 ± 0.66	5.23 ± 0.81	4.89 ± 0.92
	KCD 129	5.22 ± 1.81	5.16 ± 0.81	6.98 ± 1.24	5.58 ± 0.92
	KCD 191	5.17 ± 1.72	4.62 ± 0.68	6.19 ± 1.04	4.98 ± 0.82
	KCD 192	5.71 ± 1.83	3.92 ± 0.68	4.05 ± 0.75	4.12 ± 0.78
	KCD 193	5.48 ± 1.64	3.93 ± 0.60	4.19 ± 0.63	4.04 ± 0.87
	all	5.35 ± 1.72	$\mathbf{4.48 \pm 0.69}$	5.26 ± 0.88	4.75 ± 0.85
MAPE [%]	KCD 65	5.35 ± 1.93	4.34 ± 0.67	4.73 ± 0.71	4.76 ± 0.78
	KCD 74	4.78 ± 1.59	4.22 ± 0.62	4.79 ± 0.71	4.69 ± 0.89
	KCD 129	5.06 ± 1.83	4.82 ± 0.72	6.52 ± 1.17	5.38 ± 0.88
	KCD 191	5.01 ± 1.71	4.21 ± 0.67	5.89 ± 1.13	4.77 ± 0.78
	KCD 192	5.35 ± 1.61	3.59 ± 0.69	3.99 ± 0.81	3.96 ± 0.73
	KCD 193	5.01 ± 1.39	3.52 ± 0.57	3.87 ± 0.71	3.84 ± 0.85
	all	5.09 ± 1.68	$\mathbf{4.12 \pm 0.66}$	4.97 ± 0.87	4.57 ± 0.82
PPMCC [–]	KCD 65	0.84 ± 0.08	0.87 ± 0.05	0.87 ± 0.05	0.87 ± 0.05
	KCD 74	0.87 ± 0.06	0.88 ± 0.05	0.84 ± 0.05	0.89 ± 0.05
	KCD 129	0.86 ± 0.08	0.87 ± 0.06	0.85 ± 0.06	0.85 ± 0.07
	KCD 191	0.84 ± 0.07	0.87 ± 0.05	0.87 ± 0.05	0.87 ± 0.06
	KCD 192	0.85 ± 0.06	0.88 ± 0.05	0.90 ± 0.05	0.89 ± 0.05
	KCD 193	0.86 ± 0.07	0.90 ± 0.07	0.87 ± 0.07	0.87 ± 0.08
	all	0.85 ± 0.07	$\mathbf{0.88 \pm 0.06}$	0.87 ± 0.06	0.87 ± 0.06

PM or the corresponding DDM for the different propellers. As reported in Table 6.2, the PM commits a MAE of 7.53 ± 1.02[dB] for KCD 193, whereas the same metric is higher and equal to 7.99 ± 1.00[dB] for KCD 65, which corresponds to a difference of approximately 6[%] The same behavior is also observed for the ANN, according to the discussion on Section 6.3.2. Although these differences are smaller for the PM and the DDMs, they appear to be amplified for the HMs, although the high error variance within each propeller does not render these differences statistically significant. The H-ELM commits errors of 4.03 ± 0.61[dB], 3.82 ± 0.59[%], and 0.91 ± 0.03[–] for the MAE, MAPE, and PPMCC, respectively. Once again, the performance difference between the various propellers is noticeable. For instance, the MAE for KCD 192 is equal to 2.97 ± 0.54[dB], whereas the same error for KCD 129 amounts to 5.42 ± 0.83, roughly 45[%] higher. H-

Table 6.4: HMs performance measured with the MAE, MAPE, and PPMCC on Scenario I (average value and 95% confidence interval).

Metric	Propeller	H-ANN	H-KRLS	H-ELM	H-RF
MAE [dB]	KCD 65	5.15 ± 1.67	4.04 ± 0.48	4.35 ± 0.54	4.30 ± 0.56
	KCD 74	4.04 ± 1.57	3.48 ± 0.44	3.91 ± 0.54	3.65 ± 0.61
	KCD 129	4.64 ± 1.46	4.01 ± 0.54	5.42 ± 0.83	4.34 ± 0.61
	KCD 191	4.98 ± 1.55	3.29 ± 0.48	4.41 ± 0.73	3.55 ± 0.58
	KCD 192	4.05 ± 1.49	2.87 ± 0.49	2.97 ± 0.54	3.02 ± 0.56
	KCD 193	4.04 ± 1.46	2.92 ± 0.44	3.11 ± 0.46	3.00 ± 0.64
	all	4.48 ± 1.53	$\mathbf{3.44 \pm 0.48}$	4.03 ± 0.61	3.64 ± 0.59
MAPE [%]	KCD 65	4.72 ± 1.23	3.83 ± 0.37	4.12 ± 0.53	4.07 ± 0.55
	KCD 74	3.86 ± 1.25	3.15 ± 0.31	3.70 ± 0.52	3.46 ± 0.60
	KCD 129	4.39 ± 1.21	3.75 ± 0.43	5.14 ± 0.80	4.11 ± 0.60
	KCD 191	4.46 ± 1.31	3.00 ± 0.37	4.18 ± 0.71	3.36 ± 0.56
	KCD 192	3.76 ± 1.27	2.63 ± 0.38	2.81 ± 0.52	2.86 ± 0.55
	KCD 193	3.78 ± 1.25	2.62 ± 0.32	2.95 ± 0.45	2.84 ± 0.62
	all	4.16 ± 1.25	$\mathbf{3.16 \pm 0.36}$	3.82 ± 0.59	3.45 ± 0.58
PPMCC [–]	KCD 65	0.85 ± 0.05	0.91 ± 0.03	0.91 ± 0.03	0.91 ± 0.03
	KCD 74	0.92 ± 0.04	0.91 ± 0.03	0.87 ± 0.03	0.92 ± 0.03
	KCD 129	0.86 ± 0.03	0.91 ± 0.03	0.89 ± 0.03	0.89 ± 0.04
	KCD 191	0.85 ± 0.05	0.92 ± 0.02	0.92 ± 0.02	0.92 ± 0.02
	KCD 192	0.93 ± 0.03	0.93 ± 0.02	0.95 ± 0.02	0.94 ± 0.02
	KCD 193	0.94 ± 0.04	0.93 ± 0.03	0.90 ± 0.03	0.90 ± 0.03
	all	0.89 ± 0.04	$\mathbf{0.92 \pm 0.03}$	0.91 ± 0.03	0.91 ± 0.03

RF commits errors of 3.64 ± 0.59[dB], 3.45 ± 0.58[%], and 0.91 ± 0.03[–], for the MAE, MAPE, and PPMCC, respectively. A maximum relative performance difference of approximately 30[%] is observed among the various propellers, with the highest errors occurring for KCD 129, and the lowest for KCD 193. For what regards H-KRLS, it commits the lowest average errors, with values of 3.44 ± 0.48[dB], 3.16 ± 0.36[%], and 0.92 ± 0.03[–] for the MAE, MAPE, and PPMCC, respectively. Furthermore, it is also fairly robust, with an average relative performance difference of 28[%] between different propellers. Nevertheless, similar to DDMs, the overlap of the confidence intervals does not allow the author to draw statistically significant conclusions regarding the choice of the learning algorithm.

6.3.4 Results summary

To facilitate comparison between all models discussed in this work, Table 6.5 gathers their performance on this scenario as measured with the MAE, MAPE, and PPMCC.

6.4 Results of Scenario II

According to Section 6.2, this is the LOWO scenario, in which the models have been trained with all data except the experiments referring to a particular wakefield. In this scenario, each $\mathcal{T}_t^r$ consists of all experiments conducted with one of the 3 wakefields of Section 5.3. Section 6.4.1 discusses the results of the PMs, Section 6.4.2 presents the results of the DDMs, and Section 6.4.3 discusses the results of the HMs. Finally, Section 6.4.4 summarises the performance of all models for this scenario.

6.4.1 Physics-based model results

Table 6.6 reports the various error metrics on this scenario for both the PSO-calibrated PM, and the PM with the parameter values reported in Table 4.9. Similar to Section 6.3.1, the accuracy of the PMs is fairly consistent for all metrics and across all wakefields, with no significant variance. It can be observed that the calibrated PM once again provides satisfactory results, with a MAE of 8.75 ± 1.35[dB], a MAPE of 8.41 ± 1.35[%], and PPMCC equal to 0.79 ± 0.11[–]. Utilising the parameter values of Table 4.9 has a significant effect in performance, with errors increasing by approximately 200[%]. These results also confirm the findings discussed in Section 6.3.1, namely that the calibration process can drastically improve the performance of the PM on this dataset. It should also be noted that for both scenarios I and II, the parameter values arising from the calibration process are largely similar, regardless of which propeller or wakefield appears in $\mathcal{T}_t^r$, which partially explains the similarity of the results. For this reason, the parameter values are further discussed in the dedicated Section 6.9.

Table 6.5: PM, DDMs, and HMs performance measured with the MAE, MAPE, and PPMCC on Scenario I.

Metric	Propeller	PM	PM$^{\diamond}$	ANN	KRLS	ELM	RF	H-ANN	H-KRLS	H-ELM	H-RF
MAE [dB]	KCD 65	18.5 ± 2.3	8.0 ± 1.1	5.6 ± 1.7	4.6 ± 0.7	4.9 ± 0.8	4.9 ± 0.8	5.2 ± 1.7	4.0 ± 0.5	4.3 ± 0.5	4.3 ± 0.6
	KCD 74	19.7 ± 3.1	7.5 ± 1.0	4.9 ± 1.6	4.7 ± 0.7	5.2 ± 0.8	4.9 ± 0.9	4.0 ± 1.6	3.5 ± 0.4	3.9 ± 0.5	3.7 ± 0.6
	KCD 129	19.3 ± 3.1	7.7 ± 1.0	5.2 ± 1.8	5.2 ± 0.8	7.0 ± 1.2	5.6 ± 0.9	4.6 ± 1.5	4.0 ± 0.5	5.4 ± 0.8	4.3 ± 0.6
	KCD 191	19.2 ± 3.0	7.7 ± 1.0	5.2 ± 1.7	4.6 ± 0.7	6.2 ± 1.0	5.0 ± 0.8	5.0 ± 1.6	3.3 ± 0.5	4.4 ± 0.7	3.5 ± 0.6
	KCD 192	18.8 ± 2.9	7.8 ± 1.0	5.7 ± 1.8	3.9 ± 0.7	4.1 ± 0.8	4.1 ± 0.8	4.1 ± 1.5	2.9 ± 0.5	3.0 ± 0.5	3.0 ± 0.6
	KCD 193	19.3 ± 2.7	7.5 ± 1.0	5.5 ± 1.6	3.9 ± 0.6	4.2 ± 0.6	4.0 ± 0.9	4.0 ± 1.5	2.9 ± 0.4	3.1 ± 0.5	3.0 ± 0.6
	all	19.3 ± 2.9	7.7 ± 1.0	5.4 ± 1.7	4.5 ± 0.7	5.3 ± 0.9	4.7 ± 0.9	4.5 ± 1.5	$\mathbf{3.4 \pm 0.5}$	4.0 ± 0.6	3.6 ± 0.6
MAPE [%]	KCD 65	17.0 ± 2.3	7.7 ± 1.0	5.4 ± 1.9	4.3 ± 0.7	4.7 ± 0.7	4.8 ± 0.8	4.7 ± 1.2	3.8 ± 0.4	4.1 ± 0.5	4.1 ± 0.5
	KCD 74	19.1 ± 3.4	7.1 ± 1.0	4.8 ± 1.6	4.2 ± 0.6	4.8 ± 0.7	4.7 ± 0.9	3.9 ± 1.3	3.2 ± 0.3	3.7 ± 0.5	3.5 ± 0.6
	KCD 129	18.2 ± 3.5	7.3 ± 0.9	5.1 ± 1.8	4.8 ± 0.7	6.5 ± 1.2	5.4 ± 0.9	4.4 ± 1.2	3.7 ± 0.4	5.1 ± 0.8	4.1 ± 0.6
	KCD 191	18.2 ± 3.6	7.1 ± 0.9	5.0 ± 1.7	4.2 ± 0.7	5.9 ± 1.1	4.8 ± 0.8	4.5 ± 1.3	3.0 ± 0.4	4.2 ± 0.7	3.4 ± 0.6
	KCD 192	18.0 ± 2.4	7.3 ± 1.0	5.4 ± 1.6	3.6 ± 0.7	4.0 ± 0.8	4 ± 0.7	3.8 ± 1.3	2.6 ± 0.4	2.8 ± 0.5	2.9 ± 0.5
	KCD 193	17.8 ± 3.2	7.0 ± 0.9	5.0 ± 1.4	3.5 ± 0.6	3.9 ± 0.7	3.8 ± 0.9	3.8 ± 1.3	2.6 ± 0.3	3.0 ± 0.4	2.8 ± 0.6
	all	18.0 ± 3.1	7.2 ± 1.0	5.1 ± 1.7	4.1 ± 0.7	5.0 ± 0.9	4.6 ± 0.8	4.2 ± 1.3	$\mathbf{3.2 \pm 0.4}$	3.8 ± 0.6	3.5 ± 0.6
PPMCC $\times 10$[–]	KCD 65	4.1 ± 1.7	8.0 ± 1.2	8.4 ± 0.8	8.7 ± 0.5	8.7 ± 0.5	8.7 ± 0.5	8.5 ± 0.5	9.1 ± 0.3	9.1 ± 0.3	9.1 ± 0.3
	KCD 74	2.8 ± 2.4	8.5 ± 0.8	8.7 ± 0.6	8.8 ± 0.5	8.4 ± 0.5	8.9 ± 0.5	9.2 ± 0.4	9.1 ± 0.3	8.7 ± 0.3	9.2 ± 0.3
	KCD 129	3.2 ± 2.2	8.4 ± 0.8	8.6 ± 0.8	8.7 ± 0.6	8.5 ± 0.6	8.5 ± 0.7	8.6 ± 0.3	9.1 ± 0.3	8.9 ± 0.3	8.9 ± 0.4
	KCD 191	3.4 ± 2.1	8.2 ± 1.1	8.4 ± 0.7	8.8 ± 0.5	8.7 ± 0.5	8.7 ± 0.6	8.5 ± 0.5	9.2 ± 0.2	9.2 ± 0.2	9.2 ± 0.2
	KCD 192	3.1 ± 1.9	8.0 ± 1.0	8.5 ± 0.6	9.0 ± 0.5	9.0 ± 0.5	8.9 ± 0.5	9.3 ± 0.3	9.3 ± 0.2	9.5 ± 0.2	9.4 ± 0.2
	KCD 193	3.0 ± 2.6	8.3 ± 0.9	8.6 ± 0.7	8.8 ± 0.7	8.7 ± 0.7	8.7 ± 0.8	9.4 ± 0.4	9.3 ± 0.3	9.0 ± 0.3	9.0 ± 0.3
	all	3.3 ± 2.2	8.2 ± 1.0	8.5 ± 0.8	8.8 ± 0.5	8.7 ± 0.6	8.7 ± 0.7	8.9 ± 0.4	$\mathbf{9.2 \pm 0.3}$	9.1 ± 0.3	9.1 ± 0.3

Table 6.6: PMs performance measured with the MAE, MAPE and PPMCC on Scenario II (average value and 95% confidence interval).

	Calibrated Parameters			Initial Parameters		
Wake	MAE	MAPE	PPMCC	MAE	MAPE	PPMCC
W1	8.91 ± 1.31	8.53 ± 1.41	0.78 ± 0.12	19.32 ± 2.34	18.09 ± 3.11	0.34 ± 0.27
W2	8.61 ± 1.30	8.24 ± 1.33	0.80 ± 0.11	19.24 ± 3.11	18.05 ± 3.56	0.33 ± 0.27
W3	8.74 ± 1.35	8.47 ± 1.38	0.81 ± 0.14	19.37 ± 2.96	17.49 ± 2.85	0.30 ± 0.28
all	8.75 ± 1.35	8.41 ± 1.35	0.79 ± 0.11	19.35 ± 2.98	18.03 ± 3.06	0.33 ± 0.22

6.4.2 Data-driven models results

Table 6.7 reports the results obtained with the DDMs of Chapter D for this scenario. Compared to the PMs discussed in Section 6.4.1, a higher accuracy is obtained with the DDMs, regardless of the wakefield considered. Furthermore, the conclusions that can be drawn in this scenario are similar to Section 6.3.2 for scenario I.

The ANN commits the highest average errors among all DDMs, with a MAE equal to 7.28 ± 1.83[dB], a MAPE of 6.83 ± 1.65[%], and a PPMCC equal to 0.81 ± 0.12[–]. The ELM commits errors of 6.41 ± 1.59[dB], 6.29 ± 1.49[%], and 0.84 ± 0.08[–] for the MAE, MAPE, and PPMCC, respectively, with a considerable decrease in variance with respect to the ANN. Nevertheless, the 95[%] confidence intervals show partial overlap between the two models, not allowing the author to draw statistically significant conclusions regarding the relative performance of these DDMs. Similar performance is observed for the RF, with errors of 5.99 ± 1.47[dB], 5.64 ± 1.34[%], and 0.85 ± 0.08[–] for the MAE, MAPE, and PPMCC, respectively. Similar to scenario I, KRLS is the most accurate DDM, committing errors of 5.14 ± 1.37[dB], 4.79 ± 1.29[%], and 0.86 ± 0.07[–] for the MAE, MAPE, and PPMCC, respectively.

All DDMs exhibit similar performance deviations among the different wakefields. With the exception of the ELM, all DDMs commit the lowest errors on W2. This can be explained by the selection of the wakefields made by [7] and discussed in Section 5.3: W2 corresponds to the wakefield of mild severity, and can be considered as an interpolation between W1 and W3, which justifies the small errors when it appears on $\mathcal{T}_t^r$. On the other hand, when considering wakefields W1 or W3, a relative performance difference

Table 6.7: DDMs performance measured with the MAE, MAPE, and PPMCC on Scenario II (average value and 95% confidence interval).

Metric	Wake	ANN	KRLS	ELM	RF
MAE [dB]	W1	7.38 ± 1.81	5.91 ± 1.35	7.02 ± 1.31	6.16 ± 1.45
	W2	6.31 ± 1.75	4.59 ± 1.36	6.30 ± 2.03	5.78 ± 1.47
	W3	8.14 ± 1.95	4.92 ± 1.41	5.92 ± 1.43	6.04 ± 1.48
	all	7.28 ± 1.83	$\mathbf{5.14 \pm 1.37}$	6.41 ± 1.59	5.99 ± 1.47
MAPE [%]	W1	6.71 ± 1.59	5.49 ± 1.22	6.85 ± 1.20	5.86 ± 1.32
	W2	5.83 ± 1.54	4.28 ± 1.28	6.16 ± 1.88	5.38 ± 1.35
	W3	7.94 ± 1.81	4.61 ± 1.36	5.86 ± 1.39	5.69 ± 1.36
	all	6.83 ± 1.65	$\mathbf{4.79 \pm 1.29}$	6.29 ± 1.49	5.64 ± 1.34
PPMCC [–]	W1	0.82 ± 0.12	0.85 ± 0.07	0.81 ± 0.08	0.83 ± 0.08
	W2	0.81 ± 0.10	0.87 ± 0.06	0.87 ± 0.07	0.86 ± 0.07
	W3	0.80 ± 0.13	0.86 ± 0.07	0.85 ± 0.08	0.85 ± 0.08
	all	0.81 ± 0.12	$\mathbf{0.86 \pm 0.07}$	0.84 ± 0.08	0.85 ± 0.08

of approximately 23[%] is observed for the ANN, and 22[%] for KRLS. The differences between different wakefields are smaller for the ELM, with only 15[%] difference being observed between wakefields W1 and W3, whereas a minimal difference of only 5[%] is present for the RF for the same wakefields. Similar to the previous scenario, the results indicate that the URN spectra can be predicted with satisfactory accuracy from all DDMs.

6.4.3 Hybrid model results

Table 6.8 reports the results obtained with the HMs for this scenario. Once again, the 95[%] confidence intervals do not allow the author to draw statistically significant conclusions with respect to the choice of the best HM.

Starting with the H-ANN that commits the highest average errors, MAE of 5.17 ± 2.40[dB] is observed, MAPE equal to 4.78 ± 2.41[%], and PPMCC of 0.89 ± 0.05[%]. The H-RF follows the H-ANN with errors of 4.75 ± 0.99[dB], 4.41 ± 0.89[%], and 0.90 ± 0.03[%] measured with the MAE, MAPE, and PPMCC, respectively. For the H-ELM, the same errors correspond to 4.74 ± 1.07[dB], 4.40 ± 0.97[%], and 0.89 ± 0.03[–]. Finally, H-KRLS is once again the most accurate HM on average, with errors of 4.06 ± 0.93[dB],

Table 6.8: HMs performance measured with the MAE, MAPE, and PPMCC on Scenario II (average value and 95% confidence interval).

Metric	Wake	H-ANN	H-KRLS	H-ELM	H-RF
MAE [dB]	W1	5.78 ± 2.49	4.45 ± 0.91	5.29 ± 0.88	4.64 ± 0.98
	W2	3.74 ± 2.20	3.72 ± 0.92	4.11 ± 1.37	4.68 ± 0.99
	W3	5.99 ± 2.50	4.01 ± 0.95	4.83 ± 0.96	4.92 ± 1.00
	all	5.17 ± 2.40	$\mathbf{4.06 \pm 0.93}$	4.74 ± 1.07	4.75 ± 0.99
MAPE [%]	W1	5.32 ± 2.40	4.13 ± 0.90	4.91 ± 0.80	4.31 ± 0.88
	W2	3.38 ± 2.36	3.46 ± 0.88	3.82 ± 1.24	4.35 ± 0.90
	W3	5.64 ± 2.48	3.73 ± 1.35	4.48 ± 0.87	4.57 ± 0.90
	all	4.78 ± 2.41	$\mathbf{3.77 \pm 1.04}$	4.40 ± 0.97	4.41 ± 0.89
PPMCC [–]	W1	0.87 ± 0.05	0.90 ± 0.03	0.86 ± 0.03	0.88 ± 0.03
	W2	0.93 ± 0.04	0.92 ± 0.03	0.92 ± 0.04	0.91 ± 0.04
	W3	0.88 ± 0.05	0.91 ± 0.03	0.90 ± 0.03	0.90 ± 0.03
	all	0.89 ± 0.05	$\mathbf{0.91 \pm 0.03}$	0.89 ± 0.03	0.90 ± 0.03

3.77 ± 1.04[%], and 0.91 ± 0.03 for the MAE, MAPE, and PPMCC, respectively.

Furthermore, the relative performance difference of each HM with respect to different wakefields is similar to the one observed in Section 6.3.3: Variance as high as 37[%] is observed for the H-ANN between W2 and W3, 22[%] for the H-ELM between W1 and W2, 16[%] for the H-KRLS, and only 6[%] for the H-RF. These results closely follow the differences observed with the DDMs according to the discussion of Section 6.4.2. Finally, it should also be mentioned that the overlap of the confidence intervals does not allow the author to draw statistically significant conclusions regarding the choice of the learning algorithm.

6.4.4 Results summary

To facilitate comparison between all models discussed in this work, Table 6.9 gathers their performance on this scenario as measured with the MAE, MAPE, and PPMCC.

Table 6.9: PM, DDMs, and HMs performance measured with the MAE, MAPE, and PPMCC on Scenario II.

Metric	Wake	PM	PM°	ANN	KRLS	ELM	RF	H-ANN	H-KRLS	H-ELM	H-RF
MAE [dB]	W1	19.3 ± 2.3	8.9 ± 1.3	7.4 ± 1.8	5.9 ± 1.4	7.0 ± 1.3	6.2 ± 1.5	5.8 ± 2.5	4.5 ± 0.9	5.3 ± 0.9	4.6 ± 1.0
	W2	19.2 ± 3.1	8.6 ± 1.3	6.3 ± 1.8	4.6 ± 1.4	6.3 ± 2.0	5.8 ± 1.5	3.7 ± 2.2	3.7 ± 0.9	4.1 ± 1.4	4.7 ± 1.0
	W3	19.4 ± 3.0	8.7 ± 1.3	8.1 ± 2.0	4.9 ± 1.4	5.9 ± 1.4	6.0 ± 1.5	6.0 ± 2.5	4.0 ± 1.0	4.8 ± 1.0	4.9 ± 1.0
	all	19.3 ± 3.0	8.7 ± 1.3	7.3 ± 1.8	5.1 ± 1.4	6.4 ± 1.6	6.0 ± 1.5	5.2 ± 2.4	$\mathbf{4.1 \pm 0.9}$	4.7 ± 1.1	4.7 ± 1.0
MAPE [%]	W1	18.1 ± 3.1	8.5 ± 1.4	6.7 ± 1.6	5.5 ± 1.2	6.9 ± 1.2	5.9 ± 1.3	5.3 ± 2.4	4.1 ± 0.9	4.9 ± 0.8	4.3 ± 0.9
	W2	18.0 ± 3.6	8.2 ± 1.3	5.8 ± 1.5	4.3 ± 1.3	6.2 ± 1.9	5.4 ± 1.4	3.4 ± 2.4	3.5 ± 0.9	3.8 ± 1.2	4.4 ± 0.9
	W3	17.5 ± 2.8	8.5 ± 1.4	7.9 ± 1.8	4.6 ± 1.4	5.9 ± 1.4	5.7 ± 1.4	5.6 ± 2.5	3.7 ± 1.4	4.5 ± 0.9	4.6 ± 0.9
	all	18.0 ± 3.0	8.4 ± 1.3	6.8 ± 1.6	4.8 ± 1.3	6.3 ± 1.5	5.6 ± 1.3	4.8 ± 2.4	$\mathbf{3.8 \pm 1.0}$	4.4 ± 1.0	4.4 ± 0.9
PPMCC ×10[–]	W1	3.4 ± 2.7	7.8 ± 1.2	8.2 ± 1.2	8.5 ± 0.7	8.1 ± 0.8	8.3 ± 0.8	8.7 ± 0.5	9.0 ± 0.3	8.6 ± 0.3	8.8 ± 0.3
	W2	3.3 ± 2.7	8.0 ± 1.1	8.1 ± 1.0	8.7 ± 0.6	8.7 ± 0.7	8.6 ± 0.7	9.3 ± 0.4	9.2 ± 0.3	9.2 ± 0.4	9.1 ± 0.4
	W3	3.0 ± 2.8	8.1 ± 1.4	8.0 ± 1.3	8.6 ± 0.7	8.5 ± 0.8	8.5 ± 0.8	8.8 ± 0.5	9.1 ± 0.3	9.0 ± 0.3	9.0 ± 0.3
	all	3.3 ± 2.2	7.9 ± 1.1	8.1 ± 1.2	8.6 ± 0.7	8.4 ± 0.8	8.4 ± 0.8	8.9 ± 0.5	$\mathbf{9.1 \pm 0.3}$	8.9 ± 0.3	9.0 ± 0.3

6.5 Results of Scenario III

Following the discussion of Section 6.2, this is the LORSO scenario, in which the models have been trained with all data except the experiments referring to a particular rotational speed. Section 6.5.1 discusses the results of the PMs, Section 6.5.2 presents the results of the DDMs, and Section 6.5.3 discusses the results of the HMs. Finally, Section 6.5.4 summarises the performance of all models for this scenario.

6.5.1 Physics-based model results

Table 6.10 reports the various error metrics on this scenario for both the PSO-calibrated PM, and the PM with the parameter values reported in Table 4.9. It can be observed that in this scenario, which is characterised by a significant data reduction, the calibration process improves the performance of the PM only marginally. More specifically, the calibrated PM commits errors of 7.03 ± 1.08[dB], 6.57 ± 1.03[%], and 0.81 ± 0.07[–], as measured with the MAE, MAPE, and PPMCC, respectively. The PM with the initial values for the parameters is significantly less accurate, with a MAE of 19.35 ± 2.98[dB], a MAPE of 18.03 ± 3.06[%], and a PPMCC equal to 0.33 ± 0.22[–].

The reported results do not agree with the findings of Sections 6.3.1 - 6.4.1, in which the calibrated PM committed approximately 50[%] lower errors. This can be explained by the fact that a subset of the parameters given in Table 4.9 act as scaling factors for the predicted URN spectra. This aspect is further discussed in Section 6.9.

6.5.2 Data-driven models results

Table 6.11 reports the results obtained with the DDMs of Chapter D for this scenario. It can be observed that, similar to the discussion of Section 6.5.1 for the PMs, the performance of the DDMs also suffers compared to the previous scenarios. Nevertheless, the errors observed are still lower than the ones for the PMs.

More in detail, the ANN commits errors of 3.62 ± 0.51[dB], 3.22 ± 0.43[%], and 0.89 ± 0.05[–] for the MAE, MAPE, and PPMCC, respectively. The ELM exhibits similar performance to the ANN, with slightly lower, but not statistically significant,

Table 6.10: PMs performance measured with the MAE, MAPE and PPMCC on Scenario III (average value and 95% confidence interval).

	Calibrated Parameters			Initial Parameters		
n [rpm]	MAE	MAPE	PPMCC	MAE	MAPE	PPMCC
600	7.02 ± 1.07	6.05 ± 0.96	0.78 ± 0.06	18.55 ± 2.49	17.58 ± 2.42	0.43 ± 0.15
800	7.05 ± 1.02	6.19 ± 1.11	0.84 ± 0.07	19.28 ± 3.16	18.12 ± 3.29	0.27 ± 0.16
1000	7.02 ± 1.12	6.87 ± 0.99	0.84 ± 0.08	19.29 ± 2.72	18.19 ± 2.95	0.36 ± 0.17
1200	7.02 ± 1.08	6.64 ± 1.05	0.88 ± 0.07	19.45 ± 2.14	18.42 ± 3.27	0.32 ± 0.23
1400	7.01 ± 1.09	6.58 ± 1.03	0.82 ± 0.07	18.90 ± 3.03	17.74 ± 3.18	0.39 ± 0.17
1600	7.05 ± 1.05	6.92 ± 1.09	0.75 ± 0.07	19.93 ± 3.13	17.51 ± 2.62	0.26 ± 0.24
1800	7.04 ± 1.01	7.12 ± 0.98	0.82 ± 0.07	19.60 ± 2.95	18.05 ± 3.21	0.23 ± 0.13
2000	7.03 ± 1.14	6.20 ± 1.00	0.76 ± 0.07	18.89 ± 2.49	18.27 ± 2.68	0.38 ± 0.22
all	7.03 ± 1.08	6.57 ± 1.03	0.81 ± 0.07	19.35 ± 2.98	18.03 ± 3.06	0.33 ± 0.22

errors. The MAE observed for the ELM is equal to 4.23 ± 0.63[dB], the MAPE equals 4.01 ± 0.48[%], and the PPMCC equals 0.88 ± 0.06[–]. The corresponding errors for the RF are equal to 4.23 ± 0.62[dB], 3.79 ± 0.52[%], and 0.88 ± 0.04[–], for the MAE, MAPE, and PPMCC, respectively. KRLS commits the lowest average errors, similar to the findings of the previous two scenarios presented in Sections 6.3.2 - 6.4.2. The observed errors correspond to 3.63 ± 0.58[dB], 3.22 ± 0.43[%], and 0.89 ± 0.04[–] for the MAE, MAPE, and PPMCC, respectively. Also in this scenario, the differences in the performance of the DDMs is not statistically significant.

6.5.3 Hybrid model results

Table 6.12 reports the results obtained with the HMs for this scenario. Overall, similar conclusions to Sections 6.3.3 - 6.4.3 can be drawn. In particular, the errors of the H-ANN correspond to 3.62 ± 0.51[dB], 3.22 ± 0.43[%], and 0.89 ± 0.05[–], for the MAE, MAPE, and PPMCC, respectively. The H-ELM commits slightly lower average errors, with MAE being equal to 4.23 ± 0.63[dB], MAPE of 4.01 ± 0.48[%], and PPMCC of 0.88 ± 0.06[–]. H-RF commits errors of 4.23 ± 0.62[dB], 3.79 ± 0.52[%], and 0.88 ± 0.04[–] for the MAE, MAPE, and PPMCC, respectively. Finally, H-KRLS commits errors equal to 3.63 ± 0.58[dB] for MAE, 3.22 ± 0.50[%] for MAPE, and 0.89 ± 0.04[–] for PPMCC. Similar to Sections 6.3.3 - 6.4.3, the author cannot draw statistically

Table 6.11: DDMs performance measured with the MAE, MAPE, and PPMCC on Scenario III (average value and 95% confidence interval).

Metric	n [rpm]	ANN	KRLS	ELM	RF
MAE [dB]	600	3.82 ± 0.47	3.70 ± 0.55	4.30 ± 0.58	4.24 ± 0.58
	800	3.46 ± 0.46	3.80 ± 0.57	4.42 ± 0.60	4.08 ± 0.66
	1000	3.63 ± 0.56	3.83 ± 0.56	4.45 ± 0.59	4.43 ± 0.63
	1200	3.78 ± 0.56	3.63 ± 0.75	4.22 ± 0.79	3.92 ± 0.56
	1400	3.33 ± 0.56	3.44 ± 0.63	4.00 ± 0.66	3.92 ± 0.63
	1600	3.93 ± 0.46	3.93 ± 0.6	4.57 ± 0.63	4.42 ± 0.58
	1800	3.42 ± 0.48	3.28 ± 0.59	3.81 ± 0.62	3.82 ± 0.58
	2000	3.58 ± 0.54	3.52 ± 0.57	4.09 ± 0.60	4.35 ± 0.67
	all	$\mathbf{3.62 \pm 0.51}$	3.63 ± 0.58	4.23 ± 0.63	4.23 ± 0.62
MAPE [%]	600	3.30 ± 0.44	3.42 ± 0.50	4.13 ± 0.50	3.44 ± 0.51
	800	3.30 ± 0.43	3.48 ± 0.46	4.20 ± 0.46	3.47 ± 0.53
	1000	3.37 ± 0.40	3.44 ± 0.46	4.15 ± 0.46	3.94 ± 0.51
	1200	3.08 ± 0.39	3.08 ± 0.50	3.72 ± 0.50	3.78 ± 0.48
	1400	3.27 ± 0.39	3.52 ± 0.46	4.25 ± 0.46	3.99 ± 0.57
	1600	3.09 ± 0.43	3.02 ± 0.49	3.65 ± 0.49	4.09 ± 0.49
	1800	2.92 ± 0.42	3.37 ± 0.47	4.07 ± 0.47	3.82 ± 0.47
	2000	3.37 ± 0.43	3.26 ± 0.50	3.94 ± 0.50	3.80 ± 0.50
	all	$\mathbf{3.22 \pm 0.43}$	3.22 ± 0.50	4.01 ± 0.48	3.79 ± 0.52
PPMCC [–]	600	0.80 ± 0.05	0.94 ± 0.04	0.92 ± 0.07	0.85 ± 0.04
	800	0.84 ± 0.05	0.88 ± 0.04	0.86 ± 0.07	0.88 ± 0.04
	1000	0.85 ± 0.05	0.96 ± 0.04	0.94 ± 0.05	0.89 ± 0.04
	1200	0.90 ± 0.05	0.89 ± 0.04	0.87 ± 0.07	0.89 ± 0.04
	1400	0.84 ± 0.05	0.81 ± 0.04	0.79 ± 0.07	0.96 ± 0.04
	1600	0.93 ± 0.05	0.87 ± 0.04	0.85 ± 0.06	0.84 ± 0.04
	1800	0.97 ± 0.03	0.98 ± 0.04	0.85 ± 0.06	0.92 ± 0.04
	2000	0.96 ± 0.04	0.80 ± 0.04	0.95 ± 0.04	0.84 ± 0.04
	all	0.89 ± 0.05	$\mathbf{0.89 \pm 0.04}$	0.88 ± 0.06	0.88 ± 0.04

significant conclusions regarding the choice of the learning algorithm.

6.5.4 Results summary

To facilitate comparison between all models discussed in this work, Tables 6.13 - 6.14 gathers their performance on this scenario as measured with the MAE, MAPE, and PPMCC.

Table 6.12: HMs performance measured with the MAE, MAPE, and PPMCC on Scenario III (average value and 95% confidence interval).

Metric	n [rpm]	H-ANN	H-KRLS	H-ELM	H-RF
MAE [dB]	600	2.92 ± 0.44	3.07 ± 0.46	3.57 ± 0.48	3.22 ± 0.56
	800	3.11 ± 0.47	3.19 ± 0.45	3.71 ± 0.47	3.67 ± 0.55
	1000	2.99 ± 0.47	3.14 ± 0.52	3.65 ± 0.54	3.74 ± 0.51
	1200	3.25 ± 0.46	3.03 ± 0.50	3.52 ± 0.52	3.58 ± 0.50
	1400	2.92 ± 0.49	3.22 ± 0.50	3.74 ± 0.52	3.86 ± 0.48
	1600	3.13 ± 0.46	2.74 ± 0.50	3.19 ± 0.52	3.47 ± 0.57
	1800	3.19 ± 0.43	2.82 ± 0.51	3.28 ± 0.49	3.66 ± 0.52
	2000	2.84 ± 0.42	3.18 ± 0.47	3.70 ± 0.51	3.32 ± 0.52
	all	$\mathbf{3.03 \pm 0.46}$	3.04 ± 0.49	3.55 ± 0.51	3.55 ± 0.52
MAPE [%]	600	3.00 ± 0.35	2.71 ± 0.44	3.27 ± 0.47	3.01 ± 0.32
	800	3.03 ± 0.41	3.01 ± 0.45	3.64 ± 0.48	2.93 ± 0.35
	1000	2.54 ± 0.38	2.53 ± 0.42	3.06 ± 0.45	3.32 ± 0.33
	1200	2.67 ± 0.41	2.62 ± 0.40	3.16 ± 0.43	3.52 ± 0.36
	1400	2.55 ± 0.41	2.97 ± 0.39	3.59 ± 0.42	3.29 ± 0.37
	1600	3.00 ± 0.39	2.71 ± 0.38	3.27 ± 0.41	3.01 ± 0.38
	1800	2.61 ± 0.39	2.57 ± 0.43	3.10 ± 0.46	3.29 ± 0.37
	2000	2.75 ± 0.37	2.97 ± 0.43	3.59 ± 0.46	3.49 ± 0.33
	all	$\mathbf{2.76 \pm 0.38}$	2.77 ± 0.41	3.34 ± 0.45	3.24 ± 0.35
PPMCC [–]	600	0.89 ± 0.03	0.88 ± 0.04	0.86 ± 0.07	0.93 ± 0.04
	800	0.90 ± 0.03	0.93 ± 0.04	0.91 ± 0.06	0.86 ± 0.04
	1000	0.95 ± 0.03	0.94 ± 0.04	0.92 ± 0.05	0.96 ± 0.03
	1200	0.89 ± 0.03	0.94 ± 0.04	0.92 ± 0.06	0.84 ± 0.04
	1400	0.86 ± 0.03	0.96 ± 0.03	0.94 ± 0.05	0.94 ± 0.04
	1600	0.96 ± 0.03	0.97 ± 0.03	0.95 ± 0.04	0.90 ± 0.04
	1800	0.87 ± 0.03	0.88 ± 0.04	0.86 ± 0.07	0.96 ± 0.03
	2000	0.86 ± 0.03	0.91 ± 0.04	0.89 ± 0.04	0.96 ± 0.04
	all	$\mathbf{0.93 \pm 0.03}$	0.93 ± 0.04	0.91 ± 0.06	0.92 ± 0.04

6.6 The best physics-based, data-driven and hybrid models

Having discussed the performance of all PMs, DDMs, and HMs on the various scenarios, this section compares only the best PM, DDM, and HM for each scenario with the error metrics discussed in Section 4.6. The relevant results from Sections 6.3 - 6.5 are

Table 6.13: PM, DDMs, and HMs performance measured with the MAE and MAPE on Scenario III.

Metric	n [rpm]	PM	PM$^{\diamond}$	ANN	KRLS	ELM	RF	H-ANN	H-KRLS	H-ELM	H-RF
MAE [dB]	600	18.5 ± 2.5	7.0 ± 1.0	3.8 ± 0.5	3.7 ± 0.5	4.3 ± 0.6	4.2 ± 0.6	2.9 ± 0.4	3.1 ± 0.5	3.6 ± 0.5	3.2 ± 0.6
	800	19.3 ± 3.2	7.0 ± 1.0	3.5 ± 0.5	3.8 ± 0.6	4.4 ± 0.6	4.1 ± 0.7	3.1 ± 0.5	3.2 ± 0.4	3.7 ± 0.5	3.7 ± 0.5
	1000	19.3 ± 2.7	7.0 ± 1.1	3.6 ± 0.6	3.8 ± 0.6	4.4 ± 0.6	4.4 ± 0.6	3.0 ± 0.5	3.1 ± 0.5	3.6 ± 0.5	3.7 ± 0.5
	1200	19.4 ± 2.1	7.0 ± 1.1	3.8 ± 0.6	3.6 ± 0.7	4.2 ± 0.8	3.9 ± 0.6	3.2 ± 0.5	3.0 ± 0.5	3.5 ± 0.5	3.6 ± 0.5
	1400	18.9 ± 3.0	7.0 ± 1.1	3.3 ± 0.6	3.4 ± 0.6	4.0 ± 0.7	3.9 ± 0.6	2.9 ± 0.5	3.2 ± 0.5	3.7 ± 0.5	3.9 ± 0.5
	1600	19.9 ± 3.1	7.0 ± 1.0	3.9 ± 0.5	3.9 ± 0.6	4.6 ± 0.6	4.4 ± 0.6	3.1 ± 0.5	2.7 ± 0.5	3.2 ± 0.5	3.5 ± 0.6
	1800	19.6 ± 2.9	7.0 ± 1.0	3.4 ± 0.5	3.3 ± 0.6	3.8 ± 0.6	3.8 ± 0.6	3.2 ± 0.4	2.8 ± 0.5	3.3 ± 0.5	3.7 ± 0.5
	2000	18.9 ± 2.5	7.0 ± 1.1	3.6 ± 0.5	3.5 ± 0.6	4.1 ± 0.6	4.3 ± 0.7	2.8 ± 0.4	3.2 ± 0.5	3.7 ± 0.5	3.3 ± 0.5
	all	19.3 ± 3.0	7.0 ± 1.1	$\mathbf{3.6 \pm 0.5}$	3.6 ± 0.6	4.2 ± 0.6	4.2 ± 0.6	$\mathbf{3.0 \pm 0.5}$	3.0 ± 0.5	3.5 ± 0.5	3.5 ± 0.5
MAPE [%]	600	17.6 ± 2.4	6.0 ± 1.0	3.3 ± 0.4	3.4 ± 0.5	4.1 ± 0.5	3.4 ± 0.5	3.0 ± 0.3	2.7 ± 0.4	3.3 ± 0.5	3.0 ± 0.3
	800	18.1 ± 3.3	6.2 ± 1.1	3.3 ± 0.4	3.5 ± 0.5	4.2 ± 0.5	3.5 ± 0.5	3.0 ± 0.4	3.0 ± 0.4	3.6 ± 0.5	2.9 ± 0.3
	1000	18.2 ± 2.9	6.9 ± 1.0	3.4 ± 0.4	3.4 ± 0.5	4.1 ± 0.5	3.9 ± 0.5	2.5 ± 0.4	2.5 ± 0.4	3.1 ± 0.4	3.3 ± 0.3
	1200	18.4 ± 3.3	6.6 ± 1.0	3.1 ± 0.4	3.1 ± 0.5	3.7 ± 0.5	3.8 ± 0.5	2.7 ± 0.4	2.6 ± 0.4	3.2 ± 0.4	3.5 ± 0.4
	1400	17.7 ± 3.2	6.6 ± 1.0	3.3 ± 0.4	3.5 ± 0.5	4.2 ± 0.5	4.0 ± 0.6	2.5 ± 0.4	3.0 ± 0.4	3.6 ± 0.4	3.3 ± 0.4
	1600	17.5 ± 2.6	6.9 ± 1.1	3.1 ± 0.4	3.0 ± 0.5	3.6 ± 0.5	4.1 ± 0.5	3.0 ± 0.4	2.7 ± 0.4	3.3 ± 0.4	3.0 ± 0.4
	1800	18.0 ± 3.2	7.1 ± 1.0	2.9 ± 0.4	3.4 ± 0.5	4.1 ± 0.5	3.8 ± 0.5	2.6 ± 0.4	2.6 ± 0.4	3.1 ± 0.5	3.3 ± 0.4
	2000	18.3 ± 2.7	6.2 ± 1.0	3.4 ± 0.4	3.3 ± 0.5	3.9 ± 0.5	3.8 ± 0.5	2.7 ± 0.4	3.0 ± 0.4	3.6 ± 0.5	3.5 ± 0.3
	all	18.0 ± 3.0	6.6 ± 1.0	$\mathbf{3.2 \pm 0.4}$	3.2 ± 0.5	4.0 ± 0.5	3.8 ± 0.5	$\mathbf{2.7 \pm 0.4}$	2.8 ± 0.4	3.3 ± 0.4	3.2 ± 0.3

Table 6.14: PM, DDMs, and HMs performance measured with the PPMCC on Scenario III.

Metric	n [rpm]	PM	PM$^{\diamond}$	ANN	KRLS	ELM	RF	H-ANN	H-KRLS	H-ELM	H-RF
PPMCC $\times 10$[–]	600	4.3 ± 1.5	7.8 ± 0.6	8.0 ± 0.5	9.4 ± 0.4	9.2 ± 0.7	8.5 ± 0.4	8.9 ± 0.3	8.8 ± 0.4	8.6 ± 0.7	9.3 ± 0.4
	800	2.7 ± 1.6	8.4 ± 0.7	8.4 ± 0.5	8.8 ± 0.4	8.6 ± 0.7	8.8 ± 0.4	9.0 ± 0.3	9.3 ± 0.4	9.1 ± 0.6	8.6 ± 0.4
	1000	3.6 ± 1.7	8.4 ± 0.8	8.5 ± 0.5	9.6 ± 0.4	9.4 ± 0.5	8.9 ± 0.4	9.5 ± 0.3	9.4 ± 0.4	9.2 ± 0.5	9.6 ± 0.3
	1200	3.2 ± 2.3	8.8 ± 0.7	9.0 ± 0.5	8.9 ± 0.4	8.7 ± 0.7	8.9 ± 0.4	8.9 ± 0.3	9.4 ± 0.4	9.2 ± 0.6	8.4 ± 0.4
	1400	3.9 ± 1.7	8.2 ± 0.7	8.4 ± 0.5	8.1 ± 0.4	7.9 ± 0.7	9.6 ± 0.4	8.6 ± 0.3	9.6 ± 0.3	9.4 ± 0.5	9.4 ± 0.4
	1600	2.6 ± 2.4	7.5 ± 0.7	9.3 ± 0.5	8.7 ± 0.4	8.5 ± 0.6	8.4 ± 0.4	9.6 ± 0.3	9.7 ± 0.3	9.5 ± 0.4	9.0 ± 0.4
	1800	2.3 ± 1.3	8.2 ± 0.7	9.7 ± 0.3	9.8 ± 0.4	8.5 ± 0.6	9.2 ± 0.4	8.7 ± 0.3	8.8 ± 0.4	8.6 ± 0.7	9.6 ± 0.3
	2000	3.8 ± 2.2	7.6 ± 0.7	9.6 ± 0.4	8.0 ± 0.4	9.5 ± 0.4	8.4 ± 0.4	8.6 ± 0.3	9.1 ± 0.4	8.9 ± 0.4	9.6 ± 0.4
	all	3.3 ± 2.2	8.1 ± 0.7	8.9 ± 0.5	$\mathbf{8.9 \pm 0.4}$	8.8 ± 0.6	8.8 ± 0.4	$\mathbf{9.3 \pm 0.3}$	9.3 ± 0.4	9.1 ± 0.6	9.2 ± 0.4

gathered and reported in Table 6.15.

In general, it can be observed that the PM is the least accurate model, followed by the DDM, and the HM, which commits the lowest average errors. However, this ranking is not always statistically significant. The error metrics of the PM and the DDM do indicate a statistically significant difference at a confidence level of 95[%] for all scenarios and error metrics. This can be attributed to the variance of the errors in the various scenarios tested, which is visualised in Figures 6.2 - 6.4 for all models in scenarios I - III, respectively (the colors indicate probability density). It can be seen that for all scenarios all models are able to predict the majority of the SPLs correctly, as indicated by the yellow regions of the graphs. Nevertheless, the variance of the predictions is evident, particularly for the PM. Lower variance is observed for the DDM, and even lower for the HM.

When comparing the errors reported across different scenarios, all models commit the lowest average errors for scenario III (LORSO), which corresponds to extrapolation on rotational speed. In this scenario, errors lower than 7.6[%] can be observed with the PM, whereas a maximum error of 4.1[%], and 3.5[%] occurs for the DDM, and HM, respectively. Higher errors are observed on scenario II, in which the models extrapolate on the wakefield that the propellers operate on. Nevertheless, the differences are marginal for the DDMs and HMs. As briefly explained in Section 6.4, the difficulty of this scenario is attributed to the considerable differences in the cavitation patterns occurring with each wakefield, resulting in more “severe” extrapolation cases. Note that the wakefields employed in this work were chosen specifically for this reason, as discussed in [7, 8]. Nevertheless, the performance of the models is widely acceptable even for this scenario, with errors lower than 9[%] for the PM, 6[%] for the DDM, and 5[%] for the HM, respectively. As Figure 6.3 illustrates, even though the predictions of all models seem to be well-centered around the recorded SPLs, the variance appears to be higher with respect to the rest of the scenarios. Nevertheless, the maximum error of 9.5[%] for the PM indicates acceptable, for the early design stage, performance. In addition, maximum errors of 5.5[%] for the DDM, and 5[%] for the HM, can be certainly considered acceptable for the early stage design process.

Table 6.15: Best PM, DDM, and HM performance in scenarios I to III as measured with the MAE, MAPE, and PPMCC (average value and 95% confidence interval).

		PM	DDM	HM
Scenario I	MAE [dB]	7.70 ± 1.03	4.48 ± 0.69	3.44 ± 0.48
	MAPE [%]	7.20 ± 0.97	4.12 ± 0.66	3.16 ± 0.36
	PPMCC [–]	0.82 ± 0.10	0.88 ± 0.06	0.92 ± 0.03
Scenario II	MAE [dB]	8.75 ± 1.35	5.14 ± 1.37	4.06 ± 0.93
	MAPE [%]	8.41 ± 1.35	4.79 ± 1.29	3.77 ± 1.04
	PPMCC [–]	0.79 ± 0.11	0.86 ± 0.07	0.91 ± 0.03
Scenario III	MAE [dB]	7.03 ± 1.08	3.62 ± 0.51	3.03 ± 0.46
	MAPE [%]	6.57 ± 1.03	3.22 ± 0.43	2.76 ± 0.38
	PPMCC [–]	0.81 ± 0.07	0.89 ± 0.05	0.93 ± 0.03

For the sake of brevity, individual results on each experiment are not reported. However, Figure 6.5 reports for a single representative spectrum the comparison between the best PM, DDM, and HM in the different scenarios (LORSO, LOWO, and LOGO) and in Figure 6.6 the comparison between the different scenarios for the best PM, DDM, and HM (the dual version of Figure 6.5). The representative spectra have been selected as they correspond to the experiment for which the errors committed by the PM, DDMs and HMs closely follow the average performance reported in Sections 6.3 - 6.5. As can be seen, the predicted spectra follow the measurements rather well, across all scenarios and for all models. From Figure 6.5 it can be seen that the PM commits the highest errors across all scenarios, followed by the DDM, and the HM. Figure 6.6 illustrates the difference in complexity between the various scenarios. All models commit the highest errors on Scenario II (LOWO), and the lowest errors on Scenario III (LORSO).

6.7 Results of Scenario IV

This section discusses the performance of the various models presented in Chapter 4, for scenario IV of Section 6.2. All models have been parameterised on the dataset of [7, 8]. The available measurements cover a frequency range between 400[Hz] - 80[kHz]. However the models considered provide predictions up to 20[kHz]. As such, the comparisons

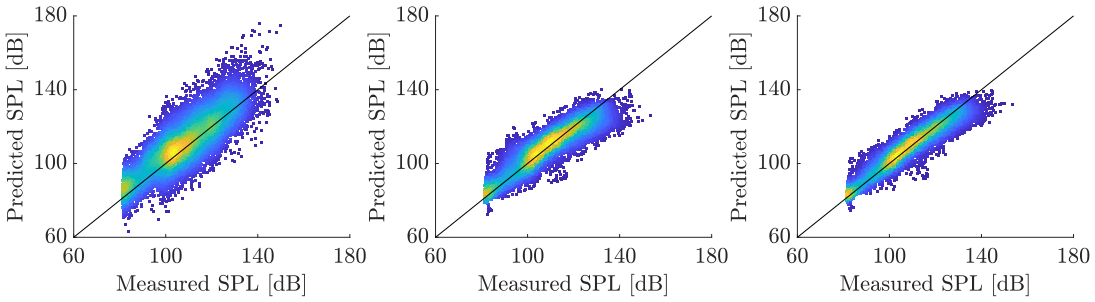

(a) PM. (b) DDM. (c) HM.

Figure 6.2: Measured vs. predicted plot for the best PM, DDM, and HM on scenario I.

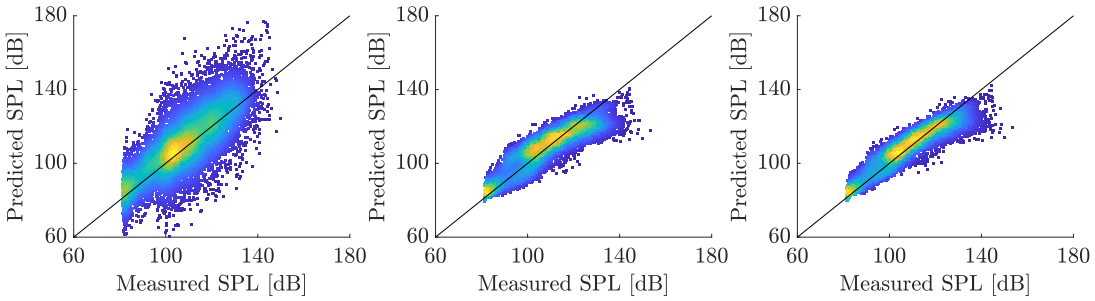

(a) PM. (b) DDM. (c) HM.

Figure 6.3: Measured vs. predicted plot for the best PM, DDM, and HM on scenario II.

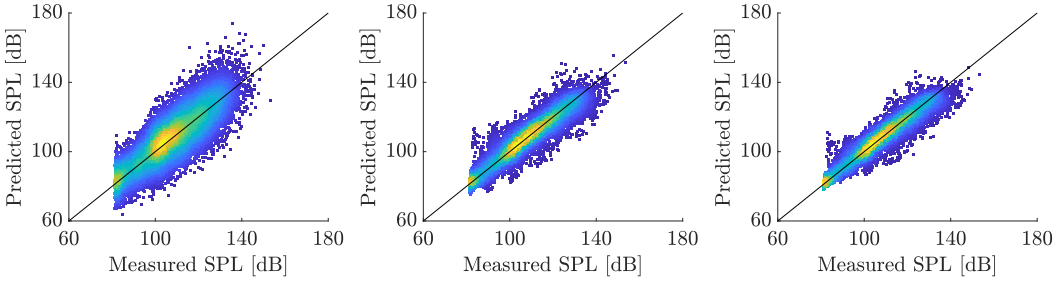

(a) PM. (b) DDM. (c) HM.

Figure 6.4: Measured vs. predicted plot for the best PM, DDM, and HM on scenario III. Colours indicate probability density.

provided in this section are valid for a frequency range between 400[Hz] - 20[kHz].

Figure 6.7 provides the measured URN spectrum, and the predicted URN spectra with the best PM, DDM, and HM of Section 6.6. As can be observed, the trends are

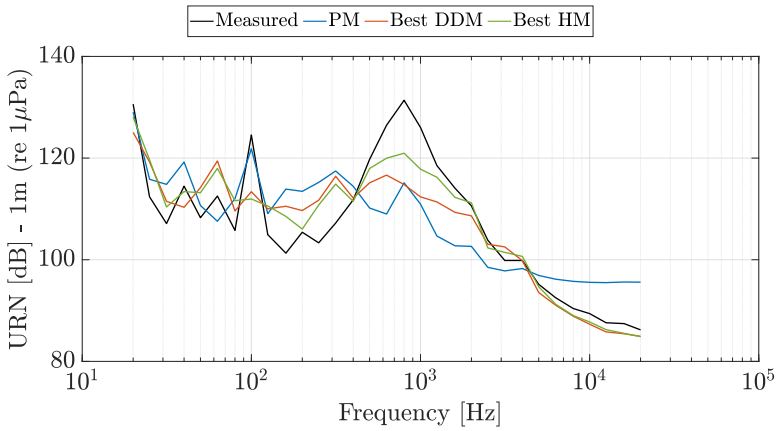

(a) Scenario I (LOGO) - Measured, Best PM, DDM, and HM.

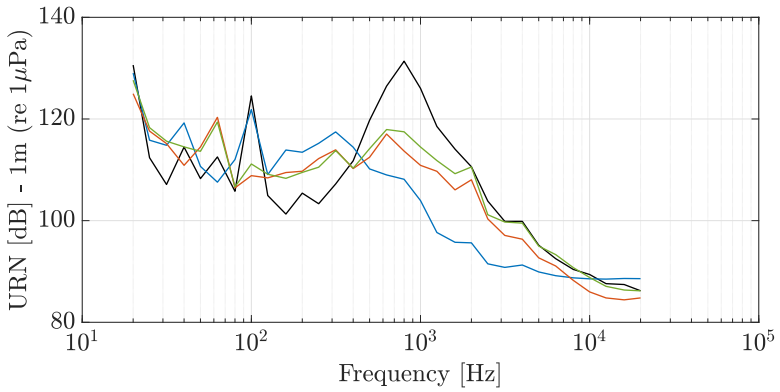

(b) Scenario II (LOWO) - Measured, Best PM, DDM, HM.

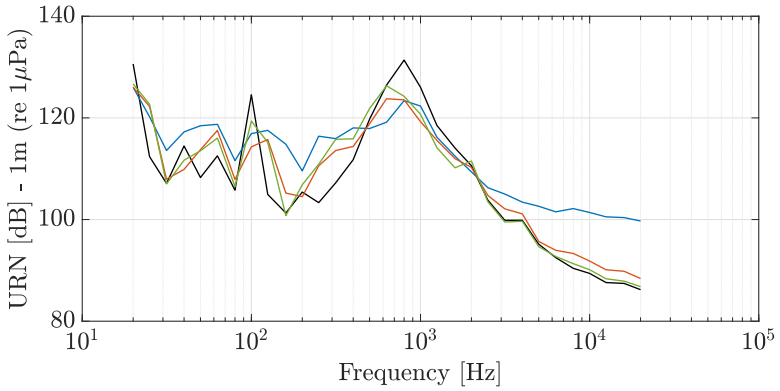

(c) Scenario III (LORSO) - Measured, Best PM, DDM, and HM.

Figure 6.5: Comparison between the best PM, DDM, and HM in the different scenarios for a single representative spectrum.

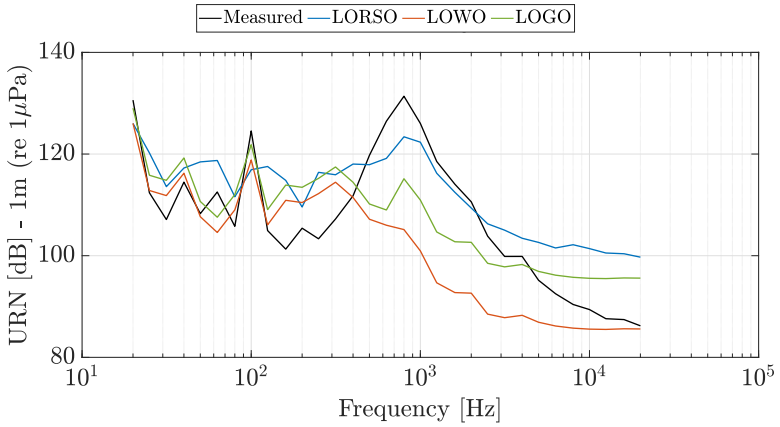

(a) Measured, LORSO PM, LOWO PM, and LOGO PM

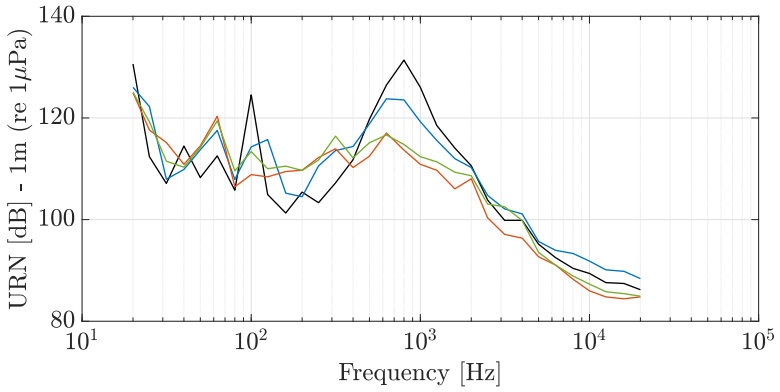

(b) Measured, LORSO Best DDM, LOWO Best DDM, and LOGO Best DDM

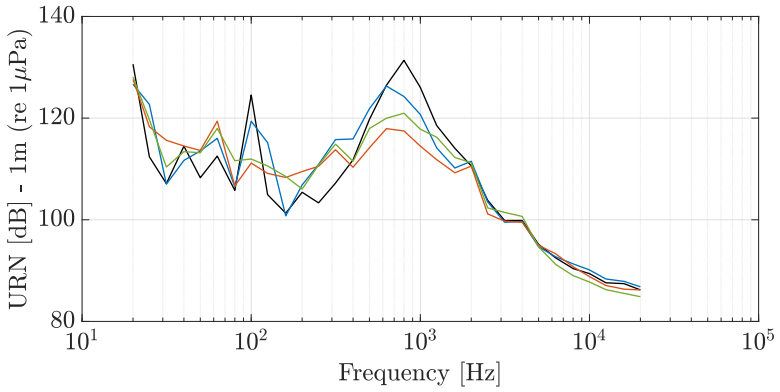

(c) Measured, LORSO Best HM, LOWO Best HM, and LOGO Best HM

Figure 6.6: Comparison between the scenarios I - III (LOGO, LOWO, and LORSO) of the best PM, DDM, and HM in for a single representative spectrum.

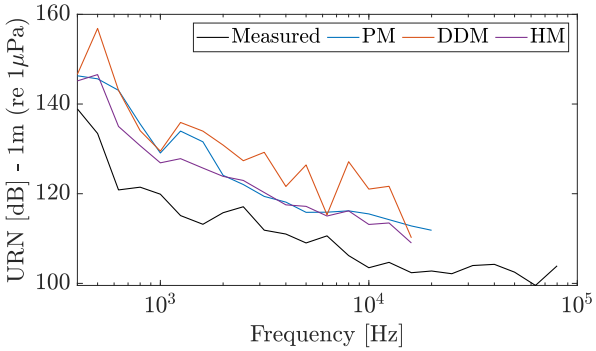

Figure 6.7: Measured URN spectra and PM, DDM, and HM predictions for Scenario IV.

Table 6.16: PM, DDM, and HM performance on Scenario IV.

Model	MAE [dB]	MAPE [%]	PPMCC [–]
PM	12.74	11.41	0.911
DDM	17.04	15.17	0.863
HM	10.91	9.76	0.962

physically realistic, nevertheless all models tend to overestimate the URN. Table 6.16 reports the error metrics for all models. More in detail, the PM commits errors of 12.74[dB], 11.41[%], and 0.911[–] for the MAE, MAPE, and PPMCC respectively, with the maximum error occurring at approximately 300[Hz] with a difference of roughly 25[dB]. The DDM commits higher errors in this case, with a MAE equal to 17.04[dB], a MAPE of 15.17[%], and PPMCC equal to 0.863[–]. High errors are observed for a variety of frequencies. For instance, errors of approximately 27[dB] occur at a frequency range between 400÷700[Hz], and errors of 33[dB] for frequencies around 25[kHz]. The HM is the most accurate model, committing errors of 10.91[dB], 9.76[%], 0.962[–], for the MAE, MAPE, and PPMCC, respectively and a maximum error of 18[dB], or 20[%], occurring at approximately 1[kHz].

Higher errors were expected from all models, as this scenario corresponds to a rather severe extrapolation case due to the highly different geometry of the propeller and the uniform wakefield which was not present in the dataset of [7, 8]. Nevertheless, this is the first case in which the accuracy of the PM surpasses the DDM, with errors approximately 25[%] lower for the MAE and MAPE. This is not a surprising result,

considering that the PM is based on physics-based input-output relations, whereas the DDM infers those purely from the limited experimental data available. Impressive is the performance of the HM, which encapsulates the knowledge of the PM, plus the available experimental data. Although it overestimates the SPLs of the entire URN spectrum, it provides acceptable performance for the early design stage, with much lower inference time requirements than the more sophisticated CFD-based models according to the literature review of Chapter 3.

6.8 Physical plausibility analysis results

As stated in Section 5.5, it is critical to assess if the predictions of the HMs are aligned with general theory on cavitation noise. Two procedures have been utilised to verify this: The FR procedure, described in Section 4.7.1, and the TPK, discussed in Section 4.7.2. The results of these procedures are provided in Sections 6.8.1 - 6.8.2, respectively.

6.8.1 Feature ranking results

Evaluating the performance of the DDMs and HMs on the various scenarios of Sections 6.3 - 6.5 is just the first step towards understanding them. More insight can be gained by the FR procedure described in Section 4.7.1, which allows the author to establish that the DDMs and HMs have learned theoretically grounded input - output relations. Nevertheless, it should be noted that the majority of the features in $\mathcal{D}_n$ are strongly correlated, or even redundant. For this reason, the FR procedure of Section 4.7.1 might recognise some, or all of the highly correlated features as important, even if they contain the same information. As such, the author will not make very specific comments on the results, however it is still reasonable to comment on global trends.

Tables 6.17 - 6.18 provide the results of the FR process for the best DDM and HM according to Section 6.6. Focusing on Table 6.17 it can be observed that most of the top 20 important features relate to the propeller geometry and inflow conditions, as well as

features that provide information regarding the type of cavitation. More specifically, the best DDM relies on the propeller skew angle, pitch and rake at 75[%] or 95[%] of the propeller radius, which are known to affect cavitation occurrence and extent as discussed in Section 4.4.1, as well as the number of propeller blades. Furthermore, the cavitation index and the tunnel pressure are also highly important, as they are both indicators of cavitation occurrence. Several coefficients from the harmonic analysis of the wakefield also appear in the top features, both at 70[%] and 90[%] of the propeller radius, as well as features originating from the strength of the vortex near the tip, which indicate the occurrence of TVC. The angular locations in which the size of the blade area on the propeller suction side having pressure lower than the vapour pressure reaches its minimum and maximum value are also highly ranked. Note that these features were included as an estimation of the region where true cavitation starts.

For what regards the HM, Table 6.18 indicates that, unsurprisingly, the outputs of the PM at various frequencies occupy 6 out of the top 20 features, as well as as the top 2 places. In addition, the relative tunnel pressure and the cavitation index based on rotational speed, are also ranked highly, as they are directly related with the URN levels. Similar to the DDM, several Fourier coefficients extracted from the wakefield as well as propeller design parameters are also present, including the number of propeller blades, the total rake and skew angle at 70[%] and 90[%] of the propeller radius. In general it can be observed the most influencing variables in the noise generation are among the most important ones according to the FR process. It is interesting to note the absence in the top positions of features assumed to be strongly related to the cavitation noise, such as the features related to the angle of attack. This can be justified recalling that these features are directly dependent on, or derived by, the wakefield. Hence these features might be redundant.

6.8.2 Test against prior knowledge results

For what regards the TPK, HM predictions for the cases of Table 5.4 are compared with the models of Brown [15], Bosschers [173]. In general, these models do not provide highly accurate results in terms of absolute SPL values. Therefore only relative trends

Table 6.17: 20 most important features for the best DDM.

Rank	Feature	Rank	Feature
1	$\sigma_{\mathtt{n}}$	11	$d\theta/dw_t\|^{(0.7)}_{\text{left}}$
2	$\mathtt{s}$ at 75% of $D/2$	12	$\bar{\alpha}^{0.7}_{\text{G,atk}}$
3	p_{tunnel}	13	$\mathtt{a}_w^{(0.9)}(3)$
4	$\mathtt{r}$ at 75% of $D/2$	14	$d\theta/dw_t\|^{(0.7)}_{\text{right}}$
5	$\mathtt{a}_w^{(0.7)}(1)$	15	$\mathtt{p}$ at 75% of $D/2$
6	$\mathtt{a}_w^{(0.7)}(3)$	16	$\Gamma^{\max(0.95)}$
7	$\mathtt{a}^{\min}_{\text{c,suc.}}$	17	$\mathtt{p}$ at 95% of $D/2$
8	$\theta^{\min}_{\text{c,suc.}}$	18	$\mathtt{a}^{\max}_{\text{c,suc.}}$
9	$\mathtt{s}$ at 95% of $D/2$	19	$\mathtt{a}_{\Gamma^{0.95}}(1)$
10	Z	20	$\mathtt{a}_w^{(0.7)}(2)$

Table 6.18: 20 most important features for the best HM.

Rank	Feature	Rank	Feature
1	$h_{\text{PM}}(\boldsymbol{x})$ at $f = 500$[Hz]	11	$h_{\text{PM}}(\boldsymbol{x})$ at $f = 630$[Hz]
2	$h_{\text{PM}}(\boldsymbol{x})$ at $f = 1000$[Hz]	12	Z
3	p_{tunnel}	13	$\mathtt{a}_w^{(0.7)}(1)$
4	$\sigma_{\mathtt{n}}$	14	$h_{\text{PM}}(\boldsymbol{x})$ at $f = 800$[Hz]
5	$\theta^{\min}_{\text{c,suc.}}$	15	$\mathtt{a}_w^{(0.7)}(3)$
6	$\theta^{\max}_{\text{c,suc.}}$	16	$\mathtt{a}_w^{(0.7)}(2)$
7	$h_{\text{PM}}(\boldsymbol{x})$ at $f = 400$[Hz]	17	$h_{\text{PM}}(\boldsymbol{x})$ at $f = 1250$[Hz]
8	$\mathtt{s}$ at 75% of $D/2$	18	$\mathtt{a}_w^{(0.9)}(1)$
9	$\mathtt{s}$ at 95% of $D/2$	19	$\mathtt{a}_w^{(0.9)}(2)$
10	$\mathtt{r}$ at 75% of $D/2$	20	$\Gamma^{\max(0.95)}$

are analysed in this section. Figure 6.8 presents the predictions of all HMs, and the extent and thickness of cavitation as evaluated with the cavitating BEM numerical code for all cases of Table 5.4. It can be observed that the predictions of the HMs are highly similar across all cases, particularly in the region below 200[Hz], whereas for higher frequencies relative differences are observed. Most notable differences occur in the the mid-frequency region of the URN spectrum for the cases C_1 and C_3 with deviations of approximately 5[dB], as well as the high-frequency region of case C_4, with the predictions of the DDMs varying by a maximum of 10[dB].

According to Section 5.5, to interpret if these predictions are valid from a physical point of view, the noise increments of the HMs, estimated on the frequency range between $4 \div 20$[kHz], are compared with the noise increment predicted with the formula

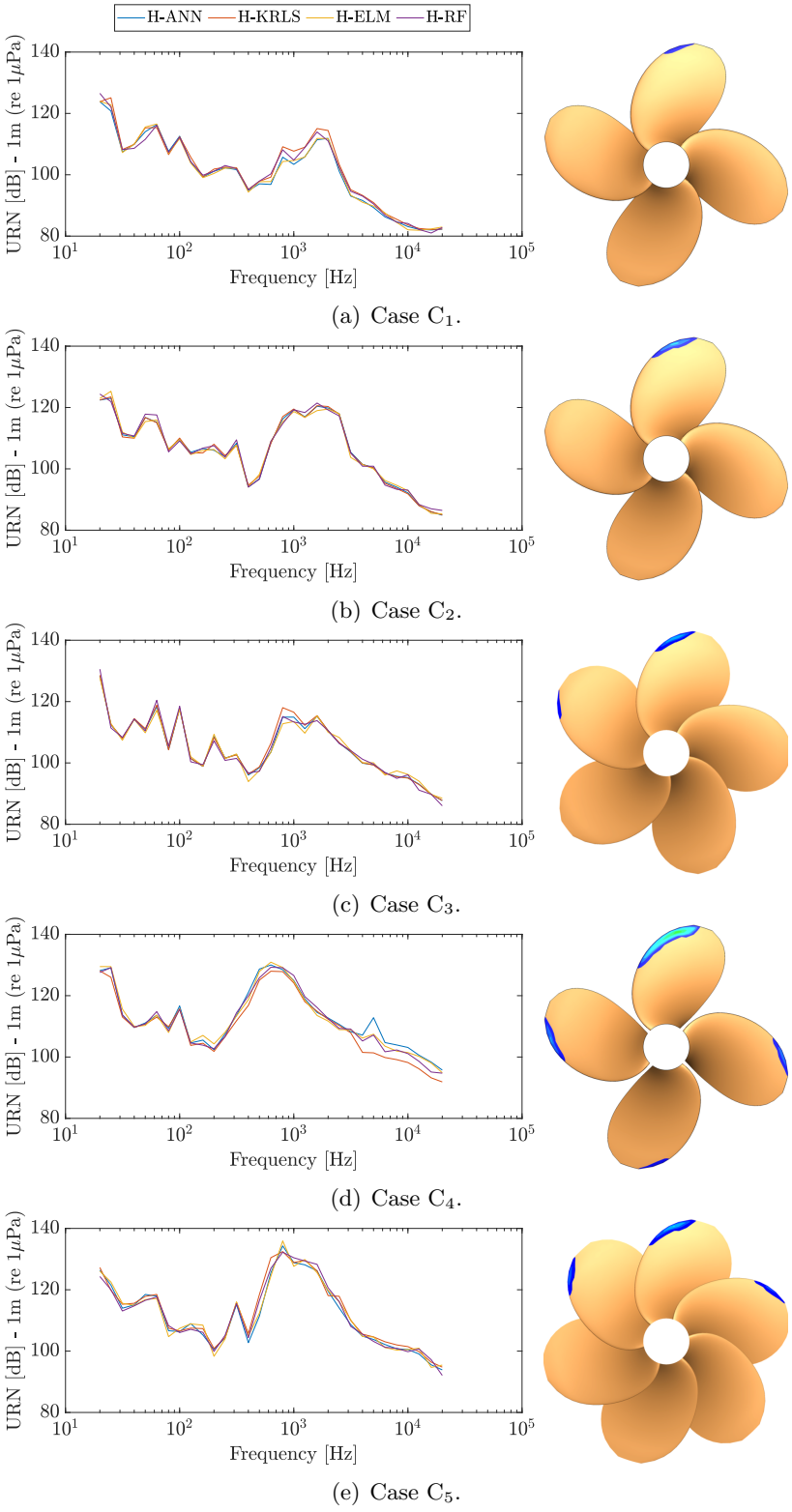

(a) Case C_1.

(b) Case C_2.

(c) Case C_3.

(d) Case C_4.

(e) Case C_5.

Figure 6.8: URN predicted with the HMs, and cavitation extent and thickness computed by cavitating BEM for the cases of Table 5.4.

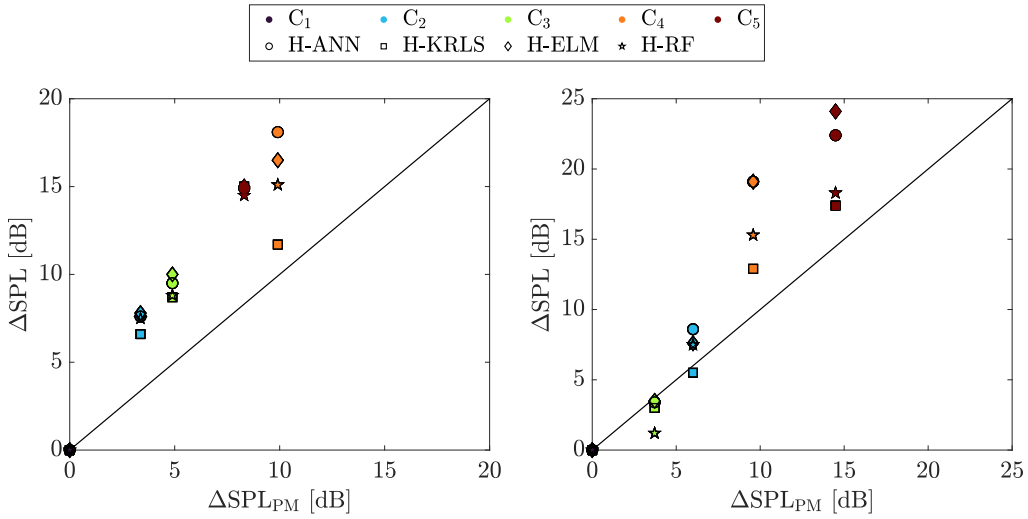

(a) URN increment.

(b) URN peak level.

Figure 6.9: URN increment and peak levels predicted with the HMs and the models of Brown [15], Bosschers [16] for the cases of Table 5.4.

of Brown [15], and are presented in Figure 6.9(a). Utilising the SPLs of case C_1 as a reference value, which represents the origin of the axes in Figure 6.9(a), the relative noise increase ΔSPL with respect to C_1 is evaluated with the DDMs and is plotted along the y-axis. The same predictions ΔSPL_{PM} from the formula of Brown are plotted along the x-axis. A perfect correlation between the HMs' and Brown's predictions is expected when $\Delta SPL = \Delta SPL_{PM}$ for all cases, which corresponds to the straight line of Figure 6.9(a). Whereas this is not the case for Figure 6.9(a), the predictions of the HMs do correlate with Brown's formula. For instance, it can be observed that the predicted ΔSPL for Case C_5 is highly similar across all HMs, and equal to approximately 15[dB], whereas the formula of Brown estimates an increase of 7.5[dB]. Similarly for cases C_2 and C_3, the HMs estimate that ΔSPL lies between 6$\div$8[dB], and 8.5$\div$10[dB], respectively. According to Brown, ΔSPL should be equal to 4[dB], and 5[dB] respectively. The largest discrepancies occur for Case C_4, with all HMs correctly predicting a positive ΔSPL with respect to C_1, however the predicted values vary between 11$\div$18[dB], whereas a value of 10[dB] is expected according to Brown. Overall, the predictions of H-KRLS present the lowest deviations with respect to Brown, which is also the HM consistently providing the most accurate predictions.

Figure 6.9(b) presents the results of the same analysis conducted for the peak noise levels predicted by the HMs and the model of [16]. As before, case C_1 is considered as the reference (axis origin), and the relative increase of the peak SPL with respect to this case ΔSPL is evaluated with the HMs and plotted along the y-axis. The x-axis contains the same values (ΔSPL_{PM}) as reported by the model of Bosschers. Similarly to the previous analysis, the HM predictions present a strong correlation with the model of Bosschers. However, they either over- or under-predict the peak SPL increase with respect to the predictions obtained from Bosschers. The lowest discrepancies are observed for case C_2, with all HMs apart from the H-RF estimating that $\Delta SPL = 3 \div 4$, with the estimations obtained from Bosschers being equal to 4[dB]. Slightly higher deviations are observed for case C_3, with differences of $1 \div 4$[dB] being observed between the DDMs and the model of Bosschers. Cases C_4 and C_5 show the highest discrepancies, both among the HMs predictions, and also between the DDMs' predictions and the predictions of Bosschers. The biggest differences are observed for the H-ELM in these cases, whereas the predictions of KRLS are consistently close to the predictions of Bosschers, with near zero deviations being observed for cases C_2 and C_3.

Overall, all HMs provide physically plausible predictions, which are in line with the theoretical models of [15, 16]. The highest discrepancies are observed either with the H-ANN or, occasionally, with the H-ELM. The most consistent HM is H-KRLS, which also provides the highest accuracy according to the discussion in Sections 6.3 - 6.5.

6.9 Optimal parameters of the physics-based model

The high accuracy of the HMs presented in this work can be partially attributed to the quality of the predictions of the PM. From the discussion of Sections 6.3 - 6.5 it is clear that the calibration process greatly improved the accuracy of the PM, with errors being approximately 50% lower for the first two scenarios. For this reason, the optimal values of the PM's parameters are presented and discussed in this section. It should be noted that for every scenario and resampling index slightly different values are obtained, as each $\mathcal{L}_l^r$ varies. However, the values that will be utilised in practice or

Table 6.19: Optimal parameter values for the physics-based models.

Method	Symbol	Equation	Value	Symbol	Equation	Value
Matusiak Model (Section A.3)	β_f	Eq. (A.5)	0.6	m	Eq. (A.6)	5
	n_b^C	Eq. (A.5)	50	c_b	Eq. (A.6)	3.8
	n_{bo}	Eq. (A.11)	300			
ETV Model (Section A.4)	$c_P^{(2)}$	Eq. (A.19)	11.6	c_f	Eq. (A.36)	13.8
	c_{lo}	Eq. (A.37)	3.85	c_{hi}	Eq. (A.37)	-1.86
	c_{fc}	Eq. (A.26)	0.72	c_s	Eq. (A.38)	0.65
	c_a	Eq. (A.35)	118			

further work are the ones obtained when the PM is parameterised on $\mathcal{D}_n$ in its entirety. These values are presented in Table 6.19.

It is worth noting that the values of the calibration constants for the ETV model of Section A.4 showed deviations no more than $\pm 10\%$ compared to the values proposed in [82], in line with their physical interpretation. However, significant differences are observed for the parameters of the Matusiak model, presented in Section A.3, which are worthy of attention due to their inherent physical meaning. More in detail, the parameter n_{bo}, which controls the number of oscillations for which the bubble motion is simulated, has an optimal value of 350[–]. This value corresponds to the upper limit of the bounded space for the calibration process according to Table 4.10. From a theoretical point of view, this implies that bubble motion was simulated as long as possible, until the oscillations have been essentially dampened out. During the model verification phase, it was observed that increasing the number of these oscillations increases the SPLs at high frequencies, with the simulations converging for values higher than $100 \div 150$ depending on the propeller geometry and inflow conditions. The SPLs at the high frequency spectrum are also highly affected by the fractal order m of the size distribution of the bubbles. In general, lower values of m correspond to the generation of a larger number of smaller bubbles in the flow [5]. As reported in Table 6.19, the value of m was reduced from its initial value of 9[–] to 5[–], which indicates the presence of larger bubbles with respect to the initial value. In addition, the gas / vapour fraction β_f was also reduced to 0.6[–] from its initial value of 0.8[–], meaning that 60% of the retreating sheet cavity is shed in the form of bubbles. Furthermore, the constant c_b

that controls the cavity thickness at the point of break-off was increased to a value of 2.8 from the recommended value of 1.8[–] in Table 4.9, signifying the presence of larger bubbles. Finally, the number of bubble classes n_b^C increased from the initial value of 5[–] to 50[–], which corresponds to the upper limit set during the calibration process according to Table 4.10. This allows for the simulation of a larger set of bubble classes, each class containing a smaller number of bubbles, with a different initial radius. This essentially implies the requirement that each bubble be treated individually, as also reported in [164].

6.10 Summary

In this chapter the methodology presented in Chapter 4 has been applied to the series of analyses discussed in Chapter 5. An in-depth comparison of the performance of the various models has been carried out, and a summary of the results is reported in Table 6.20 From these results it is observed that:

- all models commit the lowest errors on Scenario III (LORSO), followed by Scenarios I - II (LOGO and LOWO), which exhibit similar errors;
- considering the performance of each individual model, the errors committed are fairly consistent within each scenario, irrespective of the wakefield (Scenario II - LOWO), propeller geometry (Scenario I - LOGO), or rotational speed (Scenario III - LORSO), being present in the test set;
- the HMs are the most accurate models across all scenarios, followed by the DDMs, and the PM which is consistently the least accurate model. Specifically, the error reduction of the DDMs and HMs with respect to the PM is approximately 30% and 45%, respectively;
- The relative performance of the DDMs and HMs with respect to the PM decreases with the complexity of the scenario: for the least complex LORSO scenario, the DDMs commit approximately 50% lower errors than the PM, whereas for the HMs the same error reduction approaches 60%. On the other hand, for the LOGO scenario, the same error reductions correspond to 35% (DDMs) and 50% (HMs).

Table 6.20: Overall average performance measured according to MAE, MAPE, and PPMCC for the PMs, DDMs, and HMs for the different scenarios examined in this work.

Scenario	Metric	PM	PM$^{\diamond}$	ANN	KRLS	ELM	RF	H-ANN	H-KRLS	H-ELM	H-RF
Scenario I (LOGO)	MAE [dB]	19.3 ± 2.3	7.7 ± 1.0	5.3 ± 1.7	4.5 ± 0.7	5.3 ± 0.9	4.7 ± 0.8	4.5 ± 1.5	3.4 ± 0.5	4.0 ± 0.6	3.6 ± 0.6
	MAPE [%]	18.0 ± 3.1	7.2 ± 1.0	5.1 ± 1.7	4.1 ± 0.7	5.0 ± 0.9	4.6 ± 0.8	4.2 ± 1.2	3.2 ± 0.4	3.8 ± 0.6	3.4 ± 0.6
	10× PPMCC [–]	3.3 ± 2.2	8.2 ± 1.0	8.5 ± 0.7	8.8 ± 0.6	8.7 ± 0.6	8.7 ± 0.6	8.9 ± 0.4	9.2 ± 0.3	9.1 ± 0.3	9.1 ± 0.3
Scenario II (LOWO)	MAE [dB]	19.3 ± 3.0	8.7 ± 1.3	7.3 ± 1.8	5.1 ± 1.4	6.4 ± 1.6	6.0 ± 1.5	5.2 ± 2.4	4.1 ± 0.9	4.7 ± 1.1	4.7 ± 1.0
	MAPE [%]	18.0 ± 3.1	8.4 ± 1.3	6.8 ± 1.6	4.8 ± 1.3	6.3 ± 1.5	5.6 ± 1.3	4.8 ± 2.4	3.8 ± 1.0	4.4 ± 1.0	4.4 ± 0.9
	10× PPMCC [–]	3.3 ± 2.2	7.9 ± 1.1	8.1 ± 1.2	8.6 ± 0.7	8.4 ± 0.8	8.5 ± 0.8	8.9 ± 0.5	9.1 ± 0.3	8.9 ± 0.3	9.0 ± 0.3
Scenario III (LORSO)	MAE [dB]	19.3 ± 3.0	7.0 ± 1.1	3.6 ± 0.5	3.6 ± 0.6	4.2 ± 0.6	4.2 ± 0.6	3.0 ± 0.5	3.0 ± 0.5	3.5 ± 0.5	3.5 ± 0.5
	MAPE [%]	18.0 ± 3.1	6.6 ± 1.0	3.2 ± 0.4	3.2 ± 0.5	4.0 ± 0.5	3.8 ± 0.5	2.8 ± 0.4	2.8 ± 0.4	3.3 ± 0.4	3.2 ± 0.3
	10× PPMCC [–]	3.3 ± 2.2	8.1 ± 0.7	8.9 ± 0.5	8.9 ± 0.4	8.8 ± 0.6	8.8 ± 0.4	9.3 ± 0.3	9.3 ± 0.4	9.1 ± 0.6	9.2 ± 0.4

As expected, the advantage of an HM becomes more evident with increasingly complex extrapolation scenarios.

- The performance of the various DDMs is similar, except for the SNN which is consistently the least accurate DDM. RF, ELM, and KRLS experience relatively small performance differences across all scenarios with KRR being the top performing DDM. One exception is Scenario III (LORSO), in which the ANN commits slightly lower errors, however the differences between the two is not statistically significant. Similar conclusions can be drawn for the HMs, with the HM based on KRR being the top performing model for all scenarios;
- The PM is able to capture the general trends of the URN spectrum, however it tends to underestimate the noise levels at frequencies higher than 500[Hz]. The DDMs exhibit the opposite behaviour, with the highest accuracy being observed for frequencies lower than 1[kHz]. Finally, the HMs, leveraging on the advantages of both the PM and DDMs, are able to capture the noise levels over the entire frequency range.
- On Scenario IV both the propeller geometry and inflow conditions where different than the ones used to develop the models, constituting an even more difficult extrapolation scenario. Also in this case the HM provided predictions of high quality, with an average error lower than 10[%].

In all scenarios, the HMs showed remarkable ability to predict the URN spectra, with errors lower than 7[%] being reported. Furthermore, a set of analyses was conducted in order to better understand the DDMs and HMs. In particular, the author assessed whether they are able to learn theoretically grounded input-output relationships, and whether the predictions provided agree with general theory on cavitation noise. Both analyses provided results that confirm the feasibility of the proposed approach. On several occasions, the variance of the results did not allow the author to draw statistically significant conclusions with respect to the relative performance of each DDM and HM. Nevertheless, the HMs have generally shown sufficient capabilities in predicting the URN spectra, with errors that are certainly acceptable during early stage design.

Chapter 7

Conclusions

In this work, the problem of accurately predicting noise from cavitating marine propellers at an early design stage has been addressed. Physics-based, data-driven, and hybrid models have been investigated. In general, physics-based models rely on the knowledge of the phenomena under consideration and can be quite accurate and reliable, at the expense of huge computational requirements which prevent their use during design stage. On the other hand, data-driven models rely on historical observations of the phenomena. They can be computationally inexpensive and accurate, but may produce physically implausible results. Hybrid models provide the best of both worlds, combining the knowledge encapsulated in physical models with the robust statistical learning methods exploited by data-driven models. In this work, the hybrid models developed originate from computationally inexpensive physics-based models, relying primarily on semi-empirical formulas, with state-of-the-art data-driven models from the field of Machine Learning. This allows them to combine the strengths of each model family, while limiting its corresponding weaknesses. In addition, considering that current hybridization approaches do not fully achieve their true potential, as they naively combine physics-based and data-driven models without actually blending them, a novel hybridization strategy has been proposed, able to truly blend the knowledge of the phenomena with the information contained in the historical data. This strategy produces models that are able to properly, i.e., physically plausible, extrapolate as physics-based model, while also being extremely accurate and computationally inex-

pensive as data-driven models.

The models have been developed and tested on an extensive set of experiments conducted on six propellers and three wakefields, at a variety of operating conditions that resemble real-world scenarios encountered in practice. More specifically, the extrapolation tests that have been conducted include:

- extrapolation on the rotational speed, in which the models are tested with previously unseen rotational speeds;
- extrapolation on the wakefield, in which the models are tested with previously unseen wakefields,
- extrapolation on the propeller geometry, in which the models are tested with previously unseen geometries.
- simultaneous extrapolation on propeller geometry, wakefield, and rotational speed.

Additional tests have been conducted to test their robustness on significantly different propeller geometries and inflow conditions, as well as their agreement with prior knowledge on the physics of cavitation and noise modelling.

All tests conducted in this work have demonstrated that the hybrid models have excellent predictive capabilities, robustness in extrapolation, and they are able to capture the noise levels due to tip-vortex and sheet cavitation from a variety of propeller geometries and inflow conditions. The proposed hybrid models consistently demonstrate the lowest average errors in all scenarios, with various tests showing that the top performing hybrid model learns and delivers predictions which are in agreement with the state-of-the-art engineering knowledge of the phenomena.

The approach proposed is certainly promising, however further validations are needed, which have to be the object of future work. The most important aspect is to test the capability of the proposed approach to predict cavitation noise for a much larger variety of propeller geometries and/or wakefields, significantly different from those used to learn the various models. The extrapolation scenarios conducted in this work can be considered as the first tests towards understanding, and most importantly trusting, these models. From this point of view, a much needed development is the enlargement of the existing dataset. The dataset applied thus far, although extensive,

is still limited with respect to propeller geometries and wakefield characteristics. As such, future efforts should be made to enlarge it and improve the generalisation abilities of these models. In addition, more accurate cavitation extent estimations should be incorporated by means of sophisticated Computational Fluid Dynamics methods, such as RANS, DES and LES, as well as precise vortex noise prediction procedures by 3D analysis of the flow around a cavitating vortex. Finally, the use of the proposed models should be investigated for design optimisation studies with multiple and conflicting operating goals, towards the development of unconventional propeller designs.

Appendix A

Physics-based Models

Abstract

This chapter gives an overview of the physics-based models utilised to provide an estimation of the URN spectra for the HM, with limited computational requirements.

A.1 Introduction

In the following an overview of the PMs employed to estimate the noise spectra from cavitating marine propellers will be provided. Focus has been given on the identification and implementation of low-computational-cost methodologies that can provide predictions of acceptable accuracy. To this aim, three methodologies will be discussed in the following, the combination of which can provide a first estimation of the noise spectra from cavitating marine propellers. More specifically:

- A panel method is discussed in Section A.2, which is utilised to estimate the hydrodynamic performance of the propellers in non-uniform inflow conditions,
- the semi-empirical model of Matusiak [5] is presented in Section A.3, to estimate the broadband effects of sheet cavitation,
- the Empirical Tip Vortex (ETV) model of Bosschers [82] is discussed in Section A.4, to estimate the radiated noise due to the presence of a tip vortex cavities.

Finally, Section A.5 summarises the most important points of this chapter.

A.2 Hydrodynamic Performance

Unsteady hydrodynamic computations are performed by means of an in-house developed Boundary Element Method (BEM) code that can provide a sufficient (for the goal of the analysis), characterisation of the hydrodynamic field of the propeller at an acceptable computational cost [254, 255, 261, 364]. The utilised implementation has been verified for a variety of propeller types, including supercavitating [227], ducted [224], and tip loaded propellers [49], and for cavitating flows in both steady [260] and unsteady conditions [255], for strongly non-homegeneous wakefields in [254, 261], and for very off-design conditions in [262].

BEM models the flow field around a solid body using a scalar function, the perturbation potential ϕ, whose spatial derivatives represent the perturbation velocity vector components. Irrotationality, incompressibility, and the absence of viscosity are the hypotheses needed in order to express the continuity equation as a Laplace equation for the perturbation potential as follows:

$$\nabla^2 \phi(\boldsymbol{z}, t) = 0. \tag{A.1}$$

For the more general problem of cavitating flows, Green's third identity allows to solve the three dimensional differential problem as a simpler integral problem written only for the surfaces that bound the domain. In the context of non-cavitating flows, these surfaces include the fully wetted surface of the blades (s_B) and of the hub (s_h) plus the trailing wake surface s_w. The latter refers to the zero thickness layer, which departs at the trailing edge of the lifting surfaces, where vorticity is shed onto the downstream flow, as shown in Figure A.1. The solution is obtained as the intensity of a series of mathematical singularities distributed on the boundaries (i.e. dipoles $-\phi$ and sources $\frac{\partial \phi}{\partial e}$), for which superposition models the perturbation potential and then the inviscid flow in the entire computational domain [90] as

$$2\pi\phi\left(\tilde{\boldsymbol{z}}, t\right) = \int_{s_w} \Delta\phi_{\mathrm{w}}\left(\boldsymbol{z}, t\right) \frac{\partial}{\partial \boldsymbol{e}} \frac{1}{\boldsymbol{d}} ds +$$

$$+\int_{s_B+s_h}\phi\left(\boldsymbol{z},t\right)\frac{\partial}{\partial \boldsymbol{e}}\frac{1}{\boldsymbol{d}}ds-\int_{s_B+s_h}\frac{\partial\phi(\boldsymbol{z},t)}{\partial \boldsymbol{e}}\frac{1}{\boldsymbol{d}}ds, \tag{A.2}$$

where $\boldsymbol{e}$ is the unit normal, $\boldsymbol{d}$ is the distance between points $\tilde{\boldsymbol{z}}$ and $\boldsymbol{z}$, and Δ denotes the potential jump (i.e., the net dipole intensity) across the wake surface.

Numerically, as presented for instance in [365, 366], Equation (A.2) leads to a linear system of equations, one for each of the panels that discretize the propeller surface that can be iteratively solved at each discrete time step. The numerical solution consists of an inner iterative scheme that solves the non-linearities related to the Kutta condition at the blade trailing edge and an outer iterative cycle to integrate over time by shedding in the wake the correct amount of vorticity in accordance with Kelvin's theorem that drives the unsteadiness of the problem

$$\frac{D}{Dt}\left(\Delta\phi_w(\boldsymbol{z},t)\right)=0 \tag{A.3}$$

To this aim, the *key-blade* approach proposed by [365] is exploited: only one blade (plus its wake and portion of the hub) is solved while the influence of other blades is accounted iteratively during propeller revolutions until a periodic solution after the numerical transient is achieved.

Once solved, Equation (A.2) provides the value of the perturbation potential whose derivatives, with respect to an appropriate reference system and time, together with the application of the unsteady Bernoulli's theorem, allow the computation of the time-dependent pressure and forces, as

$$\frac{d\phi(\boldsymbol{z},t)}{dt}+\frac{p}{\rho}+\frac{\left|u_\infty+\nabla\phi(\boldsymbol{z},t)\right|^2}{2}+g\boldsymbol{z}=\frac{p_\infty}{\rho}+\frac{\left|u_\infty\right|^2}{2}, \tag{A.4}$$

where p_∞, u_∞ correspond to the reference pressure and undisturbed velocity on an appropriate reference system, and ρ refers to the fluid density.

In the analyses conducted in this work, a surface mesh for the key-blade of approximately 1000 panels plus 360 on the hub is utilised, as presented in Figure A.1. Cosinusoidal spacing is employed for $u = 44$ panels in the chord-wise direction, to increase the discretisation accuracy on the leading and trailing edges of the blade, and

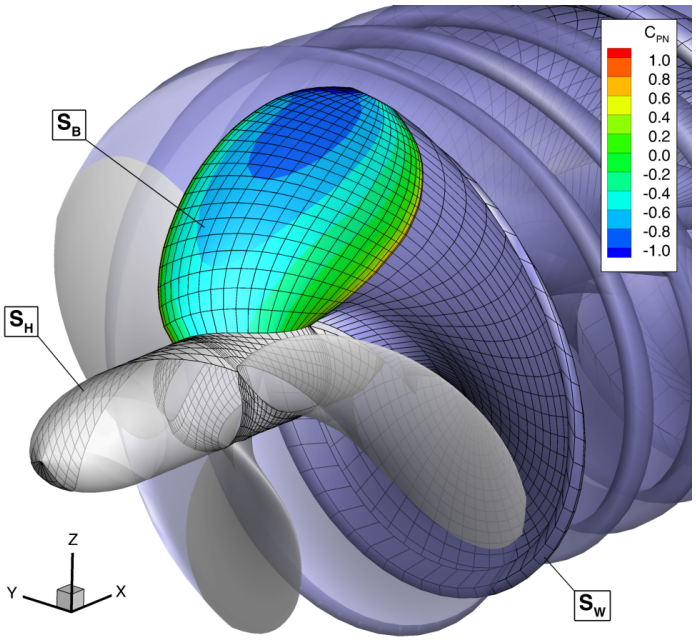

Figure A.1: Mesh arrangement on one propeller surface.

$s = 22$ sections are distributed, following a geometric progression on the radial direction. Although the discretization of the propeller geometry is considered on a case-by-case basis depending on inflow conditions and geometrical details, the number of panels employed provides acceptable discretization accuracy for conventional geometries, with an acceptable computational cost [254, 261, 364].

The trailing vortical wake extends for 8 revolutions with a spatial discretization corresponding to an equivalent time step $\Delta\theta$ of 6 [deg], or $\Delta t = \Delta\theta/\omega_p$, with ω_p being the angular velocity of the propeller. Having computed the unsteady pressures $\boldsymbol{p} \in \mathbb{R}^s$ at the $\boldsymbol{r}_p = \{r_p^{(1)}, \cdots, r_p^{(s)}\}$ radial sections of Figure A.1, the sheet cavity lengths and areas $\boldsymbol{l}_c \in \mathbb{R}^s$, $\boldsymbol{a}_c \in \mathbb{R}^s$ can also be straightforwardly estimated from $\boldsymbol{p}$, using for instance the method of Geurst [367].

A.3 Broadband Effects of Sheet Cavitation

The prediction of the noise levels in the frequency range, between 10 - 80[kHz] are mostly dominated by sheet and bubble cavitation and have been accounted for with the semi-empirical model of Matusiak [5], referred to as the "Matusiak model" hereafter.

A.3.1 Generation of free cavitation bubbles

Attached sheet cavitation on a propeller blade initiates and grows while an upcoming propeller blade enters the wake peak. After the sheet cavity volume reaches its maximum, it starts to retreat, a process which is associated with parts of the cavity breaking off into bubble clouds. The Matusiak model assumes spherical bubbles, excludes condensation, disregards the spanwise flow of vapour and gas mixture contained by the cavitation sheet towards the blade tip, as well as the effect of the solid boundary on the dynamics of the bubbles. Considering a single time step dt, it further assumes that any change in the volume $\boldsymbol{v}_b^{(i)} \in \mathbb{R}^s$ of bubble i from the $\boldsymbol{n}_b \in \mathbb{R}^s$ bubbles generated at $\boldsymbol{r}_p$, equals the rate at which the sheet cavity volume decreases, multiplied by the gas-vapour fraction β_f. This is represented as

$$\frac{d}{dt}\left(\sum_{i=\mathbf{1}}^{\boldsymbol{n}_b} \boldsymbol{v}_b^{(i)}\right) = \frac{d}{dt}\left(\boldsymbol{n}_b^\intercal \bar{\boldsymbol{v}}_b\right) = \begin{cases} -\beta_f \frac{d\boldsymbol{a}_c^\intercal}{dt} d\boldsymbol{r}, & \text{for } \frac{d\boldsymbol{a}_c^\intercal}{dt} < 0 \\ \mathbf{0}, & \text{otherwise} \end{cases} \tag{A.5}$$

where $\bar{\boldsymbol{v}}_b \in \mathbb{R}^s$ refers to the average volume of all the bubbles generated due to cavity break-off in the vicinity of each section within a time step.

A.3.2 Size distribution of the cavitation bubbles

The remainder of Section A.3 focuses on the analysis required for a single bubble i from the $n_b^{(j,k)}$ bubbles with average volume $\bar{v}_b^{(j,k)}$, generated in the vicinity of a section $r_p^{(j)}$ at time $t^{(k)},\ k \in \{0, \cdots, q\}$, having a radius $r_b^{(i,j,k)}$ and volume $v_b^{(i,j,k)}$, due to the break-off a cavity in the vicinity of $r_p^{(j)}$ characterised by $a_c^{(j,k)}$, $l_c^{(j,k)}$. Unless necessary, simplified notation will be adopted until the end of Section A.3.3 for the sake of readability, by omitting the index notation and redefining $r_b \coloneqq r_b^{(i,j,k)}$, $v_b \coloneqq v_b^{(i,j,k)}$, $n_b \coloneqq n_b^{(j,k)}$, $\bar{v}_b \coloneqq \bar{v}_b^{(j,k)}$, $a_c \coloneqq a_c^{(j,k)}$, $l_c \coloneqq l_c^{(j,k)}$.

The initial size of a bubble generated as an effect of the fixed cavity break-off is represented by a β-distribution, having a Probability Density Function (PDF) κ_b as

$$\kappa_b(r_b^*) = m(1 - r_b^*)^{m-1}, \quad r_b^* = \frac{2r_b}{\tau_c}, \quad \tau_c = c_b \frac{a_c}{l_c}, \tag{A.6}$$

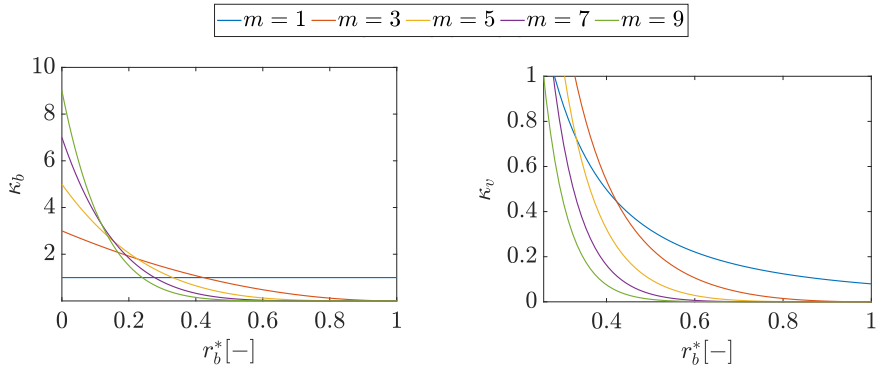

(a) Radius. (b) Volume.

Figure A.2: Radius and volume PDFs of the cavitation bubbles generated as the result of the tearing-off of the fixed cavity.

where $m \in \mathbb{P}$, $c_b \in \mathbb{R}^+$ are calibration constants, r_b^* is the non-dimensional bubble radius, and τ_c is the (fixed) cavity thickness at the point of break-off. A visual impression of p_b for various values of m is presented in Figure A.2(a). The choice of m is known to have a significant effect on the noise prediction of the model [164]. Higher values imply that small bubbles with high resonance frequencies dominate the spectrum, whereas smaller values simulate the generation of bigger and fewer bubbles.

The volume PDF $\kappa_v(v_b)$ of the bubbles is obtained from Equation (A.6), considering that $v_b(r_b) = {}^4\!/_3 \pi r_b^3$ for a spherical bubble, according to

$$\kappa_v(r_b) = \kappa_b(r_b)\frac{dr_b}{dv_b} = \frac{m}{4\pi}\frac{(1-r_b)^{m-1}}{r_b^2}, \tag{A.7}$$

with the mean volume of all the bubbles generated being

$$\bar{v}_b = \left(\frac{\tau_c}{2}\right)^3 \int_0^{v(1)} v f_v(v) dv. \tag{A.8}$$

Assuming that $\bar{v}_b$ remains constant within one time-step, the total number of bubbles generated can be estimated as

$$n_b = -\frac{\beta_f}{\bar{v}}\frac{da_c}{dt}dr. \tag{A.9}$$

A.3.3 Bubble dynamics

The newly-generated bubbles are transported towards the trailing edge at the local velocity of the flow u, and the blade pressure is assumed to increase monotonically from the vapour pressure p_v, to the static pressure p_{te} at the trailing edge. Under the assumption of linear pressure growth, the ambient pressure at the location of the bubble can be approximated as

$$p_b(t) = p_v + \frac{t}{t_{\mathrm{te}}}(p_{\mathrm{te}} - p_v), \quad t_{\mathrm{te}} = (u_s - l_c)/u, \tag{A.10}$$

with t_{te} being the bubble travelling time to the trailing edge, and u_s being the local sound velocity.

To compute the pressure trace generated by each bubble, a bubble dynamics equation must be integrated over time. In this work, the Gilmore [320] equation is employed, as suggested by [5]. Nevertheless, the choice of the bubble dynamics equation can significantly affect the results obtained by the Matusiak model and are worth investigating [164]. Possible alternatives include the Rayleigh-Plesset [167, 368], Keller and Miksis [369], and Flynn [370] equations. For the sake of completeness, these are briefly discussed in Appendix B. More detailed descriptions can be found in [256].

The Gilmore equation can be solved analytically for constant internal bubble pressure (p_{bi}), and approximately for a linearly increasing p_{bi}. Utilising Newton's notation for the time derivative, it is given by

$$\left(1 - \frac{\dot{r}_b(t)}{\zeta_1(r_b)}\right) r_b(t)\ddot{r}_b(t) + \frac{3}{2}\left(1 - \frac{\dot{r}_b(t)}{3\zeta_1(r_b)}\right)\dot{r}_b^2(t) = \left(1 + \frac{\dot{r}_b(t)}{\zeta_1(r)}\right)\zeta_2(r_b) + \left(1 - \frac{\dot{r}_b(t)}{\zeta_1(r_b)}\right)\frac{r_b(t)}{\zeta_1(r_b)}\dot{\zeta}_2(r_b). \tag{A.11}$$

Assuming isentropic compression and linearly increasing pressure, the terms ζ_1, ζ_2, and $\dot{\zeta}_2$ are evaluated as

$$\zeta_1(r_b) = \zeta_{1_0}\left[\frac{1}{p_b(t) + c_{\mathrm{T}}^{(0)}}\left(p_v + p_{g,0}\left(\frac{r_{b,0}}{r_b}\right)^{3c_{\mathrm{pi}}} - 2\frac{c_{\mathrm{st}}}{r_b} + c_{\mathrm{T}}^{(0)}\right)\right]^{\frac{c_{\mathrm{T}}^{(1)}-1}{2c_{\mathrm{T}}^{(1)}}}, \tag{A.12}$$

$$\zeta_2(r_b) = \frac{c_{\mathrm{T}}^{(1)}}{c_{\mathrm{T}}^{(1)} - 1} \frac{p_b + c_{\mathrm{T}}^{(0)}}{\rho} \left[\left(\frac{p_{\mathrm{bi}} + c_{\mathrm{T}}^{(0)}}{p_b + c_{\mathrm{T}}^{(0)}} \right)^{\frac{c_{\mathrm{T}}^{(1)} - 1}{c_{\mathrm{T}}^{(1)}}} - 1 \right], \tag{A.13}$$

$$\begin{aligned} \dot{\zeta}_2(r_b) = {} & \frac{p_{\mathrm{bw}}}{p_v + p_{\mathrm{bw}} t + c_{\mathrm{T}}^{(0)}} \zeta_2 - \frac{p_{\mathrm{bw}}}{\rho} \left(\frac{p_{\mathrm{bi}} + c_{\mathrm{T}}^{(0)}}{p_v + p_{\mathrm{bw}} t + c_{\mathrm{T}}^{(0)}} \right)^{\frac{c_{\mathrm{T}}^{(1)} - 1}{c_{\mathrm{T}}^{(1)}}} + \\ & + \frac{\dot{r}_b}{\rho r_b} \left(\frac{p_v + p_{\mathrm{bw}} t + c_{\mathrm{T}}^{(0)}}{p_{bi} + c_{\mathrm{T}}^{(0)}} \right)^{\frac{1}{c_{\mathrm{T}}^{(1)}}} \left[\frac{2 c_{\mathrm{st}}}{r_b} - 3 c_{\mathrm{pi}} p_{g,0} \left(\frac{r_{b,0}}{r_b} \right)^{3 c_{\mathrm{pi}}} \right], \end{aligned} \tag{A.14}$$

$$p_{\mathrm{bw}} = \frac{p_0 - p_v}{t_{\mathrm{te}}}, \tag{A.15}$$

where $c_{\mathrm{T}}^{(0)}$ and $c_{\mathrm{T}}^{(1)}$ are the constants of Tait's law of compressibility, $p_{g,0}$ is the initial gas pressure, c_{pi} is the polytropic index, c_{st} is the surface tension coefficient, and p_{bi} corresponds to the internal bubble pressure. The subscript 0 refers to initial values within the current time-step, and p_{bw} describes the linearly increasing pressure on the liquid side of the bubble wall.

The constants specified by Matusiak for the Gilmore equation are given in Table A.1, and it is also mentioned in [5] that $p_{g,0} = p_v$. It is worth noting that a refinement of the Gilmore equation was suggested in Leighton [371], where it was proposed to directly compute p_{g0} on the basis of the initial (undisturbed) pressure outside the bubble and its surface tension. Nevertheless, this suggestion did not increase the predictive capabilities of the model, as reported in Lafeber et al. [164].

Subsequently, the acoustic pressure $p_{b,\infty}$ caused at a point in the fluid domain at a radial distance $r \gg r_b$ by the oscillations of the bubble can be evaluated as [5]

$$p_{b,\infty} = \frac{\rho}{4\pi r} \ddot{v}_b \left(t - \frac{r}{u_s} \right), \tag{A.16}$$

$$\ddot{v}_b = 4\pi \left(r_b^2 \ddot{r}_b + 2 r_b \dot{r}_b^2 \right). \tag{A.17}$$

To ensure a random instant of bubble generation within an interval $\Delta\theta$, the time-traces obtained for each bubble are offset by a time delay $t_d \sim \mathcal{U}(t, t + \Delta t)$.

Table A.1: Constants of Gilmore equation [5]

Parameter	Symbol	Value [5]	Units
Polytropic index	c_{pi}	1.4	[–]
Tait's law constant	$c_{\mathrm{T}}^{(0)}$	3×10^8	[Pa]
Tait's law constant	$c_{\mathrm{T}}^{(1)}$	7	[–]

A.3.4 Spectral analysis

As stated in the beginning of Section A.3, the above analysis is performed for every time step $t^{(k)}$ and each radial section $r_p^{(j)}$ of the key-blade. If the local cavity is shrinking, i.e., a bubble cloud is generated, $n_b^{(j,k)}$, $\bar{v}_b^{(j,k)}$ are evaluated. Let $\mathcal{B} = \left\{(n_b, \bar{v}_b) : n_b \in \boldsymbol{N}_b, \bar{v}_b \in \bar{\boldsymbol{V}}_b\right\}$, with $\boldsymbol{N}_b = \left[n_b^{(j,k)}\right]_{s\times q}$, $\bar{\boldsymbol{V}}_b = \left[\bar{v}_b^{(j,k)}\right]_{s\times q}$ be the set of all (n_b, $\bar{v}_b$) pairs evaluated for one blade passage period t_{bp}. If r_b on Equation (A.6) is discretized with a small fixed number n_b^C of r_b^*, $\mathcal{B}$ will have limited cardinality. By solving the Gilmore equation only for the members of $\mathcal{B}$, instead of each individual bubble, the computational complexity of the model will be significantly reduced, at the expense of accuracy. In this work, n_b^C is treated as a calibration constant, and the Gilmore equation is solved with the 4^{th} order Runge-Kutta method [372] for a fixed number of oscillations (n_{bo}), also considered a calibration constant.

This procedure is applied to all members of $\mathcal{B}$, with the summation of all time traces over all blades, after the appropriate time-shift is applied, forming the total field pressure $\boldsymbol{p}_{\mathrm{tf}}$. Subsequently, the Fast Fourier Transformation [373] of $\boldsymbol{p}_{\mathrm{tf}}$ is evaluated, yielding the complex pressure spectrum $\boldsymbol{p}_{\mathrm{rms}}(\boldsymbol{f})$, for the frequency $\boldsymbol{f} \in \mathbb{R}_{>0}^u$ with resolution $\Delta f = {}^1/_{\Delta t}$. Subsequently, the one-sided spectral density of the pressure is obtained, from which the source level spectrum $\boldsymbol{S}_{\mathrm{pl}}^1(\boldsymbol{f})$ in 1[Hz] band can be obtained [374], according to

$$\boldsymbol{S}_{\mathrm{pl}}^1(\boldsymbol{f}) = 20 \log_{10}\left(\frac{\boldsymbol{p}_{\mathrm{rms}}(\boldsymbol{f})}{p_{\mathrm{ref}}}\right), \tag{A.18}$$

where p_{ref} is a reference pressure value, equal to 1[μPa] for water.

As per standard practice, the spectrum is converted to ${}^1/_3$ octave band $\boldsymbol{S}_{\mathrm{pl}}(\boldsymbol{f})$ and corrected to a standard measuring distance of 1[m] using the spherical acoustic wave

propagation relationship [375]. For the sake of completeness, an overview of the model is provided in Algorithm A.1.

Algorithm A.1: Matusiak Model

Input: $\boldsymbol{P}, \boldsymbol{L}_c, \boldsymbol{A}_c, \boldsymbol{f}, \boldsymbol{r}, \Delta_t, s, q$
Parameters : $\beta_f, m, p_v, p_{\mathrm{g},0}, n_b^C, n_{\mathrm{bo}}, c_b, c_{\mathrm{pi}}, c_{\mathrm{T}}^{(0)}, c_{\mathrm{T}}^{(1)}, c_{\mathrm{st}}$
Result: $\boldsymbol{S}_{\mathrm{pl}}(\boldsymbol{f})$
$\boldsymbol{p}_{\mathrm{tf}} \leftarrow \boldsymbol{0}$ `// Total field pressure vector`
`/* Loop over all timesteps */`
for $k \leftarrow 1$ **to** q **do**
  $t^{(k)} \leftarrow k \cdot \Delta t$
  `/* Loop over all radial sections */`
  for $j \leftarrow 1$ **to** s **do**
    if $\left(A_c^{(j,k)} - A_c^{(j,k-1)}\right) {}^{1}/_{\Delta t} < 0$ **then**
      `/* Loop over all bubble classes */`
      for $i \leftarrow 1$ **to** n_b^C **do**
        Evaluate $\bar{v}^{(i,j,k)}$ according to Eq. (A.8)
        Evaluate $n_b^{(i,j,k)}$ according to Eq. (A.9)
        Evaluate $\boldsymbol{r}_b^{(i,j,k)}(\boldsymbol{t}_b)$ according to Eqs. (A.11) - (A.14)
        Evaluate $\boldsymbol{p}_b^{(i,j,k)}(\boldsymbol{t}_b)$ according to Eq. (A.16) - (A.17)
        $\boldsymbol{t}_b \leftarrow \boldsymbol{t}_b + t_d,\ t_d \sim \mathcal{U}(t, t + \Delta t)$ `// Random time offset`
        $\boldsymbol{p}_{\mathrm{tf}}(\boldsymbol{t}_b) \leftarrow \boldsymbol{p}_{\mathrm{tf}}(\boldsymbol{t}_b) + \boldsymbol{p}_b^{(i,j,k)}(\boldsymbol{t}_b)$
      end
  end
end
Evaluate $\boldsymbol{S}_{\mathrm{pl}}(\boldsymbol{f})$ according to Eq. (A.18)

A.4 Tip Vortex Induced Noise

For the estimation of URN due to Tip Vortex Cavitation TVC, the ETV model is employed [82], which is a semi-empirical model based on the TVI method of Raestad [168]. TVI relates the measured URN to the predicted size of the vortex cavity, using a computed circulation distribution on the propeller blade. The ETV model follows a similar approach, but it predicts the broadband spectrum of URN slightly differently. The vortex cavity size is predicted using a vortex model, which requires as input the vortex strength and the size of the viscous core. The vortex strength is obtained from the hydrodynamic performance analysis according to Section A.2. Subsequently, the vortex cavity is estimated, and is used in semi-empirical relations to estimate the

resonance frequency of the vortex and the corresponding sound pressure level, and subsequently the broadband hump of the URN spectrum [82].

A.4.1 Vortex cavity size

To compute the frequency and noise amplitude due to vortex pulsation, the cavity radius r_{vc}, which is defined as the radial distance from the vortex center, has to be estimated. This estimation requires the use of a vortex model. Among the several vortex models available in the literature the Proctor vortex model [376] has been utilised. The Proctor model assumes constant axial velocity, which occurs on two-dimensional and axisymmetric flows, negligible radial velocity with respect to the tangential velocity, and constant velocity distribution in the azimuthal direction. Under these assumptions, the azimuthal velocity profile $v_\theta(r)$ is given by

$$v_\theta(r) = \begin{cases} 1.094\frac{\Gamma}{2\pi r}\left[1-\exp\left(-c_P^{(2)}\left(\frac{2.8r_{\mathrm{v}}}{D}\right)^{c_P^{(1)}}\right)\right]\left[1-\exp\left(-c_P^{(0)}\left(\frac{r}{r_{\mathrm{v}}}\right)^2\right)\right], & \text{for } r \leq 1.4r_{\mathrm{v}} \\ \frac{\Gamma}{2\pi r}\left[1-\exp\left(-c_P^{(2)}\left(\frac{2r}{D}\right)^{c_P^{(1)}}\right)\right], & \text{for } r > 1.4r_{\mathrm{v}} \end{cases} \tag{A.19}$$

where Γ is the circulation on the tip blade section, D is the propeller diameter, and r_{v} corresponds to the viscous core radius. Furthermore, $c_P^{(0)} = 1.26$, $c_P^{(1)} = 0.75$ as suggested in [377], and $c_P^{(2)}$, which was set equal to 10 in [377], is considered a calibration constant. Several other semi-empirical vortex models are available in the literature and can be employed instead of the Proctor vortex model. A brief overview of those is provided in Appendix C, whereas a comparison of most common models with experimental data can be found in [378], and a complete treatise is given in [2].

As can be seen from Equation (A.19), the Proctor vortex model is characterised by the following unknown quantities: the viscous core radius, and the circulation on the tip blade section. The viscous core radius is an input which may differ for every propeller and functioning condition, and ideally its values should have been computed based on direct measurements of the azimuthal velocity distribution. Unfortunately, these measurements are not readily available during the early stages of the design process, hence a different strategy for the estimation of r_{v} is adopted. A first approximation can be

Table A.2: Model scale propeller used in [18].

Variable	Value	Units	Variable	Value	Units
Z	3	[–]	D	305.5	[mm]
$c_{0.95}$	84.6	[mm]	J	0.833	[–]
n	10	[Hz]	u_a	2.54	[m/s]
$u_{0.95\mathrm{r}}$	7.17	[m/s]	$Re_{0.95\mathrm{r}}$	7.99×10^5	[–]
r_v	0.915	[mm]			

obtained from analysis of data available in the literature. To this aim, reference values from Jessup [18] can be utilised. The authors of [18] have conducted Laser Doppler Velocimetry measurements in a cavitation tunnel for a 3-bladed propeller model, whose main characteristics are reported in Table A.2. The Reynolds number is based on the chord length $\mathtt{c}$ and on the resultant velocity at $0.95r$. Since the viscous core size is dependent on the Reynolds number, the values derived by the measurements of Jessup must be scaled to the current case study. This can be accomplished according to the law of McCormick [379]

$$\frac{r_v}{\mathtt{c}} = \left(\frac{r_v}{\mathtt{c}}\right)_{\mathrm{ref}} \left(\frac{Re}{Re_{\mathrm{ref}}}\right)^{\frac{m}{2}}. \tag{A.20}$$

The exponent m has been estimated by the formula proposed by Shen et al. [380]

$$m = 5.16 \log\left(\frac{\log Re}{\log Re_{\mathrm{ref}}}\right)\left[\log\left(\frac{Re}{Re_{\mathrm{ref}}}\right)\right]^{-1}. \tag{A.21}$$

According to this approach, the value of m decreases as the Reynolds number increases, approaching zero at the limit of very high Reynolds numbers. This agrees well with the evidence that the effects of viscocity on cavitation diminish as the Reynolds number approaches infinity, analogous to the general trend of flow to become inviscid at higher Reynolds numbers. This scaling provides a first reasonable estimate of the viscous core. Nevertheless, the viscous core size may also depend on other variables not considered in the scaling, and subsequently the scaled values may not allow to obtain a very good agreement with any available data. For this reason, the obtained values for r_v have been adjusted utilising a constant multiplication factor, as also suggested by Miglianti et al. [11], which is considered a calibration constant.

The vortex strength is generally not known but it can be related to the blade

circulation at a large blade radius, with the latter being evaluated with the BEM method of Section A.2. This circulation, for a propeller operating in non-uniform inflow, is naturally dependent on the blade position, which results in a variable vortex strength during one complete revolution. As a consequence, the cavitating vortex radius, and its corresponding resonance frequency is also dependent on the blade position. However, a unique value should be used in the employed model, representing the prevalent vortex strength. Different approaches can be considered, such as evaluating the average over one complete revolution, the maximum, or percentiles. Arbitrarily, the average value over a complete blade revolution has been utilised in this work.

With all the quantities of v_θ fully defined, the pressure distribution can be obtained by integrating the momentum equation in the radial direction [378], according to

$$\frac{1}{\rho}\int_{p_v}^{p_\infty} dp = \int_{r_{\text{vc}}}^{\infty} \frac{u_\theta^2(r)}{r} dr, \tag{A.22}$$

from which the cavity radius can be evaluated as the radial position for which

$$p_v \geq p(r) - p_\infty. \tag{A.23}$$

A.4.2 Resonance frequency of a cavitating vortex

The resonance frequency of a cavitating vortex can be estimated following the theory of the single gas bubble. Different formulations exist in the literature [272, 381, 382], with various degrees of complexity. In this work, the formulation of Minnaert [382] has been utilised, according to which the resonance frequency of a single bubble of gas immersed in an infinite domain of water, neglecting the effects of surface tension and viscous attenuation, can be approximated from

$$f_{\text{vc}} = \frac{1}{r_{\text{vc}}}\left(\frac{\Delta p}{\rho}\right)^{0.5} \tag{A.24}$$

with Δp being the pressure difference inside and outside of the bubble. For cavitating vortices, this pressure difference is related to the cavitation index evaluated at the blade

tip σ_{tip} as

$$f_{\text{vc}} \propto \frac{1}{r_{\text{vc}}} \sqrt{\sigma_{\text{tip}}} n D, \tag{A.25}$$

or alternatively

$$\frac{f_{\text{vc}}}{f_{\text{bp}}} \propto \frac{D}{r_{\text{vc}}} \frac{\sqrt{\sigma_{\text{tip}}}}{Z} = c_{\text{fc}} \frac{D}{r_{\text{vc}}} \frac{\sqrt{\sigma_{\text{tip}}}}{Z}, \tag{A.26}$$

from which r_{vc} can be evaluated by the procedure of Section A.4.1, c_{fc} is a calibration constant indicating the relative loading between blade and tip, and f_{bp} refers to the blade passing frequency.

A.4.3 Noise level of a cavitating vortex

The acoustic power for a spherical pressure wave is proportional to the second power of the acoustic pressure. The power is given by Equation (A.18). Considering a cavitating vortex, its noise level $S^1_{\text{pl,max}}$ can be evaluated with respect to the non-dimensional pressure as

$$S^1_{\text{pl,max}} = 20 \log \left(\frac{4\pi^2 p_{\text{vc}}}{\rho \omega_p^2 D^2} \right), \tag{A.27}$$

where p_{vc} is the acoustic pressure of the vortex at a distance r from the source. Authors of [168], utilising measurements taken during full-scale trials, found that p_{vc} can be accurately modelled as a function of the volume acceleration of the tip vortex cavities, considering the noise from each vortex as an incoherent source, the acoustic pressure of the vortex can be evaluated as

$$p_{\text{vc}} = c_{\text{pvc}} \text{TVI} \rho \omega_p^2 D^2, \tag{A.28}$$

with c_{pvc} being a proportionality factor. TVI is a non-dimensional factor describing the pressure field from the propeller tip vortex, and is given by

$$\text{TVI} = \left(c_{\text{fc}} \frac{K_t}{Z} \right)^2 \frac{\sqrt{Z}}{\sigma_{\text{tip}}}, \tag{A.29}$$

with K_t being the thrust coefficient.

Introducing Equation (A.29) in Equation (A.27), $S^1_{\text{pl,max}}$ can be evaluated as

$$S^1_{\text{pl,max}} = c_a + 20\log_{10}\left[\left(\frac{c_{\text{fc}}K_t}{Z\sqrt{\sigma_n}}\right)^{c_d}\sqrt{Z}\right], \tag{A.30}$$

with c_a and c_d being calibration constants, and σ_n the cavitation index based on the rotational speed of the propeller. In Raestad [168] $c_d = 2$ is suggested, whereas $c_d = 3$ was reported to provide more accurate results in Bosschers [173], and is the value employed in this work.

By utilising Equation (A.29), the vortex noise level can be predicted with an acceptable error utilising only the general working parameters of the propeller. Furthermore, this relation can be rewritten in terms of cavity radius, enabling the inclusion of more advanced vortex models, as follows: Kutta's theorem expresses the lift of a 2D airfoil when encountering a fluid at constant velocity in relation with the fluid density and the circulation around the foil. The propeller is a 3D body, and the force of interest is the thrust, rather than the lift. In addition, the incident flow changes radially and is unstable due to inflow turbulence, so the total thrust can be only approximated by Kutta's theorem as

$$T = \rho\frac{\omega_p}{2\pi}D^2\bar{\Gamma}Z, \tag{A.31}$$

or alternatively in non-dimensional form,

$$K_t = \frac{2\pi\bar{\Gamma}Z}{\omega_p D^2}, \tag{A.32}$$

with $\bar{\Gamma}$ being the mean circulation on the blade. Assuming that the proportionality between of the thrust at the tip and the thrust of the blade can be represented by the constant factor c_{fc} of Equation (A.29), the circulation at the tip Γ_{tip} can be evaluated as

$$\Gamma_{\text{tip}} = c_{\text{fc}}\frac{K_t\omega_p D^2}{2\pi Z}. \tag{A.33}$$

In addition, the relation for a cavity radius near the hydrofoil tip can be written as a function of the tip circulation under the assumption of potential flow and viscous core

as a rotating solid body [174, 381], according to

$$\frac{r_{\mathrm{vc}}}{D} = \frac{\Gamma_{\mathrm{tip}}}{\omega_p D^2} \frac{1}{\sqrt{\sigma_n}}. \tag{A.34}$$

Combining Equations (A.33) - (A.34) with the formulation of Equation (A.30), the final formula for the evaluation of $S^1_{\mathrm{pl,max}}$ as a function of r_{vc} can be obtained

$$S^1_{\mathrm{pl,max}} = c_a + 20\log_{10}\left[\left(\frac{c_{\mathrm{fc}} r_{\mathrm{vc}}}{D}\right)^{c_d}\sqrt{Z}\right]. \tag{A.35}$$

A.4.4 Spectral shape

Subsequently, f_{vc} and $S^1_{\mathrm{pl,max}}$ are utilised to estimate the source level spectrum, which is divided in two frequency parts:

- The part $\boldsymbol{S}^{1a}_{\mathrm{pl}}$ that is characterised by a hump around the resonance frequency of the vortex cavity f_{vc}, due to the overall growth, collapse and rebounds of the cavity, given by
$$\boldsymbol{S}^{1a}_{\mathrm{pl}}(\boldsymbol{f}) = 20\log_{10}\left[sinc\left(\frac{\boldsymbol{f} - f_{\mathrm{vc}}}{c_f}\right)\right], \tag{A.36}$$
- and the part $\boldsymbol{S}^{1b}_{\mathrm{pl}}$ related to the final phase of the cavity collapse process, which consists of prescribed slopes at frequencies much lower and much higher than the resonance frequency, computed as
$$\boldsymbol{S}^{1b}_{\mathrm{pl}}(\boldsymbol{f}) = 10\log_{10}\left[\left(2\left(\frac{\boldsymbol{f}}{f_{\mathrm{vc}}}\right)^{\circ c_{\mathrm{lo}}}\right) \oslash \left(1 + \left(\frac{\boldsymbol{f}}{f_{\mathrm{vc}}}\right)^{\circ(c_{\mathrm{lo}} - c_{\mathrm{hi}})}\right)\right]. \tag{A.37}$$

The operator $(\cdot^{\circ\cdot})$ refers to element-wise (Hadamard) raising to a power, and the operator $(\cdot \oslash \cdot)$ refers to element-wise division. c_{hi}, c_{lo} correspond to the slopes of the spectrum for the high and low-frequencies, and c_f refers to the bandwidth of the hump for which the pressure amplitude is equal to half the maximum amplitude. A small value of c_f corresponds to a time trace with multiple rebounds (small damping) resulting in a narrow hump in the spectrum. A large value of c_f corresponds to a highly damped system resulting in a wide hump in the spectrum.

The source level spectrum is then modelled as a weighted sum of $\boldsymbol{S}^{1a}_{\mathrm{pl}}(\boldsymbol{f})$ and $\boldsymbol{S}^{1b}_{\mathrm{pl}}(\boldsymbol{f})$

as

$$\boldsymbol{S}^1_{\mathrm{pl}} = S^1_{\mathrm{pl,max}} + 10\log_{10}\left[c_s 10^{\boldsymbol{S}^{1a}_{\mathrm{pl}}(\boldsymbol{f})/10} + (1-c_s)10^{\boldsymbol{S}^{1b}_{\mathrm{pl}}(\boldsymbol{f})/10}\right], \tag{A.38}$$

where c_s is a calibration constant. Subsequently, similar to Section A.3.4, $\boldsymbol{S}^1_{\mathrm{pl}}$ is converted to 1/3 octave band $\boldsymbol{S}_{\mathrm{pl}}(\boldsymbol{f})$ and corrected to a standard measuring distance of 1[m] using the spherical acoustic wave propagation relationship [375].

A.5 Summary

This chapter provided an overview of the PMs employed to estimate the noise spectra from cavitating marine propellers. Focus has been given on the identification of low-computational-cost methodologies that will provide an approximate indication of cavitation noise with affordable computational requirements. To this aim, a combination of three models has been utilised:

- A panel method discussed in Section A.2, which is responsible for the hydrodynamic performance analysis of the propellers in non-uniform inflow conditions, and provides the unsteady pressure distributions on the key-blade of the propellers for one complete revolution.
- The semi-empirical model of Matusiak, which estimates the broadband effects of sheet cavitation, under the assumption that the radius size of the generated bubbles can be described by a statistical distribution.
- The ETV model for the estimation of the radiated noise due to the presence of a tip vortex cavity, which utilises a vortex model to estimate the tip vortex cavity radius, and a set of semi-empirical formulations for the estimation of the centre frequency and level of the broadband hump of the spectrum.

The semi-empirical models proposed are characterised by a set of parameters, which require careful calibration in order to provide accurate results. To ensure that no loss of prediction accuracy occurs due to the poor choice of their values, the calibration process has been formulated as an optimisation problem for the solution of which a metaheuristic method has been chosen.

Appendix B

Bubble dynamics models

Abstract

The Matusiak model of Section A.3 requires a bubble dynamics equation to be integrated over time. Whereas the Gilmore [320] equation was utilised in this work, it is worth investigating the effects of other models on the prediction capabilities of the Matusiak model. A brief description of the available bubble dynamics models and their assumptions is presented in the following.

Rayleigh-Plesset

Rayleigh [167] developed one of the first models for bubble dynamics for a single spherical bubble in an infinite domain. The model assumes incompressible fluid, neglects surface tension and viscosity, and is given by

$$r_b\ddot{r}_b + \frac{3}{2}r_b\dot{r}_b = \frac{1}{\rho}\left(p_{\mathrm{bw}}(r_b) - p_{b,\infty}\right). \tag{B.1}$$

where p_{bw} is the pressure at the bubble wall.

The model was subsequently adapted by Plesset [368], with the aim of describing bubble growth and collapse, considering a time-dependent $p_{b,\infty}$. This model includes the effects of viscosity and surface tension, as

$$r_b\ddot{r}_b + \frac{3}{2}r_b\dot{r}_b = \frac{1}{\rho}\left(p_{\mathrm{bi}} - p_{b,\infty} - 2\frac{c_\sigma}{r_b} - 4\frac{\nu}{r_b}\dot{r}_b\right) \tag{B.2}$$

where ν refers to the kinematic viscosity.

Keller-Miksis

Keller and Miksis [369] developed their model after reaching the conclusion that earlier methods [167, 320, 368] cannot accurately describe bubble dynamics for acoustic fields near the eigenfrequency of the bubble, which leads to large oscillations. This model assumes constant density in space and constant sound velocity. The Keller and Miksis [369] model is given by

$$\ddot{r}_b \left[4 r_b \frac{\nu}{\rho} \left(\dot{r}_b - v_s \right) \right] = \frac{1}{2} \dot{r}_b^3 + \dot{r}_b \nabla(r_b) - u_s \left(\frac{3}{2} \dot{r}_b{}^2 + \frac{4\nu}{\rho} \frac{\dot{r}_b}{r_b} + \frac{2 c_\sigma}{\rho r_b} - \nabla^2(r_b) \right) + \\ + r_b \dot{r}_b \dot{\nabla}^2(r_b) + 2 \left(1 + \frac{\dot{r}_b}{u_s} \right) \ddot{f} \left(t + \frac{r_b}{v_s} \right) \quad \text{(B.3)}$$

where f is an arbitrary function, arising from the integration of the wave equation, related to the incident field.

Flynn

The model of Flynn [370] was developed to describe the motion of a bubble that expands to a maximum radius and subsequently collapses violently, and provides reliable estimations of several quantities relevant to this motion. This model accounts for heat conduction, shear viscosity, compressibility, and surface tension in both the bubble and the surrounding medium. Assumption of the model include spherical bubbles with uniform internal pressure distribution, constant fluid density, and excludes diffusion, the effects of translation velocity, whereas the viscosity relations are assumed to be those of an incompressible fluid. In its final form, the Flynn [370] model is given by

$$r_b \left(1 - \dot{r}_b \right) \left(1 + \frac{4\nu}{\rho_{\mathrm{eq}} r_b} \right) \ddot{r}_b + \frac{3}{2} \left(1 - \frac{\dot{r}_b}{3} \right) \dot{r}_b^2 = \\ \frac{1}{\rho_{\mathrm{eq}}} \left[\left(1 + \dot{r}_b \right) \left(p_g(t) + p_v(t) \right) - 1 + \frac{\dot{r}_b^2}{r_b} \left(2 c_{\mathrm{st}} + 4 \nu \dot{r}_b \right) + r_b \left(1 - \dot{r}_b \right) \frac{d}{dt} \left(p_g(t) + p_v(t) \right) \right] \quad \text{(B.4)}$$

Appendix C

Semi-empirical models for cavitating vortices

Abstract

The ETV model of Section A.4 requires the prediction of the vortex cavity, which can be predicted from a vortex model for the distribution of the azimuthal velocity with cavity radius. Whereas the Proctor [383] model is utilised in this work, it is worth investigating the effects of other models on the prediction capabilities of the ETV model. A non-exhaustive list of alternative vortex models that could be used is presented in the following.

Burnham - Hallock model

The Burnham and Hallock [384] model was obtained from experimental data measured behind two aircrafts. It is the most widely employed model for wake vortex applications [385]. The profile of u_θ according to this model is defined as

$$u_\theta(r) = \frac{\Gamma}{2\pi r} \frac{r^2}{r^2 + r_{\text{vc}}^2} \tag{C.1}$$

Lamb-Oseen model

The Lamb [177] vortex has been extensively used for initialising large eddy simulations, and is an analytical solution of the one-dimensional laminar Navier-Stokes equations, i.e. an anti-symmetric solution for the swirl velocity, with the added assumption that the axial and radial velocity components are equal to zero. According to this model,

the tangential velocity as a function of the radial distance from the vortex center is given by

$$u_\theta(r) = \frac{\Gamma}{2\pi r_{\text{vc}}}\left[1 - \exp\left(c\left(\frac{r}{r_{\text{vc}}}\right)^2\right)\right], \tag{C.2}$$

with $c = 1.256431$, being used to place the peak of the velocity at the core radius.

Smooth blending vortex model

This model originates from the work of Winckelmans et al. [386], who smoothly blended the Proctor vortex [383], and further adjusted it to a wind tunnel experiment with a rectangular grid, and in two-dimensional vortex roll-up studies. The profile of u_theta in this model is evaluated as

$$u_\theta(r) = \frac{\Gamma}{2\pi r}\left[1 - \exp\left(\frac{c_i\left(\frac{2r}{D_p}\right)^2}{\left[1 + \left(\frac{c_i}{c_o}\left(\frac{2r}{D_p}\right)^{\frac{5}{4}}\right)^p\right]^{\frac{1}{p}}}\right)\right], \tag{C.3}$$

with $c_o = 10$, $c_i = 500$, $p = 3$, respectively.

Multiple scale vortex model

This model results from the analysis of wind tunnel data gathered in a wake of a small transport aircraft, at various spans of the wing [387]. It distinguishes 3 regions around the center of the vortex: a small internal ore where u_θ increases, an intermediate region for which u_θ decreases, and a region for which the vortex follows the potential law r_{vc}^{-1}. In this model the profile of u_θ is given by

$$u_\theta(r) = \begin{cases} \dfrac{\Gamma}{2\pi r_i}\dfrac{r}{(r_i r_o)^{\frac{1}{2}}}, & \text{for } r \le r_i \\ \dfrac{\Gamma}{2\pi\,(r_o r)^{\frac{1}{2}}}, & \text{for } r_i < r \le r_o \\ \dfrac{\Gamma}{2\pi r}, & \text{for } r > r_o \end{cases} \tag{C.4}$$

with $r_i \le 0.005 D_p$, and $r_o \approx 0.05 D_p$.

Appendix D

Data-driven Models

Abstract

This chapter provides an overview of the data-driven and hybrid models utilised to approximate the URN spectra, and further discusses their model selection and error estimation process. Data-driven models models will be able to estimate the underwater radiated noise of cavitating propellers without any prior knowledge of the underlying physical phenomena.

D.1 Introduction

This chapter provides an overview of the DDMs employed within the HM. These cover three main families: KMs covered in Section D.2, EMs discussed in Section D.3, and shallow ANNs presented in Section D.4. Finally, Section D.5 summarizes the relevant information.

D.2 Kernel methods

KMs can be employed for both supervised and unsupervised learning, and have been extensively covered in many ML and pattern recognition textbooks [199, 248, 279, 388, 389]. They have been successfully applied to a number of real-world problems and are now considered state-of-the-art in various domains. The main idea behind these algorithms is based on *kernels* [390], which enable them to implicitly operate in higher-dimensional spaces with respect to $\mathcal{X}$.

D.2.1 Kernels

Kernels provide a general framework to represent data, i.e $\mathcal{X}$. How to represent data is a fundamental question that needs to be answered prior to the application of any $\mathscr{A}_{\mathcal{H}}$. The majority of ML algorithms, with the exception of KMs, answer this question in a natural way: Define a representation $\boldsymbol{\phi}(\boldsymbol{x}) \in \mathcal{G} \subseteq \mathbb{R}^{\mathtt{d}}$ for each object $\boldsymbol{x} \in \mathcal{X}$, and subsequently represent $\mathcal{X}$ by the set of all the objects' representations $\mathcal{G}$. In the context of this work, an object can be the propeller blade geometry, which is most often represented as a two-dimensional matrix containing the main characteristics of several blade sections (pitch, skew, rake, etc.). The set of all these matrices, represent the set of all possible propeller blades.

Kernels provide a radically different answer to the question of data representation: Data is not represented individually, but through a set of pairwise comparisons. Instead of using a mapping $\boldsymbol{\phi} : \mathcal{X} \to \mathcal{G}$ to represent each $\boldsymbol{x} \in \mathcal{X}$ by $\boldsymbol{\phi}(\boldsymbol{x}) \in \mathcal{G}$, a real-valued "comparison function" $\mathtt{K} : \mathcal{X} \times \mathcal{X} \to \mathbb{R}$ is used, representing $\mathcal{X}$ by an $n \times n$ matrix of pairwise comparisons $\boldsymbol{K} \in \mathbb{R}^{n \times n}$ with $k_{i,j} = \mathtt{K}(\boldsymbol{x}_i, \boldsymbol{x}_j)$, also known as the *Gram* or *kernel matrix*. This idea is very powerful for the following reasons:

- The representation of the data does not depend on the nature of the objects that have to be analysed, suggesting that an algorithm based on kernels can process any type of data, as long as valid $\mathtt{K}$ can be defined.
- Moreover, the complexity of the objects is no more relevant. n objects can always be represented by an $n \times n$ matrix, even if each object requires thousands of quantities to characterise it.
- In various problems encountered in practice, an explicit representation of $\boldsymbol{x}_i$ might be a more difficult task than defining meaningful pairwise comparison. methods [391].

Considering that an inner product is a measure of the similarity of two vectors, it is natural to define a kernel as the inner product of the mappings $\boldsymbol{\phi}(\boldsymbol{x}_i)$, $\boldsymbol{\phi}(\boldsymbol{x}_j)$ for any two points $\boldsymbol{x}_i$, $\boldsymbol{x}_j, \in \mathcal{X}$, according to [392, 393]

$$\mathtt{K}(\boldsymbol{x}_i, \boldsymbol{x}_j) = \boldsymbol{\phi}(\boldsymbol{x}_i) \cdot \boldsymbol{\phi}(\boldsymbol{x}_j). \tag{D.1}$$

The substitution of $\boldsymbol{\phi}(\boldsymbol{x}_i), \boldsymbol{\phi}(\boldsymbol{x}_j)$ for $\mathtt{K}(\boldsymbol{x}_i, \boldsymbol{x}_j)$ is known as the *kernel trick* in the ML community. The kernel trick allows for the straightforward transformation of linear models into non-linear ones, while maintaining all their favourable properties: Approximation capabilities, practical effectiveness, and computational requirements [200].

Several kernel functions can be retrieved from literature, each one with a particular property that can be exploited based on the problem being investigated. The first kernels investigated in the ML community included the polynomial [394], Gaussian [199], and hyperbolic tangent kernels [395, 396]. Other useful kernels include spline [397], convolutional [398], ANOVA [199], tree [399], and graph [400] kernels. Usually the Gaussian kernel is chosen, given by

$$\mathtt{K}(\boldsymbol{x}_i, \boldsymbol{x}) = e^{-\gamma \|\boldsymbol{x}_i - \boldsymbol{x}\|^2}, \tag{D.2}$$

because of the theoretical reasons described in [280] and its effectiveness [281, 282]. More specifically, the Gaussian kernel is able to implicitly create an infinite-dimensional $\boldsymbol{\phi}$, which allows KMs to learn any possible function [280], requiring only the computation of dot products in $\mathcal{X}$, and not in $\mathcal{G}$. Note that, to simplify notation for the remainder of this section, the dependence of $\mathtt{K}$ on $\gamma \in \mathbb{R}_{>0}$ is omitted. Similar to λ, $\gamma \in \mathbb{R}_{>0}$ is a problem-dependent hyperparameter that needs to be calibrated, using the methodology described in Section 4.6.

D.2.2 Learning with kernels

To demonstrate how kernels can be employed for regression, linear models must be briefly revisited. To simplify notation, it is assumed that $\mathcal{Y}$ is mono-dimensional, i.e. $o = 1$. In $\mathcal{X}$, a linear model is defined as

$$h(\boldsymbol{x}) = \boldsymbol{w} \cdot \boldsymbol{x} + b, \tag{D.3}$$

with $\boldsymbol{w} \in \mathbb{R}^{\iota}$, and $b \in \mathbb{R}$.

Depending on the choice of $\hat{L}$ and C many linear regression algorithms can be defined from Equation (D.3). For instance, ridge regression [401] is derived using the mean

squared error for $\hat{L}$ and the Euclidean norm of $\boldsymbol{w}$ for C, whereas Lasso regression [402] is obtained when the Manhattan norm is utilised for C. It should be noted that when both $\hat{L}$, and C are convex, the linear model of Equation (D.3) transforms Problem (3.3) into a convex optimisation problem that can be solved very effectively [321]. Under certain conditions for $\hat{L}$ and C [403], $h(\boldsymbol{x})$ can be reformulated as a linear combination of the predictors, according to

$$h(\boldsymbol{x}) = \sum_{i=1}^{n} \alpha_i \boldsymbol{x}_i \cdot \boldsymbol{x} + b, \tag{D.4}$$

with $\alpha_i \in \mathbb{R}$, and $b \in \mathbb{R}$. For non-linear models, Equation (D.4) generalises to

$$h(\boldsymbol{x}) = \boldsymbol{w} \cdot \boldsymbol{\phi}(\boldsymbol{x}) + b, \tag{D.5}$$

which, by reformulating as a linear combination of the predictors and by employing the kernel trick, it can be written as

$$h(\boldsymbol{x}) = \sum_{i=1}^{n} \alpha_i \boldsymbol{\phi}(\boldsymbol{x}_i) \cdot \boldsymbol{\phi}(\boldsymbol{x}) + b = \sum_{i=1}^{n} \alpha_i \mathtt{K}(\boldsymbol{x}_i, \boldsymbol{x}) + b, \tag{D.6}$$

which retains the property of convexity if Problem (3.3) is convex with the linear model of Equation (D.3).

To retain the convexity of Problem (3.3), a convex function must also be employed for $\hat{\mathtt{L}}$. The squared loss has been adopted for its convexity, smoothness, and statistical properties [317], for which $\hat{\mathtt{L}}$ takes the form

$$\hat{\mathtt{L}}(h) = \frac{1}{n} \sum_{i=1}^{n} \ell(h(\boldsymbol{x}_i), y_i) = \frac{1}{n} \sum_{i=1}^{n} [h(\boldsymbol{x}_i) - y_i]^2. \tag{D.7}$$

Regarding $\mathtt{C}$, the classic L2 regulariser of the model's weights in $\mathcal{G}$ has been employed, which can be formulated as [237, 404]

$$\mathtt{C}(h) = \sum_{i=1}^{n} \sum_{j=1}^{n} \alpha_i \alpha_j \mathtt{K}(\boldsymbol{x}_i, \boldsymbol{x}_j). \tag{D.8}$$

Combining all definitions, the learning problem of Equation (3.3) can be written as

$$\begin{aligned}\boldsymbol{\alpha}^{\diamond} : \underset{\boldsymbol{\alpha}\in\mathbb{R}^n}{\arg\min} \quad & g_{\text{obj}}(\boldsymbol{\alpha}, \gamma, \lambda, \mathcal{D}_n) = \\ & = \frac{1}{n}\sum_{i=1}^{n}\left(\sum_{j=1}^{n}\alpha_j e^{-\gamma\|\boldsymbol{x}_i-\boldsymbol{x}_j\|^2} - y_i\right)^2 + \lambda\sum_{i=1}^{n}\sum_{j=1}^{n}\alpha_i\alpha_j e^{-\gamma\|\boldsymbol{x}_i-\boldsymbol{x}_j\|^2} = \\ & = (\boldsymbol{y}-\boldsymbol{K}\cdot\boldsymbol{a})^{\intercal}\cdot(\boldsymbol{y}-\boldsymbol{K}\cdot\boldsymbol{a}) + \lambda\boldsymbol{\alpha}^{\intercal}\cdot\boldsymbol{\alpha}, \end{aligned} \tag{D.9}$$

with $\boldsymbol{\alpha} = [\alpha_1, \cdots, \alpha_n]^{\intercal}$. It should be noted that the parameter b has been omitted from Equation D.9. It can be neglected due to the property of the Gaussian kernel alone to learn any possible function [280]. Being an unconstrained convex optimisation problem with a differentiable objective function, the necessary and sufficient condition [321] to obtain $\boldsymbol{\alpha}^{\diamond}$ is by solving

$$\nabla_{\boldsymbol{\alpha}} g_{\text{obj}}(\boldsymbol{\alpha}, \gamma, \lambda, \mathcal{D}_n) = \mathbf{0} \Rightarrow (\boldsymbol{K} + \lambda I)\cdot\boldsymbol{\alpha}^{\diamond} = \boldsymbol{y}, \tag{D.10}$$

where $I \in \mathbb{R}^{n\times n}$ is the identity matrix.

Therefore, the learning problem reduces to a system of linear algebraic equations, for which effective solvers exist that can handle even very large datasets [405]. This approach is known as KRLS [13]. Finally, it should be noted that when $\mathcal{Y}$ is multidimensional, i.e. $o > 1$, as is the case in this work, KMs require to develop a different h for each quantity of $\mathcal{Y}$.

D.3 Ensemble methods

From a cognitive perspective, EMs [250] are based on the *wisdom of crowds* principle [406]. Namely, they rely on the collective opinion of a group of individuals to reach decisions that are often better than those of a single expert. This principle is valid under certain requirements, the most important being diversity among these experts.

More formally, instead of utilising a single learner, EMs construct a set of base learners and combine them. The earliest examples of EMs originate from the work of Tukey [407], who proposed an ensemble of two liner regression models, suggesting

to train the first model directly on the available data, and the second model to the residual errors of the first one. Soon after, the work of Dasarathy and Sheela [408] presented an approach to partition the input space using multiple classifiers. Ever since, EMs have experienced an evolution, with different flavours of algorithms appearing in the literature, such as bagging [285], boosting [409], random forests [235], mixtures of experts [410, 411] and combination of multiple classifiers [412–414], and stacked generalisation [415]. All these methods, differ primarily on three key aspects:

- the selection of subsets of data for the each base learner,
- the procedure employed for the generation of the base learners,
- the combination rules for obtaining the consensus decision.

These aspects form the basic elements of any EM. Currently, EMs are considered a state-of-the-art ML approach, characterised by high numerical robustness and effectiveness, and the ability to handle both regression and classification problems [416, 417].

From the available EMs, Random Forests (RFs) have been employed in this work. RFs combine a series of Binary Decision Trees (BDTs) as base learners. BDTs are often chosen as base learners since they are quite easy to tune, computationally efficient, numerically robust and able to natively and easily handle missing values and categorical features [416]. Before describing the RF in detail, the definition and construction of a BDT will be briefly discussed. Similar to the discussion on Section D.2 for the KMs, to simplify notation $\mathcal{Y}$ is assumed to be mono-dimensional.

D.3.1 Binary decision trees

BDTs are flowchart-like structures, characterised by nodes and branches, that partition $\mathcal{D}_n$ in a series of disjoint regions $\mathcal{R}_i$, $i \in \{1, \cdots, n_{\mathcal{R}}\}$, and fit a simple model, either a simple regression model or a constant, in each region. Each internal node of the BDT represents a test of a predictor, each branch represents the outcome of a test, and each leaf node represents the BDT's predicted value for a quantity of interest. A path from the root node, i.e. the initial node of the BDT, to a leaf node represents a classification or regression rule. BDTs are grown with a recursive schema until a termination criterion is satisfied. For regression problems, it is suggested that they are

grown until their terminal nodes contain fewer than a predefined number of samples $n_{\text{BDT}} \in \mathbb{Z} : \ 1 \leq n_{\text{BDT}} \leq n$ [418]. The number of samples is a hyperparameter that governs the BDTs complexity, and is not an output of the learning phase. Instead it needs to be calibrated from the available data, which is the topic of Section 4.6.

Starting from the root node, each node is built by choosing the feature and the cut that most effectively partition $\mathcal{D}_n$ into two subsets based on Problem (3.3) [419]. Similar to KMs, $\hat{\mathtt{L}}$ is usually a convex differentiable metric, the most common on which is the squared loss of Equation (D.7) for regression problems [307, 420].

Formally, this partition requires splitting a variable $j \in \{1, \cdots, d\}$ of $\mathcal{X}$ and a node test (or cut)

$$x_j < c_{\mathtt{s}}, \tag{D.11}$$

with $c_{\mathtt{s}} \in \mathbb{R}$. This cut defines a pair of half-planes that split $\mathcal{D}_n$ into two regions $\mathcal{R}^{\text{left}}$ and $\mathcal{R}^{\text{right}}$, according to

$$\begin{aligned} \mathcal{R}^{\text{left}}(j, c_{\mathtt{s}}) &= \{(\boldsymbol{x}, y) \in \mathcal{D}_n | \mathtt{x}_j < c_{\mathtt{s}}\}, \\ \mathcal{R}^{\text{right}}(j, c_{\mathtt{s}}) &= \mathcal{D}_n \setminus \mathcal{R}^{\text{left}}(j, c_{\mathtt{s}}). \end{aligned} \tag{D.12}$$

Combining all definitions, the best cut can be defined as

$$(j^{\diamond}, c_{\mathtt{s}}^{\diamond}) : \underset{j \in \{1, \cdots, d\}, c_{\mathtt{s}} \in \mathcal{C}_j}{\arg\min} \left[\min_{c \in \mathbb{R}} \left(\sum_{\boldsymbol{x}_i \in \mathcal{R}^{\text{left}}(j, c_{\mathtt{s}})} (y_i - c_{\text{left}})^2 \right) + \min_{c_2 \in \mathbb{R}} \left(\sum_{\boldsymbol{x}_i \in \mathcal{R}^{\text{right}}(j, c_{\mathtt{s}})} (y_i - c_{\text{right}})^2 \right) \right] \tag{D.13}$$

where $\mathcal{C}_j$ refers to the set of all possible cuts for the predictor j. For any choice of j and $c_{\mathtt{s}}$, it can be shown that the constants c_i of the inner minimisation problems correspond to [307]

$$c_i = \frac{1}{|\mathcal{R}^{(i)}|} \sum_{j=1}^{n} y_j \mathtt{I}\left(\boldsymbol{x}_j \in \mathcal{R}^{(i)}\right), \ i \in \{\text{left}, \text{right}\}, \tag{D.14}$$

with $\mathtt{I} : \mathcal{X} \to \{0, 1\}$ being an indicator function, indicating whether $\boldsymbol{x}$ belongs to region $\mathcal{R}_i$.

For numerical features, the optimal cuts of Problem (D.13) can be efficiently com-

puted by sorting the values of x_j and by using the mean values between two consecutive sorted values as cuts. An extension of this approach for categorical features is reported in [418]. In the forward phase, the values of a new data point are utilised to "move" the point down the tree until it reaches a subset of the $n_{\mathcal{R}}$ terminal nodes, each of which is characterised by the corresponding $c_i,\ i \in \{1, \cdots, n_{\mathcal{R}}\}$. Combining all definitions, the BDT model can be written as

$$h(\boldsymbol{x}) = \sum_{i=1}^{n_{\mathcal{R}}} \sum_{j=1}^{n} \frac{1}{|\mathcal{R}^{(i)}|} y_j \mathtt{I}\left(\boldsymbol{x}_j \in \mathcal{R}^{(i)}\right). \tag{D.15}$$

For the sake of clarity, the learning and forward phases of a BDT are reported in Algorithm D.1 [419], for which $\iota_{\text{BDT}} = \iota$.

Algorithm D.1: Binary Decision Tree

```
/* Learning phase */
Input: D_n,n_BDT,ι_BDT
Result: Tree (T)
Function BDTlearn(D_n,n_BDT,ι_BDT):
    if |D_n| ≤ n_BDT then
        R^left ← D_n
        R^right ← ∅
        Evaluate c_left according to Eq. (D.14)
        T.h ← c_left
    else
        Evaluate (j^◇, c_s^◇) according to Eq. (D.13) chosen over ι_RF input variables
          randomly sampled without repetition
        Evaluate R^left, R^right according to Eq. (D.12)
        Evaluate c_left, c_right according to Eq. (D.14)
        T.cut ← (j^◇, c_s^◇)
        T.T^left ←BDTlearn(R^left,n_BDT,ι_BDT)
        T.T^right ←BDTlearn(R^right,n_BDT,ι_BDT)

/* Forward phase */
Input: x,T
Result: Predicted value y
while True do
    if exists T.h then
        y ← T.h
    else
        Based on T.s: T ← T.T^left or T ← T.T^right
end
```

Often, BDTs are deliberately grown larger than necessary, and are subsequently

"pruned" back to prevent over-fitting, as reported in [418, 421]. Although pruning is very important for stand-alone BDTs, it is not used in RFs, therefore it is not reported in this section.

D.3.2 Random forests

RFs were first introduced by Breiman [235] who, inspired by the earlier work of Amit and Geman [284], extended the bagging strategy of Breiman [285], in an attempt to optimise the generalisation performance of a model that combines several classifiers. With this idea, Breiman developed a robust learning algorithm that turns out to perform very well compared to many other approaches, is suitable for both regression and classification problems, and it has a computationally efficient forward phase.

In bagging, as in RFs, each one of the $n_{\mathrm{RF}} \in \mathbb{Z}_{\geq 1}$ BDTs is independently constructed using $\lfloor bn \rfloor,\ b \in (0, 1]$ samples, sampled with replacement from $\mathcal{D}_n$, to generate $\mathcal{D}_{\lfloor bn \rfloor}$. However, RFs add an additional layer of randomness: they also modify the construction process of the BDTs. As discussed earlier in this section, each node of a BDT is split by solving Problem (D.13), which aims to find the best cut among all $\iota_{\mathrm{BDT}} = \iota$ predictors. Instead, in RFs the nodes are split using the best cut among a subset of $\iota_{\mathrm{BDT}} < \iota$ randomly chosen predictors.

Breiman [235] showed that the predictive power of the RF depends primarily on three different factors: the number of BDTs composing it, the prediction quality of each BDT, and the correlation between BDTs. Furthermore, it was shown that the predictive power of the RF converges to a limit as the number of BDTs composing it increases, while it rises in line with the prediction quality of each BDT, as well as when the correlation between BDTs decreases. RFs' counter intuitive learning strategy turns out to perform very well compared to many other approaches, and is robust against over-fitting [235, 281].

During the forward phase of a previously unseen $\boldsymbol{x}$, each BDT assigns a value $\hat{y}_i,\ i \in \{1, \cdots, n_{\mathrm{RF}}\}$ to $y \in \mathcal{Y}$, and the final response is the unweighted average of all

$\hat{y}_i$, according to

$$h(\boldsymbol{x}) = \frac{1}{n_{\mathrm{RF}}} \sum_{k=1}^{n_{\mathrm{RF}}} \sum_{i=1}^{n_{\mathcal{R}}^{(k)}} \sum_{j=1}^{n} \frac{1}{|\mathcal{R}_k^{(i)}|} y_j \mathtt{I}\left(\boldsymbol{x}_j \in \mathcal{R}_k^{(i)}\right). \tag{D.16}$$

To summarise, the hyperparameters of the RF include: The number of trees n_{RF}, the number of samples to extract during the Bootstrap (BTS) procedure bn for each BDT, the number of samples in the terminal nodes of each BDT n_{BDT}, and the number of predictors utilised in each subset during the growth of each BDT ι_{BDT}. In [235], Breiman suggested to set $b = 1$, and $\iota_{\mathrm{BDT}} = \sqrt{\iota}$ for regression problems, while n_{RF} can be chosen according to some consistency measure, or based on the out-of-bag error [235]. The estimation of their values is discussed in Section 4.6. Several other hyperparameters exist, but they are set to default values, since they are not as influential, according to some recent work in the field [286, 287]. Finally, it should be noted that for multidimensional $\mathcal{Y}$, RFs require to develop a different h for each quantity of $\mathcal{Y}$.

D.4 Artificial neural networks

ANNs have been developed as generalisations of mathematical models of human cognition or neural biology, which consist of a large number of neurons that are connected to each other in a complex communication framework, through which the human brain is able to carry out highly complex computations. They are considered important pillars to ML theory and they have for a long time been a dominant force in ML [203, 239, 279, 422]. ANNs were originally conceived as a model that would imitate the function of the human brain: A set of *neurons* joined together by a set of *connections* [288, 423]. ANNs appear in many flavours and are utilised in a variety of tasks, having demonstrated the ability to perform well on supervised and unsupervised learning tasks, particularly when there is abundance of training data [203]. Conceptually, ANNs for regression problems are quite similar to KMs, with one exception: In ANNs, the non-linar projection from $\mathcal{X}$ to $\mathcal{G}$ is not fixed a-priori via the kernel trick. Rather, it is learned directly from the data. In other words, ANNs are able to simulta-

neously learn an appropriate representation of $\mathcal{X}$, as well as the regressor. The caveat is that the learning problem with ANNs is highly non-convex, and it relies on heuristic methods to find reasonable solutions [203].

A generic ANN containing L layers can be represented as the composition of L functions $\mathtt{f}_i : \mathcal{X}_i \times \mathcal{W}_i \to \mathcal{X}_{i+1}$, where $\mathcal{X}_i$, $\mathcal{W}_i$ correspond to the variable and parameter spaces of layer i, and each $\mathtt{f}_i$ being dependent on the parameters in $\mathcal{W}_i$. The output of a generic ANN for the input $\boldsymbol{x} \in \mathcal{X}$ is given by the function $h : \mathcal{X} \times (\mathcal{W}_1 \times \cdots \mathcal{W}_{L+1}) \to \mathcal{Y}$ according to

$$h(\boldsymbol{x}) = (\mathtt{f}_L \circ \cdots \circ \mathtt{f}_1)(\boldsymbol{x}). \tag{D.17}$$

D.4.1 Feed-forward artificial neural networks

This work focuses on standard *feed-forward* ANNs that can consist of several layers of Rosenblatt's perceptron [288], which is a particular type of ANN. Nevertheless, this type is referred to as an ANN throughout this work for simplicity. Each component of the input to layer i is generated by computing the weighted sum of the outputs of the previous layer, and then applying a non-linearity $\boldsymbol{\psi} : \mathbb{R}^{\mathtt{h}_i} \to \mathbb{R}^{\mathtt{h}_i}$, known as an *activation function*. The parameters of layer i include the weight matrix $\boldsymbol{W}_i \in \mathbb{R}^{\mathtt{h}_i \times \mathtt{h}_{i-1}}$ and the bias vector $\boldsymbol{b}_i \in \mathbb{R}^{\mathtt{h}_i}$. Note that $\mathtt{h}_{L+1} = o$, and $\mathtt{h}_1 = \iota$. In this context, each $\mathtt{f}_i$ can be written as

$$\mathtt{f}_i = \boldsymbol{\psi}(\boldsymbol{W}_i \cdot \boldsymbol{x} + \boldsymbol{b}_i), \tag{D.18}$$

and an L-layered ANN can be represented as

$$h(\boldsymbol{x}; \boldsymbol{\xi}) = \boldsymbol{W}_L \cdot \boldsymbol{\psi}_L(\cdots \boldsymbol{\psi}_2(\boldsymbol{W}_2 \cdot \boldsymbol{\psi}_1(\boldsymbol{W}_1 \cdot \boldsymbol{x}) + \boldsymbol{b}_2) \cdots) + \boldsymbol{b}_L, \tag{D.19}$$

where $\boldsymbol{\xi} = [(\boldsymbol{W}_1, \boldsymbol{b}_1), \cdots, (\boldsymbol{W}_{L+1}, \boldsymbol{b}_{L+1})]$. To simplify notation, the dependency of h on $\boldsymbol{\xi}$ is omitted for the remainder of this section.

The hyperparameters of the ANN include the number of layers $L \in \mathbb{Z}_{>0}$, the number of neurons in each layer $\mathtt{h}_i \in \mathbb{Z}_{>0},\ i \in \{2, \cdots, L\}$, along with each $\boldsymbol{\psi}_i$, which basically represent $\mathcal{F}$ for ANNs. Setting $L = 1$, results in a *shallow* ANN, which consists of the input and output layers, and a single hidden layer, whereas ANNs with $L > 1$

are known as *deep* ANNs. It should be noted that shallow and deep ANNs have the same approximation properties, i.e. a there will exist equivalent shallow and deep ANN architectures, meaning that a single layer is sufficient to represent any function [290, 424]. Nevertheless, the layer might be infeasibly large. In many circumstances, using deeper ANNs can reduce the number of units required to represent the desired function, and can also reduce the generalisation error [203]. A representation of a shallow ANN is given in Fig. D.1(a), whereas a deep ANN is illustrated in Fig. D.1(b).

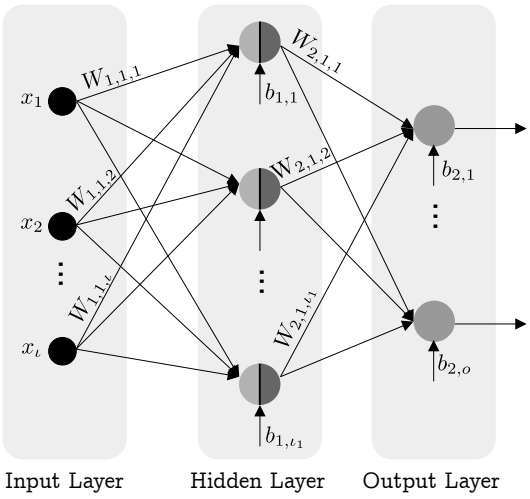

(a) Shallow ANN.

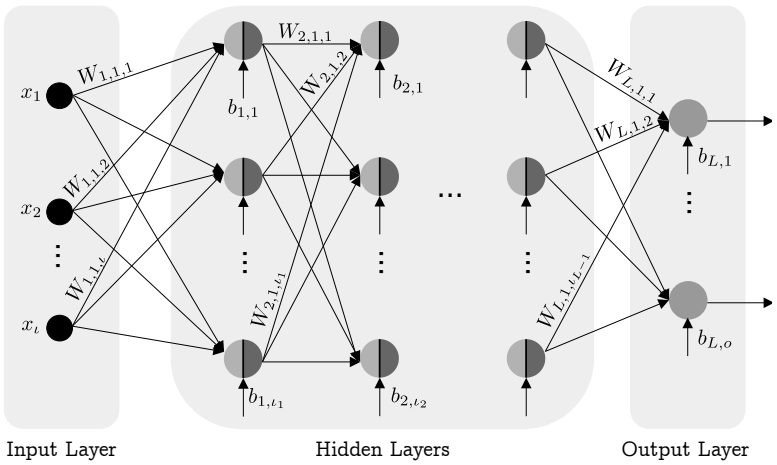

(b) Deep ANN.

Figure D.1: Shallow and deep ANN architectures.

Several activation functions can be retrieved from the literature [425], and several researchers [426, 427] have also developed methodologies that allow to actually learn the best activation function for a particular problem, instead of choosing one. The choice of the activation function is crucial for the ANN's learning process. For instance, with linear activation functions Equation (D.19) corresponds to a linear model. To allow the ANN to learn complex non-linear mapping functions, non-linear activation functions are more suitable. Nevertheless, linear activation functions are still utilised on the output layer of ANNs in regression problems [200]. In particular, if $\mathcal{X}$ is information-rich, a linear representation is powerful enough. Most commonly used non-linear activation functions include the logistic or sigmoid, the hyperbolic tangent, or the Rectified Linear Unit (ReLU) function and its variants. The first two were considered a default choice for ANNs, while ReLU and its variants became quite popular during the last decades due to their advantages in the learning phase of deep ANNs [203]. It should also be noted that, based on the functional form of $\boldsymbol{W}_i$, different kinds of layers can be obtained [203], such as convolutions, pooling, dropout, and dense layers. The choice of a particular layer type is also a hyperparameter that defines the architecture of the ANN and needs to be chosen based on the problem at hand [428].

Since the entire space of hyperparameters cannot be fully explored, it is often required to utilise experience and theoretical properties to reduce the space of exploration [203, 428]. For this reason, some hyperparameters of the ANNs have been fixed and kept constant in this work. Firstly, simple dense layers are utilised, since there is no particular structure in $\mathcal{D}_n$ [203, 239]. Moreover, only shallow ANNs have been employed ($L = 1$), as the cardinality of $\boldsymbol{W}_i$ increases exponentially with the number of layers, and in order to learn ANNs effectively, millions of samples need to be available [203]. Unfortunately, as will be discussed in Chapter 5, the cardinality of the dataset utilised in this work is very limited and fixed. Finally, the hyperbolic tangent is utilised for $\boldsymbol{\psi}_1$ due to its approximation properties [290]. Thus far, the only hyperparameter required to define the architecture of the ANN is the number of neurons of the single hidden layer $\mathtt{h}_1$, which will be revisited in Section 4.6. For the remainder of this section, it can be assumed that the value of $\mathtt{h}_1$ is fixed and known.

Having defined the hyperparameters of the ANN, $\hat{\mathtt{L}}$ and $\mathtt{C}$ must be chosen to solve Problem (3.3), i.e. to evaluate $\boldsymbol{W}_1$, and $\boldsymbol{b}_1$. For ANNs the learning problem is not convex regardless of the choice of $\hat{\mathtt{L}}$ and $\mathtt{C}$, due to the presence of the non-linearity $\boldsymbol{\psi}_i$. For this reason, $\hat{\mathtt{L}}$ and $\mathtt{C}$ do not necessarily need to be convex, but only differentiable. Furthermore, contrary to KMs and EMs, ANNs are able, by construction, to predict all quantities in $\mathcal{Y}$. For these reasons, the mean squared error averaged over all o outputs has been chosen for $\hat{\mathtt{L}}$ as it is one of the most effective, differentiable, and convex metrics for regression [307, 317], and is given by

$$\hat{\mathtt{L}}(h) = \frac{1}{o}\frac{1}{n}\sum_{i=1}^{o}\sum_{j=1}^{n}\left[y_{j,i} - h_i\left(\boldsymbol{x}_j\right)\right]. \tag{D.20}$$

Similar to the error metric of Problem (4.34), normalisation of the different outputs is required, to ensure that their order of magnitude is similar, according to

$$\hat{\mathtt{L}}(h) = \frac{1}{o}\frac{1}{n}\sum_{j=1}^{n}\sum_{i=1}^{o}\left[\frac{h_i\left(\boldsymbol{x}_j\right) - y_{j,i}}{\left[\frac{1}{n}\sum_{k=1}^{n} y_{j,k}^2 - \left(\frac{1}{n}\sum_{k=1}^{n} y_{j,k}\right)^2\right]^{1/2}}\right]^2. \tag{D.21}$$

Regarding $\mathtt{C}$, the L2 regulariser of the ANN's weights has been chosen [203] according to

$$\mathtt{C}(h) = \frac{1}{2}\sum_{i=1}^{L+1}\|\boldsymbol{W}_i\| = \frac{1}{2}\sum_{i=1}^{L+1}\sum_{j=1}^{\mathtt{h}_i}\sum_{k=1}^{\mathtt{h}_{i+1}}\left(W_{i,j,k}\right)^2, \tag{D.22}$$

which is the equivalent of Equation (D.8) for KMs.

Having defined h, $\hat{\mathtt{L}}$, and $\mathtt{C}$, Problem (3.3) can be written for ANNs as

$$\begin{aligned} h^{\diamond}: \underset{h\in\mathcal{F}}{\arg\min} \quad & g_{\text{obj}}(\lambda, \mathtt{h}_1, \mathcal{D}_n) = \hat{\mathtt{L}}(h) + \lambda\mathtt{C}(h) = \\ & = \frac{1}{o}\frac{1}{n}\sum_{j=1}^{n}\sum_{i=1}^{o}\left[\frac{h_i\left(\boldsymbol{x}_j\right) - y_{j,i}}{\left[\frac{1}{n}\sum_{k=1}^{n} y_{j,k}^2 - \left(\frac{1}{n}\sum_{k=1}^{n} y_{j,k}\right)^2\right]^{1/2}}\right]^2 + \frac{\lambda}{2}\sum_{i=1}^{L+1}\sum_{j=1}^{\mathtt{h}_i}\sum_{k=1}^{\mathtt{h}_{i+1}} W_{i,j,k}^2. \end{aligned} \tag{D.23}$$

D.4.2 Learning with Artificial Neural Networks

As stated earlier in this section, due to the non-linearity $\boldsymbol{\psi}$, Problem (D.23) is not convex. However, h, $\hat{\mathtt{L}}$, and $\mathtt{C}$ are differentiable. This property allows ANNs to learn by using iterative, gradient-based optimisers that reduce the value of the objective function, albeit without convergence guarantees. These optimisers require the evaluation of $\nabla_{\boldsymbol{\xi}} g_{\text{obj}}$, i.e. the gradients of g_{obj} of Problem (D.23) with respect to the parameters $\boldsymbol{\xi}$. Computing an analytical expression for $\nabla_{\boldsymbol{\xi}} g_{\text{obj}}$ is straightforward, but numerically evaluating these expressions can be computationally expensive This task is accomplished by the use of the *back-propagation* algorithm [289]. Back-propagation is a computationally effective and simple procedure to evaluate the required gradients by recursively applying the chain rule of calculus.

Having an algorithm for the evaluation of $\nabla_{\boldsymbol{\xi}} g_{\text{obj}}$, another algorithm is utilised to perform learning using their values. Several algorithms are available for this task [429], all of which are based on gradient descent. Gradient descent allows to minimise Problem (D.23) by updating the ANN's parameters in the opposite direction of the gradients. Usually, the parameters of the ANN are being updated after every *batch* $\mathbb{B} = \{(\boldsymbol{x}_1, \boldsymbol{y}_1), \cdots, (\boldsymbol{x}_{n_{\text{btc}}}, \boldsymbol{y}_{n_{\text{btc}}})\}$, of $n_{\text{btc}} \in \mathbb{Z} : \ 1 \leq n_{\text{btc}} \leq n$ samples drawn uniformly from $\mathcal{D}_n$, according to

$$\boldsymbol{\xi}_i = \boldsymbol{\xi}_{i-1} - \epsilon \Delta \boldsymbol{\xi}_i, \tag{D.24}$$

$$\Delta \boldsymbol{\xi}_i = \frac{1}{n_{\text{btc}}} \nabla_{\boldsymbol{\xi}} \left[\sum_{(\boldsymbol{x}_j, \boldsymbol{y}_j) \in \mathbb{B}} g_{\text{obj}} \left(\lambda, \mathtt{h}_1, (\boldsymbol{x}_j, \boldsymbol{y}_j) \right) \right], \tag{D.25}$$

which is known as mini-batch Stochastic Gradient Descent (SGD). In Equation (D.24), i refers to the iteration (or update) number, and $\epsilon \in \mathbb{R}_{>0}$ corresponds to the learning rate of the ANN. It should be noted that two additional hyperparameters have been introduced by SGD: n_{btc}, and ϵ, which regulate the speed of the optimizer and its effectiveness in reaching good local minima [203].

SGD is highly sensitive to ϵ, and choosing an appropriate value for it can be difficult: A value that is too small leads to slow convergence, thus higher computational

time requirements, whereas too high a value can hinder convergence, or even result in divergence. To avoid this issue, several extensions to SGD have been proposed over the years [429–431], which adapt ϵ for each parameter individually. One of these extensions is known as the Adam algorithm of Kingma and Ba [432], which has been employed in this work. Adam computes individual adaptive learning rates for the different parameters from estimates of the first and second moments of the gradients, and is a combination of AdaGrad [433] and RMSProp [203]. It has been employed since it is regarded as being fairly robust to the choice of hyperparameters [203], it works well in practice, and compares favourably to other adaptive learning algorithms [429].

In brief, Adam stores exponentially decaying averages of past gradients $\mathtt{m}$ and past squared gradients $\mathtt{u}$, controlled by two hyperparameters $\zeta_1, \zeta_2 \in [0, 1)$ that regulate the exponential decay rates of the moving averages. These moving averages are estimates of the mean and variance of the gradients $\nabla_{\boldsymbol{\xi}} g_{\mathrm{obj}}$, and are given by

$$\mathtt{m}_i = \zeta_1 \mathtt{m}_{i-1} + (1 - \zeta_1)\, \Delta\boldsymbol{\xi}_i \tag{D.26}$$

$$\mathtt{u}_i = \zeta_2 \mathtt{u}_{i-1} + (1 - \zeta_2)\, \Delta\boldsymbol{\xi}_i \odot \Delta\boldsymbol{\xi}_i, \tag{D.27}$$

with the operator $(\cdot \odot \cdot)$ denoting element-wise (Hadamard) product, and $\mathtt{m}_0 = \mathtt{u}_0 = \mathbf{0}$. Since $\mathtt{m}_i$ and $\mathtt{u}_i$ are initialised as zero vectors, Kingma and Ba [432] observed that they are biased towards zero, especially during the initial iterations, and with small decay rates. To counteract this bias, it was proposed to evaluate bias-corrected averages, according to

$$\hat{\mathtt{m}}_i = \frac{\mathtt{m}_i}{1 - \zeta_1^i} \tag{D.28}$$

$$\hat{\mathtt{u}}_i = \frac{\mathtt{u}_i}{1 - \zeta_2^i}, \tag{D.29}$$

and modify the update rule as

$$\boldsymbol{\xi}_i = \boldsymbol{\xi}_{i-1} - \epsilon \frac{1}{(\delta + \hat{\mathtt{u}}_i)^{\circ 2}} \odot \hat{\mathtt{m}}_i, \tag{D.30}$$

with recommended values for the additional parameters being $\zeta_1 = 0.9$, $\zeta_2 = 0.99$, and

$\delta = 10^{-8}$. The constant δ is necessary purely from a numerical standpoint: To stabilise division by small numbers. These recommended values have been utilised in this work.

To summarise, having defined the architecture of the ANN, Problem (D.23) is solved iteratively by using the back-propagation algorithm to compute the necessary gradients for the evaluation of $\Delta\boldsymbol{\xi}$ according to Equation (D.25), and the Adam algorithm is employed to update $\boldsymbol{\xi}$ at each iteration. This process outputs the values of $\boldsymbol{\xi}$ that provide low objective function values, albeit without convergence guarantees [203]. The choice of the necessary hyperparameter values, namely the number of neurons on the single hidden layer $\mathtt{h}_1$, the trade-off between accuracy and complexity λ, and the learning rate ϵ, is addressed in Section 4.6.

D.4.3 Extreme Learning Machines

Extreme Learning Machines (ELMs) represent a state-of-the-art method [12, 238, 291, 292] that was introduced to overcome the problems posed by the back-propagation algorithm [293, 294]: potentially slow convergence rates, sensitivity to some optimisation parameters, and the presence of local minima that call for multi-start and retraining strategies. Originally, ELMs were developed as single-hidden-layer feedforward ANNs [295–297], and were later extended to their deep version [298–300], in order to cope with problems intractable by shallow architectures [301–303]. In this work, shallow ELMs have been employed, and are referred to as ELMs throughout for simplicity. ELM models are given by

$$h(\boldsymbol{x}) = \sum_{i=1}^{\mathtt{h}} w_i \mathtt{f}_i(\boldsymbol{x}). \tag{D.31}$$

where $\mathtt{f}_i : \mathbb{R}^{\iota} \to \mathbb{R},\ i \in \{1, \cdots, \mathtt{h}\}$ is the hidden-layer output corresponding to the input sample $\boldsymbol{x}$, and $\boldsymbol{w} \in \mathbb{R}^{\mathtt{h}}$ is the output weight vector between the hidden layer and the output layer. In this case, the input layer has ι neurons and connects to the hidden layer (having $\mathtt{h}$ neurons) through a set of weights $\boldsymbol{W} \in \mathbb{R}^{\mathtt{h}\times(0,\cdots,\iota)}$ and a nonlinear activation function, $\varphi : \mathbb{R} \to \mathbb{R}$. Similar to ANNs, a variety of activation functions are available. In this work the tanh function was adopted as suggested in the original work of Huang et al. [297]. Nevertheless, using other activation functions does not really

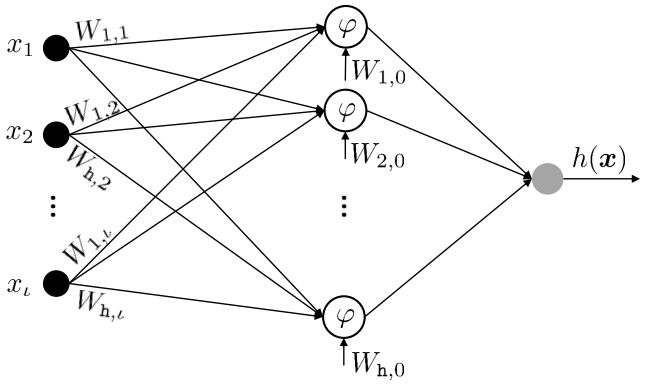

Figure D.2: Shallow extreme learning machine structure.

affect the final performance. In light of the above, the i-th hidden neuron's response to an input stimulus $\boldsymbol{x}$ is evaluated as

$$g_i(\boldsymbol{x}) = \varphi\left(W_{i,0} + \sum_{j=1}^{\iota} W_{i,j} x_j\right). \tag{D.32}$$

Note that Equation (D.32) can be further generalised to include a wider class of functions [296, 297, 434]; Therefore, the response of a neuron to an input stimulus $\boldsymbol{x}$ can be generally represented by any non-linear piece-wise continuous function characterised by a set of parameters. A vector of weighted links $\boldsymbol{w} \in \mathbb{R}^{\mathtt{h}}$ connects the hidden neurons to the output neuron without any bias. As such, the overall output function h of the ELM is

$$h(\boldsymbol{x}) = \sum_{i=1}^{\mathtt{h}} w_i \varphi\left(W_{i,0} + \sum_{j=1}^{\iota} W_{i,j} x_j\right) = \sum_{i=1}^{\mathtt{h}} w_i \varphi_i(\boldsymbol{x}), \tag{D.33}$$

for which a visual impression is provided in Figure D.2.

It is convenient to define an activation matrix, $\mathtt{A} \in \mathbb{R}^{n \times \mathtt{h}}$, such that the entry $\mathtt{A}_{i,j}$ is the activation value of the j-th hidden neuron for the i-th input sample. The matrix $\mathtt{A}$ can be written as

$$\mathtt{A} = \begin{bmatrix} \varphi_1(\boldsymbol{x}_1) & \cdots & \varphi_h(\boldsymbol{x}_1) \\ \vdots & \ddots & \vdots \\ \varphi_1(\boldsymbol{x}_n) & \cdots & \varphi_h(\boldsymbol{x}_n) \end{bmatrix}. \tag{D.34}$$

In the ELM model the weights $\boldsymbol{W}$ are set randomly and are not subject to any adjustment, and the quantity $\boldsymbol{w}$ in Equation (D.33) is the only degree of freedom. Hence, the learning problem reduces to the minimisation of the convex problem

$$\boldsymbol{w}^{\diamond} : \arg\min_{\boldsymbol{w}} \quad \|\mathtt{A}\boldsymbol{w} - \boldsymbol{y}\|^2 , \tag{D.35}$$

for which a matrix pseudo-inversion yields the unique L2 solution as [238, 296]

$$\boldsymbol{w}^{\diamond} = A^{+}\boldsymbol{y}. \tag{D.36}$$

Thus far, the simple, efficient procedure to train an ELM involves the following steps:

1. Randomly generate the hidden node parameters ($\boldsymbol{W}$),
2. evaluate the activation matrix $\mathtt{A}$ of Equation (D.34),
3. evaluate the output weights $\boldsymbol{w}^{\diamond}$ according to Equation (D.36).

Despite the simplicity of the approach, even the random weights in the hidden layer endow a network with notable representation ability. Moreover, the theory derived in [238] proves that regularisation strategies can further improve the approach's generalisation performance. As a result, the cost function of Equation (D.35) is augmented by a regularisation factor [238]. Similar to KMs, EMs, and ANNs, a common approach is to utilise the L2 regulariser. Thus, the learning problem takes the form

$$\boldsymbol{w}^{\diamond} = \arg\min_{\boldsymbol{w}} \|\mathtt{A}\boldsymbol{w} - \boldsymbol{y}\|^2 + \lambda \|\boldsymbol{w}\|^2 , \tag{D.37}$$

Consequently, the vector of weights $\boldsymbol{w}^{\diamond}$ is then obtained as

$$\boldsymbol{w}^{\diamond} = (\mathtt{A}^{\intercal}\mathtt{A} + \lambda I)^{+}\mathtt{A}^{\intercal}\boldsymbol{y}, \tag{D.38}$$

where $I \in \mathbb{R}^{\mathtt{h}\times\mathtt{h}}$ is an identity matrix, and $(\cdot)^{+}$ is the Moore-Penrose pseudo inverse matrix. It should be noted that $\mathtt{h}$, the number of hidden neurons, is another hyperparameter that needs to be calibrated based on the problem under consideration, similar to λ, which will be discussed in Section 4.6.

D.5 Summary

In this chapter an overview of the DDMs and HMs employed to estimate the noise spectra from cavitating marine propellers has been provided. The mathematical framework of a supervised ML regression problem has been addressed and all the necessary components for the development of the DDMs and HMs has been presented. Three main ML algorithm families will be utilised for the problem under consideration, including:

- Kernel methods, which employ the kernel trick that allows them to implicitly operate in higher-dimensional spaces w.r.t. $\mathcal{X}$,
- ensemble methods, which are based on the wisdom of crowds principle and rely on the collective decision of a series of base learners,
- and artificial neural networks that emulate the activities of the human brain.

All these DDMs can be extended to HMs with the use of the PM outputs, which allows them to combine the physical knowledge encapsulated in the PMs and the statistical inference procedures of the DDMs.

Appendix E

Propeller Geometries

Abstract

Supplementary material regarding the geometric characteristics of the Meridian Standard Propeller Series is presented in the following. The particulars of the propeller geometries are provided in Table E.1, whereas the section details are presented in Figure E.1, and Tables E.2-E.3.

Table E.1: Geometries of the Meridian standard propeller series in $\mathcal{D}_n$.

	$2r/D$	$\mathtt{c}/D$	$\mathtt{s}^*$ [^{o}]	$\mathtt{r}/D^{**}$	$\mathtt{p}/D$	$\tau_{\max}/\mathtt{c}$	$\mathtt{z}_{\max}/\mathtt{c}$
KCD 65 (Z = 6)	0.2	0.243	-4.60	0.007	0.753	0.232	0.114
	0.3	0.281	1.35	0.030	0.801	0.175	0.087
	0.4	0.302	6.21	0.050	0.830	0.132	0.066
	0.5	0.316	9.97	0.067	0.842	0.099	0.050
	0.6	0.325	12.70	0.082	0.839	0.076	0.038
	0.7	0.324	14.54	0.095	0.823	0.059	0.030
	0.8	0.298	15.70	0.105	0.797	0.046	0.023
	0.9	0.228	16.47	0.115	0.763	0.036	0.018
	0.95	0.167	16.81	0.119	0.743	0.031	0.016
	0.98	0.120	17.03	0.121	0.731	0.029	0.015
	1.0	0.083	17.19	0.123	0.723	0.027	0.014
	0.2	0.269	-5.51	0.004	0.821	0.167	0.084
	0.3	0.335	0.48	0.027	0.83	0.119	0.059
	0.4	0.373	5.35	0.048	0.835	0.084	0.042

Continued on next page

Table E.1 – *Continued from previous page*

	$2r/D$	$\mathtt{c}/D$	$\mathtt{s}^*$ [^{o}]	$\mathtt{r}/D^{**}$	$\mathtt{p}/D$	$\tau_{\max}/\mathtt{c}$	$\mathtt{z}_{\max}/\mathtt{c}$
KCD 74 (Z = 6)	0.5	0.397	9.21	0.066	0.835	0.061	0.030
	0.6	0.410	12.16	0.081	0.829	0.045	0.023
	0.7	0.408	14.31	0.094	0.815	0.036	0.019
	0.8	0.375	15.77	0.105	0.793	0.029	0.016
	0.9	0.285	16.63	0.115	0.762	0.023	0.014
	0.95	0.209	16.87	0.119	0.742	0.020	0.013
	0.98	0.150	16.97	0.121	0.729	0.017	0.012
	1.0	0.105	17.01	0.122	0.719	0.016	0.011
KCD 129 (Z = 5)	0.2	0.256	-5.09	0.002	0.763	0.161	0.080
	0.3	0.319	0.59	0.027	0.802	0.111	0.056
	0.4	0.356	5.48	0.049	0.823	0.080	0.040
	0.5	0.379	9.44	0.066	0.830	0.059	0.029
	0.6	0.393	12.41	0.081	0.827	0.045	0.023
	0.7	0.391	14.45	0.094	0.817	0.035	0.019
	0.8	0.357	15.69	0.105	0.800	0.026	0.017
	0.9	0.267	16.37	0.115	0.776	0.020	0.016
	0.95	0.190	16.60	0.119	0.761	0.019	0.016
	0.98	0.131	16.72	0.122	0.751	0.018	0.015
	1.0	0.085	16.81	0.124	0.744	0.017	0.015
KCD 191 (Z = 4)	0.2	0.244	-7.551	-0.013	0.608	0.195	0.089
	0.3	0.306	-4.279	0.003	0.617	0.122	0.061
	0.4	0.339	-0.488	0.019	0.620	0.083	0.043
	0.5	0.36	3.376	0.034	0.620	0.063	0.032
	0.6	0.372	6.996	0.048	0.616	0.051	0.025
	0.7	0.371	10.189	0.062	0.608	0.040	0.021
	0.8	0.342	12.905	0.076	0.599	0.029	0.018
	0.9	0.259	15.226	0.088	0.587	0.020	0.016
	0.95	0.186	16.30	0.094	0.581	0.019	0.014
	0.98	0.13	16.938	0.097	0.576	0.018	0.013
	1.0	0.086	17.366	0.100	0.573	0.017	0.013
	0.2	0.244	-6.63	-0.015	0.808	0.195	0.089
	0.3	0.306	-3.85	0.002	0.819	0.122	0.061
	0.4	0.34	-0.42	0.019	0.824	0.083	0.043
	0.5	0.362	3.22	0.035	0.823	0.063	0.032

Continued on next page

Table E.1 – *Continued from previous page*

	$2r/D$	$\mathtt{c}/D$	$\mathtt{s}^*$ [^{o}]	$\mathtt{r}/D^{**}$	$\mathtt{p}/D$	$\tau_{\max}/\mathtt{c}$	$\mathtt{z}_{\max}/\mathtt{c}$
KCD 192 (Z = 4)	0.6	0.376	6.72	0.052	0.817	0.051	0.025
	0.7	0.377	9.90	0.067	0.808	0.040	0.021
	0.8	0.351	12.65	0.082	0.795	0.029	0.018
	0.9	0.272	15.02	0.096	0.781	0.021	0.016
	0.95	0.201	16.10	0.102	0.771	0.019	0.014
	0.98	0.146	16.73	0.106	0.765	0.020	0.013
	1.0	0.103	17.15	0.108	0.761	0.022	0.013
KCD 193 (Z = 4)	0.2	0.244	-5.758	-0.016	1.014	0.195	0.089
	0.3	0.306	-3.489	0.001	1.028	0.122	0.061
	0.4	0.339	-0.386	0.018	1.034	0.083	0.043
	0.5	0.360	3.051	0.036	1.033	0.063	0.032
	0.6	0.372	6.448	0.054	1.026	0.051	0.025
	0.7	0.371	9.571	0.072	1.014	0.040	0.021
	0.8	0.342	12.314	0.088	0.998	0.029	0.018
	0.9	0.259	14.703	0.103	0.979	0.020	0.016
	0.95	0.186	15.809	0.110	0.967	0.019	0.014
	0.98	0.13	16.461	0.114	0.961	0.020	0.013
	1.0	0.086	16.897	0.117	0.955	0.021	0.013

* Skew is expressed as the rotation of the section in the transverse plane.

** Rake refers to design rake plus skew induced rake.

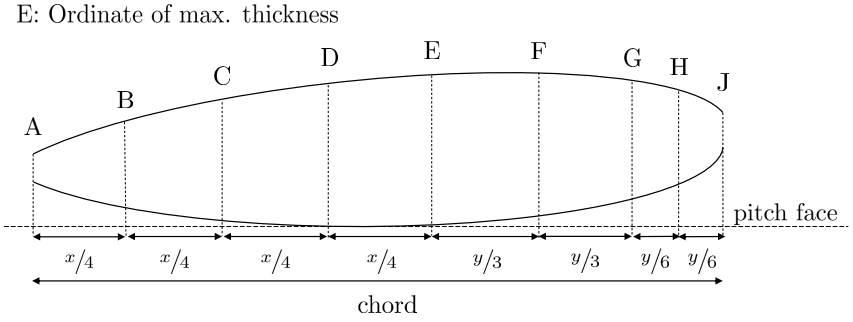

Figure E.1: Definition of the sections of the Meridian standard propeller series.

Table E.2: Section thickness offsets of the Meridian standard propeller series*.

$2r/D$	A	B	C	D	E	F	G	H	J
0.2	5.82	47.98	79.92	94.53	100	89.12	60.30	39.44	13.90
0.3	6.61	48.24	78.07	94.46	100	91.30	63.12	41.52	12.42
0.4	7.59	48.53	77.28	94.39	100	92.00	64.22	42.00	12.29
0.5	8.89	48.84	76.92	94.43	100	91.20	64.86	42.24	12.64
0.6	10.62	49.31	77.44	94.61	100	90.98	65.16	42.58	13.32
0.7	12.63	50.71	78.81	94.89	100	91.32	65.30	43.22	14.62
0.8	14.90	52.89	80.48	95.43	100	91.98	65.55	43.69	17.22
0.9	21.45	55.31	82.13	96.42	100	92.90	64.30	42.89	21.46

* In [%] of max. sectional thickness.

Table E.3: Section back offsets of the Meridian standard propeller series*.

$2r/D$	A	B	C	D	E	F	G	H	J
0.2	27.89	57.27	80.29	94.53	100	95.40	79.36	66.46	49.65
0.3	20.55	52.81	78.07	94.46	100	93.52	74.70	60.41	40.89
0.4	13.20	49.56	77.28	94.39	100	92.06	70.90	54.98	32.60
0.5	8.89	48.84	76.92	94.43	100	91.20	67.67	49.88	25.28
0.6	10.62	49.31	77.44	94.61	100	90.98	68.59	45.40	19.40
0.7	12.63	50.71	78.81	94.89	100	91.32	65.30	43.22	15.28
0.8	14.90	52.89	80.48	95.43	100	91.98	65.55	43.69	17.22
0.9	21.45	55.31	82.13	96.42	100	92.90	64.30	42.89	21.46

* Measurements from pitch face, in [%] of max. sectional thickness.

Appendix F

Wakefields

Abstract

In the following, supplementary material regarding the wake inflow characteristics is presented. More specifically, Tables F.1 - F.3 present the axial velocity distributions of the three wakefields developed by Aktas [7], and utilised in this work, at 10 radial and 36 angular locations.

Table F.1: Axial velocity distribution ratio of wakefield W1.

	$2r/D$									
θ	0.2	0.4	0.6	0.8	0.85	0.90	0.95	1.01	1.05	1.1
0	0.331	0.279	0.271	0.345	0.361	0.376	0.406	0.421	0.414	0.404
10	0.368	0.33	0.296	0.327	0.334	0.342	0.356	0.364	0.405	0.466
20	0.401	0.379	0.343	0.433	0.452	0.471	0.509	0.529	0.566	0.621
30	0.427	0.399	0.403	0.54	0.568	0.595	0.649	0.677	0.706	0.751
40	0.504	0.514	0.619	0.761	0.786	0.811	0.861	0.886	0.899	0.919
50	0.646	0.682	0.781	0.88	0.897	0.913	0.946	0.963	0.967	0.973
60	0.78	0.821	0.888	0.946	0.956	0.965	0.984	0.993	0.993	0.992
70	0.853	0.899	0.954	0.978	0.981	0.984	0.99	0.993	0.992	0.99
80	0.9	0.934	0.965	0.981	0.984	0.986	0.991	0.993	0.993	0.992
90	0.912	0.929	0.961	0.97	0.97	0.971	0.972	0.973	0.973	0.973
100	0.952	0.96	0.974	0.983	0.985	0.986	0.989	0.99	0.99	0.99
110	0.963	0.973	0.979	0.98	0.98	0.98	0.98	0.98	0.98	0.981
120	0.96	0.964	0.966	0.97	0.97	0.971	0.972	0.973	0.974	0.975
130	0.966	0.966	0.966	0.968	0.968	0.969	0.969	0.97	0.968	0.966
140	0.961	0.968	0.972	0.963	0.961	0.959	0.955	0.953	0.955	0.958

Continued on next page

Table F.1 – *Continued from previous page*

	$2r/D$									
θ	0.2	0.4	0.6	0.8	0.85	0.90	0.95	1.01	1.05	1.1
150	0.963	0.961	0.957	0.955	0.954	0.954	0.953	0.953	0.952	0.951
160	0.952	0.954	0.956	0.951	0.95	0.949	0.947	0.946	0.943	0.939
170	0.946	0.957	0.951	0.951	0.952	0.952	0.953	0.953	0.949	0.943
180	0.929	0.928	0.926	0.921	0.92	0.919	0.917	0.916	0.917	0.919
190	0.962	0.967	0.955	0.96	0.961	0.962	0.965	0.966	0.965	0.963
200	0.972	0.964	0.94	0.943	0.944	0.945	0.948	0.949	0.949	0.949
210	0.966	0.963	0.957	0.949	0.948	0.947	0.944	0.943	0.946	0.951
220	0.956	0.954	0.95	0.953	0.954	0.954	0.956	0.956	0.956	0.955
230	0.964	0.96	0.968	0.965	0.964	0.963	0.961	0.96	0.956	0.949
240	0.958	0.963	0.969	0.966	0.966	0.965	0.964	0.963	0.958	0.951
250	0.96	0.958	0.962	0.97	0.971	0.972	0.975	0.976	0.974	0.971
260	0.953	0.957	0.965	0.97	0.97	0.971	0.972	0.973	0.969	0.963
270	0.9	0.915	0.953	0.951	0.949	0.948	0.944	0.943	0.944	0.946
280	0.839	0.895	0.973	0.983	0.982	0.982	0.98	0.98	0.973	0.963
290	0.756	0.817	0.936	0.978	0.982	0.987	0.996	1.000	0.991	0.978
300	0.655	0.73	0.876	0.947	0.956	0.965	0.984	0.993	0.991	0.987
310	0.519	0.597	0.815	0.918	0.931	0.944	0.97	0.983	0.987	0.992
320	0.422	0.459	0.617	0.764	0.789	0.813	0.861	0.886	0.908	0.943
330	0.329	0.306	0.387	0.523	0.548	0.573	0.622	0.646	0.679	0.727
340	0.271	0.245	0.324	0.423	0.44	0.457	0.491	0.508	0.574	0.673
350	0.265	0.231	0.282	0.377	0.395	0.412	0.447	0.465	0.49	0.527
360	0.331	0.279	0.271	0.345	0.361	0.376	0.406	0.421	0.414	0.404

Table F.2: Axial velocity distribution ratio of wakefield W2.

	$2r/D$									
θ	0.2	0.4	0.6	0.8	0.85	0.90	0.95	1.01	1.05	1.1
0	0.371	0.34	0.357	0.392	0.399	0.405	0.418	0.425	0.442	0.467
10	0.37	0.329	0.343	0.421	0.436	0.451	0.482	0.497	0.496	0.495
20	0.408	0.378	0.395	0.406	0.408	0.409	0.413	0.414	0.443	0.486
30	0.511	0.539	0.55	0.551	0.551	0.551	0.551	0.551	0.547	0.541

Continued on next page

Table F.2 – *Continued from previous page*

	$2r/D$									
θ	0.2	0.4	0.6	0.8	0.85	0.90	0.95	1.01	1.05	1.1
40	0.563	0.592	0.572	0.565	0.564	0.564	0.562	0.562	0.574	0.592
50	0.598	0.652	0.674	0.637	0.629	0.621	0.604	0.596	0.597	0.598
60	0.593	0.621	0.67	0.651	0.645	0.64	0.629	0.623	0.652	0.695
70	0.681	0.705	0.773	0.777	0.776	0.775	0.772	0.771	0.795	0.832
80	0.821	0.87	0.876	0.906	0.912	0.917	0.929	0.935	0.925	0.911
90	0.869	0.915	0.945	0.922	0.916	0.911	0.899	0.894	0.891	0.887
100	0.891	0.917	0.962	0.91	0.898	0.886	0.861	0.849	0.861	0.878
110	0.953	0.962	0.969	0.947	0.943	0.938	0.929	0.925	0.934	0.949
120	0.971	0.975	0.979	0.985	0.986	0.987	0.989	0.99	0.991	0.993
130	0.984	0.984	0.986	0.985	0.984	0.984	0.983	0.983	0.984	0.985
140	0.982	0.983	0.983	0.981	0.981	0.98	0.98	0.979	0.984	0.99
150	0.979	0.978	0.967	0.976	0.978	0.98	0.984	0.986	0.984	0.979
160	0.968	0.977	0.973	0.974	0.975	0.975	0.976	0.976	0.974	0.971
170	0.946	0.965	0.972	0.973	0.973	0.973	0.973	0.973	0.971	0.967
180	0.934	0.952	0.952	0.949	0.948	0.947	0.946	0.945	0.948	0.952
190	0.963	0.98	0.983	0.983	0.983	0.983	0.983	0.983	0.979	0.973
200	0.975	0.976	0.976	0.973	0.972	0.971	0.97	0.969	0.97	0.971
210	0.989	0.989	0.981	0.976	0.975	0.975	0.973	0.973	0.973	0.973
220	0.979	0.98	0.974	0.967	0.966	0.965	0.963	0.962	0.963	0.964
230	0.958	0.966	0.975	0.976	0.976	0.976	0.976	0.976	0.975	0.973
240	0.966	0.969	0.969	0.973	0.973	0.974	0.975	0.976	0.975	0.974
250	0.961	0.965	0.969	0.942	0.937	0.931	0.92	0.914	0.904	0.889
260	0.895	0.909	0.961	0.899	0.885	0.871	0.843	0.829	0.839	0.854
270	0.84	0.858	0.937	0.895	0.883	0.872	0.85	0.839	0.845	0.853
280	0.832	0.855	0.894	0.911	0.913	0.915	0.919	0.921	0.907	0.885
290	0.796	0.813	0.824	0.837	0.84	0.842	0.847	0.849	0.85	0.851
300	0.646	0.617	0.652	0.697	0.705	0.713	0.728	0.736	0.74	0.745
310	0.553	0.532	0.59	0.615	0.618	0.621	0.627	0.63	0.647	0.671
320	0.529	0.534	0.555	0.586	0.591	0.597	0.608	0.613	0.619	0.628
330	0.489	0.491	0.473	0.545	0.56	0.575	0.605	0.62	0.642	0.676
340	0.412	0.406	0.418	0.501	0.517	0.534	0.566	0.582	0.597	0.618
350	0.373	0.36	0.394	0.431	0.437	0.444	0.456	0.462	0.471	0.483
360	0.371	0.34	0.357	0.392	0.399	0.405	0.418	0.425	0.442	0.467

Table F.3: Axial velocity distribution ratio of wakefield W3.

	$2r/D$									
θ	0.2	0.4	0.6	0.8	0.85	0.90	0.95	1.01	1.05	1.1
0	0.517	0.538	0.475	0.477	0.479	0.481	0.486	0.488	0.523	0.576
10	0.469	0.492	0.473	0.472	0.473	0.473	0.474	0.475	0.486	0.503
20	0.508	0.555	0.491	0.509	0.515	0.521	0.533	0.539	0.562	0.597
30	0.537	0.601	0.514	0.564	0.576	0.589	0.614	0.627	0.641	0.663
40	0.486	0.532	0.518	0.63	0.654	0.677	0.723	0.746	0.748	0.751
50	0.581	0.637	0.658	0.722	0.734	0.746	0.771	0.783	0.782	0.781
60	0.68	0.714	0.698	0.697	0.697	0.697	0.698	0.698	0.738	0.798
70	0.761	0.78	0.739	0.783	0.793	0.803	0.824	0.834	0.843	0.856
80	0.769	0.808	0.789	0.802	0.805	0.808	0.814	0.817	0.847	0.892
90	0.74	0.781	0.792	0.825	0.832	0.838	0.851	0.858	0.872	0.893
100	0.765	0.821	0.876	0.937	0.948	0.958	0.979	0.99	0.99	0.99
110	0.82	0.857	0.869	0.936	0.948	0.961	0.987	1.00	0.999	0.998
120	0.799	0.836	0.895	0.951	0.96	0.969	0.987	0.997	0.993	0.986
130	0.826	0.885	0.946	0.964	0.966	0.968	0.971	0.973	0.974	0.975
140	0.894	0.967	0.969	0.978	0.98	0.981	0.985	0.986	0.981	0.973
150	0.91	0.963	0.963	0.961	0.961	0.96	0.96	0.959	0.959	0.959
160	0.917	0.95	0.952	0.959	0.961	0.962	0.965	0.966	0.961	0.954
170	0.934	0.969	0.969	0.944	0.939	0.934	0.924	0.919	0.925	0.934
180	0.923	0.94	0.942	0.937	0.936	0.935	0.933	0.932	0.934	0.937
190	0.946	0.971	0.967	0.969	0.97	0.971	0.972	0.973	0.968	0.961
200	0.952	0.971	0.973	0.973	0.973	0.973	0.973	0.973	0.965	0.954
210	0.946	0.965	0.963	0.959	0.959	0.958	0.957	0.956	0.954	0.951
220	0.922	0.961	0.957	0.961	0.962	0.963	0.965	0.966	0.965	0.963
230	0.829	0.882	0.957	0.973	0.974	0.974	0.976	0.976	0.971	0.963
240	0.807	0.851	0.932	0.954	0.956	0.958	0.961	0.963	0.962	0.961
250	0.818	0.852	0.895	0.939	0.946	0.954	0.969	0.976	0.972	0.964
260	0.768	0.792	0.851	0.912	0.922	0.932	0.953	0.963	0.96	0.956
270	0.695	0.724	0.795	0.825	0.829	0.833	0.84	0.844	0.848	0.854
280	0.746	0.798	0.808	0.822	0.824	0.827	0.832	0.834	0.86	0.898
290	0.751	0.798	0.80	0.82	0.824	0.828	0.837	0.841	0.842	0.844
300	0.719	0.748	0.74	0.80	0.812	0.824	0.849	0.861	0.873	0.89
310	0.633	0.63	0.601	0.678	0.694	0.711	0.743	0.759	0.789	0.834
320	0.563	0.56	0.522	0.651	0.678	0.705	0.759	0.786	0.787	0.788

Continued on next page

Table F.3 – *Continued from previous page*

	$2r/D$									
θ	0.2	0.4	0.6	0.8	0.85	0.90	0.95	1.01	1.05	1.1
330	0.567	0.591	0.513	0.56	0.572	0.584	0.608	0.62	0.649	0.692
340	0.53	0.562	0.492	0.504	0.509	0.514	0.524	0.529	0.585	0.669
350	0.535	0.566	0.484	0.482	0.485	0.487	0.492	0.495	0.509	0.531
360	0.517	0.538	0.475	0.477	0.479	0.481	0.486	0.488	0.523	0.576

Bibliography

[1] J.A. Hildebrand. Anthropogenic and natural sources of ambient noise in the ocean. *Marine Ecology Progress Series*, 395:5–20, 2009.

[2] J.P. Franc and J.M. Michel. *Fundamentals of cavitation*, volume 76. Springer science & Business media, 2006.

[3] R.D. Collier. Ship and platform noise, propeller noise. *Handbook of acoustics*, pages 407–415, 1998.

[4] S. Yaser, M.I. Malik, and H.S. Lin. *Learning from data: A short course*. AML-Book, 2012.

[5] J. Matusiak. *Pressure and noise induced by a cavitating marine screw propeller*. PhD thesis, Aalto University, 1992.

[6] B. Aktas, M. Atlar, S. Turkmen, W. Shi, R. Sampson, E. Korkut, and P. Fitzsimmons. Propeller cavitation noise investigations of a research vessel using medium size cavitation tunnel tests and full-scale trials. *Ocean Engineering*, 120:122–135, 2016.

[7] B. Aktas. *A systematic experimental approach to cavitation noise prediction of marine propellers*. PhD thesis, Newcastle University, 2017.

[8] B. Aktas, M. Atlar, P. Fitzsimmons, and W. Shi. An advanced joint time-frequency analysis procedure to study cavitation-induced noise by using standard series propeller data. *Ocean Engineering*, 170:329–350, 2018.

[9] A. Arapakopoulos, R. Polichshuk, Z. Segizbayev, S. Ospanov, A.I. Ginnis, and K.V. Kostas. Parametric models for marine propellers. *Ocean Engineering*, 192: 106595, 2019.

[10] A Odabasi and P.A. Fitzsimmons. Alternative methods for wake quality assessment. *International Shipbuilding Progress*, 25(282):34–42, 1978.

[11] F. Miglianti, F. Cipollini, L. Oneto, G. Tani, and M. Viviani. Model scale cavitation noise spectra prediction: Combining physical knowledge with data science. *Ocean Engineering*, 178:185–203, 2019.

[12] G.B. Huang, Q.Y. Zhu, and C.K. Siew. Extreme learning machine: theory and applications. *Neurocomputing*, 70(1-3):489–501, 2006.

[13] J. Hainmueller and C. Hazlett. Kernel regularized least squares: Reducing misspecification bias with a flexible and interpretable machine learning approach. *Political Analysis*, 5(2):143–168, 2014.

[14] C. Audet and M. Kokkolaras. Blackbox and derivative-free optimization: theory, algorithms and applications, 2016.

[15] N.A. Brown. Cavitation noise problems and solutions. In *International Symposium on Shipboard Acoustics*, 1976.

[16] J. Bosschers. A semi-empirical method to predict broadband hull pressure fluctuations and underwater radiated noise by cavitating tip vortices. In *Fifth International Symposium on Marine Propulsors*, 2017.

[17] J. Bosschers, G.H. Choi, H.I. Hyundai, K.T. Farabee, D. Fréchou, E. Korkut, K. Sato, et al. Specialist committee on hydrodynamic noise. *Final report and recommendations to the 28th International Towing Tank Conference*, 45, 2017.

[18] S.D. Jessup. *An experimental investigation of viscous aspects of propeller blade flow*. PhD thesis, The Catholic University of America, 1989.

[19] N. Trivyza, A. Rentizelas, G. Theotokatos, and E. Boulougouris. Decision support methods for sustainable ship energy systems: A state-of-the-art review. *Energy*, page 122288, 2021.

[20] F. G. Torres and G. E. De-la Torre. Environmental pollution with antifouling paint particles: Distribution, ecotoxicology, and sustainable alternatives. *Marine Pollution Bulletin*, 169:112529, 2021.

[21] E. Lakshmi, M. Priya, and V. S. Achari. An overview on the treatment of ballast water in ships. *Ocean & Coastal Management*, 199:105296, 2021.

[22] S. Song, Y. K. Demirel, C. Muscat-Fenech, T. Tezdogan, and M. Atlar. Fouling effect on the resistance of different ship types. *Ocean Engineering*, 216:107736, 2020.

[23] S.V. Vakili, A.I. Ölcer, and F. Ballini. The development of a policy framework to mitigate underwater noise pollution from commercial vessels. *Marine Policy*, 118:104004, 2020.

[24] S. Sezen, T. Cosgun, A. Yurtseven, and M. Atlar. Numerical investigation of marine propeller underwater radiated noise using acoustic analogy part 2: The influence of eddy viscosity turbulence models. *Ocean Engineering*, 220:108353, 2021.

[25] C. Ferrier-Pagès, M.C. Leal, R. Calado, D.W. Schmid, F. Bertucci, D. Lecchini, and D. Allemand. Noise pollution on coral reefs?—a yet underestimated threat to coral reef communities. *Marine Pollution Bulletin*, 165:112129, 2021.

[26] E. Di Franco, P. Pierson, L. Di Iorio, A. Calò, J.M. Cottalorda, B. Derijard, A. Di Franco, A. Galvé, M. Guibbolini, J. Lebrun, et al. Effects of marine noise pollution on mediterranean fishes and invertebrates: A review. *Marine Pollution Bulletin*, 159:111450, 2020.

[27] M. Oldenburg, X. Baur, and C. Schlaich. Occupational risks and challenges of seafaring. *Journal of occupational health*, pages 1007–1036, 2010.

[28] E. Chou, B.L. Southall, M. Robards, and H.C. Rosenbaum. International policy, recommendations, actions and mitigation efforts of anthropogenic underwater noise. *Ocean & Coastal Management*, 202:105427, 2021.

[29] S.V. Vakili, A.I. Ölçer, and F. Ballini. The development of a policy framework to mitigate underwater noise pollution from commercial vessels: The role of ports. *Marine Policy*, 120:104132, 2020.

[30] European Union. United nations open-ended informal consulative process on oceans and the law of the sea - the effects of anthropogenic underwater noise, contribution of the european union, 2017.

[31] J. D. Tucker and M. R. Azimi-Sadjadi. Coherence-based underwater target detection from multiple disparate sonar platforms. *IEEE Journal of Oceanic Engineering*, 36(1):37–51, 2011.

[32] Y. Li and L. Wang. A novel noise reduction technique for underwater acoustic signals based on complete ensemble empirical mode decomposition with adaptive noise, minimum mean square variance criterion and least mean square adaptive filter. *Defence Technology*, 16(3):543–554, 2020.

[33] X. Lurton. *An introduction to underwater acoustics: principles and applications*. Springer Science & Business Media, 2002.

[34] J. Carlton. *Marine propellers and propulsion*. Butterworth-Heinemann, 2018.

[35] D. Ross. *Mechanics of underwater noise*. Peninsula Publishing, 1976.

[36] X.D. Tong, H.Y. Chen, and Y. Chen. Low frequency broadband noise radiated by highly skewed propeller ingesting inflow turbulence. *Journal of Sound and Vibration*, 490:115709, 2021.

[37] X.D. Tong and Y. Chen. Random response of highly skewed propeller-shafting system induced by inflow turbulence. *Ocean Engineering*, 195:106750, 2020.

[38] S. Kim and S.A. Kinnas. Prediction of cavitating performance of a tip loaded propeller and its induced hull pressures. *Ocean Engineering*, 229:108961, 2021.

[39] J. Hu, Y. Wang, W. Zhang, X. Chang, and W. Zhao. Tip vortex prediction for contra-rotating propeller using large eddy simulation. *Ocean Engineering*, 194: 106410, 2019.

[40] Y.S. Huang, X.Q. Dong, C.J. Yang, W. Li, and F. Noblesse. Design of wake-adapted contra-rotating propellers for high-speed underwater vehicles. *Applied Ocean Research*, 91:101880, 2019.

[41] A. Capone, F. Di Felice, and F.A. Pereira. On the flow field induced by two counter-rotating propellers at varying load conditions. *Ocean Engineering*, 221: 108322, 2021.

[42] F. Valdenazzi, F. Conti, S. Gaggero, C. Vaccaro, D. Grassi, and D. Villa. A practical tool for the hydro-acoustic optimization of naval propellers. In *VIII International Conference on Computational Methods in Marine Engineering*, pages 296–308. CIMNE, 2019.

[43] D. Li, J. Hallander, and T. Johansson. Predicting underwater radiated noise of a full scale ship with model testing and numerical methods. *Ocean Engineering*, 161:121–135, 2018.

[44] F. Salvatore and S. Ianniello. Preliminary results on acoustic modelling of cavitating propellers. *Computational Mechanics*, 32(4-6):291–300, 2003.

[45] Y.C Pan and H.X Zhang. Numerical prediction of marine propeller noise in non-uniform inflow. *China Ocean Engineering*, 27(1):33–42, 2013.

[46] N.M. Nouri, S. Mohammadi, and M. Zarezadeh. Optimization of a marine contra-rotating propellers set. *Ocean Engineering*, 167:397–404, 2018.

[47] S. Gaggero, G. Tani, D. Villa, M. Viviani, P. Ausonio, P. Travi, G. Bizzarri, and F. Serra. Efficient and multi-objective cavitating propeller optimization: An application to a high-speed craft. *Applied Ocean Research*, 64:31–57, 2017.

[48] S. Gaggero, D. Villa, G. Tani, M. Viviani, and D. Bertetta. Design of ducted propeller nozzles through a ranse-based optimization approach. *Ocean Engineering*, 145:444–463, 2017.

[49] S. Gaggero, J. Gonzalez-Adalid, and M.P. Sobrino. Design of contracted and tip loaded propellers by using boundary element methods and optimization algorithms. *Applied Ocean Research*, 55:102–129, 2016.

[50] L. Bjørnø and I. Bjørnø. Underwater acoustics and its applications. a historical review. *Hydroacoustics*, 2, 1999.

[51] F. Dunn, W.M. Hartmann, D.M. Campbell, and N.H. Fletcher. *Handbook of acoustics*. Springer, 2015.

[52] D.G. Crighton. Basic principles of aerodynamic noise generation. *Progress in Aerospace Sciences*, 16(1):31–96, 1975.

[53] X. Lurton and L. Leviandier. Underwater acoustic wave propagation. *An introduction to underwater acoustics: principles and applications, Chapter 2*, pages 13–74, 2010.

[54] S.N. Sirimanne, J. Hoffman, W. Juan, R. Asariotis, M. Assaf, G. Ayala, H. Benamara, D. Chantrel, J. Hoffmann, A. Premti, et al. Review of maritime transport. Technical report, United Nations Conference on Trade and Development, 2019.

[55] R. Dekeling. Underwater soundscapes. *Journal of Ocean Technology*, 9:2–10, 2014.

[56] C. Erbe, S.A. Marley, R.P. Schoeman, J.N. Smith, L.E. Trigg, and C.B. Embling. The effects of ship noise on marine mammals—a review. *Frontiers in Marine Science*, 6:606, 2019.

[57] R. Chapman. Ambient noise in the ocean. *Journal of Ocean Technology*, 9:21–26, 2014.

[58] J. Ho. The international maritime organisation–littoral state meetings on enhancing the safety, security and environmental protection of the straits of malacca and singapore. *Maritime Studies*, 2007(152):16–21, 2007.

[59] IMO. Resolution msc.337(91) (xii) - code on noise levels on board ships, 2012.

[60] IMO. Guidelines for the reduction of underwater noise from commercial shipping to address adverse impacts on marine life, 2014.

[61] H.N. Psaraftis. Shipping decarbonization in the aftermath of mepc 76. *Cleaner Logistics and Supply Chain*, 1:100008, 2021.

[62] Strategy Framework Directive. Directive 2008/56/ec of the european parliament and of the council. Technical report, European Union, 2008.

[63] S. Vagle and M. Neves. Evaluation of the effects on underwater noise levels from shifting vessel traffic away from southern resident killer whale foraging areas in the strait of juan de fuca in 2018. *Canadian Technical Report of Hydrography and Ocean Sciences*, 329:6–64, 2019.

[64] Det Norske Veritas. Silent class notation - rules for classification of ships-newbuildings, 2010.

[65] Det Norske Veritas. Silent class notation - rules for classification of ships-newbuildings, 2019.

[66] P.B. Palomo, R.S. Mullor, A.M. Rodríguez, E. Baudin, and V. Lamaison. A comprehensive framework to address ship underwater radiated noise: from bureau veritas class notation to validations of numerical prediction tools. In *22nd International Congress on Sound and Vibration*, 2015.

[67] Registro Italiano Navale. Amendments to part a and part f or rules for the classification of ships - new additional class notation: Dophin quiet ship and dolphin transit ship, 2017.

[68] American Bureau of Shipping. Guide for the classification notation - underwater noise, 2018.

[69] China Classification Society. Guideline for ship underwater radiated noise, 2018.

[70] LLoyd's Register. Additional design and construction procedure for the determination of a vessel's underwater radiated noise, 2018.

[71] M.F. McKenna, D. Ross, S.M. Wiggins, and J.A. Hildebrand. Underwater radiated noise from modern commercial ships. *The Journal of the Acoustical Society of America*, 131(1):92–103, 2012.

[72] P.T. Arveson and D.J. Vendittis. Radiated noise characteristics of a modern cargo ship. *The Journal of the Acoustical Society of America*, 107(1):118–129, 2000.

[73] University National Oceanographic Laboratory System. R/v hugh r. sharp surface ship radiated noise measurement (ssrnm) ranged at atlantic undersea test and evaluation center. Technical report, UNOLS, 2009.

[74] M.J. Parsons, C. Erbe, M.G. Meekan, and S.K. Parsons. A review and meta-analysis of underwater noise radiated by small (¡ 25 m length) vessels. *Journal of Marine Science and Engineering*, 9(8):827, 2021.

[75] A. Brooker and V. Humphrey. Measurement of radiated underwater noise from a small research vessel in shallow water. *Ocean Engineering*, 120:182–189, 2016.

[76] A.K. Lidtke. *Predicting radiated noise of marine propellers using acoustic analogies and hybrid Eulerian-Lagrangian cavitation models*. PhD thesis, University of Southampton, 2017.

[77] D. Wittekind and M. Schuster. Propeller cavitation noise and background noise in the sea. *Ocean Engineering*, 120:116–121, 2016.

[78] A. Vallier. *Simulations of cavitation-from the large vapour structures to the small bubble dynamics*. PhD thesis, Lund University, 2013.

[79] M.S. Plesset and A. Prosperetti. Bubble dynamics and cavitation. *Annual review of fluid mechanics*, 9(1):145–185, 1977.

[80] C.E. Brennen, T. Colonius, and F. d'Auria. Computing shock waves in cloud cavitation. In *3rd International Symposium on Cavitation*, 1998.

[81] J. Seo and S. Lele. Numerical investigation of cloud cavitation and cavitation noise on a hydrofoil section. In *7th International Symposium on Cavitation*, 2009.

[82] J. Bosschers. *Propeller Tip-Vortex Cavitation and its Broadband Noise*. PhD thesis, University of Twente, 2018.

[83] A. Coraddu, L. Oneto, F. Baldi, and D. Anguita. Vessels fuel consumption forecast and trim optimisation: a data analytics perspective. *Ocean Engineering*, 130:351–370, 2017.

[84] L. Miglianti, F. Cipollini, L. Oneto, G. Tani, S. Gaggero, A. Coraddu, and M. Viviani. Predicting the cavitating marine propeller noise at design stage: A deep learning based approach. *Ocean Engineering*, 209:107481, 2020.

[85] A. Coraddu, L. Oneto, F. Cipollini, M. Kalikatzarakis, G.J. Meijn, and R. Geertsma. Physical, data-driven and hybrid approaches to model engine exhaust gas temperatures in operational conditions. *Ships and Offshore Structures*, pages 1–22, 2021.

[86] A. Coraddu, M. Kalikatzarakis, L. Oneto, G.J. Meijn, M. Godjevac, and R.D. Geertsmad. Ship diesel engine performance modelling with combined physical and machine learning approach. In *International Naval Engineering Conference and Exhibition*, 2018.

[87] J.E. Kerwin. The solution of propeller lifting surface problems by vortex lattice methods. Technical report, Massachusetts Institute of Technology, 1961.

[88] P.G. Esposito and K.H. Kim. Specialist committee on computational method for propeller cavitation, final report and recommendations to the 22nd ittc. In *The 22nd International Towing Tank Conference*, 1999.

[89] R.D. Ciskowski and C.A. Brebbia. *Boundary element methods in acoustics*. Springer, 1991.

[90] L. Morino and C. Kuo. Subsonic potential aerodynamics for complex configurations: a general theory. *AIAA journal*, 12(2):191–197, 1974.

[91] s. Sezen, T. Cosgun, A. Yurtseven, and M. Atlar. Numerical investigation of marine propeller underwater radiated noise using acoustic analogy part 1: The influence of grid resolution. *Ocean Engineering*, 220:108448, 2021.

[92] S. Sezen, M. Atlar, and P. Fitzsimmons. Prediction of cavitating propeller underwater radiated noise using rans & des-based hybrid method. *Ships and Offshore Structures*, pages 1–13, 2021.

[93] Y.H. Lee, C.Y. Yang, and Y.C Chow. Evaluations of the outcome variability of rans simulations for marine propellers due to tunable parameters of cavitation models. *Ocean Engineering*, 226:108805, 2021.

[94] M. Ge, U. Svennberg, and R.E. Bensow. Investigation on rans prediction of propeller induced pressure pulses and sheet-tip cavitation interactions in behind hull condition. *Ocean Engineering*, 209:107503, 2020.

[95] H. Yao, Y. Liu, H. Zhang, and Q. Zhang. Comparative study on hydrodynamic performance and induced pressure of new canard tandem propellers and conventional propellers. *Ocean Engineering*, 221:108566, 2021.

[96] T. Melissaris, S. Schenke, N. Bulten, and T. van Terwisga. On the accuracy of predicting cavitation impact loads on marine propellers. *Wear*, 456:203393, 2020.

[97] Q. Wu, B. Huang, G. Wang, S. Cao, and M. Zhu. Numerical modelling of unsteady cavitation and induced noise around a marine propeller. *Ocean Engineering*, 160: 143–155, 2018.

[98] A. Peters, U. Lantermann, and O. el Moctar. Numerical prediction of cavitation erosion on a ship propeller in model-and full-scale. *Wear*, 408:1–12, 2018.

[99] Y.S. Huang, J. Yang, and C.J. Yang. Numerical prediction of the effective wake profiles of a high-speed underwater vehicle with contra-rotating propellers. *Applied Ocean Research*, 84:242–249, 2019.

[100] A.K. Lidtke, T. Lloyd, and G. Vaz. Acoustic modelling of a propeller subject to non-uniform inflow. In *6th International Symposium on Marine Propulsors*, 2019.

[101] B Laurence. Specialist committee on cavitation, final report and recommendations to the 25th ittc. In *The 25th International Towing Tank Conference*, 2008.

[102] Y. Long, C. Han, B. Ji, X. Long, and Y. Wang. Verification and validation of large eddy simulations of turbulent cavitating flow around two marine propellers with emphasis on the skew angle effects. *Applied Ocean Research*, 101:102167, 2020.

[103] J. Hu, W. Zhang, C. Wang, S. Sun, and C. Guo. Impact of skew on propeller tip vortex cavitation. *Ocean Engineering*, 220:108479, 2021.

[104] A. Asnaghi, U. Svennberg, and R.E. Bensow. Large eddy simulations of cavitating tip vortex flows. *Ocean Engineering*, 195:106703, 2020.

[105] Y. Long, X. Long, B. Ji, and T. Xing. Verification and validation of large eddy simulation of attached cavitating flow around a clark-y hydrofoil. *International Journal of Multiphase Flow*, 115:93–107, 2019.

[106] A. Asnaghi, U. Svennberg, and R.E. Bensow. Numerical and experimental analysis of cavitation inception behaviour for high-skewed low-noise propellers. *Applied Ocean Research*, 79:197–214, 2018.

[107] P.R. Spalart. Comments on the feasibility of les for wings, and on a hybrid rans/les approach. In *1st Air force office of scientific research international conference on DNS/LES*. Greyden Press, 1997.

[108] G. Ku, J. Cho, C. Cheong, and H. Seol. Numerical investigation of tip-vortex cavitation noise of submarine propellers using hybrid computational hydro-acoustic approach. *Ocean Engineering*, 238:109693, 2021.

[109] O. Usta and E. Korkut. Prediction of cavitation development and cavitation

erosion on hydrofoils and propellers by detached eddy simulation. *Ocean Engineering*, 191:106512, 2019.

[110] Y. Long, C. Han, X. Long, B. Ji, and H. Huang. Verification and validation of delayed detached eddy simulation for cavitating turbulent flow around a hydrofoil and a marine propeller behind the hull. *Applied Mathematical Modelling*, 96:382–401, 2021.

[111] N. Yilmaz, B. Aktas, M. Atlar, P.A. Fitzsimmons, and M. Felli. An experimental and numerical investigation of propeller-rudder-hull interaction in the presence of tip vortex cavitation (tvc). *Ocean Engineering*, 216:108024, 2020.

[112] N. Sakamoto and H. Kamiirisa. Prediction of near field propeller cavitation noise by viscous cfd with semi-empirical approach and its validation in model and full scale. *Ocean Engineering*, 168:41–59, 2018.

[113] A. Travin, M. Shur, M. Strelets, and P. Spalart. Detached-eddy simulations past a circular cylinder. *Flow, turbulence and combustion*, 63(1):293–313, 2000.

[114] F. Salvatore, H. Streckwall, and T. Van Terwisga. Propeller cavitation modelling by cfd-results from the virtue 2008 rome workshop. In *1st International Symposium on Marine Propulsors*, pages 22–24, 2009.

[115] M. Hoekstra, T. Van Terwisga, and E.J. Foeth. Smp11 workshop-case 1: Delftfoil. In *2nd International Symposium on Marine Propulsors*. Citeseer, 2011.

[116] L. Luebke and U. Barkmann. 2nd international workshop on cavitating propeller performance. Technical report, University of Texas at Austin, 2015.

[117] J. Casper and F. Farassat. Broadband trailing edge noise predictions in the time domain. *Journal of Sound and Vibration*, 271(1-2):159–176, 2004.

[118] G. Rahier, J. Prieur, F. Vuillot, N. Lupoglazoff, and A. Biancherin. Investigation of integral surface formulations for acoustic post-processing of unsteady aerodynamic jet simulations. *Aerospace science and technology*, 8(6):453–467, 2004.

[119] M.J. Lighthill. On sound generated aerodynamically i. general theory. *Proceedings of the Royal Society of London. Series A. Mathematical and Physical Sciences*, 211(1107):564–587, 1952.

[120] C. Haigermoser. Application of an acoustic analogy to piv data from rectangular cavity flows. *Experiments in fluids*, 47(1):145–157, 2009.

[121] N. Curle. The influence of solid boundaries upon aerodynamic sound. *Proceedings of the Royal Society of London. Series A. Mathematical and Physical Sciences*, 231(1187):505–514, 1955.

[122] J.E. Ffowcs Williams and D.L. Hawkings. Sound generation by turbulence and surfaces in arbitrary motion. *Philosophical Transactions for the Royal Society of London. Series A, Mathematical and Physical Sciences*, pages 321–342, 1969.

[123] K.S. Brentner and F. Farassat. Analytical comparison of the acoustic analogy and kirchhoff formulation for moving surfaces. *AIAA journal*, 36(8):1379–1386, 1998.

[124] k.S. Brentner and f. Farassat. Modeling aerodynamically generated sound of helicopter rotors. *Progress in Aerospace Sciences*, 39(2-3):83–120, 2003.

[125] R. Bensow and M. Liefvendahl. An acoustic analogy and scale-resolving flow simulation methodology for the prediction of propeller radiated noise. In *31st Symposium on Naval Hydrodynamics*, pages 11–16, 2016.

[126] S. Ianniello, R. Muscari, and A. Di Mascio. Ship underwater noise assessment by the acoustic analogy. part i: nonlinear analysis of a marine propeller in a uniform flow. *Journal of marine Science and technology*, 18(4):547–570, 2013.

[127] S. Ianniello, R. Muscari, and A. Di Mascio. Ship underwater noise assessment by the acoustic analogy part ii: hydroacoustic analysis of a ship scaled model. *Journal of marine Science and technology*, 19(1):52–74, 2014.

[128] S. Ianniello, R. Muscari, and A. Di Mascio. Ship underwater noise assessment

by the acoustic analogy, part iii: measurements versus numerical predictions on a full-scale ship. *Journal of marine Science and technology*, 19(2):125–142, 2014.

[129] P. Kellett, O. Turan, and A. Incecik. A study of numerical ship underwater noise prediction. *Ocean Engineering*, 66:113–120, 2013.

[130] T.P. Lloyd, A.K. Lidtkeb, D.R. Rijpkemac, E. van Wijngaardenc, S.R. Turnockb, and V.F. Humphreyd. Using the fw-h equation for hydroacoustics of propellers. In *18th Numerical Towing Tank Symposium*, pages 28–36, 2015.

[131] T. Lloyd, D. Rijpkema, and E. van Wijngaarden. Marine propeller acoustic modelling: comparing cfd results with an acoustic analogy method. In *4th International Symposium on Marine Propulsors*, 2015.

[132] T.P. Lloyd, D. Rijpkema, and E. Van Wijngaarden. Implementing the ffowcs williams-hawkings acoustic analogy into a viscous cfd solver. In *17th Numerical Towing Tank Symposium*, 2014.

[133] H. Seol, B. Jung, J.C. Suh, and S. Lee. Prediction of non-cavitating underwater propeller noise. *Journal of Sound and Vibration*, 257(1):131–156, 2002.

[134] H. Seol, J.C. Suh, and S. Lee. Development of hybrid method for the prediction of underwater propeller noise. *Journal of Sound and Vibration*, 288(1-2):345–360, 2005.

[135] C. Testa, S. Ianniello, F. Salvatore, and M. Gennaretti. Numerical approaches for hydroacoustic analysis of marine propellers. *Journal of ship research*, 52(01): 57–70, 2008.

[136] F. Farassat and K.S. Brentner. The uses and abuses of the acoustic analogy in helicopter rotor noise prediction. *Journal of the American Helicopter Society*, 33 (1):29–36, 1988.

[137] F. Farassat. Derivation of formulations 1 and 1a of farassat. Technical report, NASA Langley Research Center, 2007.

[138] F. Farassat. Numerical investigations on the hydroacoustics behaviour of a marine propeller in uniform flow. Technical report, Italian National Institute for Naval Architecture Studies and Testing, 2010.

[139] F. Salvatore, C. Testa, and L. Greco. Coupled hydrodynamics-hydroacoustics bem modelling of marine propellers operating in a wakefield. In *5th International Symposium on Marine Propulsors*, volume 9, pages 537–547. Citeseer, 2009.

[140] H.W. Coleman and W.G. Steele. *Experimentation, validation, and uncertainty analysis for engineers*. John Wiley & Sons, 2018.

[141] C.J. Freitas. The issue of numerical uncertainty. *Applied Mathematical Modelling*, 26(2):237–248, 2002.

[142] H. Seol. Time domain method for the prediction of pressure fluctuation induced by propeller sheet cavitation: Numerical simulations and experimental validation. *Ocean engineering*, 72:287–296, 2013.

[143] S. Ianniello and E. De Bernardis. Farassat's formulations in marine propeller hydroacoustics. *International Journal of Aeroacoustics*, 14(1-2):87–103, 2015.

[144] S. Ianniello. Sheet cavitation noise prediction from a marine propeller. In *International Congress on Sound and Vibration*, 2015.

[145] S. Ianniello. Hydroacoustic analysis of a marine propeller through the ffowcs williams-hawkings equation. In *31st Symposium on Naval Hydrodynamics*, 2016.

[146] A.K. Lidtke, S. Turnock, and V. Humphrey. Use of acoustic analogy for marine propeller noise characterisation. In *4th International Symposium on Marine Propulsors*, 2015.

[147] A.K. Lidtke, V.F. Humphrey, and S.R. Turnock. Feasibility study into a computational approach for marine propeller noise and cavitation modelling. *Ocean Engineering*, 120:152–159, 2016.

[148] C. Testa, F. Porcacchia, L. Greco, and R. Muscari. Effectiveness of boundary element method hydrodynamic data for propeller hydroacoustics. In *3rd International Meeting-Progress in Propeller Cavitation and Its Consequences: Experimental and Computational Methods for Predictions*, pages 77–85, 2018.

[149] C. Testa, S. Ianniello, and F. Salvatore. A ffowcs williams and hawkings formulation for hydroacoustic analysis of propeller sheet cavitation. *Journal of Sound and Vibration*, 413:421–441, 2018.

[150] T. Lampe, L. Radtke, U. Göttsche, A. Düster, and M. Abdel-Maksoud. Evaluation of performance and acoustic signature of flexible marine propellers under consideration of fluid-structure interaction by means of partitioned simulation. In *6th International Symposium on Marine Propulsors*, 2019.

[151] M. Cianferra, A. Petronio, and V. Armenio. Numerical prediction of ship propeller noise through acoustic analogy. In *6th International Symposium on Marine Propulsors*, 2019.

[152] S. Sezen, M. Atlar, P. Fitzsimmons, N. Sasaki, G. Tani, N. Yilmaz, and B. Aktas. Numerical cavitation noise prediction of a benchmark research vessel propeller. *Ocean Engineering*, 211:107549, 2020.

[153] C. Testa, F. Porcacchia, S. Zaghi, and M. Gennaretti. Study of a fwh-based permeable-surface formulation for propeller hydroacoustics. *Ocean Engineering*, 240:109828, 2021.

[154] M.C. Özden, A.Y. Gürkan, Y.A. Özden, T.G. Canyurt, and E. Korkut. Underwater radiated noise prediction for a submarine propeller in different flow conditions. *Ocean Engineering*, 126:488–500, 2016.

[155] Y. Wei, Y. Shen, S. Jin, P. Hu, R. Lan, S. Zhuang, and D. Liu. Scattering effect of submarine hull on propeller non-cavitation noise. *Journal of sound and vibration*, 370:319–335, 2016.

[156] D.K. Wittekind. A simple model for the underwater noise source level of ships. *Journal of Ship Production & Design*, 30(1), 2014.

[157] S. Ekinci, F. Celik, and M. Guner. A practical noise prediction method for cavitating marine propellers. *Shipbuilding: Theory and practice of shipbuilding and marine engineering*, 61(4):359–366, 2010.

[158] N. Okamura and T. Asano. Prediction of propeller cavitation noise and its comparison with full scale measurement. *Journal of the Society of Naval Architects of Japan*, 1988(164):43–53, 1988.

[159] A.C. Takinacı and T. Taralp. Prediction and simulation of broadband propeller noise. *Journal of Marine Science and Technology*, 21(5):6, 2013.

[160] N.A. Brown. Thruster noise. In *Dynamic Positioning Conference*, 1999.

[161] F.H. Lafeber and J. Bosschers. Validation of computational and experimental prediction methods for the underwater radiated noise of a small research vessel. In *Proceedings of PRADS*, 2016.

[162] H. Kamiirisa and H. Goto. Development of prediction method for ship underwater noise by bubble dynamics. *Mitsui Zosen Technical Review*, 2(185):38–44, 2005.

[163] T. Ando, K. Kimura, N. Suyama, and K Yamamoto. Study on cavitation and noise performance of marine propellers using cfd analysis. In *18th Symposium on Cavitation*, 1976.

[164] F.H. Lafeber, J. Bosschers, and E. van Wijngaarden. Computational and experimental prediction of propeller cavitation noise. In *Oceans 2015*, pages 1–9, 2015.

[165] T. Veikonheimo, J. Roivainen, T. Huttunen, et al. Underwater noise of an azipod propulsion unit with heavy ice class. In *Arctic Technology Conference*. Offshore Technology Conference, 2016.

[166] T. Yamada and C. Kawakita. Study on practical cfd for unsteady vortices from trailing edge of propeller blades. *Mitsubishi Heavy Industries Technical Review*, 52(4):56, 2015.

[167] L. Rayleigh. On the pressure developed in a liquid during the collapse of a spherical cavity. *The London, Eninburgh, and Dublin Philosophical Magazine and Journal of Science*, 34:94–98, 1917.

[168] A.E. Raestad. Tip vortex index - an engineering approach to propeller noise prediction. *The Naval Architect*, 1996.

[169] J. Bosschers. Investigation of hull pressure fluctuations generated by cavitating vortices. In *First Symposium on Marine Propulsors*, 2009.

[170] W. Thomson. Vibrations of a columnar vortex. In *Royal Society of Edinburgh*, pages 443–456, 1880.

[171] B. Maines and R.E.A. Arndt. The case of the singing vortex. *Journal of Fluids Engineering*, 119:271–276, 1997.

[172] A. Pustoshnyy, V. Borusevich, and A. Koval. Alternative hypothesis on broad band pressure generated by propeller on the hull. In *10th International Conference on Hydrodynamics*, 2012.

[173] J. Bosschers. A semi-empirical prediction method for broadband hull-pressure fluctuations and underwater radiated noise by propeller tip vortex cavitation. *Journal of Marine Science and Engineering*, 6(2):49, 2018.

[174] G. Kuiper. *Cavitation inception on ship propeller models.* PhD thesis, Delft University of Technology, 1981.

[175] B. Kipple. Southeast alaska cruise ship underwater acoustic noise, nswccd-71-tr-2002/574. Technical report, Naval Surface Warface Center, 2002.

[176] J. Bosschers. An analytical and semi-empirical model for the viscous flow around a vortex cavity. *International Journal of Multiphase Flow*, 105:122–133, 2018.

[177] H. Lamb. *Hydrodynamics, 6th Edition*. Cambridge University Press, 1932.

[178] P.C. Pennings, J. Westerweel, and T.J.C. Van Terwisga. Flow field measurement around vortex cavitation. *Experiments in Fluids*, 56(11):1–13, 2015.

[179] P.C. Pennings, J. Bosschers, J. Westerweel, and T.J.C. Van Terwisga. Dynamics of isolated vortex cavitation. *Journal of Fluid Mechanics*, 778:288–313, 2015.

[180] M. Giuni and E. Benard. Analytical/experimental comparison of the axial velocity in trailing vortices. In *49th AIAA Aerospace Sciences Meeting including the New Horizons Forum and Aerospace Exposition*, page 990, 2011.

[181] S. Ando, K. Kimura, K. Segawa, and K. Yamamoto. Study on the hybrid method of cfd and bubble dynamics for marine propeller cavitation noise prediction. In *10th International Symposium on Cavitation (CAV2018)*, volume 12, 2018.

[182] A. Coraddu, L. Oneto, M. Kalikatzarakis, D. Ilardi, and M. Collu. Floating spar-type offshore wind turbine hydrodynamic response characterisation: a computational cost aware approach. In *Global Oceans 2020*, pages 1–8. IEEE, 2020.

[183] A. Coraddu, L. Oneto, F. Baldi, F. Cipollini, M. Atlar, and S. Savio. Data-driven ship digital twin for estimating the speed loss caused by the marine fouling. *Ocean Engineering*, 186:106063, 2019.

[184] F. Cipollini, L. Oneto, A. Coraddu, A.J. Murphy, and D. Anguita. Condition-based maintenance of naval propulsion systems: Data analysis with minimal feedback. *Reliability Engineering & System Safety*, 177:12–23, 2018.

[185] F. Cipollini, L. Oneto, A. Coraddu, A. J. Murphy, and D. Anguita. Condition-based maintenance of naval propulsion systems: Data analysis with minimal feedback. *Reliability Engineering & System Safety*, 177:12–23, 2018.

[186] Y. Yang, L. Linlin, S.X. Ding, J. Qiu, and K. Peng. Fault detection for piecewise affine systems with application to ship propulsion systems. *ISA Transactions*, 78: 3 – 9, 2018.

[187] H.R. Karimi, H. Zhang, and S. Ding. Advanced methods in control and signal processing for complex marine systems. *ISA Transactions*, 78:1 – 2, 2018.

[188] A. Baldini, L. Ciabattoni, R. Felicetti, F. Ferracuti, A. Freddi, and A. Monteriu. Dynamic surface fault tolerant control for underwater remotely operated vehicles. *ISA Transactions*, 78:10 – 20, 2018. Advanced Methods in Control and Signal Processing for Complex Marine Systems.

[189] M. Zhang, T. Wang, T. Tang, M. Benbouzid, and D. Diallo. An imbalance fault detection method based on data normalization and emd for marine current turbines. *ISA Transactions*, 68:302 – 312, 2017.

[190] Y. Gao, M. Karimi, A. Kudreyko, and W. Song. Sparse optimistic based on improved admm and the minimum entropy deconvolution for the early weak fault diagnosis of bearings in marine systems. *ISA Transactions*, 78:98 – 104, 2018.

[191] A. Silva, S. Gupta, A. Bazzi, and A. Ulatowski. Wavelet-based information filtering for fault diagnosis of electric drive systems in electric ships. *ISA Transactions*, 78:105 – 115, 2018. Advanced Methods in Control and Signal Processing for Complex Marine Systems.

[192] Y. Wang, K. Wang, and M. Abdel-Maksoud. noisenet: A neural network to predict marine propellers' underwater radiated noise. *Ocean Engineering*, 236: 109542, 2021.

[193] S. Gaggero, A. Coppede, D. Villa, G. Vernengo, and L. Bonfiglio. A data-driven probabilistic learning approach for the prediction of controllable pitch propellers performance. In *MARINE VIII: proceedings of the VIII International Conference on Computational Methods in Marine Engineering*, pages 544–555. CIMNE, 2019.

[194] F. Vesting and R.E. Bensow. On surrogate methods in propeller optimisation. *Ocean engineering*, 88:214–227, 2014.

[195] S.Y Kung. *Kernel methods and machine learning*. Cambridge University Press, 2014.

[196] R.O. Duda, P.E. Hart, et al. *Pattern classification and scene analysis*, volume 3. Wiley, 1973.

[197] T. Kailath. *Linear systems*, volume 156. Prentice-Hall, 1980.

[198] T. Mitchell. *Machine learning*. McGraw Hill, 1997.

[199] V. Vapnik. *Statistical learning theory*. Wiley, 1998.

[200] S. Shalev-Shwartz and S. Ben-David. *Understanding machine learning: From theory to algorithms*. Cambridge university press, 2014.

[201] W. Zhao. Research on the deep learning of the small sample data based on transfer learning. In *AIP Conference Proceedings*, 2017.

[202] Y. Wang and Q. Yao. Few-shot learning: A survey. *arxiv.org/abs/1904.05046*, 2019.

[203] I. Goodfellow, Y. Bengio, and A. Courville. *Deep learning*. MIT press, 2016.

[204] L. Oneto. *Model Selection and Error Estimation in a Nutshell*. Springer science & business media, 2020.

[205] M. Mohri, A. Rostamizadeh, and A. Talwalkar. *Foundations of machine learning*. MIT press, 2018.

[206] A.N. Tikhonov and V.Y. Arsenin. *Methods for solving ill-posed problems*. Nauka, 1979.

[207] L. Bonfiglio, P. Perdikaris, S. Brizzolara, and G.E. Karniadakis. A multi-fidelity framework for investigating the performance of super-cavitating hydrofoils under uncertain flow conditions. In *19th AIAA Non-Deterministic Approaches Conference*, page 1328, 2017.

[208] L. Bonfiglio, P. Perdikaris, S. Brizzolara, and G.E. Karniadakis. Multi-fidelity optimization of super-cavitating hydrofoils. *Computer Methods in Applied Mechanics and Engineering*, 332:63–85, 2018.

[209] L. Bonfiglio, P. Perdikaris, J. del Águila, and G.E. Karniadakis. A probabilistic framework for multidisciplinary design: Application to the hydrostructural optimization of supercavitating hydrofoils. *International Journal for Numerical Methods in Engineering*, 116(4):246–269, 2018.

[210] J.O. Royset, L. Bonfiglio, G. Vernengo, and S. Brizzolara. Risk-adaptive set-based design and applications to shaping a hydrofoil. *Journal of Mechanical Design*, 139(10):101403, 2017.

[211] K. Koushan. Prediction of propeller induced pressure pulses using artificial neural networks. In *1st International Conference on Computer Application and Information Technology in Maritime Industries*, pages 248–254, 2000.

[212] R. Roddy, D. Hess, and W. Falleer. Utilizing neural networks to predict forces and moments on a submarine propeller. In *46th AIAA Aerospace Sciences Meeting and Exhibit*, page 888, 2008.

[213] D. Calcagni, F. Salvatore, G. Bernardini, and M. Miozzi. Automated marine propeller design combining hydrodynamics models and neural networks. In *1st International Symposium on Fishing Vessel Energy Efficiency*, pages 18–20, 2010.

[214] G. Kuiper. The wageningen propeller series. Technical report, Maritime Research Institute Netherlands, 1992.

[215] J.W. Jiang, Y. Yang, T.W. Ren, F. Wang, and W.X. Huang. Evolutionary optimisation for reduction of the low-frequency discrete-spectrum force of marine propeller based on a data-driven surrogate model. *Journal of Marine Science and Engineering*, 9(1):18, 2021.

[216] L. He, Y. Tian, and SA. Kinnas. Mpuf-3a (version 3.1) user's manual and documentation 11-1. Technical report, Ocean Engineering, University of Texas at Austin, 2011.

[217] H. Sun, J. Young, and S.A. Kinnas. Hullfpp (version 1.3) hull field point potential–user's manual. Technical report, Report, 2004.

[218] N.X. Lu, R.E. Bensow, and G. Bark. Large eddy simulation of cavitation development on highly skewed propellers. *Journal of Marine Science and Technology*, 19(2):197–214, 2014.

[219] S. Gaggero, G. Vernengo, and D. Villa. A two-fidelity level approach for marine propeller design. In *9th Conference on Computational Methods in Marine Engineering*, 2021.

[220] Siemens Digital Industries Software. Simcenter STAR-CCM+ User Guide, version 2021.1. In *Adaptive Mesh Refinement for Overset Meshes*, pages 3067–3070. Siemens, 2021.

[221] F. Cipollini, F. Miglianti, L. Oneto, G. Tani, M. Viviani, and D. Anguita. Cavitation noise spectra prediction with hybrid models. In *INNS Big Data and Deep Learning conference*, pages 152–157. Springer, 2019.

[222] F. Cipollini, F. Miglianti, L. Oneto, G. Tani, and M. Viviani. Hybrid model for cavitation noise spectra prediction. In *2019 International Joint Conference on Neural Networks (IJCNN)*, pages 1–8. IEEE, 2019.

[223] L. Oneto, F. Cipollini, L. Miglianti, G. Tani, S. Gaggero, M. Viviani, and A. Coraddu. Deep learning for cavitating marine propeller noise prediction at design stage. In *2020 International Joint Conference on Neural Networks*, pages 1–10. IEEE, 2020.

[224] S. Gaggero, M. Viviani, G. Tani, F. Conti, P. Becchi, and F. Valdenazzi. Comparison of different approaches for the design and analysis of ducted propellers. In *5th International Conference on Computational Methods in Marine Engineering*, pages 723–736, 2013.

[225] J. Baxter. A model of inductive bias learning. *Journal of artificial intelligence research*, 12:149–198, 2000.

[226] R. Caruana. Multitask learning. *Machine learning*, 28(1):41–75, 1997.

[227] S. Gaggero and S. Brizzolara. A panel method for trans-cavitating marine propellers. In *7th International Symposium on Cavitation*, 2009.

[228] L.E. Jones, R.D. Sandberg, and N.D. Sandham. Direct numerical simulations of forced and unforced separation bubbles on an airfoil at incidence. *Journal of Fluid Mechanics*, 602:175–207, 2008.

[229] R.D. Sandberg, L.E. Jones, N.D. Sandham, and P.F. Joseph. Direct numerical simulations of tonal noise generated by laminar flow past airfoils. *Journal of Sound and Vibration*, 320(4-5):838–858, 2009.

[230] T. Lloyd. *Large eddy simulations of inflow turbulence noise: application to tidal turbines*. PhD thesis, University of Southampton, 2013.

[231] T. Evgeniou and M. Pontil. Regularized multi–task learning. In *10th international conference on Knowledge discovery and data mining*, pages 109–117, 2004.

[232] B.J. Bakker and T.M. Heskes. Task clustering and gating for bayesian multitask learning. *Journal of Machine Learning Research*, 2003.

[233] A. Argyriou, T. Evgeniou, and M. Pontil. Convex multi-task feature learning. *Machine learning*, 73(3):243–272, 2008.

[234] P. Duboue. *The art of feature engineering: Essentials for machine learning*. Cambridge University Press, 2020.

[235] L. Breiman. Random forests. *Machine learning*, 45(1):5–32, 2001.

[236] T. Chen and C. Guestrin. Xgboost: A scalable tree boosting system. In *ASM SIGKDD international conference on knowledge discovery and data mining*, 2016.

[237] J. Shawe-Taylor and N. Cristianini. *Kernel methods for pattern analysis*. Cambridge university press, 2004.

[238] G. Huang, H. Zhou, X. Ding, and R. Zhang. Extreme learning machine for regression and multiclass classification. *IEEE Transactions on Systems, Man, and Cybernetics, Part B (Cybernetics)*, 42(2):513–529, 2011.

[239] C.M. Bishop et al. *Neural networks for pattern recognition*. Oxford university press, 1995.

[240] D. Cireşan, U. Meier, J. Masci, and J. Schmidhuber. A committee of neural networks for traffic sign classification. In *International joint conference on neural networks*, 2011.

[241] A. Hekler, J. S. Utikal, A. H. Enk, W. Solass, and Others. Deep learning outperformed 11 pathologists in the classification of histopathological melanoma images. *European Journal of Cancer*, 118:91–96, 2019.

[242] D. Silver, J. Schrittwieser, K. Simonyan, et al. Mastering the game of go without human knowledge. *Nature*, 550(7676):354–359, 2017.

[243] J. Jumper, R. Evans, A. Pritzel, T. Green, and Others. Highly accurate protein structure prediction with alphafold. *Nature*, 596(7873):583–589, 2021.

[244] K. Grace, J. Salvatier, A. Dafoe, B. Zhang, and O. Evans. Viewpoint: When will AI exceed human performance? evidence from AI experts. *Journal of Artificial Intelligence Research*, 62:729–754, 2018.

[245] C. Molnar. *Interpretable machine learning*. Lulu.com, 2020.

[246] B. Biggio and F. Roli. Wild patterns: Ten years after the rise of adversarial machine learning. *Pattern Recognition*, 84:317–331, 2018.

[247] R. Duan, X. Ma, Y. Wang, J. Bailey, A. K. Qin, and Y. Yang. Adversarial camouflage: Hiding physical-world attacks with natural styles. In *IEEE/CVF Conference on Computer Vision and Pattern Recognition*, 2020.

[248] B. Schölkopf, A.J. Smola, F. Bach, et al. *Learning with kernels: support vector machines, regularization, optimization, and beyond*. MIT press, 2002.

[249] C. K. Williams and C. E. Rasmussen. *Gaussian processes for machine learning*. MIT press, 2006.

[250] L. Rokach. *Ensemble learning: Pattern classification using ensemble methods.* World Scientific, 2019.

[251] A.J. Fraser. The prediction and minimisation of propeller induced waterborne noise. Technical report, British Maritime Technology Limited, Hydromechanics Division, Computational Hydromechanics Department, 1986.

[252] A.C. Takinacı, E. Korkut, M. Atlar, E.J. Glover, and I. Paterson. Cavitation observation and noise measurements with model propeller of a fisheries research vessel. Technical report, Department of Marine Technology, University of Newcastle upon Tyne, UK, 2000.

[253] K. Kimura, T. Kawamura, Z. Huang, A. Fujii, and T. Taketani. Study on unsteady cavitating flow simulation around marine propeller using a rans cfd code. In *7th International Symposium on Cavitation (CAV2009)*, 2009.

[254] S. Gaggero, D. Villa, and S. Brizzolara. Rans and panel method for unsteady flow propeller analysis. *Journal of Hydrodynamics, Ser. B*, 22(5):564–569, 2010.

[255] S. Gaggero and D. Villa. Cavitating propeller performance in inclined shaft conditions with openfoam: Pptc 2015 test case. *Journal of Marine Science and Application*, 17(1):1–20, 2018.

[256] C.E. Brennen. *Cavitation and bubble dynamics.* Cambridge University Press, 2014.

[257] L.E. Schwer. An overview of the ptc 60/v&v 10: guide for verification and validation in computational solid mechanics. *Engineering with Computers*, 23(4): 245–252, 2007.

[258] W.L. Oberkampf, T.G. Trucano, and C. Hirsch. Verification, validation, and predictive capability in computational engineering and physics. *Applied Mechanics Reviews*, 57(5):345–384, 2004.

[259] MATLAB. *version 9.11.0 (R2021b).* The MathWorks Inc., Natick, Massachusetts, 2021.

[260] S. Gaggero and D. Villa. Steady cavitating propeller performance by using openfoam, starccm+ and a boundary element method. *Proceedings of the Institution of Mechanical Engineers, Part M: Journal of Engineering for the Maritime Environment*, 231(2):411–440, 2017.

[261] S. Gaggero, D. Villa, and M. Viviani. An investigation on the discrepancies between ranse and bem approaches for the prediction of marine propeller unsteady performances in strongly non-homogeneous wakes. In *International Conference on Offshore Mechanics and Arctic Engineering*, 2014.

[262] S. Gaggero, G. Dubbioso, D. Villa, R. Muscari, and M. Viviani. Propeller modeling approaches for off–design operative conditions. *Ocean Engineering*, 178: 283–305, 2019.

[263] Inc. The MathWorks. Global optimisation toolbox: For use with matlab 9.11.0 (r2021b). `https://nl.mathworks.com/help/gads/`, 2021.

[264] C.D. Ohl, T. Kurz, R. Geisler, O. Lindau, and W. Lauterborn. Bubble dynamics, shock waves and sonoluminescence. *Philosophical Transactions of the Royal Society of London. Series A: Mathematical, Physical and Engineering Sciences*, 357(1751):269–294, 1999.

[265] K. Johansen, J.H. Song, K. Johnston, and P. Prentice. Deconvolution of acoustically detected bubble-collapse shock waves. *Ultrasonics*, 73:144–153, 2017.

[266] ITTC. Fresh water and seawater properties. In *Recommended Procedures and Guidelines 7.5-01-02-03 International Towing Tank Conference*, 2011.

[267] M. Renilson, R. Leaper, and O. Boisseau. Hydro-acoustic noise from merchant ships–impacts and practical mitigation techniques. In *3rd International symposium on marine propulsors*, volume 13, pages 201–208, 2013.

[268] J.E. Kerwin, S.D. Lewis, and S. Kobayashi. Systematic experiments to determine the influence of skew and rake on hull vibratory excitation due to transient

cavitation. Technical report, Society of Naval Architects and Marine Engineers, 1978.

[269] M.A. Mossad and W. Yehia. Skewed propeller design for minimum induced vibrations. In *1st International Symposium on Naval Architecture and Maritime*, pages 24–25, 2011.

[270] A. Ebrahimi, A.H. Razaghian, M.S. Seif, F. Zahedi, and A. Nouri-Borujerdi. A comprehensive study on noise reduction methods of marine propellers and design procedures. *Applied Acoustics*, 150:55–69, 2019.

[271] O. Asimakopoulos, A. Airis, and P. Kaklis. Effects of propeller geometry on cavitation. *University of Strathclyde*, pages 1–15, 2016.

[272] G. Kuiper. Scale effects on propeller cavitation inception. In *12th International symposium on Naval Hydrodynamics*, pages 400–429, 1978.

[273] P. van Oossanen. A method for minimizing the occurrence of cavitation on propellers in a wake. *International Shipbuilding Progress*, 18(205):321–333, 1971.

[274] A. Konno, K. Wakabayashi, H. Yamaguchi, M. Maeda, N. Ishii, S. Soejima, and K. Kimura. On the mechanism of the bursting phenomena of propeller tip vortex cavitation. *Journal of marine science and technology*, 6(4):181–192, 2002.

[275] Y. Zhao, Q. Fu, R. Zhu, G. Zhang, C. Wang, and X. Wang. Transient process and micro-mechanism of hydrofoil cavitation collapse. *Processes*, 8(11):1387, 2020.

[276] ITTC Specialist Committee on Hydrodynamic Noise. Model scale cavitation test. In *Recommended Procedures and Guidelines 7.5-01-02-05 International Towing Tank Conference*, 2017.

[277] S. Gaggero. Numerical design of a rim-driven thruster using a rans-based optimization approach. *Applied Ocean Research*, 94:101941, 2020.

[278] S. P. Adam, S. A. N. Alexandropoulos, P. M. Pardalos, and M. N. Vrahatis. No free lunch theorem: A review. *Approximation and optimization*, pages 57–82, 2019.

[279] C.M. Bishop. *Pattern recognition and machine learning*. Springer science & business media, 2006.

[280] S. S. Keerthi and C. J. Lin. Asymptotic behaviors of support vector machines with gaussian kernel. *Neural computation*, 15(7):1667–1689, 2003.

[281] M. Fernández-Delgado, E. Cernadas, S. Barro, and D. Amorim. Do we need hundreds of classifiers to solve real world classification problems? *The Journal of machine learning research*, 15(1):3133–3181, 2014.

[282] M. Wainberg, B. Alipanahi, and B. J. Frey. Are random forests truly the best classifiers? *The Journal of Machine Learning Research*, 17(1):3837–3841, 2016.

[283] P. Germain, A. Lacasse, F. Laviolette, M. Marchand, and J.F. Roy. Risk bounds for the majority vote: From a pac-bayesian analysis to a learning algorithm. *arXiv preprint arXiv:1503.08329*, 2015.

[284] Y. Amit and D. Geman. Shape quantization and recognition with randomized trees. *Neural computation*, 9(7):1545–1588, 1997.

[285] L. Breiman. Bagging predictors. *Machine learning*, 24(2):123–140, 1996.

[286] L. Oneto, A. Coraddu, P. Sanetti, O. Karpenko, F. Cipollini, T. Cleophas, and D. Anguita. Marine safety and data analytics: Vessel crash stop maneuvering performance prediction. In *International conference on artificial neural networks*, pages 385–393. Springer, 2017.

[287] I. Orlandi, L. Oneto, and D. Anguita. Random forests model selection. In *24th European Symposium on Artificial Neural Networks, Computational Intelligence and Machine Learning*, pages 441–446, 2016.

[288] F. Rosenblatt. The perceptron: a probabilistic model for information storage and organization in the brain. *Psychological review*, 65(6):386, 1958.

[289] D. E. Rumelhart, G. E. Hinton, and R. J. Williams. Learning representations by back-propagating errors. *Nature*, 323(6088):533–536, 1986.

[290] G. Cybenko. Approximation by superpositions of a sigmoidal function. *Mathematics of control, signals and systems*, 2(4):303–314, 1989.

[291] G.B. Huang, D.H. Wang, and Y. Lan. Extreme learning machines: a survey. *International journal of machine learning and cybernetics*, 2(2):107–122, 2011.

[292] G. Huang, G.B. Huang, S. Song, and K. You. Trends in extreme learning machines: A review. *Neural Networks*, 61:32–48, 2015.

[293] G.B. Huang. An insight into extreme learning machines: random neurons, random features and kernels. *Cognitive Computation*, 6(3):376–390, 2014.

[294] G.B. Huang. What are extreme learning machines? filling the gap between frank rosenblatt's dream and john von neumann's puzzle. *Cognitive Computation*, 7 (3):263–278, 2015.

[295] G.B. Huang, M.B. Li, L. Chen, and C.K. Siew. Incremental extreme learning machine with fully complex hidden nodes. *Neurocomputing*, 71(4-6):576–583, 2008.

[296] G.B. Huang, L. Chen, C.K. Siew, et al. Universal approximation using incremental constructive feedforward networks with random hidden nodes. *IEEE Transactions on Neural Networks*, 17(4):879–892, 2006.

[297] G.B. Huang, Q.Y. Zhu, and C.K. Siew. Extreme learning machine: a new learning scheme of feedforward neural networks. In *2004 IEEE international joint conference on neural networks*, volume 2, pages 985–990. Ieee, 2004.

[298] L. Kasun, H. Zhou, G.B. Huang, and C.M. Vong. Representational learning with elms for big data. *IEEE Intelligent Systems*, 28:31–34, 2013.

[299] J. Tang, C. Deng, and G.B. Huang. Extreme learning machine for multilayer perceptron. *IEEE transactions on neural networks and learning systems*, 27(4): 809–821, 2015.

[300] M.D. Tissera and M.D. McDonnell. Deep extreme learning machines: supervised autoencoding architecture for classification. *Neurocomputing*, 174:42–49, 2016.

[301] Y. Bengio. *Learning deep architectures for AI.* Now Publishers Inc, 2009.

[302] Y. Bengio, A. Courville, and P. Vincent. Representation learning: A review and new perspectives. *IEEE transactions on pattern analysis and machine intelligence*, 35(8):1798–1828, 2013.

[303] H. Zhou, G.B. Huang, Z. Lin, H. Wang, and Y.C. Soh. Stacked extreme learning machines. *IEEE transactions on cybernetics*, 45(9):2013–2025, 2014.

[304] F. Pedregosa, G. Varoquaux, A. Gramfort, V. Michel, B. Thirion, O. Grisel, M. Blondel, P. Prettenhofer, R. Weiss, V. Dubourg, J. Vanderplas, A. Passos, D. Cournapeau, M. Brucher, M. Perrot, and E. Duchesnay. Scikit-learn: Machine learning in Python. `https://scikit-learn.org/stable/index.html`, 2011.

[305] A. Paszke, S. Gross, F. Massa, A. Lerer, J. Bradbury, G. Chanan, T. Killeen, Z. Lin, et al. Pytorch: An imperative style, high-performance deep learning library. In *Advances in Neural Information Processing Systems 32*, pages 8024–8035. Curran Associates, Inc., 2019.

[306] D. Dua and C. Graff. UCI machine learning repository, 2017. URL `http://archive.ics.uci.edu/ml`.

[307] J.H. Friedman. *The elements of statistical learning: Data mining, inference, and prediction.* Springer Science & Business Media, 2017.

[308] G. Casella and R.L. Berger. *Statistical inference.* Cengage Learning, 2021.

[309] N. Reid and D.R. Cox. On some principles of statistical inference. *International Statistical Review*, 83(2):293–308, 2015.

[310] L. Oneto. Model selection and error estimation without the agonizing pain. *WIREs Data Mining and Knowledge Discovery*, 2018.

[311] D. Anguita, A. Ghio, L. Oneto, and S. Ridella. In-sample and out-of-sample model selection and error estimation for support vector machines. *IEEE Transactions on Neural Networks and Learning Systems*, 23(9):1390–1406, 2012.

[312] S. Arlot and A. Celisse. A survey of cross-validation procedures for model selection. *Statistics surveys*, 4:40–79, 2010.

[313] A. Inoue and L. Kilian. In-sample or out-of-sample tests of predictability: Which one should we use? *Econometric Reviews*, 23(4):371–402, 2005.

[314] R. Kohavi et al. A study of cross-validation and bootstrap for accuracy estimation and model selection. In *International Joint Conference on Artificial Intelligence*, volume 14, pages 1137–1145. Montreal, Canada, 1995.

[315] K. Fukunaga and D.M. Hummels. Leave-one-out procedures for nonparametric error estimates. *IEEE Transactions on Pattern Analysis and Machine Intelligence*, 11(4):421–423, 1989.

[316] B. Efron and R.J. Tibshirani. *An introduction to the bootstrap*. CRC press, 1994.

[317] L. Rosasco, E. De Vito, A. Caponnetto, M. Piana, and A. Verri. Are loss functions all the same? *Neural computation*, 16(5):1063–1076, 2004.

[318] C. J. Willmott and K. Matsuura. Advantages of the mean absolute error (mae) over the root mean square error (rmse) in assessing average model performance. *Climate research*, 30(1):79–82, 2005.

[319] L. Shao, A. Mahajan, T. Schreck, and D. J. Lehmann. Interactive regression lens for exploring scatter plots. In *Computer Graphics Forum*, 2017.

[320] F.R. Gilmore. The growth or collapse of a spherical bubble in a viscous compressible liquid. Technical report, California Institute of Technology, 1952.

[321] S. Boyd and L. Vandenberghe. *Convex optimization*. Cambridge university press, 2004.

[322] A.R. Conn, K. Scheinberg, and L.N. Vicente. *Introduction to derivative-free optimization*. SIAM, 2009.

[323] P. Galinier, J.P. Hamiez, J.K. Hao, and D. Porumbel. *Handbook of optimization*. Springer science & business media, 2013.

[324] C.A. Floudas and P. Pardalos. *Encyclopedia of optimization*. Springer Science & Business Media, 2008.

[325] M. Kokkolaras. When, why, and how can derivative-free optimization be useful to computational engineering design? *Journal of Mechanical Design*, 142(1):010301, 2020.

[326] M. Kokkolaras, C. Audet, and J.E. Dennis. Mixed variable optimization of the number and composition of heat intercepts in a thermal insulation system. *Optimization and Engineering*, 2(1):5–29, 2001.

[327] G. Marwaha and M. Kokkolaras. System-of-systems approach to air transportation design using nested optimization and direct search. *Structural and Multidisciplinary Optimization*, 51(4):885–901, 2015.

[328] A.E. Gheribi, J.P. Harvey, E. Bélisle, C. Robelin, P. Chartrand, A.D. Pelton, C.W. Bale, and S. Le Digabel. Use of a biobjective direct search algorithm in the process design of material science applications. *Optimization and Engineering*, 17(1):27–45, 2016.

[329] A.E. Gheribi, A.D. Pelton, E. Bélisle, S. Le Digabel, and J.P. Harvey. On the prediction of low-cost high entropy alloys using new thermodynamic multi-objective criteria. *Acta Materialia*, 161:73–82, 2018.

[330] D.E. Ciaurri, T. Mukerji, and L.J. Durlofsky. Derivative-free optimization for oil field operations. In *Computational Optimization and Applications in Engineering and Industry*, pages 19–55. Springer science & business media, 2011.

[331] D.E. Ciaurri, O.J. Isebor, and L.J. Durlofsky. Application of derivative-free methodologies to generally constrained oil production optimization problems. *Procedia Computer Science*, 1(1):1301–1310, 2010.

[332] N. Le Carrer, S. Ferson, and P.L. Green. Optimising cargo loading and ship scheduling in tidal areas. *European Journal of Operational Research*, 280(3): 1082–1094, 2020.

[333] S. Li, J. Liu, R.R. Negenborn, and F. Ma. Optimizing the joint collision avoidance operations of multiple ships from an overall perspective. *Ocean Engineering*, 191: 106511, 2019.

[334] A. Serani, G. Fasano, G. Liuzzi, S. Lucidi, U. Iemma, E. Campana, F. Stern, and M. Diez. Ship hydrodynamic optimization by local hybridization of deterministic derivative-free global algorithms. *Applied Ocean Research*, 59:115–128, 2016.

[335] A. Papanikolaou. *A holistic approach to ship design.* Springer science & business media, 2019.

[336] S. Koziel and S. Yang. *Computational optimization, methods and algorithms.* Springer science & business media, 2011.

[337] X. Hu and R. Eberhart. Solving constrained nonlinear optimization problems with particle swarm optimization. In *6th world multiconference on systemics, cybernetics and informatics*, 2002.

[338] Rezaee J.A. and J. Jasni. Parameter selection in particle swarm optimisation: a survey. *Journal of Experimental & Theoretical Artificial Intelligence*, 25(4): 527–542, 2013.

[339] C. M. Martinez and D. Cao. *iHorizon-Enabled Energy management for electrified vehicles.* Butterworth-Heinemann, 2018.

[340] E.G. Talbi. *Metaheuristics: from design to implementation*, volume 74. John Wiley & Sons, 2009.

[341] R. Eberhart and J. Kennedy. Particle swarm optimization. In *IEEE international conference on neural networks*, 1995.

[342] B. Li and R.Y. Xiao. The particle swarm optimization algorithm: How to select the number of iteration. In *Third International Conference on Intelligent Information Hiding and Multimedia Signal Processing (IIH-MSP 2007)*, volume 2, pages 191–196. IEEE, 2007.

[343] M.E. Pedersen. Good parameters for particle swarm optimization. Technical report, Hvass Laboratory, Copenhagen, Denmark, Tech. Rep. HL1001, 2010.

[344] M.E. Pedersen and A.J. Chipperfield. Simplifying particle swarm optimization. *Applied Soft Computing*, 10(2):618–628, 2010.

[345] A. El-Gallad, M. El-Hawary, A. Sallam, and A. Kalas. Enhancing the particle swarm optimizer via proper parameters selection. In *IEEE Canadian Conference on Electrical and Computer Engineering*, volume 2, pages 792–797. IEEE, 2002.

[346] E. Mezura-Montes and C.A. Coello. Constraint-handling in nature-inspired numerical optimization: past, present and future. *Swarm and Evolutionary Computation*, 1(4):173–194, 2011.

[347] I.C. Trelea. The particle swarm optimization algorithm: convergence analysis and parameter selection. *Information processing letters*, 85(6):317–325, 2003.

[348] Y. Shi and R.C. Eberhart. Parameter selection in particle swarm optimization. In *International conference on evolutionary programming*, pages 591–600. Springer science & business media, 1998.

[349] M. Juneja and S.K. Nagar. Particle swarm optimization algorithm and its parameters: A review. In *International Conference on Control, Computing, Communication and Materials (ICCCCM)*, pages 1–5. IEEE, 2016.

[350] Y. Feng, G.F. Teng, A.X. Wang, and Y.M. Yao. Chaotic inertia weight in particle swarm optimization. In *2nd International Conference on Innovative Computing, Information and Control*, pages 475–485. IEEE, 2007.

[351] W. Han, P. Yang, H. Ren, and J. Sun. Comparison study of several kinds of inertia weights for pso. In *IEEE international conference on progress in informatics and computing*, volume 1, pages 280–284. IEEE, 2010.

[352] J. Kennedy and R. Mendes. Neighborhood topologies in fully informed and best-of-neighborhood particle swarms. *IEEE Transactions on Systems, Man, and Cybernetics, Part C (Applications and Reviews)*, 36(4):515–519, 2006.

[353] H. Liu and H. Motoda. *Computational methods of feature selection*. CRC Press, 2007.

[354] I. Guyon and A. Elisseeff. An introduction to variable and feature selection. *Journal of machine learning research*, 3:1157–1182, 2003.

[355] P. Good. *Permutation tests: a practical guide to resampling methods for testing hypotheses*. Springer Science & Business Media, 2013.

[356] D. François, V. Wertz, and M. Verleysen. The permutation test for feature selection by mutual information. In *European Symposium on Artificial Neural Networks, Computational Intelligence and Machine Learning*, 2006.

[357] A. Fisher, C. Rudin, and F. Dominici. All models are wrong, but many are useful: Learning a variable's importance by studying an entire class of prediction models simultaneously. *Journal of Machine Learning Research*, 20(177):1–81, 2019.

[358] T. Spruegel, T. Schröppel, S. Wartzack, et al. Generic approach to plausibility checks for structural mechanics with deep learning. In *21st International Conference on Engineering Design Vol 1: Resource Sensitive Design, Design Research Applications and Case Studies*, pages 299–308, 2017.

[359] M. Lutter, C. Ritter, and J. Peters. Deep lagrangian networks: Using physics as model prior for deep learning. In *7th International Conference on learning Representations*, 2019.

[360] M. Atlar. Recent upgrading of marine testing facilities at newcastle university. In *Second international conference on advanced model measurement technology for the EU maritime industry*, pages 4–6, 2011.

[361] LIFE-PIAQUO: Underwater noise impact reduction of the maritime traffic and real-time adaptation to ecosystems. http://lifepiaquo-urn.eu/en/home/, 2019. Accessed: 2021-11-01.

[362] A. Emerson. Propeller design and model experiments. *Transactions of the North-east coast institution of engineers and shipbuilders*, 94:199–234, 1978.

[363] A. Angelopoulos, P.A. Fitzsimmons, and A.Y. Odabasi. A semi-empirical method for propeller broad-band noise. Technical report, British Maritime Technology Limited, 1988.

[364] D. Bertetta, S. Brizzolara, S. Gaggero, M. Viviani, and L. Savio. Cpp propeller cavitation and noise optimization at different pitches with panel code and validation by cavitation tunnel measurements. *Ocean engineering*, 53:177–195, 2012.

[365] C. Hsin. *Development and analysis of panel methods for propellers in unsteady flow*. PhD thesis, Massachusetts Institute of Technology, 1990.

[366] S. Gaggero. *Development of a potential panel method for the analysis of propellers performances in cavitating and supercavitating conditions*. PhD thesis, University of Genoa, Italy, 2010.

[367] J.A. Geurst. *Linearized theory of two-dimensional cavity flows*. PhD thesis, Delft University of Technology, 1961.

[368] M.S. Plesset. Dynamics of cavitation bubbles. *Journal of Applied Mechanics*, 16: 228–231, 1948.

[369] J.B. Keller and M. Miksis. Bubble oscillations of large amplitude. *The Journal of the Acoustical Society of America*, 68(2):628–633, 1980.

[370] H.G. Flynn. Cavitation dynamics. i. a mathematical formulation. *The Journal of the Acoustical Society of America*, 57(6):1379–1396, 1975.

[371] T. Leighton. *The acoustic bubble*. Southampton University Academic press, 2012.

[372] M. Renardy and R.C. Rogers. *An introduction to partial differential equations*, volume 13. Springer Science & Business Media, 2006.

[373] R.N. Bracewell. *The Fourier transform and its applications*. McGraw-Hill New York, 1986.

[374] International Organization for Standardization. Iso 18405:underwater acoustics-terminology, 2017.

[375] K.R. Suhrbier. Report of the cavitation committee. In *18th International Towing Tank Conference*, pages 159–269, 1987.

[376] P.G. Saffman. *Vortex dynamics*. Cambridge university press, 1992.

[377] F. Proctor, N. Ahmad, G. Switzer, and F. Limon Duparcmeur. Three-phased wake vortex decay. In *AIAA Atmospheric and Space Environments Conference*, 2010.

[378] T. Hommes, J. Bosschers, and H.W. Hoeijmakers. Evaluation of the radial pressure distribution of vortex models and comparison with experimental data. In *Journal of Physics: Conference Series*, volume 656, page 012182, 2015.

[379] B.W. McCormick. On cavitation produced by a vortex trailing from a lifting surface. *Journal of basic engineering*, 84.3:369–378, 1962.

[380] Y.T. Shen, S. Gowing, and S. Jessup. Tip vortex cavitation inception scaling for high reynolds number applications. *Journal of Fluids Engineering*, 131(7), 2009.

[381] L. Prandtl, O.G. Tietjens, and J.P. Den Hartog. *Applied hydro-and aeromechanics*, volume 35. Dover New York, 1957.

[382] M. Minnaert. On musical air-bubbles and the sounds of running water. *Journal of Science*, 16:235–248, 1933.

[383] F. Proctor. The nasa-langley wake vortex modelling effort in support of an operational aircraft spacing system. In *36th AIAA Aerospace Sciences Meeting and Exhibit*, page 589, 1998.

[384] D.C. Burnham and J.N. Hallock. Chicago monostatic acoustic vortex sensing system, volume iv: Wake vortex decay. Technical report, Transportation Systems Center, Cambridge, 1982.

[385] I. De Visscher, L. Bricteux, and G. Winckelmans. Aircraft vortices in stably stratified and weakly turbulent atmospheres: Simulation and modeling. *AIAA journal*, 51(3):551–566, 2013.

[386] G.S. Winckelmans, F. Thirifay, and P. Ploumhans. Effect of non-uniform wind shear onto vortex wakes: parametric models for operational systems and comparison with cfd studies. In *4th WakeNet Workshop on Wake Vortex Encounter*, 2000.

[387] L. Jacquin, D. Fabre, P. Geffroy, and E. Coustols. The properties of a transport aircraft wake in the extended near field-an experimental study. In *39th Aerospace Sciences Meeting and Exhibit*, page 1038, 2001.

[388] N. Cristianini, J. Shawe-Taylor, et al. *An introduction to support vector machines and other kernel-based learning methods*. Cambridge university press, 2000.

[389] V. Vapnik. *The nature of statistical learning theory*. Springer science & business media, 1999.

[390] M.G. Genton. Classes of kernels for machine learning: a statistics perspective. *Journal of machine learning research*, 2(Dec):299–312, 2001.

[391] A. Ben-Hur and W.S. Noble. Kernel methods for predicting protein–protein interactions. *Bioinformatics*, 21(1):138–146, 2005.

[392] M.A. Aizerman. Theoretical foundations of the potential function method in pattern recognition learning. *Automation and remote control*, 25:821–837, 1964.

[393] B.E. Boser, I.M. Guyon, and V. Vapnik. A training algorithm for optimal margin classifiers. In *5th annual workshop on Computational learning theory*, pages 144–152, 1992.

[394] T. Poggio. On optimal nonlinear associative recall. *Biological Cybernetics*, 19(4): 201–209, 1975.

[395] C.J. Burges. A tutorial on support vector machines for pattern recognition. *Data mining and knowledge discovery*, 2(2):121–167, 1998.

[396] T. Hofmann, B. Schölkopf, and A.J. Smola. Kernel methods in machine learning. *The annals of statistics*, 36(3):1171–1220, 2008.

[397] V. Vapnik, S.E. Golowich, A. Smola, et al. Support vector method for function approximation, regression estimation, and signal processing. *Advances in neural information processing systems*, pages 281–287, 1997.

[398] D. Haussler. Convolution kernels on discrete structures. Technical report, University of California, Department of Computer Science, 1999.

[399] M. Collins and N. Duffy. Convolution kernels for natural language. In *Advances in neural information processing systems*, pages 625–632, 2001.

[400] T. Gärtner. A survey of kernels for structured data. *ACM SIGKDD explorations newsletter*, 5(1):49–58, 2003.

[401] A. E. Hoerl and R. W. Kennard. Ridge regression: Biased estimation for nonorthogonal problems. *Technometrics*, 12(1):55–67, 1970.

[402] R. Tibshirani. Regression shrinkage and selection via the lasso. *Journal of the Royal Statistical Society: Series B (Methodological)*, 58(1):267–288, 1996.

[403] B. Schölkopf, R. Herbrich, and A.J. Smola. A generalized representer theorem. In *International conference on computational learning theory*, pages 416–426. Springer, 2001.

[404] A. J. Smola and B. Schölkopf. A tutorial on support vector regression. *Statistics and computing*, 14(3):199–222, 2004.

[405] D.M. Young. *Iterative solution of large linear systems*. Elsevier, 2014.

[406] F. Galton. Vox populi (the wisdom of crowds). *Nature*, 75(7):450–451, 1907.

[407] J.W Tukey. *Exploratory data analysis*, volume 2. Addison - Wesley, 1977.

[408] B. Dasarathy and B.V. Sheela. A composite classifier system design: Concepts and methodology. *Proceedings of the IEEE*, 67(5):708–713, 1979.

[409] R.E. Schapire. A brief introduction to boosting. In *6th International Joint Conference on Artificial Intelligence*, volume 99, pages 1401–1406. Citeseer, 1999.

[410] R.A. Jacobs, M.I. Jordan, S.J. Nowlan, and G.E. Hinton. Adaptive mixtures of local experts. *Neural computation*, 3(1):79–87, 1991.

[411] M.I. Jordan and R.A. Jacobs. Hierarchical mixtures of experts and the em algorithm. *Neural computation*, 6(2):181–214, 1994.

[412] L. Xu, A. Krzyzak, and C.Y. Suen. Methods of combining multiple classifiers and their applications to handwriting recognition. *IEEE transactions on systems, man, and cybernetics*, 22(3):418–435, 1992.

[413] T.K. Ho, J.J. Hull, and S.N. Srihari. Decision combination in multiple classifier systems. *IEEE transactions on pattern analysis and machine intelligence*, 16(1): 66–75, 1994.

[414] G. Rogova. Combining the results of several neural network classifiers. In *Classic Works of the Dempster-Shafer Theory of Belief Functions*, pages 683–692. Springer, 2008.

[415] D.H. Wolpert. Stacked generalization. *Neural networks*, 5(2):241–259, 1992.

[416] C. Zhang and Y. Ma. *Ensemble machine learning: methods and applications*. Springer, 2012.

[417] R. Polikar. Ensemble based systems in decision making. *IEEE Circuits and systems magazine*, 6(3):21–45, 2006.

[418] L. Breiman, J.H. Friedman, R.A. Olshen, and C.J. Stone. *Classification and regression trees*. Routledge, 2017.

[419] A. Lulli, L. Oneto, and D. Anguita. Mining big data with random forests. *Cognitive Computation*, 11(2):294–316, 2019.

[420] L. Rokach and O.Z. Maimon. *Data mining with decision trees: theory and applications*, volume 69. World scientific, 2007.

[421] A.J. Izenman. Modern multivariate statistical techniques. *Regression, classification and manifold learning*, 10:978–0, 2008.

[422] S. Haykin. Neural networks: a comprehensive foundation. 1999. *Mc Millan*, pages 1–24, 2010.

[423] W.S. McCulloch and W. Pitts. A logical calculus of the ideas immanent in nervous activity. *The bulletin of mathematical biophysics*, 5(4):115–133, 1943.

[424] K. Hornik, M. Stinchcombe, and H. White. Multilayer feedforward networks are universal approximators. *Neural networks*, 2(5):359–366, 1989.

[425] C. Nwankpa, W. Ijomah, A. Gachagan, and S. Marshall. Activation functions: Comparison of trends in practice and research for deep learning. In *International Conference on Computational Sciences and Technology*, pages 781–801, 2021.

[426] F. Agostinelli, M. Hoffman, P. Sadowski, and P. Baldi. Learning activation functions to improve deep neural networks. *arXiv preprint arXiv:1412.6830*, 2014.

[427] G. Marra, D. Zanca, A. Betti, and M. Gori. Learning activation functions by means of kernel based neural networks. In *International Conference of the Italian Association for Artificial Intelligence*, pages 418–430. Springer, 2019.

[428] X. He, K. Zhao, and X. Chu. Automl: A survey of the state-of-the-art. *Knowledge-Based Systems*, 212:106622, 2021.

[429] S. Ruder. An overview of gradient descent optimization algorithms. *arXiv preprint arXiv:1609.04747*, 2016.

[430] D. Choi, C.J. Shallue, Z. Nado, J. Lee, C.J. Maddison, and G.E. Dahl. On empirical comparisons of optimizers for deep learning. *arXiv preprint arXiv:1910.05446*, 2019.

[431] S. Sun, Z. Cao, H. Zhu, and J. Zhao. A survey of optimization methods from a machine learning perspective. *IEEE transactions on cybernetics*, 50(8):3668–3681, 2019.

[432] D.P. Kingma and J. Ba. Adam: A method for stochastic optimization. In *International Conference on Learning Representations*, pages 1–13, 2015.

[433] J. Duchi, E. Hazan, and Y. Singer. Adaptive subgradient methods for online learning and stochastic optimization. *Journal of machine learning research*, 12 (7), 2011.

[434] F. Bisio, P. Gastaldo, R. Zunino, and E. Cambria. A learning scheme based on similarity functions for affective common-sense reasoning. In *2015 International Joint Conference on Neural Networks (IJCNN)*, pages 1–6. IEEE, 2015.